GRADUATE PROGRAM IN CHEMICAL ENGINEERING

Electrospun Biodegradable Nanofibers Applied to Air Filtration of Simulated SARS-CoV-2

GUSTAVO CARDOSO DA MATA

Doctoral thesis submitted to the Federal University of São Carlos as a requirement for obtaining a Doctorate in Chemical Engineering.

Area of Concentration: Environmental Control

Supervisor: Prof. PhD. Mônica Lopes Aguiar

Co-supervisor: Prof. PhD. Wanderley Pereira de Oliveira

Department of Chemical Engineering

São Carlos, 2024

UNIVERSIDADE FEDERAL DE SÃO CARLOS

Centro de Ciências Exatas e de Tecnologia
Programa de Pós-Graduação em Engenharia Química

Folha de Aprovação

Defesa de Tese de Doutorado do candidato Gustavo Cardoso da Mata, realizada em 27/05/2024.

Comissão Julgadora:

Profa. Dra. Mônica Lopes Aguiar (UFSCar)

Profa. Dra. Daniela Patricia Freire Bonfim (CEFET-MG)

Prof. Dr. Eduardo Hiromitsu Tanabe (UFSM)

Profa. Dra. Vádila Giovana Guerra Béttega (UFSCar)

Profa. Dra. Rosario Elida Suman Bretas (UFSCar)

O Relatório de Defesa assinado pelos membros da Comissão Julgadora encontra-se arquivado junto ao Programa de Pós-Graduação em Engenharia Química.

SUMMARY

GOOD TIMBER

by Douglas Malloch

"The tree that never had to fight
For sun and sky and air and light,
But stood out in the open plain
And always got its share of rain,
Never became a forest king
But lived and died a scrubby thing.

The man who never had to toil
To gain and farm his patch of soil,
Who never had to win his share
Of sun and sky and light and air,
Never became a manly man
But lived and died as he began.

Good timber does not grow with ease:
The stronger wind, the stronger trees;
The further sky, the greater length;
The more the storm, the more the strength.
By sun and cold, by rain and snow,
In trees and men good timbers grow.

Where thickest lies the forest growth,
We find the patriarchs of both.
And they hold counsel with the stars
Whose broken branches show the scars
Of many winds and much of strife.
This is the common law of life."

ACKNOWLEDGMENTS

I wanted to start by saying that, even though I'm an atheist, it was with God that I learned to be grateful.

First and foremost, to my family: I thank my nephews for the joy; to my sister for showing that it is possible; and to my mother, who like Atlas, carried our family on her shoulders.

I thank all the friends, old and new, with whom I shared laughter, ideas, and dreams, with a special hug to those who showed me my own worth.

And finally, I am grateful to the countless mentors, some brief, others eternal, but who somehow taught me to pave my own way.

Queria começar dizendo que, mesmo sendo ateu, foi com Deus que aprendi a ser grato.

Em primeiro lugar, à família: agradeço aos sobrinhos pela alegria; a minha irmã por mostrar que é possível; e a minha mãe, que como Atlas, sustentou nossa família em seus ombros.

Agradeço a todos os amigos, antigos e novos, com que compartilhei risadas, ideias e sonhos, com um abraço especial para àqueles que me mostraram meu próprio valor.

E por fim, agradeço aos inúmeros mentores e mentoras, alguns breves, outros eternos, mas que de alguma forma me ensinaram a pavimentar meu próprio caminho.

ABSTRACT

One of the lasting outcomes of the COVID-19 pandemic was the production and deposition of plastics. These materials, particularly disposable face masks, end up in the environment, releasing microplastics and other pollutants. Although the pandemic has ended, disposable face masks continue to be essential in healthcare services and major cities to mitigate the effects of increasing air pollution. This study aimed to create a viable alternative to disposable face masks made from non-degradable polymers. It utilized polyvinyl alcohol (PVA) and chitosan (CS) as natural and biodegradable polymers to produce air filters using the electrospinning technique. Solution properties, such as rheology and conductivity, were investigated using Design of Experiments (DoE), particularly Response Surface Methodology (RSM), to optimize nanofiber production, dimensions, and air filtration capabilities, achieving filtration efficiencies of up to 99%, superior to N95 face masks. Nanostructures present in our electrospun fiber mat, known as spider-nets, were tailored to further enhance the fiber mat properties. Our tests also examined the mechanical properties of the air filters, adjusting their mechanical strength and hydrophobicity, further improving our fibers to withstand higher air filtration velocities. This study has already achieved its main goals, providing a viable and biodegradable alternative to traditional discardable facemasks, complying with regulations worldwide, and contributing to the current trend among scientists to transition to more ecological materials.

RESUMO

Um dos resultados duradouros da pandemia de COVID-19 foi a produção e deposição de plásticos. Esses materiais, especialmente máscaras descartáveis, acabam no meio ambiente, liberando microplásticos e outros poluentes. Embora a pandemia tenha terminado, máscaras descartáveis continuam a ser essenciais em serviços de saúde e nas grandes cidades para mitigar os efeitos do aumento da poluição do ar. Este estudo teve como objetivo criar uma alternativa viável às máscaras descartáveis feitas de polímeros não degradáveis. Utilizou álcool polivinílico (PVA) e quitosana (CS) como polímeros naturais e biodegradáveis para produzir filtros de ar usando a técnica de eletrofiação. As propriedades da solução, como reologia e condutividade, foram investigadas utilizando o Design de Experimentos (DoE), particularmente a Metodologia de Superfície de Resposta (RSM), para otimizar a produção de nanofibras, suas dimensões e capacidades de filtragem do ar, alcançando eficiências de filtração de até 99%, superior às máscaras N95. Estruturas nanométricas presentes em nosso tapete de fibras eletrofiadas, conhecidas como teias de aranha, foram ajustadas para melhorar ainda mais as propriedades do tapete de fibras. Nossos testes também examinaram as propriedades mecânicas dos filtros de ar, ajustando sua resistência mecânica e hidrofobicidade, melhorando ainda mais nossas fibras para suportar maiores velocidades de filtração de ar. Este estudo já alcançou seus principais objetivos, fornecendo uma alternativa viável e biodegradável às máscaras descartáveis tradicionais, cumprindo com as regulamentações em todo o mundo e contribuindo para a tendência atual entre os cientistas de transitar para materiais mais ecológicos.

I

INTRODUCTION & OBJECTIVES

I - INTRODUCTION & OBJECTIVES

1.1 Introduction

The recent pandemic of COVID-19 truly changed the world perspectives about the usage of masks. The rapid transmission of aerosolized diseases, proved its potential to cause pandemics, being the use of facemasks the first barrier against its dissemination. Until the production of more robust defences, such as remedies and vaccines, the general population can only rely on facemasks as protection, at the early stages of an air transmissible pandemic disease.

As the need of protection rises, the production of polymeric disposable masks also rise. Because are cheap and easy to handle, those polymeric materials became a fast and reliable way to satisfy the supply demand. However, non-degradable polymers tend to be further discarded in the environment, generating pollutants, as microplastics. A recent winner of the Ocean Photography Awards can resume the consequences, as seen in **Figure 1.1**.

Figure 1.1: Seahorse attached to a surgical mask, captured by Nicholas Samaras, one of the winners of the Ocean Photography Awards of 2022.

In face of the new production of non-degradable polymeric masks, and the imminent danger of new pandemics in the years ahead, it is necessary the synthesis of new facemasks with natural or biodegradable polymers. Those new materials need to attend the demands and have the same level of protection provided by the non-degradable ones.

1.2 General Goals

Faced with the SARS-CoV-2 pandemic, materials capable of trapping bioaerosols suspended in the air are needed. At the same time, materials commonly applied in air filtration do not have ecological properties such as biodegradability. The present work aims to produce filter media with potential to eliminate airborne pathogens. Another goal is to create environmentally friendly materials, causing less damage to the environment.

1.3 Specific Goals

- To use the electrospinning technique to produce electrospun nanofibers able to collect efficiently particulate matter at the nanoscale dimensions present in the air;
- To use renewable materials (e.g., chitosan, cellulose and polyvinyl alcohol) as main compounds during the filter media manufacturing, as cheaper, biodegradable, and abundant materials;
- To use harmless solvents (e.g., water, acetic acid and ionic liquids) in substitution of total or partial of common organic solvents, aiming to minimize the environmental impact;
- To functionalize the filter media with biodegradable agents (e.g., essential oils, quaternary ammonium compounds) to add biocide properties to the electrospun fibers;
- To produce filter media with adequate properties to be applied on the air filtration (*i.e.*, with high global collection efficiency and low-pressure drops);
- To characterize the filter media, aiming to optimize the manufacture conditions and its properties.

II

THEORETICAL BACKGROUNDS

II – THEORETICAL BACKGROUNDS

Nanofibers Functionalized with Surfactants to Eliminate SARS-CoV-2 and Other Airborne Pathogens

Gustavo Cardoso da Mata[1,*], Daniela Sanches de Almeida[1], Wanderley Pereira de Oliveira[2], Mônica Lopes Aguiar[1]

[1] Department of Chemical Engineering, Federal University of São Carlos, Rod. Washington Luiz, km 235, SP310, São Carlos - SP, 13565-905, Brazil;

[2] Faculty of Pharmaceutical Science of Ribeirão Preto, University of São Paulo, Av. do Café s/no, CEP: 14040-903, Bairro Monte Alegre, Ribeirão Preto, SP, Brazil

[*]*Corresponding author*: gugs_cardoso@ufsj.edu.br / mlaguiar@ufscar.br

Abstract: The recent SARS-CoV-2 pandemic brought to light the difficulty in controlling the pathogenic bioaerosols present in the air. Therefore, several studies have sought efficient and mainly sustainable technologies to develop new filtering media and new biocidal and virucidal agents. Filter media composed of nanofibers stand out for having high collection efficiencies and high permeability. For this reason, they have been widely used in filters for indoor environments and in facemasks. Combined with nanofibers or conventional filtering media, the addition of quaternary ammonium surfactants to provide biocidal action proves to be an ecologically sustainable alternative. Thus, the present work reviews these filtering mechanisms, their applications, and perspectives for novel uses of these technologies in engineering and materials science.

Keywords: *SARS-CoV-2; air filters; electrospinning; bioaerosols; antimicrobial, antiviral, biocide.*

Published in: Conjecturas (FFCL-Car/UNESP) **DOI:** 10.53660/CONJ-708-A18

2.1 Introduction

Today, people spend around 90% of their time indoors, turning themselves into an "indoor generation" (EU, 2003). In this context, airborne diseases became an important issue, especially for crowded places like hospitals, universities, or public transport[1]. Even in outdoor areas, the possibility of virus spread remains. One evidence is the event on September 26th at the Rose Garden of the White House. At least eleven people were infected with the new coronavirus, including the President of the United State[2]. Therefore, protection against air contamination is crucial, improving the indoor infrastructure of buildings to preserve patients, health workers, caregivers, and people in general.

In the SARS pandemic of 2003, two of the Metropole Hotel guests in Kowloon, Hong Kong, spread the SARS-CoV-1 virus to 23 other people, from the 9th floor to the 7th floor of the building. Those people recently infected travelled to other countries spreading the virus worldwide[3]. At the start of the SARS-CoV-2 pandemic, various cruise ships with thousands of people on board imposed the passengers' isolation in their cabins, like the Diamond Princess cruise ship in Yokohama[4]. Their objective was to limit the contact and proceed with adequate hygiene methods. However, even with the isolation, many were still infected with the new coronavirus. Morawaska & Cao (2020) suggested that the ventilation system was responsible for the virus' continuous spread between the cabins[5].

The evidence of airborne transmission of diseases, proposed since the SARS pandemic in 2003[6], has become more robust in the recent pandemic[7]. Studies show that SARS-CoV-2 can remain in aerosol particles for longer than 3 hours[8]. It was also detected in the air and ventilation systems of houses[9], hospitals, nursing homes, and exhaustion of ferryboats[10].

One of the most applied methods for removing aerosols from the air is the filtration process[11]. In the cases previously mentioned, adequate air filters can minimize the disease's spread, catching and killing the virions traveling through ventilation systems. Recently, air filtration with antiviral activity has received more attention, preventing virus spread through the air. The benefits are the rapid inactivation, minimizing the number of active virions blowing off the filter media[12].

New strains of SARS-CoV-2 have been surging since the beginning of the COVID-19 pandemic. Variants like the United Kingdom strain[13], the South Africa strain[14], the Brazilian strain[15], the Indian strain[16], and the later omicron strain[17] has been motive of preoccupation. New strains showed stronger interactions with the binding receptors of the host cell, resulting in higher infectivity[18]. They spread worldwide, re-inflating the pandemic by causing new infection waves[19]. Therefore, the necessity for materials that can eliminate such bioaerosols during the traveling process is urgent.

2.2 Airborne Pathogens Spread Mechanism

The new Coronavirus (SARS-CoV-2) has 60 to 140 nm in diameter and spikes about 9 to 12 nm[20]. It possesses improvements on its spikes, making possible better affixation of the virions in carrier particles[21]. After being expelled from an infected person, its virions can be aerosolized by droplets or attach to solid particles[21]. It was

expected that the particles with an attached virion were too heavy to remain in the air and then descend to the ground[22]. However, after being expelled by the body, droplets start to evaporate their liquid portion and shrink[23–25]. Some become smaller, being more influenced by the airflow than gravity, making the droplet travel long distances[26,27], reaching distances greater than 3 m from its source[28]. Some viruses can remain infective even after hours, especially in higher relative humidity[29].

During the flight, the airborne virions can be transferred to ambient aerosols. The excellent ability to attach makes it possible for the virions to adhere to small solid particles, resulting in aerosols in the proportion of the virion size (60 to 140 nm). Minor combined aerosols (i.e., virion and particle) will reach longer distances[5]. This phenomenon is similar to fine particulate pollution suspended in the air. As finer as the particles, they can travel more distance[21], and already detected in the air near infected people[9]. This effect explains how the SARS-CoV-2 spread, primarily indoor[30], and can remain in the air for periods longer than 60 min, as shown in studies with MERS coronavirus[31].

Both aerosols and larger droplets can carry viruses[32,33]. During talking, breathing, and coughing, infected people, can generate a significant amount of submicron particles, including many viruses[34]. Studies show that 87% of exhaled particles of patients infected with influenza were minor than 1000 nm in diameter[35]. The number of particles emitted is so high that another person's inhalation is unavoidable, even when wearing surgical masks[36]. Particle size and concentration vary from one study to another and are summarized in **Table 2.1**.

Table 2.1: Data from different authors of average diameter and concentration of particles expelled during coughing, talking, or breathing.

Particle average diameter (μm)	Particle concentration (particles L^{-1})	Reference
0.09-3.00	150-2000[b]; 100-350[c]	37
0.32	14-3230[c]	38
13.5[a]; 16.0[b]	2400-5200[a]; 4-223[b]	39
3.5-5.0[b]	1100[b]; 100-1100[c]	27
1.6, 2.5, 145[b]; 1.6, 1.7, 123[a]	1, 69, 85[b]; 12, 16, 87[a]	40*
12-29[b]; <10[c]	1080[b]; 540[c]	41

[a]coughing; [b]talking; [c]breathing; *three different methods were used in this study to avail the particles size diameter and concentration.

Observations have found that aerosol particles with less than 5 μm of diameter contain more viruses than larger droplets[42,43]. A possible explanation is that smaller aerosols are produced in the lower respiratory tract that has a higher viral load during infections[44,45]. Unfortunately, particulate matter minor than 2.5 μm of diameter ($PM_{2.5}$)

can penetrate the respiratory system, reaching the alveoli and even the cardiovascular system[36,46].

2.3 Face Masks

Face masks are an item used for personal protection, and they have been used for medical purposes since the 17th century[47]. In 1900 their use was diffused, aiming to reduce nasal and oral bacteria in surgical procedures[48]. In the last decade, the use of masks on prevention of bioaerosol gained attention again, caused by pandemics like influenza[49,50], Middle East Respiratory Syndrome (MERS) coronavirus[51], and even Ebola[52]. With the recent pandemic of SARS-CoV-2, the mask usage has become essential, leading researchers to expand studies on the field[53–56]. The area's cutting-edge technology developed new face masks with lyophilized CRISPR sensors capable of detecting pathogens as SARS-CoV-2 *in situ*[57].

During a pandemic, health care workers' protection relies on personal protective equipment[58], and facemasks of high performance such as N95 and FFP2 models have already proved their efficacy against the SARS-CoV-2 and other pathogens[36,59,60]. Unfortunately, this material is insufficient to attend to the high world demand and needs to be directed to health care workers[54,61].

The use of masks becomes a security symbol in a pandemic[47] but can be a false sense of protection. Shortages in supply force the population to use more accessible masks, such as surgical and cloth masks. Household materials are unsuitable for retaining particles, and cloth masks were not designed for respiratory safety[34]. They have a wide range of filtration efficiency, varying from one material to another[62]. The utilization and moisture retention caused by the cloth materials' physical properties can be potential factors that increase infection rates[63]. Washing cloth masks also stretch the fabric, altering the pore size and consequently decreasing the filtering efficiency of the material[46]. Even high-performance masks during cleaning procedures can lose their capability to retain particles, becoming unsuitable to use[64].

Especially in cloth masks, small aerosols can penetrate through the mat pores as projectiles or carry by the airflow, specially droplets in the range between 0.3 to 2 µm[65]. Droplets with enough momentum can surpass the barrier of the fabric pores (as described in **Figure 2.1**). Shear stress and surface tension can force the droplet to squeeze through the interfiber spaces[26], and they may reach the respiratory tract[66]. Viruses carried by the liquid particle can remain viable on the surface mask, remaining on the retentive portion of the droplet[52].

Even though the efficiency of masks has pros and cons, the general usage by the population has already proved to diminish virus transmission[56,67–69]. For example, tests with cloth masks against particles emitted by diesel combustion (ranging between 30 – 500 nm) obtained efficiencies between 15 to 57%[70], still more effective than no masks at all. A possible way to improve the filtration efficiency of cloth masks is to use multilayers, imposing additional barriers to the penetration of the particles[26,71–73]. Nevertheless, cloth masks are still not suitable for respiratory protection. The goal is to functionalize cloth materials with a biocidal material that can remain on the fiber surface

and eliminate the pathogen (*i.e.,* viruses, bacteria, and fungi) without being dangerous to the wearer[74].

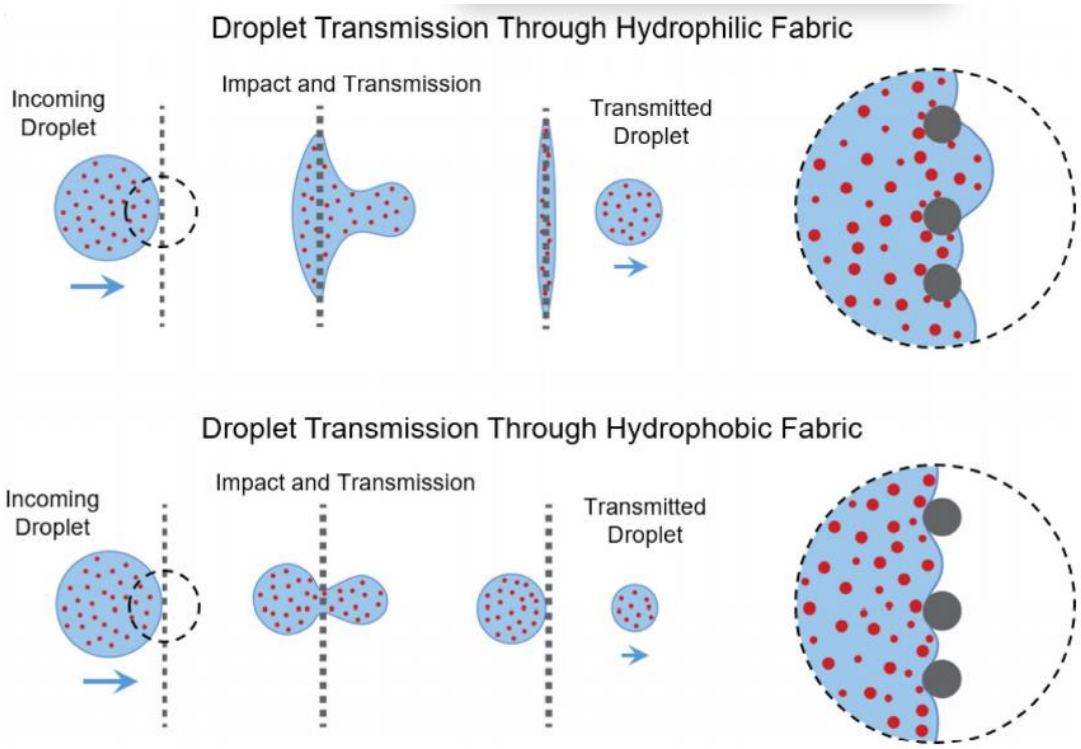

Figure 2.1: Scheme showing how the particles can squeeze through pores of cloth masks with hydrophilic and hydrophobic materials. Adapted from Aydin et al., 2020.

2.4 Retention Mechanisms onto Fiber Filter Media

The principal mechanism of collecting aerosols by facemasks and air filters is the retention onto micro or nanofibers. Nanofibers are a class of materials extensively used in the last decade as air filter media due to the low-pressure drops[75,76]. Its channels are commonly sinuous and interconnected, granting low air resistance and high filtration efficiency, essential for air filtering[77]. Many industries employ these materials in their air filters to clean large amounts of air[78], even in medical applications[79,80]. Commercial filters typically use microfibers with low air resistance and limited fine particle removal efficiency[81]. It can be a problem since small particles frequently carry compounds due to their large surface area[82,83].

Particles and aerosols can be classified accordingly with the Particulate Matter (PM) diameter range, being PM 0.1 (< 0.1 µm), or ultrafine; PM 2.5 (0.1 – 2.5 µm), or fine; and PM 10 (2.5 – 10 µm) or course[84]. Since the SARS-CoV-2 has an average diameter ranging from 60 to 140 nm, it can be defined as ultrafine (PM 0.1) or fine (PM 2.5) particles. Common air filtering methods can effectively remove PM 2.5[85]. However, the typical sieving process does not collect such particles onto filters. Fibers in the nanometric scale exhibit properties that enhance filtration efficiency, such as high surface energy and enhanced surface reactivity[86–88]. The PM's removal process by filters involves a dynamic adsorption and desorption process, and stronger interactions increase the filtering efficiency[89]. The particles retention occurs due to three distinct

mechanisms: the flow hydrodynamics that passes through a single fiber; small particulates stochastic movement; and electrostatic mechanism caused by a charge in the particles or fibers. The retention mechanisms in the filtration (**Figure 2.2**) can be classified as:

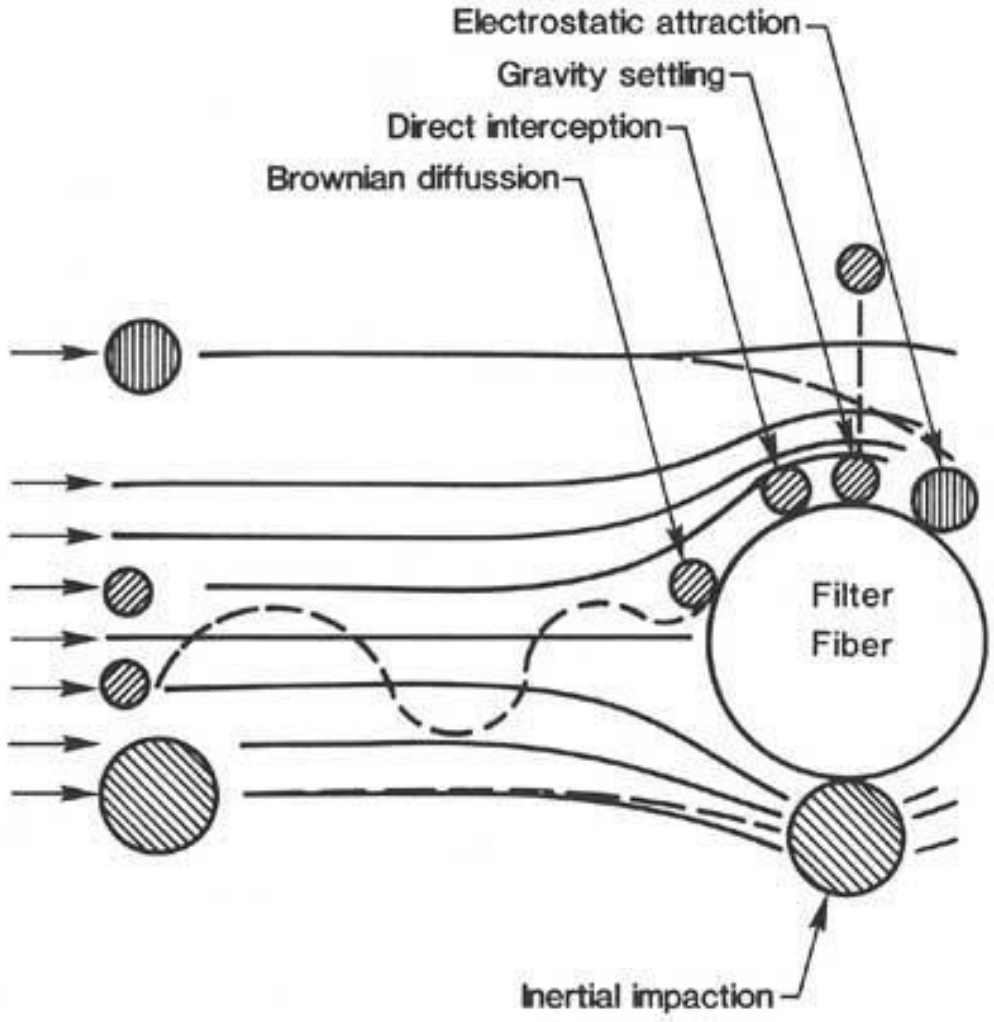

Figure 2.2: Different mechanisms of particle capture by fibers[90] during the process of air filtration. Particles are removed from the streamline and collide onto a retention site.

Direct interception: particles that find a retention site along the fluid trajectory.

Inertial impaction: particles with mass greater than the carrier fluid have difficulties following the streamlines can change their trajectory being "thrown" away into a retention site.

Diffusion: small particles do not follow a fluid streamline but diffuse across the fiber mat. In this process, they may reach a retention site. Brownian motion is higher in smaller particles and decreases with the increment in the fluid velocity.

Gravity: at low velocities, particles with a different density than the fluid can deviate from the streamlines to a retention site. Fluids with higher viscosity and velocity reduce the gravitational effect, while heavier particles are more subjected to it.

Electrostatic Attraction: particles that possess dipoles or different charges from the filter fibers can be attracted to their surfaces.

Hydrodynamic Effects: due to the non-uniformity of the flow field, nonspherical particles tend to migrate to the outside of a fluid streamline and may enter in a retention site.

One or another mechanism can dominate over the others, depending on the particle size[80]. Aerosols in the range of 1 µm to 10 µm are more influenced by hydrodynamic effect (ballistic energy) or gravity forces. In sizes from 100 nm to 1 µm, the predominant mechanism becomes diffusion caused by Brownian motion. Diffusion is the primary filtration phenomenon for the SARS family due to its tiny diameter[91]. The mechanical capture by interception is also a relevant effect[21]. Nanometer-sized particles (less than 100 nm) can easily slide through the pores on the mat, so electrostatic attraction predominates over other phenomena. Low mass particles are attracted to the fibers and then bounded by the electric field[72].

2.5 Nanofibers in Filtration Process

2.5.1 Manufacture: There are many techniques to produce micro and nanofibers, such as melt-spinning and laser spinning[92]. Electrospinning stands out among those because of its versatility and the applicability of different materials, generating fibers with controllable morphology[93]. The process is described in **Figure 2.3**.

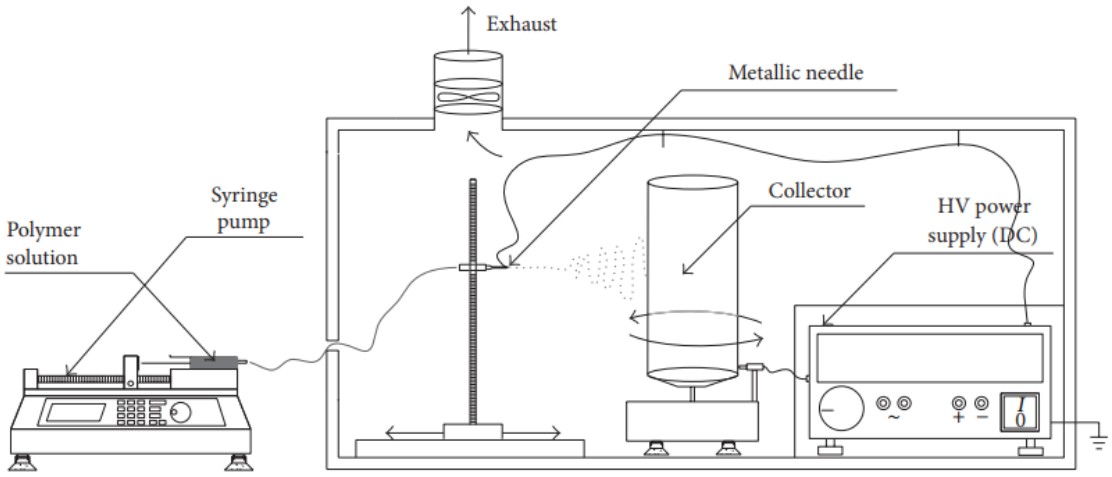

Figure 2.3: Schematic design of nanofibers production by electrospinning technique. (Adapted from Matulevicius et al., 2014).

The basic concept is to apply a high voltage electrical field between a needle and a metal plate at a defined distance. A solution of an electrostatic and viscous polymer is then squeezed through the needle and enters the electrical field[94]. The first pendant droplet at the edge of the needle tends to form a cone shape called the Taylor cone[95]. Electrical charges accumulate on the polymer surface, creating a repulsion force capable of overcoming the polymer surface tension. The electrostatic repulsion stretches the

polymer from the needle toward the metal plate, elongating the fiber to nanoscale dimensions[96]. The solvent evaporates during the trajectory between the needle and the collector, allowing the polymer to solidify on the metal plate. The metal plate is covered with a collector material, commonly aluminium foil. A series of variables can be changed to improve the properties of the fibers, like solution concentration, the molecular weight of the polymer, surface tension, conductivity, solvent, applied voltage of the electrical field, and flow rate, among others[97].

Ahn and collaborators (2006) produced Nylon 6 electrospun nanofibers for air filtration using the electrospinning technique. Their fibers ranged between 80 to 200 nm in diameter with a collection efficiency of 99,993% against 300 nm particles, at a velocity of 5 cm s^{-1} of air[94]. Matulevicius and co-workers (2014) produced polyamide (PA) nanofibers and observed spider-net shapes' formation during electrospinning. This nanostructure can improve the mechanical properties of PA mats[98] and can offer additional advantages to air filtration. The denser structure formed a layer capable of retaining more particles by interception mechanisms, raising the overall filtration efficacy. Single fibers sizes were around 465 nm in height and 220 nm in width. Spider-net structures ranged between 9-28 nm and 7-15 nm in height and width, respectively.

2.5.2 Nanofibers Filtering Efficiency: Nanofibers have already successfully captured viral particles, removing them from the air. Li and co-workers (2009) tested alumina nanofibers against aerosolized viruses' particles using MS2 bacteriophages. They observed low-pressure drops compared with HEPA filters, with high removal performance[99].

Electrospun nanofibers have excellent properties that enable the capture of efficient ultrafine particles[100,101]. Some of them are a large surface-area-to-volume ratio, low basis weight, nanoporous structures, and uniform electrospun fibers[86]. Worth mentioning that it is a low-cost technique (Nam et al., 2019). Therefore, nanofibers can be applicable for high-performance filtering.

To test the performance of nanofibers against nanoparticles, Leung & Sun (2020) used sodium chloride aerosols ranging between 50-500 nm to simulate SARS-CoV-2. They tested different nanofiber diameters of electrospun polyvinylidene fluoride (PVDF). As mentioned previously, they observed that the collection efficiency tends to rise by reducing the fiber diameter. Nanofibers with average diameters of 525, 349, 191, and 84 nm presented collection efficiencies of 39.6, 45.3, 51.8, and 61.9%, respectively

Liang and co-workers (2019) produced transparent fibers utilizing thermoplastic polyurethane, aiming at industrial-scale production. The retention efficiency was 99.654 % for PM 2.5, keeping the optical transparency of the filter at 60 %. After ten filtration cycles, the collection efficiency decreased only 1.6 %[102].

Bonfim and co-workers (2021) dissolved polyethylene terephthalate (PET) from clear soda bottles to produce nanofibers. They varied parameters such as solution concentration (10, 12, and 20 %) and needle diameter (0.3 to 0.7 mm), observing the response on structural characteristics of the electrospun fibers. The conclusion was that the fiber diameter suffers more influence from the concentration, thickening the fiber size with increased polymer content on the solution. It was also observed that the

electrospun fiber of PET 20% had the lowest filtration efficiency (41%) for particles ranging between 7 to 300 nm. Polymer solutions with high concentrations tend to form thicker fibers, less effective in collecting nanoparticles. The electrospun fiber of less concentrated solutions (PET 10 and 12%) presents good collection efficiency, higher than 99%[103].

2.5.3 Fibers Functionalization: The fine particulate matter could also include a significant amount of viruses, bacteria, and fungi present in the air[104–106]. When used for long periods, air filters are susceptible to contamination[107,108]. Hence, the fibers must also be highly active against microbes[109]. A viable option to do this is functionalizing the filters with biocidal agents. Victor and co-workers used electrospun nanofibers of polyvinylidene fluoride (PVDF) with titanium nanotubes to purify air contaminated with bacteria. They observed that the blend could eliminate 99.88 % of the airborne microorganisms [110]. The biocide agent can be both organic or inorganic compounds, with different routes of inhibition of microbes[111]. Metallic nanoparticles are a common functionalizing agent, such as silver[112,113], copper[114,115], and titanium. They have already proved effective against SARS-CoV-2[8,116,117] and other airborne microorganisms.

Machry and colleagues (2021) synthesized copper nanoparticles (CuNPs) to functionalize polyester fiber filters. Contact methodology was used to avail the bactericidal effect of the filters, proving excellent effectivity. Bacterial growth inhibition was more expressive in gram-positive bacteria (*Staphylococcus aureus*) than gram-negative (*Escherichia coli*)[118]. The proper mechanism is not entirely understood but indicates that CuNPs are responsible for producing Reactive Oxygen Species (ROS) that react with the outer layer of bacteria, leading to cell lysis and death[119,120]. Balagna and co-workers (2020) report that the use of silver nanoclusters/silica composite sputtered coating applied on FFP3 masks possessed a virucidal effect against the coronavirus. They also clarify that the nanocluster can be applied to other surfaces like metals, ceramics, glasses, and polymers. Metallic oxides have also been investigated[121].

However, the time required for the biocide action of inorganic materials is longer when compared with organic compounds[120]. Metal nanoparticles have cytotoxic effects on mammalian cells[122,123] and may harm the environment[124]. To avoid side effects is recommended the usage of more natural compounds[125]. Many organic compounds are viable to confer biocidal action to textiles, such as Essential oils[126–129], cyclodextrins[130], triclosan [131,132], chitosan[133,134], and surfactants such as sodium dodecyl sulphate[135] and cetyltrimethylammonium bromide[136,137]. The applications and mechanisms of surfactants as biocide agents are explored in the next section.

2.6 Surfactants and their biocidal activities

Surfactants are common substances found in a series of different applications. It is present in various products such as toothpaste, mouthwash, shampoos, and detergents[138]. Typically, surfactants are not harmful to the skin and mucous[139] and may exhibit microbiocidal activity[140].

The word "surfactant" is an abbreviation of "surface active agent" because they are molecules able to diminish liquids' surface tension. Surfactants are a class of

amphiphilic organic substances, having a hydrophobic group in one part of the molecule and a hydrophilic group in the other, usually called *tails* and *heads*, respectively[141]. Surfactants can modify particle-surface interactions and provide a steric barrier to contact. Adsorption of their molecules can alter a series of interfacial properties such as van der Waals forces, electrostatic attraction and, hydrophobicity[142].

The surfactants can be classified into four significant groups: cationic, anionic, amphoteric, and non-ionic[140,143]. Anionic surfactants comprise molecules with an anion at the hydrophilic head, while cationic (usually quaternary ammonium bases) have a positive functional group (cation). Non-ionic surfactants are constituted by molecules that did not undergo ionization during dissolution[144], and amphoteric surfactants possess both cationic and anionic surfactants.

The presence of hydrophobicity and positive charges in biocides agents are excellent characteristics for their antimicrobial activity[145]. Bacteria have an outer lipid-protein layer composed of lipopolysaccharides, giving the cell a negative charge[146]. Strong electrostatic attraction between a cell membrane and biocide is favourable for biocidal action[147]. Biomolecules interact with ionic surfactants leading to denaturation and biological activity decay[148]. Non-ionic surfactants have weak action to denature proteins since they cannot correctly bind themselves to biomolecules[149,150].

Amongst the cationic surfactants, the quaternary ammonium compounds (QAC) exhibit a good interaction with microorganisms. The hydrophobic tail of quaternary ammonium salts can penetrate the hydrophobic microorganism membrane core, leading to structural proteins and enzyme denaturation[125]. For example, gemini surfactants show good effectiveness against bacteria and microscopic fungi due to their molecules' high positivity[146]. The alkyl groups' compounds that present a length chain between 12-14 exhibit better activities against Gram-positive bacterial strains. Compounds with 14-16 alkyl groups favour biocidal action against Gram-negative strains[151]. The surfactant action begins by penetrating its molecules into the cell wall, reaching and reacting with the cytoplasmatic membrane. The intracellular matrix of bacteria is destabilized by the ion exchange of QAC with Ca^{2+} and Mg^{2+} from the cytoplasmatic membrane[123]. The intracellular material is leaked, leading to proteins and nucleic acid degradation. As a consequence, the cell suffers lysis and death[152].

Some bacteria are surrounded by a capsule and slime that accumulate outside the cell wall. These secreted materials are responsible for the significant bacterial insusceptibility of biocides[153]. The spore's coat proteins act as an outer barrier, making the biocide's entrance challenging[154]. Some Gram-positive bacteria form spores as an additional defence[140,155]. Gram-negative cells also have a supplementary barrier, an outer membrane, which Gram-positive cells do not have. This lipopolysaccharide layer after the polypeptidoglycan wall also difficult the biocide penetration[156]. One way to avoid those barriers is by combining different biocides to improve the biocidal action[157]. The use of EDTA (ethylenediaminetetraacetic acid) as a secondary agent, for example, raises the permeability of the cell wall, allowing a primary biocide to get closer to the cell membrane[153].

Fungi and yeasts can also be affected by cationic surfactants' antimicrobial activity[158], reducing the number of fungal spores[146]. Surfactants act by dispersing the fungi aggregates, influencing their surface structure, and changing the fugal surface's

physicochemical properties of the adsorption process[159]. The hydrophobic portion of the surfactant coats the fungal surface, also hydrophobic. The other part of the surfactant molecule is exposed to the ambient, giving hydrophilic properties to the fungus outer layer[160]. This effect, combined with the electrostatic adsorption phenomenon at the water/membrane interface, disrupts the fungi surface structure[161], causing its death.

Some surfactants also present antiviral properties, and their presence decreases viruses' survivability[148]. The inactivation of viruses under surfactants was already studied with HIV (human immunodeficiency virus)[135], Ebola[162], and H1N1 flu[163], for example. They have shown a good inhibition effect, acting against enveloped and nonenveloped viruses. The mechanism involves the denaturation of proteins in the viral capsid and dissociates the viral envelope[135]. Surfactants can also denature and unfold monomeric and subunit proteins[138] and form micelles around the capsid or membrane, enclosing the virus[164]. They also diminish viruses' sorption and consequently increase their mobility[148].

Surfactants also have a role in the recent pandemic and can be a good option against the SARS-CoV-2 virus. The inactivation by surfactants occurs through damage in their spikes[165]. Surfactants can also act *in situ* by reaching cells and extracellular fluids interfering in one or more steps of viral replication[164]. The human body has natural surfactants working on defence against the new coronavirus-2019. Our systems produce a protein surfactants monolayer to control the interface air-epithelium of lung alveoli[166]. The objective is to reduce surface tension at the end of expiration, avoiding the lung alveoli's collapse[167]. SARS-CoV-2 causes the inhibition of those natural surfactants[168], exposing the alveoli during the inhalation-expiration process.

The study performed by de Almeida et al. (2020) aimed to evaluate the filtration efficiency of cellulose acetate with cetyl pyridinium bromide, a cationic surfactant (and a quaternary ammonia salt). The authors found about 99 % efficiency for small particles for low surface air velocity, ranging from 7 to 300 nm. They also suggest that these nanofibers present biocide action[169]. Another study conducted by Jeong & co-workers (2007) prepared polyurethane cationomer nanofibers (PUC), using a mixture of QAC on its non-woven mats for antimicrobial nanofilter applications. They tested the sample's antimicrobial activity with low content of quaternary ammonium compounds against *S. aureus* and *E. coli*. The results showed a reduction of colonies in 99.9% after 24 h incubation[109]. They also observed that the fiber diameter of electrospun PUC decreases with increasing the quaternary ammonium group content.

Zhang *et al.* (2020) produced a nanofiber mat of PVA (polyvinyl alcohol), functionalizing with a quaternary ammonium salt and zwitterionic sulfopropylbetaine. They observed that only 0.5% of surfactant applied to the fibers could achieve 99.9% antimicrobial activity against *S. aureus* and *E. coli*[170]. It was much lower than the amount used in a previous research group study using cotton textiles[171]. This result is attributed to the higher surface area of PVA mats, and the bond between the quaternary ammonium salt and the PVA fiber is covalent instead of physical. The stronger bond avoids a loss of biocide agents and improves its durability. A different study also used sulfopropilbetaine (SSPB) for biocidal purposes. They functionalized cotton fabrics, observing that the addition of SSPB also improves the fabrics' mechanical resistance[172].

The presence of QAC in a membrane can also change the surface properties for other purposes. Researchers have functionalized a PVDF membrane with polydopamine and polyethylenimine to synthesize an outer layer of hydrophilic nanoparticles *in situ*. Then, the immobilized QAC on the silica layer produces an antibacterial layer. They observed that after adding QAC, the membrane gains biocidal activity. It also prevents biofouling, the adhesion of microorganisms on its surface, avoiding bacterial and fungal growth. They also tested the system's durability to wastewater treatment, obtaining 85% elimination for Gram-positive and Gram-negative bacteria after washing the filter for 9 hours[173].

2.7 HVAC's & Ventilation Systems

The recent pandemic has cast doubt on the reliability of ventilation and HVAC systems due to the mechanisms of the disease's spread through airborne droplets. Air conditioning could transfer respiratory droplets containing the virus to persons standing against the airflow direction[174]. Those droplets can also travel inside the ventilation systems, disseminating the virus by being reinserted in the room, as already proved by modeling systems [175]. There are proposed three routes of contamination[176]:

- Through air recirculation in the buildings;
- Through the ventilation exhaustion;
- Through air confinement, without renewing the ambient with fresh air.

There are many suggestions to avoid those problems, such as improving ventilation rates, adopting natural ventilation and, personalized ventilation and exhaustion systems for micro-environments[177]. The pivotal advice is to increase outdoor air in ventilation systems and keep the system running day and night[178]. On the other hand, the American Society of Heating, Refrigeration, and Air-Conditioning Engineers (ASHRAE) positioned against the advice of not running HVAC systems and defending that air conditioners can help contain the spread of the virus[179].

Nevertheless, some situations cannot adapt to the last changes proposed. For example, natural ventilation is not easy to implement in the middle east, with extremely high temperatures (38 to 42 °C)[180]. The buildings' architectural design did not allow natural and mechanical ventilation, constructed with indoor air conditioning systems to maintain thermal comfort[181]. The dependence on ventilation and HVAC systems also increases in the occident. With temperature rises, global warming, and heat waves happening more frequently and persistently worldwide[182], the necessity for air conditioning and improvements in ventilation systems only tends to rise.

There are other roles that ventilation systems can play against pathogens. When the airflow passage is blocked, there is a risk of increasing the airborne pathogens' concentration and growth, increasing the chances of airborne pathogens' transmissibility [183]. Ventilation systems can withdraw respiratory droplets from the room three times faster than natural ventilation[184], removing exhaled virus-laden air and diminishing the virus concentration[30,176]. They are also effective in eliminating airborne bacterial and fungal spores[185]. Air cleaners also reduce aerosolized virus concentration, especially when adopted alongside natural ventilation[186]. A possible improvement to ventilation, heating, and HVAC systems is air filters. HEPA's implementation can help

control the spreading in facilities with common ducts[187]. Air viral particles ' extraction was already observed in an airplane with HEPA in its ventilation systems[188]. Air recirculation also reduces infection risk in areas sharing the same central HVAC system[176].

2.8 Conclusion

Due to the growing number of studies under development in recent years, we believe that soon there will be a range of innovative products composed of specialized materials as filter media. Incorporating biocidal and virucidal compounds in commercial filters/textiles and filtering nanofibers is an effective alternative to keep indoor environments safe from nanoparticles and pathogenic organisms. Surfactants are eco-friendly compounds, unlike the metallic nanoparticles widely used today. Thus, being a compound not harmful to human health, its use will occur through its incorporation into microcapsules with controlled release in textiles and nanofibers for masks and various articles for health professionals. In addition, considering the control of indoor air pollution, its addition in solution for producing electrospinning nanofibers has already proven effective in inactivating several pathogens, such as viruses and bacteria.

2.9 Acknowledgments

The authors would like to acknowledge the Coordination for the Improvement of Higher Education Personnel (Coordenação de Aperfeiçoamento de Pessoal de Nível Superior – CAPES), process No. 88887.505019/2020-00; we also would like to thanks the National Council for Scientific and Technological Development (Conselho Nacional de Desenvolvimento Científico e Tecnológico - CNPq), process No. 424792/2018-4, for all the support.

2.9 Chapter References

1. Balagna, C., Perero, S., Percivalle, E., Nepita, E. V. & Ferraris, M. Virucidal effect against coronavirus SARS-CoV-2 of a silver nanocluster/silica composite sputtered coating. *Open Ceramics* **1**, 100006 (2020).
2. Mandavilli, A. & Tully, T. White House Is Not Tracing Contacts for 'Super-Spreader' Rose Garden Event. *The New York Times* (2020).
3. Hanage, W. The Next Pandemic: On the Front Lines Against Humankind's Gravest Dangers. *Emerging Infectious Diseases* **23**, (2017).
4. Zhang, S. *et al.* Estimation of the reproductive number of novel coronavirus (COVID-19) and the probable outbreak size on the Diamond Princess cruise ship: A data-driven analysis. *Int J Infect Dis* **93**, 201–204 (2020).
5. Morawska, L. & Cao, J. Airborne transmission of SARS-CoV-2: The world should face the reality. *Environment International* **139**, 105730 (2020).
6. Yu, I. T. S. *et al.* Evidence of Airborne Transmission of the Severe Acute Respiratory Syndrome Virus. *New England Journal of Medicine* **350**, 1731–1739 (2004).
7. Greenhalgh, T. *et al.* Ten scientific reasons in support of airborne transmission of SARS-CoV-2. *The Lancet* **397**, 1603–1605 (2021).
8. van Doremalen, N. *et al.* Aerosol and Surface Stability of SARS-CoV-2 as Compared with SARS-CoV-1. *New England Journal of Medicine* **382**, 1564–1567 (2020).
9. Shankar, S. N. *et al.* SARS-CoV-2 in residential rooms of two self-isolating persons with COVID-19. *Journal of Aerosol Science* **159**, 105870 (2022).
10. Mouchtouri, V. A. *et al.* Environmental contamination of SARS-CoV-2 on surfaces, air-conditioner and ventilation systems. *International Journal of Hygiene and Environmental Health* **230**, 113599 (2020).
11. Aliabadi, M. Effect of electrospinning parameters on the air filtration performance using electrospun polyamide-6 nanofibers. *Chemical Industry and Chemical Engineering Quarterly* **23**, 441–446 (2017).
12. Pyankov, O. V., Agranovski, I. E., Huang, R. & Mullins, B. J. Removal of Biological Aerosols by Oil Coated Filters. *CLEAN – Soil, Air, Water* **36**, 609–614 (2008).

13. Iacobucci, G. Covid-19: New UK variant may be linked to increased death rate, early data indicate. *BMJ* **372**, n230 (2021).
14. Tegally, H. *et al.* Detection of a SARS-CoV-2 variant of concern in South Africa. *Nature* **592**, 438–443 (2021).
15. Faria, N. R. *et al.* Genomics and epidemiology of the P.1 SARS-CoV-2 lineage in Manaus, Brazil. *Science* **372**, 815–821 (2021).
16. Alai, S., Gujar, N., Joshi, M., Gautam, M. & Gairola, S. Pan-India novel coronavirus SARS-CoV-2 genomics and global diversity analysis in spike protein. *Heliyon* **7**, e06564 (2021).
17. Xu, Z., Liu, K. & Gao, G. F. Omicron variant of SARS-CoV-2 imposes a new challenge for the global public health. *Biosafety and Health* (2022) doi:10.1016/j.bsheal.2022.01.002.
18. Dash, P. *et al.* Sequence analysis of Indian SARS-CoV-2 isolates shows a stronger interaction of mutant receptor-binding domain with ACE2. *International Journal of Infectious Diseases* **104**, 491–500 (2021).
19. Rendana, M. & Idris, W. M. R. New COVID-19 variant (B.1.1.7): Forecasting the occasion of virus and the related meteorological factors. *Journal of Infection and Public Health* (2021) doi:10.1016/j.jiph.2021.05.019.
20. Zhu, N. *et al.* A Novel Coronavirus from Patients with Pneumonia in China, 2019. *New England Journal of Medicine* (2020) doi:10.1056/NEJMoa2001017.
21. Leung, W. W.-F. & Sun, Q. Charged PVDF multilayer nanofiber filter in filtering simulated airborne novel coronavirus (COVID-19) using ambient nano-aerosols. *Separation and Purification Technology* **245**, 116887 (2020).
22. Stadnytskyi, V., Bax, C. E., Bax, A. & Anfinrud, P. The airborne lifetime of small speech droplets and their potential importance in SARS-CoV-2 transmission. *PNAS* **117**, 11875–11877 (2020).
23. Bourouiba, L., Dehandschoewercker, E. & Bush, J. W. M. Violent expiratory events: on coughing and sneezing. *Journal of Fluid Mechanics* **745**, 537–563 (2014).
24. Howard, J. *et al.* An evidence review of face masks against COVID-19. *Proc Natl Acad Sci U S A* **118**, e2014564118 (2021).
25. Nicas, M., Nazaroff, W. W. & Hubbard, A. Toward Understanding the Risk of Secondary Airborne Infection: Emission of Respirable Pathogens. *Journal of Occupational and Environmental Hygiene* **2**, 143–154 (2005).
26. Aydin, O. *et al.* Performance of fabrics for home-made masks against the spread of COVID-19 through droplets: A quantitative mechanistic study. *Extreme Mechanics Letters* **40**, 100924 (2020).
27. Morawska, L. *et al.* Size distribution and sites of origin of droplets expelled from the human respiratory tract during expiratory activities. *Journal of Aerosol Science* **40**, 256–269 (2009).
28. Feng, Y., Marchal, T., Sperry, T. & Yi, H. Influence of wind and relative humidity on the social distancing effectiveness to prevent COVID-19 airborne transmission: A numerical study. *Journal of Aerosol Science* **147**, 105585 (2020).
29. Oswin, H. P. *et al.* Measuring stability of virus in aerosols under varying environmental conditions. *Aerosol Science and Technology* **0**, 1–6 (2021).
30. Morawska, L. *et al.* How can airborne transmission of COVID-19 indoors be minimised? *Environment International* **142**, 105832 (2020).
31. Pyankov, O. V., Bodnev, S. A., Pyankova, O. G. & Agranovski, I. E. Survival of aerosolized coronavirus in the ambient air. *Journal of Aerosol Science* **115**, 158–163 (2018).
32. Bourouiba, L. Turbulent Gas Clouds and Respiratory Pathogen Emissions: Potential Implications for Reducing Transmission of COVID-19. *JAMA* **323**, 1837–1838 (2020).
33. Gralton, J., Tovey, E., McLaws, M.-L. & Rawlinson, W. D. The role of particle size in aerosolised pathogen transmission: a review. *J Infect* **62**, 1–13 (2011).
34. Rengasamy, S., Eimer, B. & Shaffer, R. E. Simple Respiratory Protection—Evaluation of the Filtration Performance of Cloth Masks and Common Fabric Materials Against 20–1000 nm Size Particles. *The Annals of Occupational Hygiene* **54**, 789–798 (2010).
35. Fabian, P. *et al.* Influenza Virus in Human Exhaled Breath: An Observational Study. *PLOS ONE* **3**, e2691 (2008).
36. Cheng, Y. *et al.* Face masks effectively limit the probability of SARS-CoV-2 transmission. *Science* **372**, 1439–1443 (2021).
37. Fairchild, C. I. & Stampfer, J. F. Particle concentration in exhaled breath. *Am Ind Hyg Assoc J* **48**, 948–949 (1987).
38. Edwards, D. A. *et al.* Inhaling to mitigate exhaled bioaerosols. *Proc Natl Acad Sci U S A* **101**, 17383–17388 (2004).
39. Chao, C. Y. H. *et al.* Characterization of expiration air jets and droplet size distributions immediately at the mouth opening. *Journal of Aerosol Science* **40**, 122–133 (2009).
40. Johnson, G. R. *et al.* Modality of human expired aerosol size distributions. *Journal of Aerosol Science* **42**, 839–851 (2011).
41. Alsved, M. *et al.* Exhaled respiratory particles during singing and talking. *Aerosol Science and Technology* **54**, 1245–1248 (2020).
42. Fennelly, K. P. Particle sizes of infectious aerosols: implications for infection control. *Lancet Respir Med* **8**, 914–924 (2020).
43. Leung, N. H. L. *et al.* Respiratory virus shedding in exhaled breath and efficacy of face masks. *Nat Med* **26**, 676–680 (2020).
44. Bake, B., Larsson, P., Ljungkvist, G., Ljungström, E. & Olin, A.-C. Exhaled particles and small airways. *Respiratory Research* **20**, 8 (2019).
45. Johnson, G. R. & Morawska, L. The Mechanism of Breath Aerosol Formation. *Journal of Aerosol Medicine and Pulmonary Drug Delivery* **22**, 229–237 (2009).
46. Neupane, B. B., Mainali, S., Sharma, A. & Giri, B. Optical microscopic study of surface morphology and filtering efficiency of face masks. *PeerJ* **7**, e7142 (2019).
47. Goh, Y., Tan, B. Y. Q., Bhartendu, C., Ong, J. J. Y. & Sharma, V. K. The face mask: How a real protection becomes a psychological symbol during Covid-19? *Brain, Behavior, and Immunity* **88**, 1–5 (2020).
48. Belkin, N. L. A century after their introduction, are surgical masks necessary? *AORN J* **64**, 602–607 (1996).
49. Booth, M. C., Clayton, M., Crook, B. & Gawn, J. M. Effectiveness of surgical masks against influenza bioaerosols. *Journal of Hospital Infection* **84**, 22–26 (2013).
50. Suess, T. *et al.* The role of facemasks and hand hygiene in the prevention of influenza transmission in households: results from a cluster randomised trial; Berlin, Germany, 2009-2011. *BMC Infect Dis* **12**, 26 (2012).

51. Al-Tawfiq, J. A., Abdrabalnabi, R., Taher, A., Mathew, S. & Rahman, K. A. Infection control influence of Middle East respiratory syndrome coronavirus: A hospital-based analysis. *American Journal of Infection Control* **47**, 431–434 (2019).
52. Osterholm, M. T. *et al.* Transmission of Ebola Viruses: What We Know and What We Do Not Know. *mBio* **6**, e00137-15 (2015).
53. Ganczak, M., Pasek, O., Duda – Duma, Ł., Świstara, D. & Korzeń, M. Use of masks in public places in Poland during SARS-Cov-2 epidemic: a covert observational study. *BMC Public Health* **21**, 393 (2021).
54. Ippolito, M. *et al.* Medical masks and Respirators for the Protection of Healthcare Workers from SARS-CoV-2 and other viruses. *Pulmonology* **26**, 204–212 (2020).
55. Selvaranjan, K., Navaratnam, S., Rajeev, P. & Ravintherakumaran, N. Environmental challenges induced by extensive use of face masks during COVID-19: A review and potential solutions. *Environmental Challenges* **3**, 100039 (2021).
56. Tabatabaeizadeh, S.-A. Airborne transmission of COVID-19 and the role of face mask to prevent it: a systematic review and meta-analysis. *Eur J Med Res* **26**, 1 (2021).
57. Nguyen, P. Q. *et al.* Wearable materials with embedded synthetic biology sensors for biomolecule detection. *Nat Biotechnol* 1–9 (2021) doi:10.1038/s41587-021-00950-3.
58. Lepelletier, D. *et al.* What face mask for what use in the context of COVID-19 pandemic? The French guidelines. *J Hosp Infect* S0195-6701(20)30211–5 (2020) doi:10.1016/j.jhin.2020.04.036.
59. Grinshpun, S. A. *et al.* Performance of an N95 filtering facepiece particulate respirator and a surgical mask during human breathing: two pathways for particle penetration. *J Occup Environ Hyg* **6**, 593–603 (2009).
60. Lindsley, W. G., Blachere, F. M., Law, B. F., Beezhold, D. H. & Noti, J. D. Efficacy of face masks, neck gaiters and face shields for reducing the expulsion of simulated cough-generated aerosols. *Aerosol Science and Technology* **55**, 449–457 (2021).
61. Thaper, R., Fagen, B. & Oh, J. Decontamination of respirators amid shortages due to SARS-CoV-2. *Photochem Photobiol Sci* (2021) doi:10.1007/s43630-021-00064-4.
62. Morais, F. G. *et al.* Filtration efficiency of a large set of COVID-19 face masks commonly used in Brazil. *Aerosol Science and Technology* **0**, 1–21 (2021).
63. MacIntyre, C. R. *et al.* A cluster randomised trial of cloth masks compared with medical masks in healthcare workers. *BMJ Open* **5**, e006577 (2015).
64. Ou, Q., Pei, C., Chan Kim, S., Abell, E. & Pui, D. Y. H. Evaluation of decontamination methods for commercial and alternative respirator and mask materials – view from filtration aspect. *Journal of Aerosol Science* **150**, 105609 (2020).
65. Kähler, C. J. & Hain, R. Fundamental protective mechanisms of face masks against droplet infections. *Journal of Aerosol Science* **148**, 105617 (2020).
66. Löndahl, J. *et al.* Size-Resolved Respiratory-Tract Deposition of Fine and Ultrafine Hydrophobic and Hygroscopic Aerosol Particles During Rest and Exercise. *Inhalation Toxicology* **19**, 109–116 (2007).
67. Brooks, J. T., Butler, J. C. & Redfield, R. R. Universal Masking to Prevent SARS-CoV-2 Transmission-The Time Is Now. *JAMA* **324**, 635–637 (2020).
68. Chirizzi, D. *et al.* SARS-CoV-2 concentrations and virus-laden aerosol size distributions in outdoor air in north and south of Italy. *Environment International* **146**, 106255 (2021).
69. Chu, D. K. *et al.* Physical distancing, face masks, and eye protection to prevent person-to-person transmission of SARS-CoV-2 and COVID-19: a systematic review and meta-analysis. *The Lancet* **395**, 1973–1987 (2020).
70. Shakya, K. M., Noyes, A., Kallin, R. & Peltier, R. E. Evaluating the efficacy of cloth facemasks in reducing particulate matter exposure. *J Expo Sci Environ Epidemiol* **27**, 352–357 (2017).
71. Crilley, L. R. *et al.* Non-woven materials for cloth-based face masks inserts: relationship between material properties and sub-micron aerosol filtration. *Environ. Sci.: Nano* **8**, 1603–1613 (2021).
72. Konda, A. *et al.* Aerosol Filtration Efficiency of Common Fabrics Used in Respiratory Cloth Masks. *ACS Nano* **14**, 6339–6347 (2020).
73. Nicosia, A. *et al.* Air filtration and antimicrobial capabilities of electrospun PLA/PHB containing ionic liquid. *Separation and Purification Technology* **154**, 154–160 (2015).
74. de Almeida, D. S. *et al.* Evaluation of biocidal properties of biodegradable nanofiber filters and their use in face masks. *Environmental Technology* **0**, 1–23 (2021).
75. Sambaer, W., Zatloukal, M. & Kimmer, D. 3D air filtration modeling for nanofiber based filters in the ultrafine particle size range. *Chemical Engineering Science* **82**, 299–311 (2012).
76. Sundarrajan, S., Tan, K. L., Lim, S. H. & Ramakrishna, S. Electrospun Nanofibers for Air Filtration Applications. *Procedia Engineering* **75**, 159–163 (2014).
77. Zhang, Q., Li, Q., Young, T. M., Harper, D. P. & Wang, S. A Novel Method for Fabricating an Electrospun Poly(Vinyl Alcohol)/Cellulose Nanocrystals Composite Nanofibrous Filter with Low Air Resistance for High-Efficiency Filtration of Particulate Matter. *ACS Sustainable Chem. Eng.* **7**, 8706–8714 (2019).
78. Graham, K. *et al.* Polymeric Nanofibers in Air Filtration Applications. *Adv. in Filtration and Separation Tech.* **16**, (2002).
79. Chang, C. *et al.* 1.4.6 - Medical Fibers and Biotextiles. in *Biomaterials Science (Fourth Edition)* (eds. Wagner, W. R., Sakiyama-Elbert, S. E., Zhang, G. & Yaszemski, M. J.) 575–600 (Academic Press, 2020). doi:10.1016/B978-0-12-816137-1.00038-6.
80. Kravtsov, A., Brnig, H., Zhandarov, S. & Beyreuther, R. The electret effect in polypropylene fibers treated in a corona discharge. in (2000). doi:10.1002/1098-2329(200024)19:4<312::AID-ADV7>3.0.CO;2-X.
81. Wang, Z., Pan, Z., Wang, J. & Zhao, R. A Novel Hierarchical Structured Poly(lactic acid)/Titania Fibrous Membrane with Excellent Antibacterial Activity and Air Filtration Performance. *Journal of Nanomaterials* **2016**, e6272983 (2016).
82. Dieme, D. *et al.* Relationship between physicochemical characterization and toxicity of fine particulate matter (PM2.5) collected in Dakar city (Senegal). *Environmental Research* **113**, 1–13 (2012).
83. Kendall, M., Brown, L. & Trought, K. Molecular Adsorption at Particle Surfaces: A PM Toxicity Mediation Mechanism. *Inhalation Toxicology* **16**, 99–105 (2004).
84. Kadam, V. V., Wang, L. & Padhye, R. Electrospun nanofibre materials to filter air pollutants – A review: *Journal of Industrial Textiles* (2016) doi:10.1177/1528083716676812.

85. Xiong, Z.-C., Yang, R.-L., Zhu, Y.-J., Chen, F.-F. & Dong, L.-Y. Flexible hydroxyapatite ultralong nanowire-based paper for highly efficient and multifunctional air filtration. *J. Mater. Chem. A* **5**, 17482–17491 (2017).
86. Matulevicius, J. *et al.* Design and Characterization of Electrospun Polyamide Nanofiber Media for Air Filtration Applications. *Journal of Nanomaterials* **2014**, e859656 (2014).
87. Thakur, V. K. *Nanocellulose Polymer Nanocomposites: Fundamentals and Applications*. (John Wiley & Sons, 2014).
88. Xia, T., Bian, Y., Zhang, L. & Chen, C. Relationship between pressure drop and face velocity for electrospun nanofiber filters. *Energy and Buildings* **158**, 987–999 (2018).
89. Zhu, M. *et al.* A novel cellulose acetate/poly (ionic liquid) composite air filter. *Cellulose* **27**, 3889–3902 (2020).
90. Hong, I. T. & Fitch, E. C. An Innovative Technique in Filter Rating. *SAE Transactions* **94**, 947–955 (1985).
91. Das, O. *et al.* The need for fully bio-based facemasks to counter coronavirus outbreaks: A perspective. *Science of The Total Environment* **736**, 139611 (2020).
92. Tomisawa, R. *et al.* Effect of melt spinning conditions on the fiber structure development of polyethylene terephthalate. *Polymer* **116**, 367–377 (2017).
93. Wang, Z. *et al.* Antibacterial and environmentally friendly chitosan/polyvinyl alcohol blend membranes for air filtration. *Carbohydrate Polymers* **198**, 241–248 (2018).
94. Ahn, Y. C. *et al.* Development of high efficiency nanofilters made of nanofibers. *Current Applied Physics* **6**, 1030–1035 (2006).
95. Yarin, A. L., Koombhongse, S. & Reneker, D. H. Taylor cone and jetting from liquid droplets in electrospinning of nanofibers. *Journal of Applied Physics* **90**, 4836–4846 (2001).
96. Meli, L., Miao, J., Dordick, J. S. & Linhardt, R. J. Electrospinning from room temperature ionic liquids for biopolymer fiber formation. *Green Chem.* **12**, 1883–1892 (2010).
97. Khajavi, R. & Abbasipour, M. 5 - Controlling nanofiber morphology by the electrospinning process. in *Electrospun Nanofibers* (ed. Afshari, M.) 109–123 (Woodhead Publishing, 2017). doi:10.1016/B978-0-08-100907-9.00005-2.
98. Barakat, N. A. M., Kanjwal, M. A., Sheikh, F. A. & Kim, H. Y. Spider-net within the N6, PVA and PU electrospun nanofiber mats using salt addition: Novel strategy in the electrospinning process. *Polymer -London-* **50**, 4389–4396 (2009).
99. Li, H.-W., Wu, C.-Y., Tepper, F., Lee, J.-H. & Lee, C. N. Removal and retention of viral aerosols by a novel alumina nanofiber filter. *Journal of Aerosol Science* **40**, 65–71 (2009).
100. Bonfim, D. P. F., Cruz, F. G. S., Bretas, R. E. S., Guerra, V. G. & Aguiar, M. L. A Sustainable Recycling Alternative: Electrospun PET-Membranes for Air Nanofiltration. *Polymers* **13**, 1166 (2021).
101. Zhang, B. *et al.* Chitosan nanostructures by in situ electrospinning for high-efficiency PM2.5 capture. *Nanoscale* **9**, 4154–4161 (2017).
102. Liang, W. *et al.* Transparent Polyurethane Nanofiber Air Filter for High-Efficiency PM2.5 Capture. *Nanoscale Res Lett* **14**, 361 (2019).
103. Bonfim, D. P. F., Cruz, F. G. S., Guerra, V. G. & Aguiar, M. L. Development of Filter Media by Electrospinning for Air Filtration of Nanoparticles from PET Bottles. *Membranes* **11**, 293 (2021).
104. Dowes, J., Thorne, P., Pearce, N. & Heederik, D. Bioaerosol Health Effects and Exposure Assessment: Progress and Prospects. *The Annals of Occupational Hygiene* **47**, 187–200 (2003).
105. Fung, F. & Hughson, W. G. Health Effects of Indoor Fungal Bioaerosol Exposure. *Applied Occupational and Environmental Hygiene* **18**, 535–544 (2003).
106. Sidheswaran, M. A., Destaillats, H., Sullivan, D. P., Cohn, S. & Fisk, W. J. Energy efficient indoor VOC air cleaning with activated carbon fiber (ACF) filters. *Building and Environment* **47**, 357–367 (2012).
107. Han, H. *et al.* Inherent Guanidine Nanogels with Durable Antibacterial and Bacterially Antiadhesive Properties. *Advanced Functional Materials* **29**, 1806594 (2019).
108. Yoon, Y., Kim, S., Ahn, K. H., Ko, K. B. & Kim, K.-S. Fabrication and characterization of micro-porous cellulose filters for indoor air quality control. *Environmental Technology* **37**, 703–712 (2016).
109. Jeong, E. H., Yang, J. & Youk, J. H. Preparation of polyurethane cationomer nanofiber mats for use in antimicrobial nanofilter applications. *Materials Letters* **61**, 3991–3994 (2007).
110. Victor, F. S., Kugarajah, V., Bangaru, M., Ranjan, S. & Dharmalingam, S. Electrospun nanofibers of polyvinylidene fluoride incorporated with titanium nanotubes for purifying air with bacterial contamination. *Environ Sci Pollut Res* (2021) doi:10.1007/s11356-021-13202-3.
111. Kalyon, B. D. & Olgun, U. Antibacterial efficacy of triclosan-incorporated polymers. *Am J Infect Control* **29**, 124–125 (2001).
112. Nateghi, M. R. & Shateri-Khalilabad, M. Silver nanowire-functionalized cotton fabric. *Carbohydrate Polymers* **117**, 160–168 (2015).
113. Rajaboopathi, S. & Thambidurai, S. Evaluation of UPF and antibacterial activity of cotton fabric coated with colloidal seaweed extract functionalized silver nanoparticles. *Journal of Photochemistry and Photobiology B: Biology* **183**, 75–87 (2018).
114. Huang, M.-L. *et al.* Metallic coloration on polyester fabric with sputtered copper and copper oxides films. *Vacuum* **178**, 109489 (2020).
115. Zhao, W., Xiao, X., Pan, G. & Ye, Z. Fabrication of Cu species functionalized cotton fabric with oil/water separating reusability by in-situ reduction process. *Surface and Coatings Technology* **385**, 125405 (2020).
116. Allawadhi, P. *et al.* Silver nanoparticle based multifunctional approach for combating COVID-19. *Sensors International* **2**, 100101 (2021).
117. Jeremiah, S. S., Miyakawa, K., Morita, T., Yamaoka, Y. & Ryo, A. Potent antiviral effect of silver nanoparticles on SARS-CoV-2. *Biochemical and Biophysical Research Communications* **533**, 195–200 (2020).
118. Machry, K., Souza, C. W. O. de, Aguiar, M. L. & Bernardo, A. Prevention of pathogen microorganisms at indoor air ventilation system using synthesized copper nanoparticles. *The Canadian Journal of Chemical Engineering* **n/a**, (2021).
119. Kehrer, J. P. The Haber–Weiss reaction and mechanisms of toxicity. *Toxicology* **149**, 43–50 (2000).
120. Top, A. & Ülkü, S. Silver, zinc, and copper exchange in a Na-clinoptilolite and resulting effect on antibacterial activity. (2004) doi:10.1016/j.clay.2003.12.002.

121. Mallakpour, S., Azadi, E. & Hussain, C. M. The latest strategies in the fight against the COVID-19 pandemic: the role of metal and metal oxide nanoparticles. *New J. Chem.* **45**, 6167–6179 (2021).
122. Lanone, S. H. & Boczkowski, J. Biomedical Applications and Potential Health Risks of Nanomaterials: Molecular Mechanisms. *Current Molecular Medicine* **6**, 651–663 (2006).
123. Tavakolian, M., Jafari, S. M. & van de Ven, T. G. M. A Review on Surface-Functionalized Cellulosic Nanostructures as Biocompatible Antibacterial Materials. *Nano-Micro Lett.* **12**, 73 (2020).
124. El-Rafie, M. H., Ahmed, H. B. & Zahran, M. K. Characterization of nanosilver coated cotton fabrics and evaluation of its antibacterial efficacy. *Carbohydrate Polymers* **107**, 174–181 (2014).
125. Emam, H. E. Antimicrobial cellulosic textiles based on organic compounds. *3 Biotech* **9**, 29 (2019).
126. Alonso, D., Gimeno, M., Sepúlveda-Sánchez, J. D. & Shirai, K. Chitosan-based microcapsules containing grapefruit seed extract grafted onto cellulose fibers by a non-toxic procedure. *Carbohydr Res* **345**, 854–859 (2010).
127. Das, S., Das, A., Bhavya, T. & Nivashini, S. R. Molecular characterisation and antibacterial activity of Aloe barbadensis miller on textiles. *The Journal of The Textile Institute* **111**, 1116–1122 (2020).
128. Gonçalves, J. *et al.* Zein impart hydrophobic and antimicrobial properties to cotton textiles. *Reactive and Functional Polymers* **154**, 104664 (2020).
129. Pyankov, O. V., Usachev, E. V., Pyankova, O. & Agranovski, I. E. Inactivation of Airborne Influenza Virus by Tea Tree and Eucalyptus Oils. *Aerosol Science and Technology* **46**, 1295–1302 (2012).
130. Li, R. *et al.* Preparation and antimicrobial activity of β-cyclodextrin derivative copolymers/cellulose acetate nanofibers. *Chemical Engineering Journal* **248**, 264–272 (2014).
131. Golja, B., Forte Tavčer, P., & University of Ljubljana, Faculty of Natural Sciences and Engineering, Department of Textiles, Graphic Arts and Design, 1000 Ljubljana, Snežniška 5, Slovenia. Textile Functionalisation by Printing Fragrant, Antimicrobial and Flame- Retardant Microcapsules. *TEK* **59**, 278–288 (2016).
132. Orhan, M., Kut, D. & Gunesoglu, C. Use of triclosan as antibacterial agent in textiles. *IJFTR Vol.32(1) [March 2007]* (2007).
133. Fernandez-Saiz, P., Lagaron, J. M. & Ocio, M. J. Optimization of the biocide properties of chitosan for its application in the design of active films of interest in the food area. *Food Hydrocolloids* **23**, 913–921 (2009).
134. Li, J. & Zhuang, S. Antibacterial activity of chitosan and its derivatives and their interaction mechanism with bacteria: Current state and perspectives. *European Polymer Journal* **138**, 109984 (2020).
135. Sousa, A. L. M. *et al.* Sodium dodecyl sulfate as a viral inactivator and future perspectives in the control of small ruminant lentiviruses. *Arquivos do Instituto Biológico* **86**, (2019).
136. Ramesh, S., Rajeswari, S. & Maruthamuthu, S. Effect of inhibitors and biocide on corrosion control of mild steel in natural aqueous environment. *Materials Letters* **57**, 4547–4554 (2003).
137. Simões, M., Simões, L. C., Cleto, S., Pereira, M. O. & Vieira, M. J. The effects of a biocide and a surfactant on the detachment of Pseudomonas fluorescens from glass surfaces. *International Journal of Food Microbiology* **121**, 335–341 (2008).
138. Howett, M. K. *et al.* A Broad-Spectrum Microbicide with Virucidal Activity against Sexually Transmitted Viruses. *Antimicrob Agents Chemother* **43**, 314–321 (1999).
139. Piret, J., Désormeaux, A. & Bergeron, M. G. Sodium lauryl sulfate, a microbicide effective against enveloped and nonenveloped viruses. *Curr Drug Targets* **3**, 17–30 (2002).
140. Falk, N. A. Surfactants as Antimicrobials: A Brief Overview of Microbial Interfacial Chemistry and Surfactant Antimicrobial Activity. *Journal of Surfactants and Detergents* **22**, 1119 (2019).
141. Davidovits, P. Chapter 7 - Fluids. in *Physics in Biology and Medicine (Fifth Edition)* (ed. Davidovits, P.) 85–101 (Academic Press, 2019). doi:10.1016/B978-0-12-813716-1.00007-0.
142. Free, M. L. Chapter 13 - The Use of Surfactants to Enhance Particle Removal from Surfaces. in *Developments in Surface Contamination and Cleaning (Second Edition)* (eds. Kohli, R. & Mittal, K. L.) 595–626 (William Andrew Publishing, 2016). doi:10.1016/B978-0-323-29960-2.00013-7.
143. Nakama, Y. Chapter 15 - Surfactants. in *Cosmetic Science and Technology* (eds. Sakamoto, K., Lochhead, R. Y., Maibach, H. I. & Yamashita, Y.) 231–244 (Elsevier, 2017). doi:10.1016/B978-0-12-802005-0.00015-X.
144. van Oss, C. J. Chapter Seven - Aqueous Solubility and Insolubility. in *Interface Science and Technology* (ed. van Oss, C. J.) vol. 16 85–111 (Elsevier, 2008).
145. Lin, J., Qiu, S., Lewis, K. & Klibanov, A. M. Bactericidal properties of flat surfaces and nanoparticles derivatized with alkylated polyethylenimines. *Biotechnol Prog* **18**, 1082–1086 (2002).
146. Koziróg, A., Brycki, B., Olejnik, K., Wysocka-Robak, A. & Dębska-Winkler, P. Cellulose products modified with monomeric and gemini surfactants: antimicrobial aspects. *Cellulose* **26**, 5559–5570 (2019).
147. Nechita, P., Bobu, E., Parfene, G., Dinica, R.-M. & Balan, T. Antimicrobial coatings based on chitosan derivatives and quaternary ammonium salts for packaging paper applications. *Cellulose Chemistry and Technology* **49**, 625–632 (2015).
148. Chattopadhyay, D., Chattopadhyay, S., Lyon, W. & Wilson, J. Effect of Surfactants on the Survival and Sorption of Viruses. *Environmental science & technology* **36**, 4017–24 (2002).
149. Makino, S. & Niki, R. Interaction of sodium dodecyl sulfate and of non-ionic detergents with S-carboxyamidomethyl-k-casein. *Biochim Biophys Acta* **495**, 99–109 (1977).
150. Tawfik, S. M., Zaky, M. F., Mohammad, T. G. M. & Attia, H. A. E. Synthesis, characterization, and in vitro antifungal activity of anionic and non-ionic surfactants against crop pathogenic fungi. *Journal of Industrial and Engineering Chemistry* **29**, 163–171 (2015).
151. Gilbert, P. & Moore, L. E. Cationic antiseptics: diversity of action under a common epithet. *J Appl Microbiol* **99**, 703–715 (2005).
152. McDonnell, G. E. *Antisepsis, Disinfection, and Sterilization: Types, Action, and Resistance*. *Antisepsis, Disinfection, and Sterilization* (American Society of Microbiology, 2007). doi:10.1128/9781555816445.
153. Maillard, J.-Y. Bacterial target sites for biocide action. *Journal of Applied Microbiology* **92**, 16S-27S (2002).
154. Permpoonpattana, P. *et al.* Functional characterization of Clostridium difficile spore coat proteins. *J Bacteriol* **195**, 1492–1503 (2013).

155. Kaboré, A. *et al.* Identification of spore-forming bacteria isolated from contaminated Lowenstein Jensen media and effectiveness of Vancomycin to reduce Mycobacterial culture contamination in Burkina-Faso. *Scientific Reports* **9**, 7194 (2019).
156. Denyer, S. P. Mechanisms of action of antibacterial biocides. *International Biodeterioration & Biodegradation* **36**, 227–245 (1995).
157. Denyer, S. P. Mechanisms of action of biocides. *International Biodeterioration* **26**, 89–100 (1990).
158. Bonvila, X. R., Roca, S. F. & Pons, R. S. Antiviral use of cationic surfactant. (2008).
159. Hamzah, N., Singhal, N., Padhye, L. & Swift, S. Effect of surfactants on Aspergillus brasiliensis ATCC 16404 physicochemical properties. *Journal of Environmental Chemical Engineering* **6**, 3392–3398 (2018).
160. Wu, S. H. & Pendleton, P. Adsorption of Anionic Surfactant by Activated Carbon: Effect of Surface Chemistry, Ionic Strength, and Hydrophobicity. *Journal of Colloid and Interface Science* **243**, 306–315 (2001).
161. Wu, D. *et al.* influence of non-ionic and ionic surfactants on the antifungal and mycotoxin inhibitory efficacy of cinnamon oil nanoemulsions. *Food Funct.* **10**, 2817–2827 (2019).
162. Chepurnov, A. A. *et al.* Inactivation of Ebola virus with a surfactant nanoemulsion. *Acta Tropica* **87**, 315–320 (2003).
163. Numata, M. *et al.* Pulmonary surfactant lipids inhibit infections with the pandemic H1N1 influenza virus in several animal models. *J. Biol. Chem.* **295**, 1704–1715 (2020).
164. Pramod, K. *et al.* Surfactant-based prophylaxis and therapy against COVID-19: A possibility. *Medical Hypotheses* **143**, 110081 (2020).
165. Sturman, L. S., Ricard, C. S. & Holmes, K. V. Conformational change of the coronavirus peplomer glycoprotein at pH 8.0 and 37 degrees C correlates with virus aggregation and virus-induced cell fusion. *Journal of Virology* **64**, 3042–3050 (1990).
166. Leth-Larsen, R., Zhong, F., Chow, V. T. K., Holmskov, U. & Lu, J. The SARS coronavirus spike glycoprotein is selectively recognized by lung surfactant protein D and activates macrophages. *Immunobiology* **212**, 201–211 (2007).
167. Hawgood, S. & Clements, J. A. Pulmonary surfactant and its apoproteins. *J Clin Invest* **86**, 1–6 (1990).
168. Takano, H. Pulmonary surfactant itself must be a strong defender against SARS-CoV-2. *Medical Hypotheses* **144**, 110020 (2020).
169. Almeida, D. S. *et al.* Biodegradable CA/CPB electrospun nanofibers for efficient retention of airborne nanoparticles. *Process Safety and Environmental Protection* **144**, 177–185 (2020).
170. Zhang, T. *et al.* Bactericidal and antifouling electrospun PVA nanofibers modified with a quaternary ammonium salt and zwitterionic sulfopropylbetaine. *Materials Science and Engineering: C* **111**, 110855 (2020).
171. Zhang, S. *et al.* New insights into synergistic antimicrobial and antifouling cotton fabrics via dually finished with quaternary ammonium salt and zwitterionic sulfobetaine. *Chemical Engineering Journal* **336**, 123–132 (2018).
172. Chen, S. *et al.* Environmentally Friendly Antibacterial Cotton Textiles Finished with Siloxane Sulfopropylbetaine. *ACS applied materials & interfaces* **3**, 1154–62 (2011).
173. Zhang, X. *et al.* Modification of microfiltration membranes by alkoxysilane polycondensation induced quaternary ammonium compounds grafting for biofouling mitigation. *Journal of Membrane Science* **549**, 165–172 (2018).
174. Lu, J. *et al.* COVID-19 Outbreak Associated with Air Conditioning in Restaurant, Guangzhou, China, 2020. *Emerging Infect. Dis.* **26**, 1628–1631 (2020).
175. Shao, S. *et al.* Risk assessment of airborne transmission of COVID-19 by asymptomatic individuals under different practical settings. *Journal of Aerosol Science* **151**, 105661 (2021).
176. Correia, G., Rodrigues, L., Gameiro da Silva, M. & Gonçalves, T. Airborne route and bad use of ventilation systems as non-negligible factors in SARS-CoV-2 transmission. *Medical Hypotheses* **141**, 109781 (2020).
177. Qian, H. & Zheng, X. Ventilation control for airborne transmission of human exhaled bio-aerosols in buildings. *J Thorac Dis* **10**, S2295–S2304 (2018).
178. Guo, B. M. *et al.* Review and comparison of HVAC operation guidelines in different countries during the COVID-19 pandemic. *Building and Environment* 107368 (2020) doi:10.1016/j.buildenv.2020.107368.
179. Sherri, S. ASHRAE Issues Statements on Relationship Between COVID-19 and HVAC in Buildings. https://www.ashrae.org/about/news/2020/ashrae-issues-statements-on-relationship-between-covid-19-and-hvac-in-buildings (2020).
180. Amoatey, P., Omidvarborna, H., Baawain, M. S. & Al-Mamun, A. Impact of building ventilation systems and habitual indoor incense burning on SARS-CoV-2 virus transmissions in Middle Eastern countries. *Science of The Total Environment* **733**, 139356 (2020).
181. Aljofi, E. The Measures of Light Performance of Wind Catchers in Hot Climatic Zones. *International Journal of Engineering and Technology* **8**, 45–49 (2016).
182. Li, X.-X. Heat wave trends in Southeast Asia during 1979–2018: The impact of humidity. *Science of The Total Environment* **721**, 137664 (2020).
183. Gilkeson, C. A., Camargo-Valero, M. A., Pickin, L. E. & Noakes, C. J. Measurement of ventilation and airborne infection risk in large naturally ventilated hospital wards. *Building and Environment* **65**, 35–48 (2013).
184. Lynch, R. M. & Goring, R. Practical Steps to Improve Air Flow in Long-Term Care Resident Rooms to Reduce COVID-19 Infection Risk. *Journal of the American Medical Directors Association* **21**, 893–894 (2020).
185. Kujundzic, E., Matalkah, F., Howard, C. J., Hernandez, M. & Miller, S. L. UV air cleaners and upper-room air ultraviolet germicidal irradiation for controlling airborne bacteria and fungal spores. *J Occup Environ Hyg* **3**, 536–546 (2006).
186. Lee, J. *et al.* Effect of air cleaner on reducing concentration of indoor-generated viruses with or without natural ventilation. *Aerosol Science and Technology* **55**, 1288–1303 (2021).
187. Shakoor, S., Mir, F., Zaidi, A. K. M. & Zafar, A. Hospital preparedness in community measles outbreaks—challenges and recommendations for low-resource settings. *Emerg Health Threats J* **8**, (2015).
188. Mazumdar, S. & Chen, Q. A one-dimensional analytical model for airborne contaminant transport in airliner cabins. *Indoor Air* **19**, 3–13 (2009).

III

NANOFIBER ENGINEERING

III - NANOFIBER ENGINEERING

Composition Effects on the Morphology of PVA/Chitosan Electrospun Nanofibers

Gustavo Cardoso da Mata[1, *], Maria Sirlene Morais[2], Wanderley Pereira de Oliveira[2], Mônica Lopes Aguiar[1]

[1] Department of Chemical Engineering, Federal University of São Carlos, Rod. Washington Luiz, km 235, SP310, São Carlos - SP, 13565-905, Brazil;

[2] Faculty of Pharmaceutical Science of Ribeirão Preto, University of São Paulo, Av. do Café s/no, CEP: 14040-903, Bairro Monte Alegre, Ribeirão Preto, SP, Brazil

[*] *Corresponding author*: mlaguiar@ufscar.br

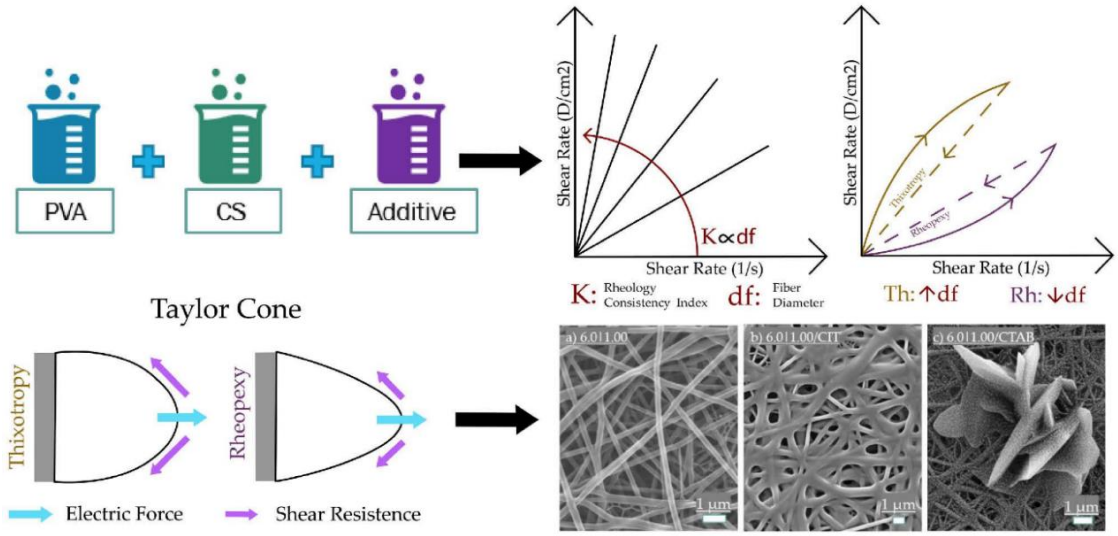

Abstract: Since the SARS-CoV-2 pandemic, the interest in applying nanofibers for air filtration and personal protective equipment has grown significantly. Due to their morphological and structural properties, nanofibers have potential applications for air filtration in masks and air filters. However, most nanofiber membrane materials used for these purposes are generally non-degradable materials, which can contribute to the disposal of plastic waste into the environment. Hence, this work aims to produce polyvinyl alcohol (PVA) and chitosan (CS) biodegradable nanofibers with controlled morphology and structure via electrospinning. An experimental design was used to investigate the effects of the PVA|CS ratio and concentration on the properties of the electrospinning compositions and electrospun nanofiber mat. The electrospinning parameters were constant for all experiments: Voltage of 20 kV, a feed rate of 0.5 mL·h^{-1}, and a distance of 10 cm between the needle and a drum collector. PVA proved to be an efficient adjuvant to the CS electrospinning, obtaining a wide range of nanofiber diameters. Furthermore, 6.0% PVA and 1% CS were the best compositions after optimization with the response surface methodology, with a mean fiber diameter of 204 nm. The addition of biocide agents using the optimized condition was also investigated, using surfactants, citric acid, and pure and encapsulated essential oils of *Lippia sidoides*. Pure oil improved the material without enlarging the nanofiber sizes compared to the other additives. The nanofiber membranes produced have the potential to be used in air filtration or wound-dressing applications where biocidal activity is needed.

Keywords: nanofibers; electrospinning; rheology; chitosan; PVA; membranes; response surface;

Published in: Polymers (MDPI) **DOI:** 10.3390/polym14224856

3.1 Introduction

Since the SARS-CoV-2 pandemic, the interest in applying nanofibers' morphological and structural properties for air filtration in masks and air filters has increased. Several studies in the current literature reported the air filtration of bioaerosols using electrospun nanofibers[1–5]. Electrospinning is a versatile technique, generating micro and nanofibers with adequate properties for air filtration, such as a high surface-area-to-volume ratio, low basis weight, and uniform size[6]. Electrospun polyacrylonitrile (PAN) presented suitable properties[7,8], especially for air filtration[9]. Leung and Sun (2020) obtained efficient polyvinylidene fluoride (PVDF) nanofiber mats with fiber diameters between 84 and 524 nm for use in filtering a simulated SARS-CoV-2 virus[10,11]. However, these disposable materials, usually made with non-degradable polymers, are discarded into the environment, turning them into pollutants. Therefore, searching for highly efficient, low-cost, biodegradable air filtration materials for use in these types of personal protective equipment is an important research subject.

Recycled materials have also gained attention, especially for air filtration[12]. Plastics such as polyethylene terephthalate (PET) can be electrospun from raw PET bottles[13,14], producing materials with promising properties[15]. However, the solvents used to dissolve the polymers (e.g., trifluoracetic acid) are also a problem as they are usually aggressive, toxic, and difficult to handle. Therefore, using natural and biodegradable polymers and mild solvents can make electrospinning more environmentally friendly.

Polyvinyl alcohol (PVA) is a non-toxic and hygroscopic compound that has already been tested for air filtration[16]. It can reticulate its chains to confer resistance to moisture and other properties[17]. The addition of other materials can also confer biocide action, higher hydrophobicity, and improved mechanical properties[18–22]. The blend of PVA with low chitosan (CS) contents modifies the solution properties by improving its spinnability[23], resulting in hydrophobic fibers. The synthesis of membrane blends with higher contents of CS is possible via methods such as NIPS (nonsolvent-induced phase separation)[24] and freezing–thawing cycles[25]. Nevertheless, the electrospinning of chitosan is still problematic because of its high viscosity[26] and the need for electrical potentials of 4 $kV \cdot cm^{-1}$ or more[27]. Other additives, such as surfactants and essential oils (EOs), can also change the morphological properties of electrospun mats, aiming to improve the quality of fibers obtained and confer biocidal activity to the fibers.

Recently, PVA has been used as an excellent adjuvant for CS electrospinning[28] and is used in food packing[29], drug delivery[30], tissue regeneration[31], and wound dressing[32]. However, its harsh properties still hinder the process in areas such as air filtration. The main goal of this study is to produce a biodegradable material with high contents of CS without a loss of quality and control and optimize the nanofiber structure for further applications in air filtration with biocidal activity against pathogens such as SARS-CoV-2. The influence of rheological and solution properties was determined and linked to the properties of the formed electrospun nanofibers. Since PVA has no antimicrobial activity and chitosan's activity depends on the pH and medium, adding a biocidal agent is necessary. Finally, certain additives such as surfactants, citric acid, and essential oil (pure and encapsulated) were investigated for the optimized PVA/CS electrospinning composition, evaluating the effects on the fiber quality and conferring biocidal activity to the material.

3.2 Materials & Methods

3.2.1 Materials: The polymers used in this study were polyvinyl alcohol (PVA) with a molecular weight of 85.500 g/mol and a degree of hydrolysis of 89.5% (Vetec Química Fina, Duque de Caxias/RJ, Brazil) and chitosan (CS) with a degree of deacetylation of 68.5% (Polymar, Rio de Janeiro/RJ, Brazil). Analytical-grade glacial acetic acid (G) at 99.0% (LabSynth, Diadema/SP, Brazil) was used as the solvent. The surfactant additives evaluated were sodium dodecyl sulfate at 95% (SDS—Neon, Suzano/SP, Brazil) and Cetyltrimethylammonium Bromide at 98% (CTAB, Sigma Aldrich, Saint Louis/MO, United States). The other additives used were citric acid (LabSynth, Diadema/SP, Brazil) and the essential oil of *Lippia Sidoides* (Produtos Naturais LTDA, Horizonte/CE, Brazil), pure and encapsulated into nanostructured lipid carriers (NLCs).

3.2.2 Electrospinning of the PVA|CS Compositions: The polymer solutions were separately prepared, with PVA varying from 6% to 12% (*w*/*v*) and CS from 1% to 4% (*w*/*v*), as described in **Table 3.1**. The polymers were weighed and dissolved in a water/glacial acetic acid system (30:70) maintained under magnetic stirring for three hours at a temperature of 80 to 90 °C for their complete dissolution. The samples of different concentrations of PVA|CS were then electrospun at varying operational parameters of the process to enhance the properties of the resulting fibers.

The electrospinning apparatus was composed of a high-voltage generator (0 to 50 kV) with a continuous current source (Electrotest HIPOT CC, Model EH6005C, Instrutemp, São Paulo/SP, Brazil), an infusion pump (Harvard Apparatus, Model Elite I/W PROGR SINGLE, Holliston/MA, USA), and a stainless-steel rotary cylinder (a diameter of 100 mm, length of 200 mm) as the nanofiber collector. The electrospinning process occurred inside a fully grounded, electrically insulated compartment to minimize the occurrence of discharges during operation.

Preliminary tests evaluated the diameters of the syringe needles (0.55, 0.60, 0.70, and 1.20 mm) and the distance between the needle and collector (10, 11, and 12 cm). The data of the preliminary runs used to set the conditions are shown in the supplementary material (**Table 3.S1**). A metallic needle with a 0.55 mm opening attached to a 5 mL plastic syringe fed the electrospinning formulations (**Table 3.1**). The electrospinning conditions were constant for all experimental runs: A flow rate of 0.5 $mL \cdot min^{-1}$, an electrical field of 20 kV, and a 3 h production duration. The metallic drum collector was covered with aluminum foil and placed at a distance of 10 cm from the needle tip, with the rotation speed set at 595 rpm. The electrospun nanofibers remained under ambient air for 1 h to volatilize the remaining acetic acid. The temperature and relative humidity in the electrospinning process was maintained at approximately 22 °C and 40%, respectively.

3.2.3 Morphology Characterization of the Electrospun Nanofiber: The morphology of the electrospun nanofibers was analyzed from micrographs obtained by scanning electron microscopy (SEM). First, 5×5 mm samples of the electrospun nanofiber mat samples were coated with carbon and gold in a Bal-Tec SCD Sputter Coater model-050 (Fürstentum/Liechtenstein) under a pressure of 0.1 mbar. The SEM micrographs were

obtained with the model SEM FEI Inspect F50 (Eindhoven, The Netherlands), a FEG electron source with ETD and vCD detectors. The diameter distribution of the electrospun nanofibers was determined by image analysis from SEM micrographs using ImageJ® software. Fourier-transform Infrared Spectroscopy (FTIR) was determined using a spectrophotometer FTIR Bomem MB-100 (ABB Bomem, Quebec, QC, Canada) with spectra ranging from 400 to 4000 cm.

Table 3.1 Composition of the blended PVA and CS (PVA|CS) formulations. The PVA and CS contents show the concentration of the previous solution. The resulting values show the concentration of polyvinyl alcohol relative to chitosan (PVA|CS) after mixing in the proportion of 75:25.

Chitosan (CS) Content	Polyvinyl Alcohol (PVA) Content			
	6%	8%	10%	12%
1%	4.5|0.25	6.0|0.25	7.5|0.25	9.0|0.25
2%	4.5|0.50	6.0|0.50	7.5|0.50	9.0|0.50
3%	4.5|0.75	6.0|0.75	7.5|0.75	9.0|0.75
4%	4.5|1.00	6.0|1.00	7.5|1.00	9.0|1.00

3.2.4 Electrical Conductivity & Rheology of the Formulations: Determination of the electrical conductivity of the samples was done by using a Metrohm 912 bench-top conductometer (Metrohm AG, Herisau, Switzerland) in triplicate measurements. To determine the rheology of each solution (duplicate assays), a Brookfield LV-DVIII coaxial cylinder Rheometer (Brookfield Engineering Laboratories Inc., Middleboro, USA) equipped with an SC4-18 spindle sensor was used. The spindle increased its rotation at a limited speed, and then the process was reversed, diminishing its velocity. Brookfield Rheocalc 3.2 software controlled the Rheometer and collected the experimental data on the shear rate and the corresponding shear stress.

3.2.5 Electrospinning of PVA|CS Compositions with Additives: The PVA|CS solution 6.0|1.00 (**Table 3.1**) was used to produce the samples loaded with additives at a concentration of 5% (*w*/*w*—dry basis). The new samples were kept under magnetic stirring for 30 min at 30 to 40 °C. The new samples were named according to their respective additive, namely, cetyltrimethylammonium bromide (6.0|1.00/CTAB), citric acid (6.0|1.00/Cit), and sodium dodecyl sulfate (6.0|1.00/SDS).

Essential oil (EO) was extracted from *Lippia sidoides*—popularly known as pepper-rosemary—an aromatic Brazilian shrub with proven antimicrobial activity[33]. Three samples with *Lippia sidoides* EO were used, namely, pure oil (6.0|1.00/EO) and the EO loaded in nanostructured lipid carriers (6.0|1.00/NLC-Com and 6.0|1.00/NLC-BC)[34]. The NLCs' constituents were the essential oil of *Lippia sidoides*, SDS, oleic acid (Vinhedo/SP, Brazil), and a solid lipid. The solid lipid for the sample NLC-Com was Compritol® 888 ATO (Gattefossé, Saint-Priest, France), while the sample NLC-BC used a mixture of beeswax (Via Farma, São Paulo/SP, Brazil) and carnauba wax (Foncepi, Fortaleza/CE, Brazil). A detailed description of the NLC-Com (F8) and NLC-BC (F18) preparations was reported by Baldim and coworkers (2022)[35].

3.3 Results & Discussion

3.3.1 Morphological Structure of the Fibers

To observe the real influence of the solutions' concentrations of PVA and CS on the fibers' properties, selected samples shown in **Table 3.1** were electrospun and submitted to an SEM analysis (**Figure 3.1**).

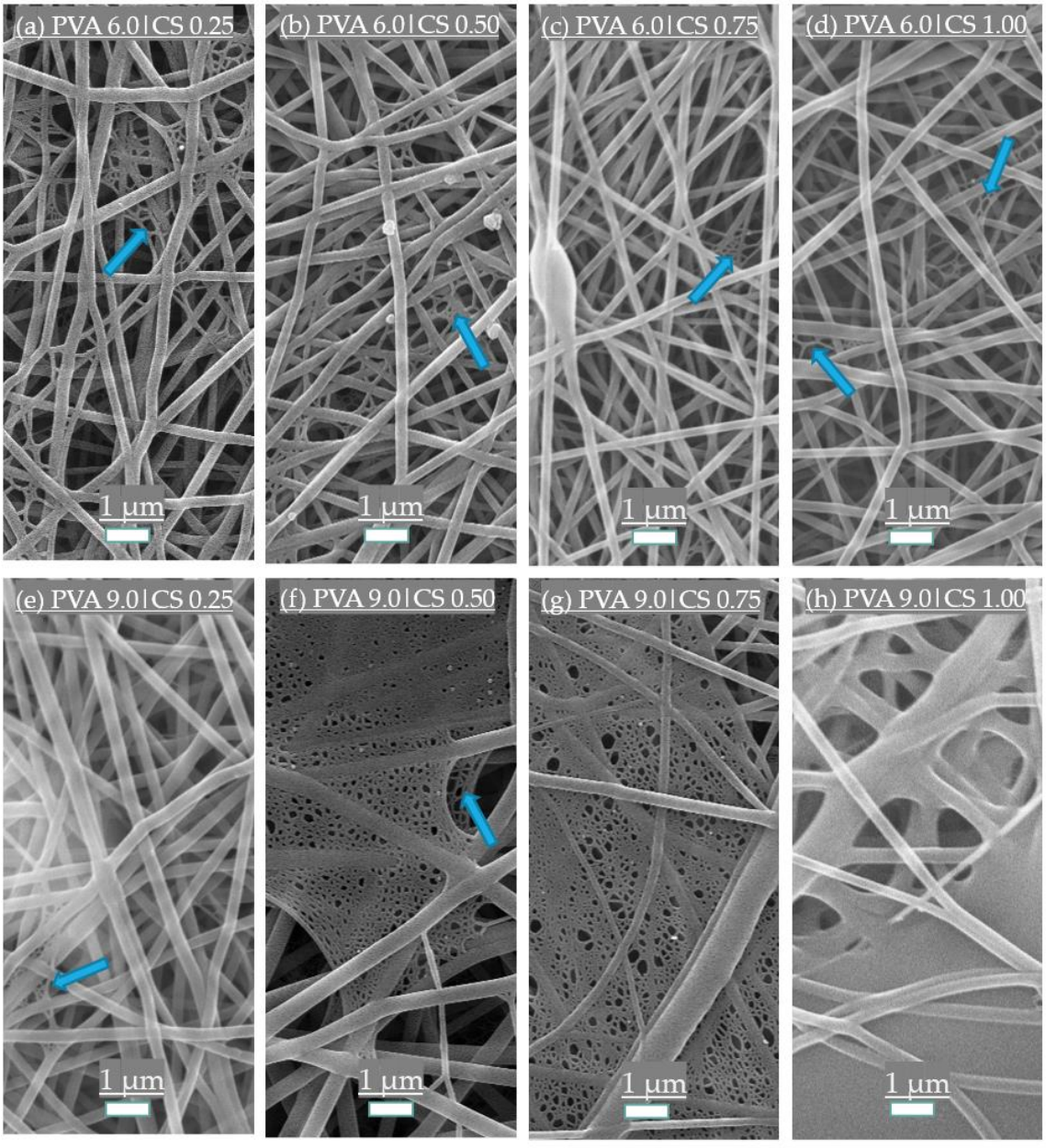

Figure 3.1. SEM photomicrographs from samples with fixed PVA series at 6.0%: (**a**) CS 0.25; (**b**) CS 0.50; (**c**) CS 0.75; and (**d**) CS 1.00%. A series with 9.0% PVA with (**e**) CS 0.25; (**f**) CS 0.50; (**g**) CS 0.75; and (**h**) CS 1.00% is also presented. Arrows indicate spider nets.

PVA has been shown to be effective as an adjuvant for the electrospun CS polymer, forming smooth fibers without beads. Chitosan solutions below 2% do not have sufficient material to form a fibrous structure, while solutions above 2% are too

viscous for electrospinning[36]. The high viscosity of the chitosan solutions occurs due to strong hydrogen bonds between the NH_2 and OH groups of the CS chains. Adding PVA seems to diminish the degree of those interactions between the CS chains due to interactions between the two polymers' chains; in this case, PVA wold act as a plasticizing agent to CS, diminishing the CS chains' entanglement, making spinnability possible. The same effect was observed by reducing the molecular weight of CS and, as a consequence, its entanglement degree[26]. Other alternatives previously investigated include using co-solvents such as DMSO to reduce entanglement and improve the chitosan's spinnability[36].

PVA addition also creates structures of different degrees in the nanofiber mat, known as spider-net webs[6,37]. PVA 6.0% shows a sparse and well-distributed spider-net structure alongside the fiber mat that appears denser at higher contents (PVA 7.5 and 9.0%) with smaller pores. At these high contents of PVA, fiber fusion, film layers, and aggregates appear more often. The formation of the spider-net structures can improve the PVA's nanofibers mat strength, increasing the network resistance to deformation[38]. However, in air filtration applications, a dense spider-net web close to forming a film may significantly increase the pressure drop to unacceptable values, impeding its use.

3.3.1.1 Fourier-Transform Infrared Spectroscopy (FTIR): Figure 3.2 shows FTIR results obtained for the pure solutions of PVA at 12.0% and CS at 4.00% and their mixtures—sample PVA 9.0|CS 1.00. The occurrence of certain interactions between the PVA and CS functional groups can be seen in **Figure 3.2**. The characteristic PVA groups, CH_2 and C–O, are represented by bands at 2923 cm^{-1} and 1082, respectively[31]. The stretching of the OH group causes a peak at 3305 cm^{-1}, and the 835 cm^{-1} band is related to the C–C resonance group[39].

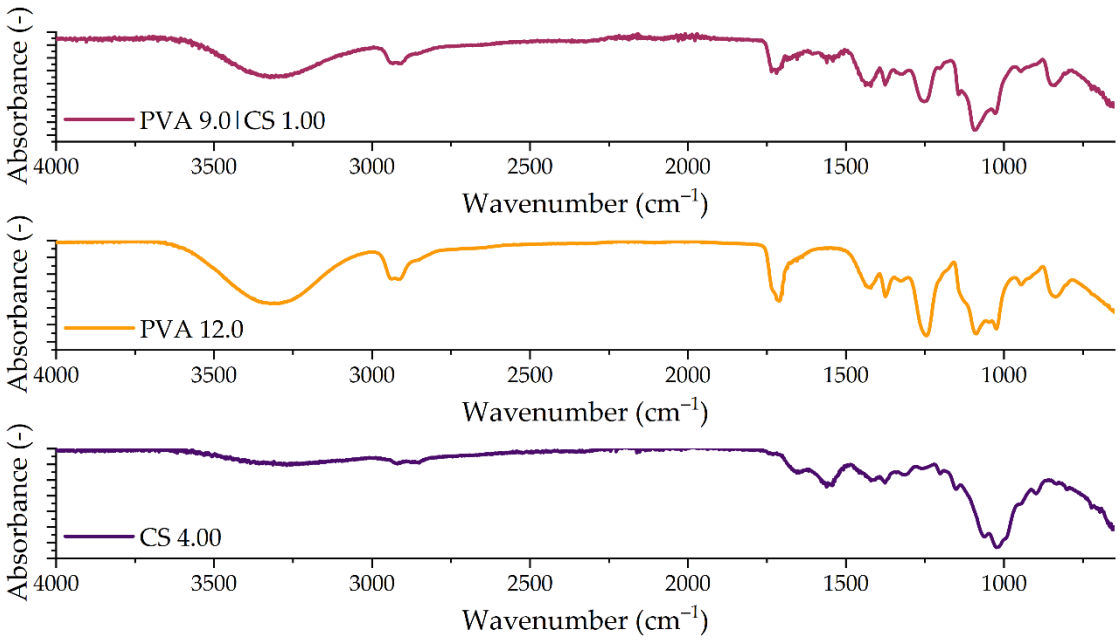

Figure 3.2. FTIR spectra of the pure samples (PVA 12.0 and CS 4.00) and after the blend at the PVACS ratio of 75:25 (PVA 9.0|CS 1.00).

The band at 1154 cm^{-1} represents the resonance of the chitosan saccharide structure. The band at 1074 cm^{-1} is related to the stretching vibrations of C–O–C glycosidic linkages[31]. Peaks at 1074 and 1380 cm^{-1} represent the amide C–N bending vibrations and the C–H amide group[39]. The absorption band in the range of 1650 to 1655 cm^{-1} is related to vibrational C=O, caused by partial deacetylation of chitin and characteristic of the secondary amide groups[40]. The broad band between 3000 and 3600 cm^{-1} is related to the N–H stretching of primary amino groups[41], while the band at 1575 cm^{-1} is associated with N–H bending[42]. The band at 896 cm^{-1} is evidence of Chitosan OH out-of-plane ring stretching[28].

The out-of-plane OH vibration band disappears after the blending of PVA and CS. The formation of hydrogen bonds between PVA and CS molecules[28] is associated with the broadening of the absorption band between 3000 and 3600 cm^{-1}. Stretching vibrations diminish with lower frequencies and hydrogen bonds, leading to intermolecular bonds between the CH_2-OH group in CS and the hydroxyl groups of PVA[31,41]. Çay and colleagues [2014] reported the disappearance of the PVA band 1260 cm^{-1} after blending with CS. In our study, the band remains after the blend, showing O-H structures[41]. The peak at 1708 cm^{-1} is associated with the carbonyl of polyvinyl acetate, showing other possible bonding structures[43].

3.3.2 Chemical Properties

3.3.2.1 Electrical Conductivity: Table 3.2 presents the electrical conductivity of the pure CS solutions and PVA|CS mixtures. The influence of PVA reduces the electrical conductivity of the solutions, as seen in the main effects and interaction plots (**Figure 3.S1 a)** and **b)** of the supplementary material). For the 9.0% PVA series, the resulting conductivity is inferior to the pure solution of PVA. The high PVA content may create more hydrogen bonds with the CS, diminishing the chemical groups responsible for electrical conductivity. The molecular structure of PVA in a medium with an excess of H^+ ions (acid solution) inhibits the protons' dissociation, diminishing the electrical conductivity of the solutions. Higher electrical conductivity may be beneficial for the electrospinning process. However, too-high electrical conductivity can prejudice fiber formation, leading to the formation of aggregates films, as usually seen in the electrospinning of chitosan solutions[27]. Values between 400 and 450 $\mu S \cdot cm^{-1}$ appear ideal for the conductivity of PVA|CS solutions. An increase in electrical conductivity leads to a decrease in the nanofiber diameter for the level ranges studied. Some authors reported similar results[37,44].

Table 3.1. Electrical conductivity ($\mu S \cdot cm^{-1}$) of pure CS solutions and CS/PVA mixtures (% *w*/*w*).

Chitosan Content	Polyvinyl Alcohol (PVA) Content				
	0.0	4.5	6.0	7.5	9.0
0.00	-	238.1 ± 6.9	231.9 ± 6.8	249.7 ± 15.6	286.4 ± 30.4
0.25	519.9 ± 7.0	312.9 ± 17.8	254.3 ± 2.6	247.6 ± 7.9	278.8 ± 6.1
0.50	826.5 ± 6.7	326.9 ± 6.2	301.8 ± 10.4	300.8 ± 1.7	180.5 ± 12.5
0.75	1176.3 ± 8.2	347.9 ± 7.2	363.2 ± 4.1	350.9 ± 8.6	195.3 ± 11.9
1.00	1505.9 ± 14.5	445.9 ± 4.5	396.2 ± 5.6	369.7 ± 1.9	211.8 ± 8.6

3.3.2.2 Rheology Consistency Index (K) & Flow Index (n): The flow behavior of the polymer solution during electrospinning can be visualized, in a very simplified form, as the flow behavior inside the needle (capillary) and outside the needle (whipping path), promoted by viscoelastic, surface and electrical forces. Inside the needle, the deformation rates are predominantly shear rates ($\dot{\gamma}$), while outside are mainly elongational rates ($\dot{\varepsilon}$). Shear rates ($^{\partial v_i}/_{\partial x_j}$), where the v_i are the velocity components along the j-axis, do not increase the length of a fluid element, while elongation rates ($^{\partial v_i}/_{\partial x_i}$), do[45]. In order to calculate those rates, the influence of the electrical field should be acknowledged. However, the experimental (and even theoretical) setup for those measurements can be quite difficult. Elongational rates between the Taylor cone and the jet section have been measured[46] and are substantially high, of the order of 10^3 s^{-1}. On the other hand, if one assumes that the needle has the shape of a capillary or tube and that the polymer solution follows a power law model, an approximation for the values of the shear rates can be found[45]. The *Ostwald* de Waele power law model is described in **Equation 3.1:**

$$\tau = K \cdot \dot{\gamma}^n \qquad \textbf{(3.1)}$$

where τ is the shear stress (or applied force/area, Dyn·cm^{-2}), $\dot{\gamma}$ is the shear rate (or resulting deformation/time or $^{d\gamma}/_{dt}$ in 1.s^{-1}), n (flow index, dimensionless) and K (consistency index, Dyn·cm^{-2}·s)[47,48]. Viscosity is defined as the ratio between τ and $\dot{\gamma}$; therefore, using the power law model, $\eta = K.\dot{\gamma}^{n-1}$. The flow index n can be lower, higher or equals to 1. When it is 1, the viscosity is equal to K and the fluid is denominated Newtonian (constant viscosity); when it is lower than 1, the viscosity will decrease (thinning) with the shear rate and the fluid is called pseudoplastic; finally, when it is higher than 1, the viscosity will increase with the shear rate and the fluid is called dilatant. Polymer melts and some polymer solutions are mostly Newtonian at low shear rates and pseudoplastic at high shear rates.

Therefore, if the value of n is calculated from a η versus $\dot{\gamma}$ curve, the shear rate at the wall ($\dot{\gamma}_w$) of a tube or capillary can be calculated from the following **Equation 3.2**[45]:

$$\dot{\gamma}_w = \left(\frac{3n+1}{4n}\right)\frac{32Q}{\pi D^3} \qquad \textbf{(3.2)}$$

where Q is the volumetric flow rate and D the diameter of the tube. If the needle has different diameters along its axis, at each diameter $\dot{\gamma}_w$ can be calculated. Recalling also, that as $\dot{\gamma} \to 0, \to K$. Therefore, experimental measurement of η versus $\dot{\gamma}$ at different shear rates can allow analyzing the flow behavior at low and high shear rates. This behavior is called time-independent flow behavior.

OriginLab® was used to process the rheological and morphological data The rheology consistency index (K) has also been correlated to the nanofiber size as it has been observed that the mean fiber diameter increases with the K value[49] when the shear rates are extremely low. Surface tension dominates the electrospun jet by reducing the ratio of polymer chains per solvent, resulting in thinner fibers[50]. On the other hand, polymeric fluids and solutions can also display time-dependent behavior[51]. Thixotropic solutions have a decrease of viscosity with time at an applied shear rate, while rheopectic solutions have an increase of viscosity over time also at an applied shear rate. The shift from rheopexy to thixotropy of the solutions with PVA increment is a factor relevant to the process. Thixotropic polymer solutions present a high initial deformation resistance. Therefore, a higher electrical field is needed to overcome the initial resistance (e.g., pure CS 1.00% is electrospun only at 40 kV[27]).

The fiber formation also depends on the polymer solution concentration and kinematic viscosity[52]. When an electrical field is applied to a polymer solution pendant droplet, it can assume the stable shape known as the Taylor cone[53]. This results from the equilibrium forces between the surface tension and the electrical charges on the droplet. Depending on the nature of the polymer solution (e.g., Newtonian, inviscid, or viscoelastic), it can assume different shapes[47]. During elongation, fibers gain resistance due to solvent evaporation evaporation, thus increasing the viscosity. Fibers with high flexibility are prone to forming better network structures due to interfiber interactions[38]. **Figure 3.3** exemplifies the process. **Figure 3.4** shows the rheograms for certain sample series studied.

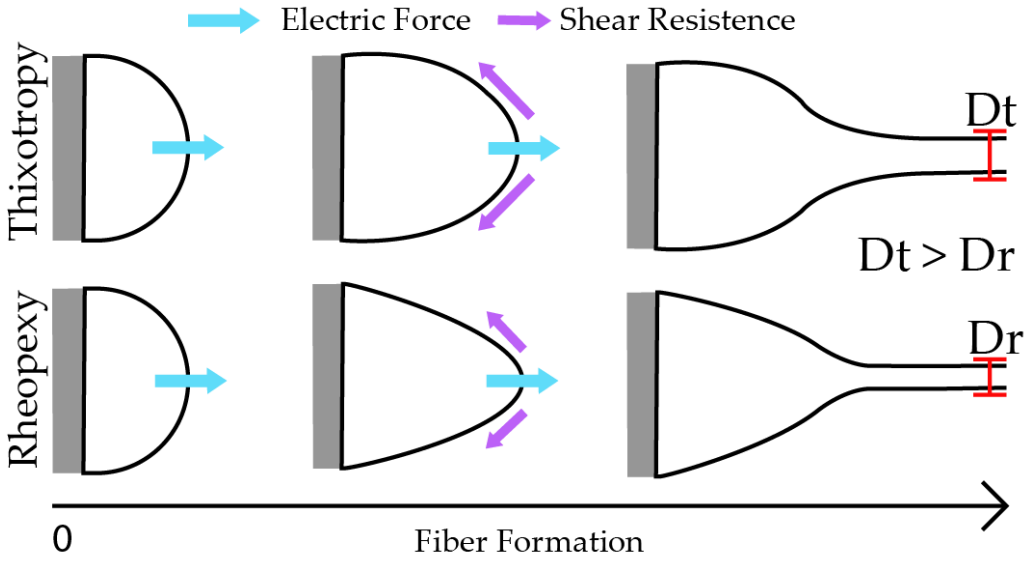

Figure 3.3. Taylor cone deformation according to the rheology properties. Thixotropic behavior leads to thicker fibers when compared with rheopetic behavior.

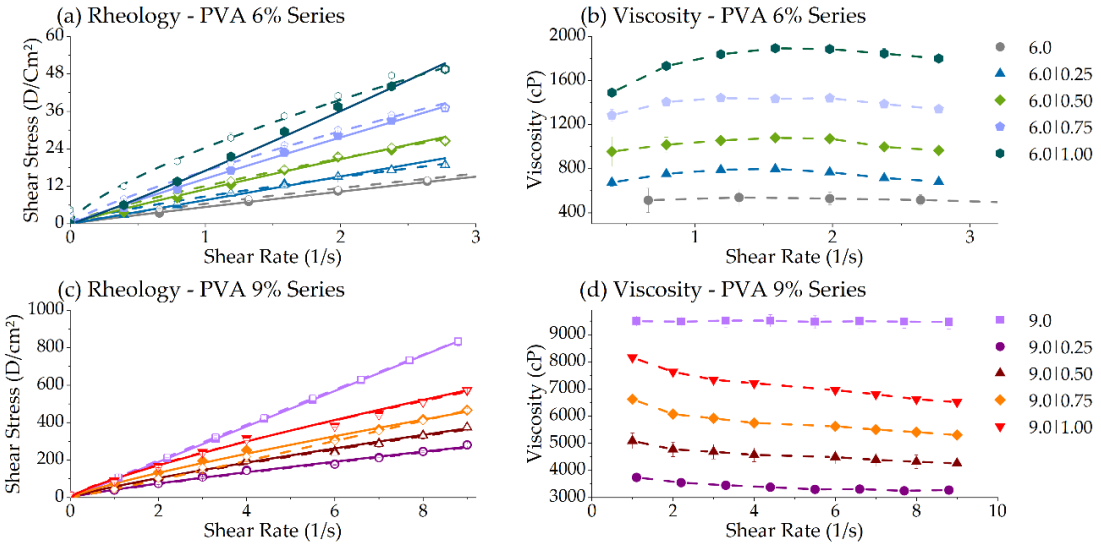

Figure 3.4. Rheograms for the PVA fixed series of 6.0% analyzed on the range of 0 to 3 s^{-1}: (**a**) Time-dependent behavior and (**b**) viscosity. Rheograms for the PVA fixed series of 9.0% analyzed in a range of 0 to 9 s^{-1}: (**c**) Time-dependent behavior and (**d**) viscosity. Close dots and solid lines show the increase in shear stress, while open dots and dash lines show tensile stress relaxation.

The surface tension dominates the electrospun jet by reducing the ratio of polymer chains per solvent molecule, resulting in thinner fibers[50]. Adding CS to the pure PVA at 6.0% increased its pseudoplastic behavior and solution viscosity. For pure PVA at 9.0%, however, adding CS produced the opposite effect, diminishing the viscosity. They are so viscous that the fibers show difficulties in flowing and elongating. These compositions also presented poor spinnability. The morphology results showed that the too-high PVA viscosities at 9.0% produced large fibers.

For PVA|CS solutions, K values under 30.0 Dyn·cm^{-2}·s lead to thinner fibers. **Table 3.S2** presents the values of K (consistency index) and *n* (flow index) for all compositions with regression plot data. The rheology consistency index is closely related to nanofiber size since the mean fiber diameter increases with the K value[49].

3.3.2.3 Fiber Size Diameter (df): The fiber mat originating from the PVA 6.0|CS 1.00 solution was chosen because of the high content of chitosan and good spinnability. The minor presence of spider-net webs guarantees structural resistance without blocking the mat pores, as seen in the other PVA solutions with high CS contents. The rheological properties of PVA 6.0|CS 1.00 and the pure CS 1.00 solution were almost identical. Therefore, adding PVA at this concentration does not change the solution's rheology significantly, causing a high decrease in the formulation's electrical conductivity (from 1505.9 for Pure CS 1.00 to 393.3 µS·cm^{-1} for PVA 6.0|CS 1.00). The fiber size distribution was determined for the different series according to PVA and CS contents, as shown in **Figure 3.5**. **Table 3.3** shows the average fiber diameter for each combination of PVA|CS blends. **Table 3.S3** shows the quality of the produced fibers. For series with low fixed PVA content (4.5 and 6.0), downward variation occurs with the increase in CS, while a wider distribution is evidenced at higher contents (7.5 and 9.0). For the fixed series of CS, the increase in PVA dislocates the distributions for the samples with low PVA (4.5 and 6.0).

Table 3.3. Average fiber diameter (nm) for the electrospun fibers obtained from different solutions of PVA and CS (PVA|CS) (%*w*/*w*).

Chitosan Content	Polyvinyl Alcohol (PVA) Content			
	4.5	**6.0**	**7.5**	**9.0**
0.25	153.1 ± 31.2	214.8 ± 38.7	240.9 ± 76.8	282.4 ± 40.2
0.50	193.4 ± 40.5	234.0 ± 34.4	242.3 ± 62.6	398.8 ± 65.5
0.75	159.3 ± 27.8	229.1 ± 39.9	286.2 ± 87.1	261.8 ± 66.6
1.00	162.4 ± 21.2	204.4 ± 32.2	376.7 ± 89.0	416.4 ± 101.8

The high proportion of PVA relative to CS overcomes the chitosan's influence on the final fiber dimensions. Fiber sizes smaller than 250 nm in diameter are beneficial for the air filtration of viruses and small nanoparticles by improving the collection mechanisms of nanoparticles[15,54,55]. Smaller fibers can create a too-sinuous passage, increasing the pressure drop.

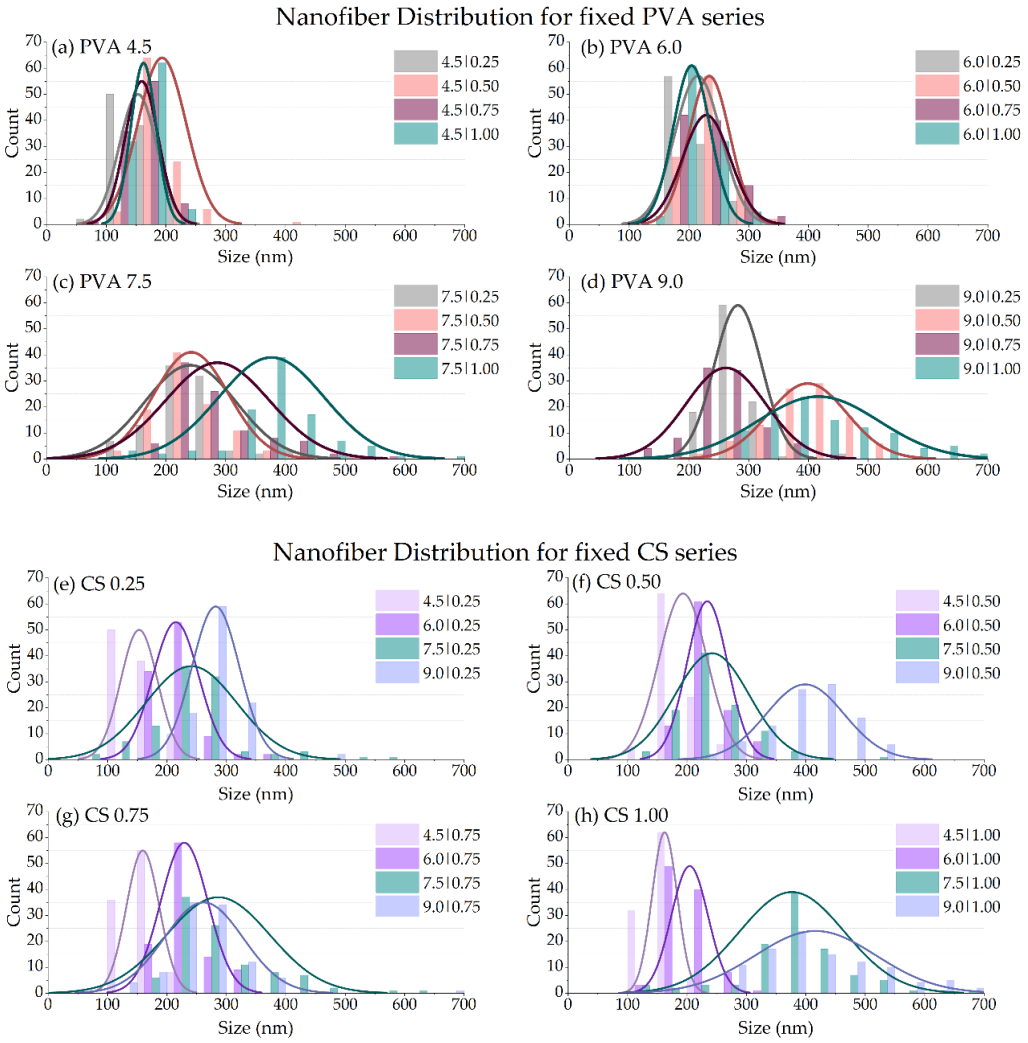

Figure 3.5. Fiber size distribution for samples with fixed PVA content series: (**a**) 4.5; (**b**) 6.0; (**c**) 7.5, and (**d**) 9.0% *w*/*w*. Fiber size distribution for the series with fixed CS at: (**e**) 0.25; (**f**) 0.50; (**g**) 0.75, and (**h**) CS 1.00%.

Other parameters can also interfere with fiber formation. The rise in flow rate squeezes more solution through the needle, increasing the fiber diameter[52]. With more material on the pendant droplet, slight changes in the surface charge density can influence the fiber's evolution[56]. Water in the atmosphere can also affect the formation of the Taylor cone structure. Depending on the relative humidity, the fibers tend to absorb the water from the air during the elongation step. Water condensation releases latent heat. In response, the fibers expel the solvent earlier, preventing fiber solidification[57]. Water retention between polymer chains may be responsible for agglomerate formation and fiber fusion[37]. PVA hygroscopicity increases the fibers' water affinity, especially in samples with content as high as PVA 9.0%. The shift in the binary solution of water-acetic acid also changes the solubility of the jet[57,58]. As chitosan is hydrophobic, the excess water is a driving force for CS agglomeration by separating the phases[58,59].

3.3.3 Statistical Analysis & Fiber Optimization

3.3.3.1 Multilevel Factorial Design with Response Suerface Analysis: This study used a 4^2-factorial design, using Minitab® to evaluate the composition effects (**Table 3.1**) on the formulation properties (rheology consistency index (K), flow index (n), and the solution conductivity (σ)), and nanofiber diameters (nm). The regression equation used to generate model $\hat{y}$ follows the structure of a polynomial sequence, with x_i representing the factors, x_i^2 representing the quadratic terms of the binary interaction between each factor (i.e., interaction with itself), and $x_i x_j$ represents the interaction between the distinct factors. **Equation 3.3** shows the regression model applied.

$$\hat{y} = \beta_0 + \beta_1 x_1 + \beta_2 x_2 + \beta_{11} x_1^2 + \beta_{22} x_2^2 + \beta_{12} x_1 x_2 \qquad \textbf{(3.3)}$$

where $\hat{y}$ represents the variable analyzed, while β_{ij} is the constant coefficient for each term. **Figure 3.6** exemplifies a scheme of the model.

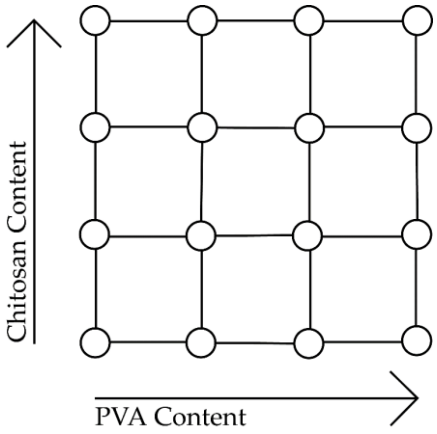

Figure 3.6. Model of a 4^2 factorial design scheme.

The linear terms (PVA and CS) and the interaction term (PVA×CS) significantly influence the electrical conductivity and rheology consistency index responses, which are consistent with the polymer interchain interactions hypothesis. Only the PVA factor is significant in the fiber Diameter (df) response and the Flow Index (*n*). This result does not necessarily mean that the CS does not influence those properties, but its effect was not high enough to be detected in the statistical analysis. **Figure 3.7** shows the contour plots resulting from the regression analysis.

The regression models took into account the linear properties' terms (PVA and CS), square terms (PVA×PVA and CS×CS), and interaction terms (PVA×CS). **Table 3.4** shows the regression analysis with the level of statistical significance (*p*-value). As can be observed, the models fitted for conductivity (σ), the rheology consistency index (K), and fiber diameter (df – nm) are highly significant. In contrast, the flow index (*n*) model does not show statistical significance.

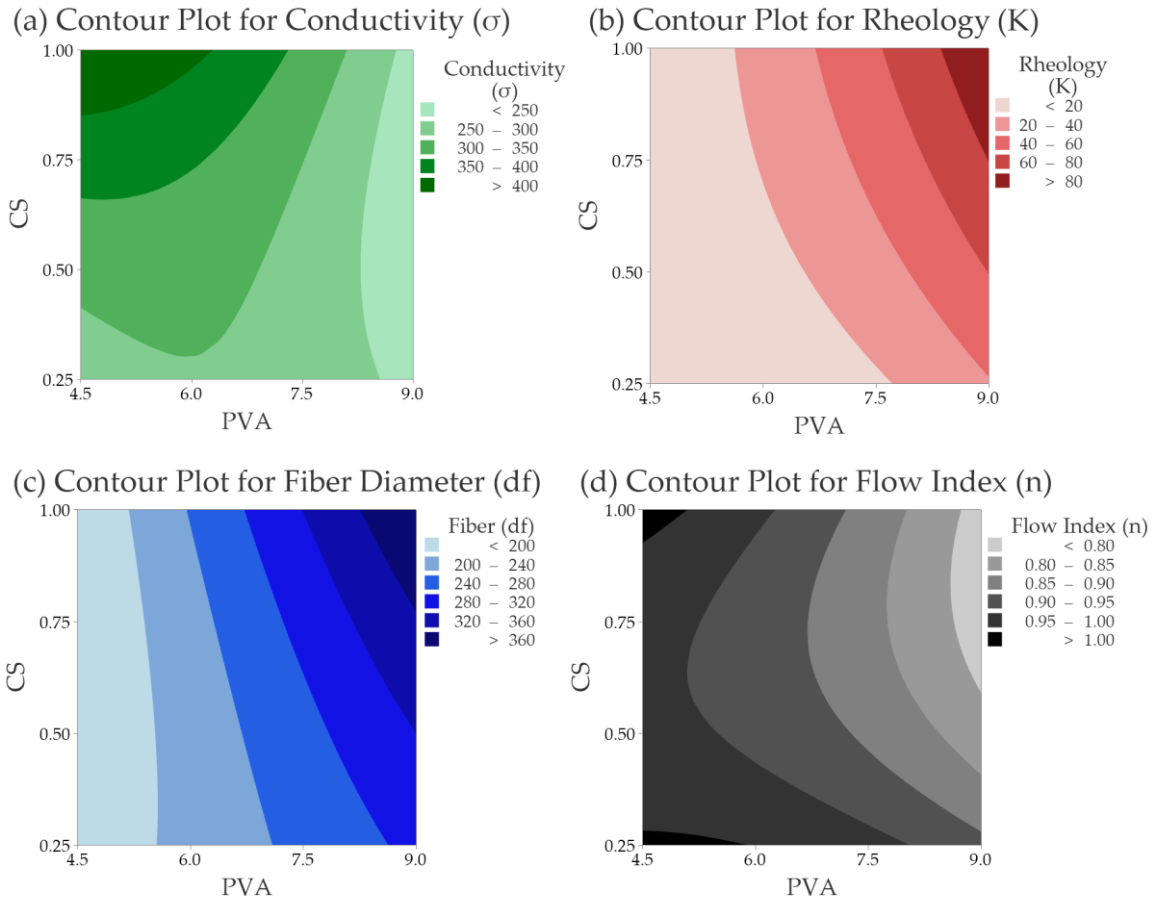

Figure 3.7. Contour plots generated by regression models for each experimental response: (**a**) Electrical conductivity; (**b**) rheology consistency index (K); (**c**) fiber diameter; and (**d**) flow index.

3.3.3.2 Validation of the Response Surface Analysis: This study aimed to find the optimal region inside the generated model. A combination of the contour plots for all responses was constructed and is shown in **Figure 3.8**.

Table 3.4. Models fitted to experimental data of electrical conductivity (σ), consistency index (K), fiber size (nm), and flow index (*n*) and its statistical significance (*p*-value).

Response	Model	*p*-Value
σ (mS·cm^{-1})	−73 + 109.0 PVA + 266 CS − 7.90 PVA×PVA + 150 CS×CS − 50.4 PVA×CS	0.001
K (Dyn·cm^{-2})	57.5 − 22.3 PVA − 53.5 CS + 1.951 PVA×PVA − 15.5 CS×CS + 16.92 PVA×CS	0.000
df (nm)	108 + 17.5 PVA − 224 CS − 0.02 PVA×PVA + 46 CS×CS + 34.7 PVA×CS	0.005
n	0.949 + 0.055 PVA − 0.268 CS − 0.00487 PVA×PVA + 0.381 CS×CS − 0.0429 PVA×CS	0.128

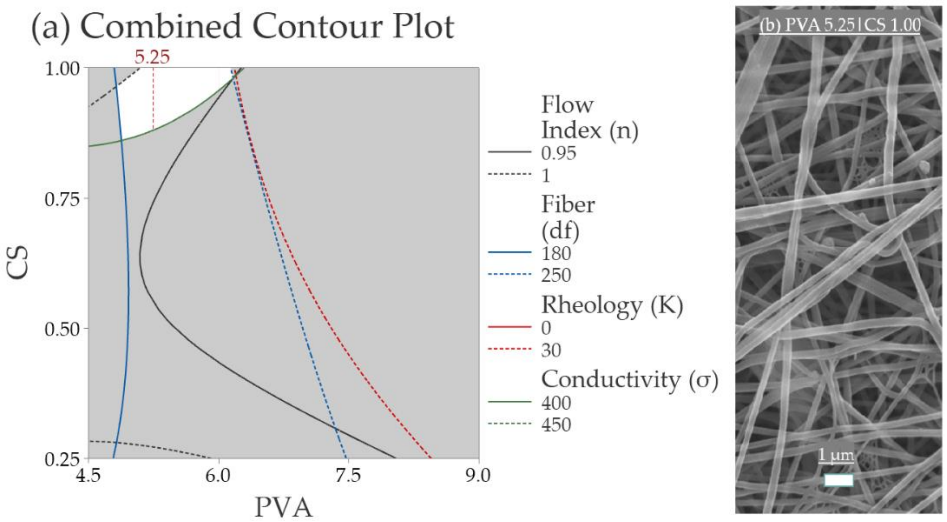

Figure 3.8. (**a**) Combined contour plots of the electrical conductivity, rheology consistency index, fiber diameter, and flow index, with defined margins for its properties. The white region shows the position of the validation assay; (**b**) SEM image of the sample with PVA 5.25%|CS 1.00%.

The blank area in the graph represents the optimal region for all responses. To validate the model, a sample containing PVA 5.25|CS 1.00 was prepared and electrospun. The resulting properties for the sample were expected to be inside the white region of **Figure 3.8a**. The experimental mean fiber diameter of the test sample was 222.0 ± 36.4 nm inside the white area. The spider-net web was also present but more significant than those observed in the optimal point (6.0|1.00). It was observed that by diminishing the PVA content from 6.0, the presence of spider-net increases.

3.3.4 Additives Influence

The addition of nanoparticles[4], surfactants[60], curcumin[21,61], and essential oils[62] has already been used to improve electrospun fibers' properties. Adding antimicrobial essential oils, such as the *L. sidoides* EO or its encapsulated forms, has proved to be a viable option for fiber functionalization, producing fiber mats with biocidal activity.

3.3.4.1 Surfactant Addition: Surfactants are known for their ability to reduce the surface tension of solutions, favoring the electrospinning process[63]. Surface tension also has an essential effect on the morphologies of natural polymers' electrospun fibers, influenced

by the solution's components[64]. **Figure 3.9** shows the SEM analysis of the electrospun fibers with the additives.

Surprisingly, the surfactant samples (6.0|1.0/CTAB and 6.0|1.0/SDS) did not show the same trend. **Figure 3.9c** shows that the samples of PVA and CS with CTAB formed crystal structures that are likely composed of CTAB. Barakat and colleagues (2009) observed similar behavior in solutions containing NaCl[37]. The presence of CTAB also appears to prejudice the gold deposition and coating of the electrospun fibers for SEM analysis. As previously reported, citric acid appears to create a crosslink between the electrospun fibers[17,65]. The crosslink improves the material resistance and reduces the hydrophobicity but prejudices the air passage.

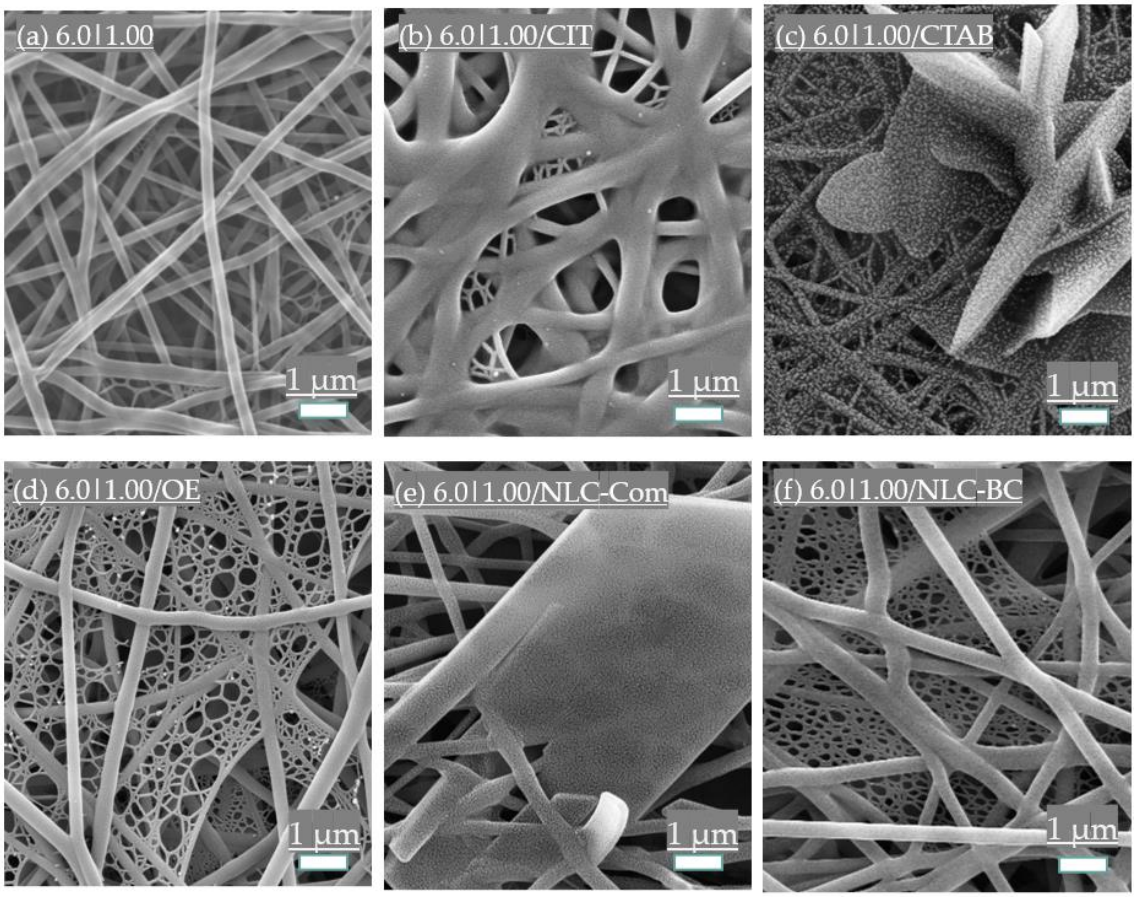

Figure 3.9. SEM images of the 6.0|1.00 solution (**a**) without additives and with 5% additions of (**b**) citric acid, (**c**) cetyltrimethylammonium bromide (CTAB), (**d**) essential oil of *Lippia sidoides* and *L. sidoides* loaded in nanostructured lipid carriers (NLC) used as solid lipids, (**e**) Compritol® 888 ATO, and (**f**) blend of beeswax and carnauba wax.

The effects of the additives on compositions' rheology and nanofiber size distributions are shown in **Figure 3.10**. The sample with SDS (6.0|1.0/SDS) was not spinnable. As shown in **Figure 3.5b**, the high initial viscosity and the rheology of the solution with SDS become a hindrance, favoring an electrospraying process. Viscoelastic force and interfacial surface tension significantly influence electrospraying[66]. Since surfactants such as Triton X-100 and SDS have already been proven beneficial for PVA

fiber formation[17], this solvent may be the answer to this distinct behavior. Yang and coworkers (2004)[67] tested different solvents with electrospun polyvinyl pyrrolidone fibers. They reduced the surface tension of the solution at constant concentrations and observed that bead formation diminished. Adjusting the solvent's ratio caused changes in the viscosity and surface tension[67]. The pH may also influence surfactant adsorption. pH can affect the number of hydroxyl groups on the surface, affecting the formation of hydrogen bonding[68]. The surfactants and citric acid also changed the entanglement of molecules and the interchain interaction, diminishing the spinnability, perhaps by changing the surface tension. The pH of the sample solutions described in **Table 3.1** is presented as supplementary data (**Table 3.S4**).

3.3.4.2 Essential Oil and Nanostructured Lipid Carriers (NCL's) Incorporation: NLCs are blends of solid and liquid lipids with a surfactant to reduce the interfacial tension between the NLC and a continuous aqueous phase. NLC presents advantages over polymeric and inorganic particles, as it is biodegradable and presents reduced toxicity. The high load capacity and its chemical versatility increase their range of applications[34]. This study used oleic acid as a liquid lipid and SDS as a surfactant carrier for the *Lippia sidoides* essential oil. Compritol® 888 ATO was used for the composition of 6.0|1.00/NLC-Com as a solid lipid, while beeswax and carnauba wax were used for the 6.0|1.00/NLC-BC composition.

Pure *Lippia sidoides* essential oil (6.0|1.0/EO) positively affects fiber formation. This sample slightly increases the mean fiber size and induces the massive formation of spider-net structures (subject of future work). However, the spider nets were opened with large pores instead of a closed membrane, as observed in other samples with those structures. This result may be a positive aspect for applying the electrospun fibers in air filtration.

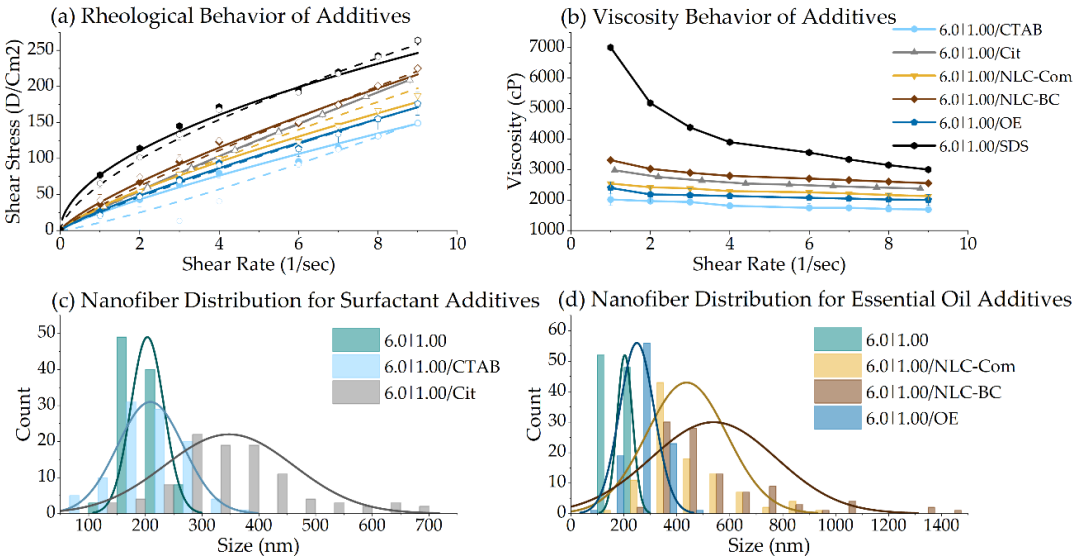

Figure 3.10. (**a**) Rheograms for the PVA 6.0|CS 1.00 solution with additives, analyzed at 0 to 10 s^{-1}. Close dots and solid lines show the increase in shear stress, while open dots and dash lines show tensile stress relaxation. (**b**) Viscosity behavior of the samples under increasing shear stress; (**c**) fiber size distribution for the samples with surfactants as additives; and (**d**) fiber size distribution for the samples with essential oil and NLCs as additives.

Since the main constituent of the essential oil of *Lippia sidoides* is composed of thymol (~68%)[33,35], this component may have primary responsibility. Thymol was already used in electrospinning to produce non-toxic and biocide polyurethane skin-like membranes [69] and hydrophobic porous fibers of cellulose acetate[70], among others[71–73]. It is a proven biocidal agent against viruses[74], bacteria[75,76], and fungi[33,77] and is a promising agent against SARS-CoV-2[78]. Our research group has ongoing studies evaluating the virucidal activity of *Lippia sidoides* compositions against SARS-CoV-2.

The NLCs increased the fiber sizes. Possible NLC disruption during the electrospinning process may release lipids amid the solution. As beeswax and carnauba wax have more complex structures than Compritol® 888 ATO, it is natural that 6.0|1.00/NLC-BC promotes an increase in fiber sizes compared with 6.0|1.00/NLC-Com. The presence of SDS in their compositions may also be relevant since the samples with the addition of SDS did not produce fibers.

3.4 Conclusions

The variation in the PVA and CS solutions' compositions significantly influenced the resulting fiber mats, changing the nanofibers' structure and size. It is possible to predict and control the final fiber diameter, a relevant factor for air filtration purposes, by optimizing the distinct composition properties, such as the rheological behavior and the electrical conductivity.

The optimal composition was set at 6% PVA and 1% CS, since a higher content of CS tended to obstruct the fiber mats' pores. Fiber with a mean size of 204.4 ± 32.2 nm was obtained for this specific composition using a voltage of 20 kV, a flow rate of 0.5 $mL \cdot h^{-1,}$ and a 10 cm distance between the needle and the drum collector. The fiber mat did not present beads but formed a spider-net web structure that can be beneficial or prejudicial to air filtration. Hence, the presence of spider-net webs in air filtration deserves further investigation. Biodegradable fiber mats loaded with additives may be suitable for air filtration or wound-dressing applications where biocidal action is needed.

Supplementary Materials: The following supporting information can be downloaded at: www.mdpi.com/xxx/s1, Table S1: Parameter data of nanofibers produced by electrospinning in this study. Table S2: Data obtained by the rheological analysis of sample solutions described in Table 1. Table S3: Qualitative analysis of fibers' electrospinnability of compositions in Table 1. Table S4: pH of the sample solutions described in Table 1. Figure S1: Main effects and the resulting interaction plot for each variable, respectively: (a,b) Conductivity; (c,d) rheology consistency index; (e,f) fiber diameter; and (g,h) flow index.

Author Contributions: Conceptualization, G.C.M. and M.S.M..; methodology, G.C.M., M.S.M. and W.P.O..; software, G.C.M.; validation, G.C.M. and M.S.M.; formal analysis, G.C.M and M.S.M.; investigation, G.C.M. and M.S.M.; resources, W.P.O. and M.L.A.; data curation, W.P.O.; writing – original draft preparation, G.C.M.; writing – review and editing, W.P.O.; visualization, G.C.M., M.S.M. and W.P.O.; supervision, W.P.O. and M.L.A.; project administration, M.L.A.; funding acquisition, W.P.O. and M.L.A. All authors have read and agreed to the published version of the manuscript.

Funding: This research was funded by Coordination for the Improvement of Higher Education Personnel (CAPES) grant number 88887.505019/2020-00, the National Council for Scientific and Technological

Development (CNPq), grant number 424792/2018-4 and the Foundation of Research Support of São Paulo State (FAPESP) grant number 2018/26069-0.

Acknowledgments: The authors acknowledge the CAPES, CNPq and FAPESP for the financial support. We also would like to thank the personnel and staff from the Environmental Control Laboratory of the Federal University of São Carlos (LCA/UFSCar), the Laboratory of P&D in Pharmaceutical Processes of the University of São Paulo (LAPROFAR/USP), the Chemistry Department of the Faculty of Philosophy, Sciences and Letters of the University of São Paulo (FFCLRP/USP) and the Laboratory of Electronic Microscopy of the Department of Materials Engineering of the University of São Paulo (EESC/USP).

Conflicts of Interest: The authors declare no conflict of interest.

3.5 References

1. Li, H.-W., Wu, C.-Y., Tepper, F., Lee, J.-H. & Lee, C. N. Removal and retention of viral aerosols by a novel alumina nanofiber filter. *Journal of Aerosol Science* **40**, 65–71 (2009).
2. Nam, C., Lee, S., Ryu, M., Lee, J. & Lee, H. Electrospun nanofiber filters for highly efficient PM2.5 capture. *Korean Journal of Chemical Engineering* **36**, 1565–1574 (2019).
3. Huang, X. *et al.* Dual-purpose high-efficiency air filter paper loaded with reactive zirconium hydroxide for the filtration aerosols and degradation of chemical warfare agents. *RSC Advances* **11**, 35245–35257 (2021).
4. Machry, K., Souza, C. W. O. de, Aguiar, M. L. & Bernardo, A. Prevention of pathogen microorganisms at indoor air ventilation system using synthesized copper nanoparticles. *The Canadian Journal of Chemical Engineering* **n/a**, (2021).
5. Thi Le, V. C. *et al.* A capture and inactivation system against pathogens in indoor air using copper nanoparticle decorated melamine sponge hybrid air filters. *Environmental Science: Advances* **1**, 356–364 (2022).
6. Matulevicius, J. *et al.* Design and Characterization of Electrospun Polyamide Nanofiber Media for Air Filtration Applications. *Journal of Nanomaterials* **2014**, e859656 (2014).
7. Almasian, A., Olya, M. E. & Mahmoodi, N. M. Synthesis of polyacrylonitrile/polyamidoamine composite nanofibers using electrospinning technique and their dye removal capacity. *Journal of the Taiwan Institute of Chemical Engineers* **49**, 119–128 (2015).
8. Wang, D., Yue, Y., Wang, Q., Cheng, W. & Han, G. Preparation of cellulose acetate-polyacrylonitrile composite nanofibers by multi-fluid mixing electrospinning method: Morphology, wettability, and mechanical properties. *Applied Surface Science* **510**, 145462 (2020).
9. Kadam, V. *et al.* Electrospun Polyacrylonitrile/β-Cyclodextrin Composite Membranes for Simultaneous Air Filtration and Adsorption of Volatile Organic Compounds. *ACS Applied Nano Materials* **1**, 4268–4277 (2018).
10. Leung, W. W. F. & Sun, Q. Electrostatic charged nanofiber filter for filtering airborne novel coronavirus (COVID-19) and nano-aerosols. *Separation and Purification Technology* **250**, 116886 (2020).
11. Leung, W. W. F. & Sun, Q. Charged PVDF multilayer nanofiber filter in filtering simulated airborne novel coronavirus (COVID-19) using ambient nano-aerosols. *Separation and Purification Technology* **245**, 116887 (2020).
12. Bonfim, D. P. F., Cruz, F. G. S., Guerra, V. G. & Aguiar, M. L. Development of Filter Media by Electrospinning for Air Filtration of Nanoparticles from PET Bottles. *Membranes* **11**, 293 (2021).
13. Sereshti, H., Amini, F. & Najarzadekan, H. Electrospun polyethylene terephthalate (PET) nanofibers as a new adsorbent for micro-solid phase extraction of chromium(VI) in environmental water samples. *RSC Advances* **5**, 89195–89203 (2015).
14. Zander, N. E., Gillan, M. & Sweetser, D. Recycled PET Nanofibers for Water Filtration Applications. *Materials* **9**, 247 (2016).
15. Bonfim, D. P. F., Cruz, F. G. S., Bretas, R. E. S., Guerra, V. G. & Aguiar, M. L. A Sustainable Recycling Alternative: Electrospun PET-Membranes for Air Nanofiltration. *Polymers* **13**, 1166 (2021).
16. Zhang, Q., Li, Q., Young, T. M., Harper, D. P. & Wang, S. A Novel Method for Fabricating an Electrospun Poly(Vinyl Alcohol)/Cellulose Nanocrystals Composite Nanofibrous Filter with Low Air Resistance for High-Efficiency Filtration of Particulate Matter. *ACS Sustainable Chemistry & Engineering* **7**, 8706–8714 (2019).
17. Oliveira, A. E. de, Aguiar, M. & Guerra, V. Improved filter media with PVA/citric acid/Triton X-100 nanofibers for filtration of nanoparticles from air. *Polymer Bulletin* (2020) doi:10.1007/s00289-020-03431-w.
18. Hulupi, M. & Haryadi, H. Synthesis and Characterization of Electrospinning PVA Nanofiber-Crosslinked by Glutaraldehyde. *Materials Today: Proceedings* **13**, 199–204 (2019).
19. Linh, N. T. B. & Lee, B.-T. Electrospinning of polyvinyl alcohol/gelatin nanofiber composites and cross-linking for bone tissue engineering application. *Journal of Biomaterials Applications* **27**, 255–266 (2012).
20. Purwar, R., Sai Goutham, K. & Srivastava, C. M. Electrospun Sericin/PVA/Clay nanofibrous mats for antimicrobial air filtration mask. *Fibers and Polymers* **17**, 1206–1216 (2016).
21. Chagas, P. A. M. *et al.* Bilayered electrospun membranes composed of poly(lactic-acid)/natural rubber: A strategy against curcumin photodegradation for wound dressing application. *Reactive and Functional Polymers* **163**, 104889 (2021).
22. Schneider, R. *et al.* Dye Adsorption Capacity of MoS2 Nanoflakes Immobilized on Poly(lactic acid) Fibrous Membranes. *ACS Applied Nano Materials* **4**, 4881–4894 (2021).

23. Lin, T., Fang, J., Wang, H., Cheng, T. & Wang, X. Using chitosan as a thickener for electrospinning dilute PVA solutions to improve fibre uniformity. *Nanotechnology* **17**, 3718–3723 (2006).
24. Wang, Z. *et al.* Antibacterial and environmentally friendly chitosan/polyvinyl alcohol blend membranes for air filtration. *Carbohydrate Polymers* **198**, 241–248 (2018).
25. Baghaie, S., Khorasani, M. T., Zarrabi, A. & Moshtaghian, J. Wound healing properties of PVA/starch/chitosan hydrogel membranes with nano Zinc oxide as antibacterial wound dressing material. *Journal of Biomaterials Science, Polymer Edition* **28**, 2220–2241 (2017).
26. Homayoni, H., Ravandi, S. A. H. & Valizadeh, M. Electrospinning of chitosan nanofibers: Processing optimization. *Carbohydrate Polymers* **77**, 656–661 (2009).
27. Geng, X., Kwon, O.-H. & Jang, J. Electrospinning of chitosan dissolved in concentrated acetic acid solution. *Biomaterials* **26**, 5427–5432 (2005).
28. Vu, T. H. N., Morozkina, S. N. & Uspenskaya, M. V. Study of the Nanofibers Fabrication Conditions from the Mixture of Poly(vinyl alcohol) and Chitosan by Electrospinning Method. *Polymers* **14**, 811 (2022).
29. Panda, P. K., Sadeghi, K. & Seo, J. Recent advances in poly (vinyl alcohol)/natural polymer based films for food packaging applications: A review. *Food Packaging and Shelf Life* **33**, 100904 (2022).
30. Duru Kamaci, U. & Peksel, A. Fabrication of PVA-chitosan-based nanofibers for phytase immobilization to enhance enzymatic activity. *International Journal of Biological Macromolecules* **164**, 3315–3322 (2020).
31. Abbas, W. A., Sharafeldin, I. M., Omar, M. M. & Allam, N. K. Novel mineralized electrospun chitosan/PVA/TiO2 nanofibrous composites for potential biomedical applications: computational and experimental insights. *Nanoscale Advances* **2**, 1512–1522 (2020).
32. Morais, M. S., Bonfim, D. P. F., Aguiar, M. L. & Oliveira, W. P. Electrospun Poly (Vinyl Alcohol) Nanofibrous Mat Loaded with Green Propolis Extract, Chitosan and Nystatin as an Innovative Wound Dressing Material. *Journal of Pharmaceutical Innovation* 1–15 (2022) doi:10.1007/s12247-022-09681-7.
33. Baldim, I., Tonani, L., von Zeska Kress, M. R. & Pereira Oliveira, W. Lippia sidoides essential oil encapsulated in lipid nanosystem as an anti-Candida agent. *Industrial Crops and Products* **127**, 73–81 (2019).
34. Souto, E. B. *et al.* SLN and NLC for topical, dermal, and transdermal drug delivery. *Expert Opinion on Drug Delivery* **17**, 357–377 (2020).
35. Baldim, I., Paziani, M. H., Grizante Barião, P. H., Kress, M. R. von Z. & Oliveira, W. P. Nanostructured Lipid Carriers Loaded with Lippia sidoides Essential Oil as a Strategy to Combat the Multidrug-Resistant Candida auris. *Pharmaceutics* **14**, 180 (2022).
36. Bhattarai, N., Edmondson, D., Veiseh, O., Matsen, F. A. & Zhang, M. Electrospun chitosan-based nanofibers and their cellular compatibility. *Biomaterials* **26**, 6176–6184 (2005).
37. Barakat, N. A. M., Kanjwal, M. A., Sheikh, F. A. & Kim, H. Y. Spider-net within the N6, PVA and PU electrospun nanofiber mats using salt addition: Novel strategy in the electrospinning process. *Polymer -London-* **50**, 4389–4396 (2009).
38. Anstey, A. *et al.* Nanofibrillated polymer systems: Design, application, and current state of the art. *Progress in Polymer Science* **113**, 101346 (2021).
39. Sharma, R. *et al.* Electrospun chitosan–polyvinyl alcohol composite nanofibers loaded with cerium for efficient removal of arsenic from contaminated water. *Journal of Materials Chemistry A* **2**, 16669–16677 (2014).
40. Qureshi, D. *et al.* Fabrication and Characterization of Poly (vinyl alcohol) and Chitosan Oligosaccharide-Based Blend Films. *Gels* **7**, 55 (2021).
41. Çay, A., Miraftab, M. & Perrin Akçakoca Kumbasar, E. Characterization and swelling performance of physically stabilized electrospun poly(vinyl alcohol)/chitosan nanofibres. *European Polymer Journal* **61**, 253–262 (2014).
42. Nguyen, N.-T. & Liu, J.-H. Fabrication and characterization of poly(vinyl alcohol)/chitosan hydrogel thin films via UV irradiation. *European Polymer Journal* **49**, 4201–4211 (2013).
43. Chen, J. *et al.* Green crosslinked nanofibers membrane based on CS/PVA combined with polybasic organic acid for tympanic membrane repair. *International Journal of Polymeric Materials and Polymeric Biomaterials* **71**, 291–301 (2022).
44. Zong, X. *et al.* Structure and process relationship of electrospun bioabsorbable nanofiber membranes. *Polymer* **43**, 4403–4412 (2002).
45. Marcos Bretas, R. *Reologia De Polimeros Fundidos*. (Edufscar, 2006).
46. Wang, C., Hashimoto, T. & Wang, Y. Extension Rate and Bending Instability of Electrospinning Jets: the Role of the Electric Field. *Macromolecules* **54**, 7193–7209 (2021).
47. Yarin, A. L., Koombhongse, S. & Reneker, D. H. Taylor cone and jetting from liquid droplets in electrospinning of nanofibers. *Journal of Applied Physics* **90**, 4836–4846 (2001).
48. Hong, E., Yeneneh, A. M., Sen, T. K., Ang, H. M. & Kayaalp, A. A comprehensive review on rheological studies of sludge from various sections of municipal wastewater treatment plants for enhancement of process performance. *Advances in Colloid and Interface Science* **257**, 19–30 (2018).
49. Yördem, O. S., Papila, M. & Menceloğlu, Y. Z. Effects of electrospinning parameters on polyacrylonitrile nanofiber diameter: An investigation by response surface methodology. *Materials & Design* **29**, 34–44 (2008).
50. Ramakrishna, S., Fujihara, K., Teo, W.-E., Lim, T.-C. & Ma, Z. *An Introduction to Electrospinning and Nanofibers*. (WORLD SCIENTIFIC, 2005). doi:10.1142/5894.
51. Ionescu, C. M., Birs, I. R., Copot, D., Muresan, C. I. & Caponetto, R. Mathematical modelling with experimental validation of viscoelastic properties in non-Newtonian fluids. *Philosophical Transactions of the Royal Society A: Mathematical, Physical and Engineering Sciences* **378**, 20190284 (2020).
52. Cramariuc, B. *et al.* Fiber diameter in electrospinning process. *Journal of Electrostatics* **71**, 189–198 (2013).
53. He, J.-H. On the height of Taylor cone in electrospinning. *Results in Physics* **17**, 103096 (2020).
54. Mata, G. C. da, Almeida, D. S. de, Oliveira, W. P. de & Aguiar, M. L. Nanofibers functionalized with surfactants to Eliminate SARS-CoV-2 and other airborne pathogens. *Conjecturas* **22**, 1929–1961 (2022).
55. Aydin, O. *et al.* Performance of fabrics for home-made masks against the spread of COVID-19 through droplets: A quantitative mechanistic study. *Extreme Mechanics Letters* **40**, 100924 (2020).

56. Rutledge, G. C. & Fridrikh, S. V. Formation of fibers by electrospinning. *Advanced Drug Delivery Reviews* **59**, 1384–1391 (2007).
57. Reyes, C. G. & Lagerwall, J. P. F. Disruption of Electrospinning due to Water Condensation into the Taylor Cone. *ACS Applied Materials & Interfaces* **12**, 26566–26576 (2020).
58. Lu, P. & Xia, Y. Maneuvering the Internal Porosity and Surface Morphology of Electrospun Polystyrene Yarns by Controlling the Solvent and Relative Humidity. *Langmuir* **29**, 7070–7078 (2013).
59. Zaarour, B., Zhu, L., Huang, C. & Jin, X. Controlling the Secondary Surface Morphology of Electrospun PVDF Nanofibers by Regulating the Solvent and Relative Humidity. *Nanoscale Research Letters* **13**, 285 (2018).
60. de Almeida, D. S. *et al.* Development and characterization of electrospun cellulose acetate nanofibers modified by cationic surfactant. *Polymer Testing* **81**, 106206 (2020).
61. Mosallanezhad, P., Nazockdast, H., Ahmadi, Z. & Rostami, A. Fabrication and characterization of polycaprolactone/chitosan nanofibers containing antibacterial agents of curcumin and ZnO nanoparticles for use as wound dressing. *Frontiers in Bioengineering and Biotechnology* **10**, (2022).
62. Golja, B., Forte Tavčer, P., & University of Ljubljana, Faculty of Natural Sciences and Engineering, Department of Textiles, Graphic Arts and Design, 1000 Ljubljana, Snežniška 5, Slovenia. Textile Functionalisation by Printing Fragrant, Antimicrobial and Flame- Retardant Microcapsules. *TEK* **59**, 278–288 (2016).
63. Khajavi, R. & Abbasipour, M. 5 - Controlling nanofiber morphology by the electrospinning process. in *Electrospun Nanofibers* (ed. Afshari, M.) 109–123 (Woodhead Publishing, 2017). doi:10.1016/B978-0-08-100907-9.00005-2.
64. Haghi, A. K. & Akbari, M. Trends in electrospinning of natural nanofibers. *Physica Status Solidi* **204**, 1830–1834 (2007).
65. Yu, D. *et al.* Fabrication, characterization, and antibacterial properties of citric acid crosslinked PVA electrospun microfibre mats for active food packaging. *Packaging Technology and Science* **34**, 361–370 (2021).
66. Haider, S. & Haider, A. *Electrospinning and Electrospraying - Techniques and Applications*. (2019). doi:10.5772/intechopen.77414.
67. Yang, Q. *et al.* Influence of solvents on the formation of ultrathin uniform poly(vinyl pyrrolidone) nanofibers with electrospinning. *Journal of Polymer Science Part B: Polymer Physics* **42**, 3721–3726 (2004).
68. Belhaj, A. F. *et al.* The effect of surfactant concentration, salinity, temperature, and pH on surfactant adsorption for chemical enhanced oil recovery: a review. *Journal of Petroleum Exploration and Production Technology* **10**, 125–137 (2020).
69. Yue, Y. *et al.* In-situ electrospinning of thymol-loaded polyurethane fibrous membranes for waterproof, breathable, and antibacterial wound dressing application. *Journal of Colloid and Interface Science* **592**, 310–318 (2021).
70. Chen, Y., Qiu, Y., Chen, W. & Wei, Q. Electrospun thymol-loaded porous cellulose acetate fibers with potential biomedical applications. *Materials Science and Engineering: C* **109**, 110536 (2020).
71. Aytac, Z., Ipek, S., Durgun, E., Tekinay, T. & Uyar, T. Antibacterial electrospun zein nanofibrous web encapsulating thymol/cyclodextrin-inclusion complex for food packaging. *Food Chemistry* **233**, 117–124 (2017).
72. Khodayari, P., Jalilian, N., Ebrahimzadeh, H. & Amini, S. Electrospun cellulose acetate /polyacrylonitrile /thymol /Mg-metal organic framework nanofibers as efficient sorbent for pipette-tip micro-solid phase extraction of anti-cancer drugs. *Reactive and Functional Polymers* **173**, 105217 (2022).
73. Ceylan, Z., Yaman, M., Sağdıç, O., Karabulut, E. & Yilmaz, M. T. Effect of electrospun thymol-loaded nanofiber coating on vitamin B profile of gilthead sea bream fillets (Sparus aurata). *LWT* **98**, 162–169 (2018).
74. Lai, W.-L. *et al.* Inhibition of Herpes Simplex Virus Type 1 by Thymol-Related Monoterpenoids. *Planta Medica* **78**, 1636–1638 (2012).
75. Alagawany, M., Farag, M. R., Abdelnour, S. A. & Elnesr, S. S. A review on the beneficial effect of thymol on health and production of fish. *Reviews in Aquaculture* **13**, 632–641 (2021).
76. Falcone, P., Speranza, B., del Nobile, M. A., Corbo, M. R. & Sinigaglia, M. A Study on the Antimicrobial Activity of Thymol Intended as a Natural Preservative. *Journal of Food Protection* **68**, 1664–1670 (2005).
77. Marchese, A. *et al.* Antibacterial and antifungal activities of thymol: A brief review of the literature. *Food Chemistry* **210**, 402–414 (2016).
78. Rathod, N. B., Kulawik, P., Ozogul, F., Regenstein, J. M. & Ozogul, Y. Biological activity of plant-based carvacrol and thymol and their impact on human health and food quality. *Trends in Food Science & Technology* **116**, 733–748 (2021).

3.6 Supplementary Material

Table 3.S1: Parameters data of the nanofibers produced by electrospinning in this study.

Sample	PVA (% w/w)	Chitosan (% w/w)	Solvent	Production Time (h)	Proportion (PVA:CS)	Needle Inner Diameter (mm)	Temperature (°C)/ Relative Humidity (%)
P1	7	4	Water	-	75:25	-	-
P2	7	4	Water	-	50:50	-	-
P3	7	4	Water	-	25:75	-	-
P4	12	4	Water	-	75:25	-	-
P5	12	4	Water	-	50:50	-	-
P6	12	4	Water	-	25:75	-	-
0	7	4	AcOH	3	75:25	0.3	-

1	7	4	Water	2	75:25	0.6	-
2	7	4	AcOH	2	75:25	0.6	-
3	7	4	AcOH	2	75:25	0.6	-
4	7	4	Water	2	75:25	0.6	-
5	7	4	Water	2	75:25	0.6	-
6	12	4	Water	2	75:25	0.6	-
7	12	4	Water	2	75:25	0.6	-
8	7	4	AcOH	2	75:25	0.6	-
9	7	1	AcOH	2	75:25	0.6	-
10	12	1	Water	2	75:25	0.6	-
11	7	1	AcOH	2	75:25	0.6	-
12	7	1	AcOH	2	75:25	1.2	-
13	12	1	AcOH	3	75:25	0.6	-
14	7	2	AcOH	2	75:25	0.7	-
A	7	4	Water	3	75:25	0.7	-
B	12	1	Water	3	75:25	0.7	-
9.0|0.25	12	1	AcOH	3	75:25	0.55	-
9.0|0.50	12	2	AcOH	3	75:25	0.55	26.3/34
9.0|0.75	12	3	AcOH	3	75:25	0.55	-
9.0|1.00	12	4	AcOH	3	75:25	0.55	-
7.5|0.25	10	1	AcOH	3	75:25	0.55	-
7.5|0.50	10	2	AcOH	3	75:25	0.55	-
7.5|0.75	10	3	AcOH	3	75:25	0.55	25.0/39
7.5|1.00	10	4	AcOH	3	75:25	0.55	-
6.0|0.25	8	1	AcOH	3	75:25	0.55	24.2/45
6.0|0.50	8	2	AcOH	3	75:25	0.55	24.9/42
6.0|0.75	8	3	AcOH	3	75:25	0.55	23.8/39
6.0|1.00	8	4	AcOH	3	75:25	0.55	25.8/35
4.5|0.25	6	1	AcOH	3	75:25	0.55	22.7/35
4.5|0.50	6	2	AcOH	3	75:25	0.55	21.6/39
4.5|0.75	6	3	AcOH	3	75:25	0.55	22/38
4.5|1.00	6	4	AcOH	3	75:25	0.55	23.5/38
PP6.2	6	2	AcOH	3	75:25	0.55	25.3/46
PP8.2	8	2	AcOH	3	75:25	0.55	24.9/42
PP8.4	8	4	AcOH	3	75:25	0.55	-
PP10.2	10	2	AcOH	3	75:25	0.55	-
PP12.1	12	1	AcOH	3	75:25	0.55	-

Table 3.S2: Data obtained by the rheological analysis of samples solutions described at the **Table 3.1**.

Sample	Consistency index – K ($dyn.cm^{-2}.s$)	Flow index – n (dimentionless)	Reduced Chi-Sqr	R-Square (COD)	Adj. R-Square
CS 0.25 ->	0.38 ± 0.07	0.63 ± 0.06	2.02	0.99	0.98
CS 0.25 <-	0.09 ± 0.02	1.01 ± 0.08	3.06	0.98	0.98
CS 0.50 ->	0.40 ± 0.05	0.70 ± 0.04	0.50	0.99	0.99
CS 0.50 <-	0.21 ± 0.02	0.88 ± 0.04	29.31	0.98	0.98
CS 0.75 ->	0.52 ± 0.03	0.74 ± 0.02	1.40	0.99	0.99
CS 0.75 <-	0.27 ± 0.05	0.91 ± 0.05	9.22	0.99	0.99
CS 1.00 ->	0.57 ± 0.03	0.83 ± 0.01	0.02	1.00	1.00
CS 1.00 <-	0.33 ± 0.03	0.97 ± 0.03	0.06	0.99	0.99
PVA 4.5 ->	2.18 ± 0.06	0.91 ± 0.01	11.27	1.00	0.99
PVA 4.5 <-	2.08 ± 0.14	0.94 ± 0.03	49.54	0.99	0.99
PVA 6.0 ->	5.36 ± 0.12	0.94 ± 0.02	0.07	1.00	0.99
PVA 6.0 <-	6.40 ± 1.76	0.84 ± 0.21	41.99	0.70	0.67
PVA 7.5 ->	16.27 ± 0.22	1.09 ± 0.03	1.55	0.99	0.99
PVA 7.5 <-	20.81 ± 0.35	0.82 ± 0.03	27.79	0.99	0.99
PVA 9.0 ->	72.52 ± 24.60	0.87 ± 0.21	15.92	0.87	0.85
PVA 9.0 <-	73.61 ± 43.27	0.87 ± 0.37	55.29	0.40	0.31
PVA 4.5|CS 0.25 ->	1.016 ± 0.02	0.99 ± 0.01	0.40	0.99	0.99
PVA 4.5|CS 0.25 <-	1.02 ± 0.03	0.99 ± 0.01	0.64	0.99	0.99
PVA 4.5|CS 0.50 ->	4.54 ± 0.15	0.99 ± 0.06	92.07	0.99	0.98
PVA 4.5|CS 0.50 <-	5.25 ± 0.80	0.70 ± 0.19	998.56	0.88	0.86
PVA 4.5|CS 0.75 ->	6.55 ± 1.06	1.09 ± 0.28	117.12	0.95	0.92
PVA 4.5|CS 0.75 <-	8.51 ± 2.11	0.76 ± 0.77	450.54	0.55	0.33
PVA 4.5|CS 1.00 ->	8.04 ± 1.08	0.92 ± 0.24	118.51	0.94	0.90
PVA 4.5|CS 1.00 <-	10.05 ± 2.46	0.73± 0.49	618.73	0.69	0.53
PVA 6.0|CS 0.25 ->	7.58 ± 0.05	1.00 ± 0.01	28.19	0.99	0.99
PVA 6.0|CS 0.25 <-	8.73 ± 0.13	0.77 ± 0.02	3.06	0.99	0.99
PVA 6.0|CS 0.50 ->	11.02 ± 0.39	0.91 ± 0.05	4.29	0.99	0.99
PVA 6.0|CS 0.50 <-	12.07 ± 0.46	0.79 ± 0.06	20.64	0.97	0.97
PVA 6.0|CS 0.75 ->	14.44 ± 0.34	0.94 ± 0.03	17.86	0.99	0.99
PVA 6.0|CS 0.75 <-	16.92 ± 0.42	0.81 ± 0.03	851.29	0.98	0.97
PVA 6.0|CS 1.00 ->	17.01 ± 0.36	1.08 ± 0.03	7.71	0.99	0.99
PVA 6.0|CS 1.00 <-	24.38 ± 2.21	0.70 ± 0.10	14.79	0.98	0.98

PVA 7.5|CS 0.25 ->	15.93 ± 0.44	1.07 ± 0.04	0.26	0.99	0.99
PVA 7.5|CS 0.25 <-	19.33 ± 2.82	0.87 ± 0.20	14.32	0.80	0.77
PVA 7.5|CS 0.50 ->	28.13 ± 1.51	0.84 ± 0.03	0.51	0.99	0.99
PVA 7.5|CS 0.50 <-	24.28 ± 1.52	0.90 ± 0.03	0.97	0.99	0.99
PVA 7.5|CS 0.75 ->	68.13 ± 4.79	0.78 ± 0.03	15.16	0.99	0.99
PVA 7.5|CS 0.75 <-	49.08 ± 6.75	0.91 ± 0.07	34.33	0.98	0.97
PVA 7.5|CS 1.00 ->	59.80 ± 2.21	0.80 ± 0.02	955.23	0.99	0.99
PVA 7.5|CS 1.00 <-	46.60 ± 5.00	0.91 ± 0.05	71.20	0.99	0.99
PVA 9.0|CS 0.25 ->	41.39 ± 1.72	0.86 ± 0.02	4.97	0.99	0.99
PVA 9.0|CS 0.25 <-	39.52 ± 2.74	0.87 ± 0.04	5.94	0.99	0.99
PVA 9.0|CS 0.50 ->	57.99 ± 3.41	0.84 ± 0.04	1.96	0.99	0.99
PVA 9.0|CS 0.50 <-	55.19 ± 9.98	0.86 ± 0.12	33.04	0.90	0.89
PVA 9.0|CS 0.75 ->	74.09 ± 1.86	0.83 ± 0.01	4.49	0.99	0.99
PVA 9.0|CS 0.75 <-	44.90 ± 1.65	1.06 ± 0.09	0.18	0.99	0.99
PVA 9.0|CS 1.00 ->	98.68 ± 4.04	0.80 ± 0.02	151.63	0.99	0.99
PVA 9.0|CS 1.00 <-	101.85 ± 5.44	0.78 ± 0.03	3601.34	0.99	0.99

Table 3.S3: Qualitative analysis of fibers electrospinnability as described at the **Table 3.1**.

PVA content (% w/w)	**Chitosan Content (% w/w)**			
	0.25	**0.50**	**0.75**	**1.00**
4.5	++	+++	+	++
6.0	+	+++	++	+++
7.5	+++	++	++	++
9.0	+++	++	+	+

*+++: Good fiber mat formation; **: medium fiber mat; poor fiber mat formation.

Table 3.S4: pH of the sample solutions described at the **Table 3.1**.

PVA content (% w/w)	Chitosan content (% w/w)							
	0.25		0.50		0.75		1.00	
	Mean	Deviation	Mean	Deviation	Mean	Deviation	Mean	Deviation
4.5	1.113	0.041	1.340	0.151	1.24	0.120	1.550	0.046
6.0	1.290	0.030	1.486	0.040	1.44	0.052	1.570	0.052
7.5	1.483	0.035	1.546	0.006	1.63	0.040	1.527	0.040
9.0	1.406	0.105	1.433	0.042	1.52	0.067	1.573	0.067

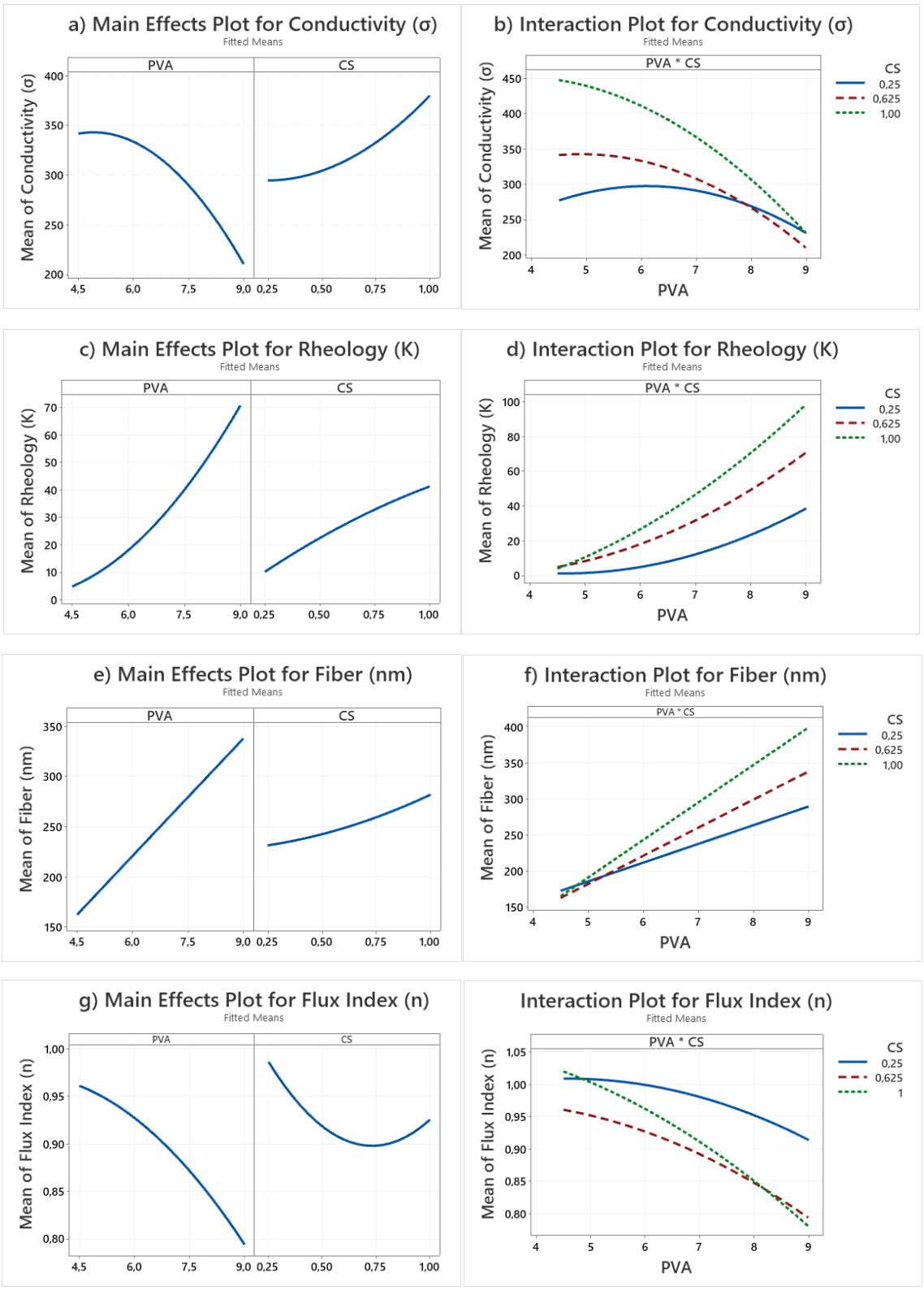

Figure 3.S1 Main Effects and the resulting Interaction Plot for each variable, respectively, being: **a)** and **b)** Electrical Conductivity; **c)** and **d)** Rheology Consistency Index; **e)** and **f)** Fiber Diameter; and **g)** and **h)** Flow Index.

IV

AIR FILTRATION ENHANCEMENT

IV - AIR FILTRATION ENHANCEMENT

Sustainable Surgical Masks: Optimizing Fine/Ultrafine Particle Filtration using PVA/Chitosan Electrospun Nanofibers

Gustavo Cardoso da Mata[1, *], Maria Sirlene Morais[2], Wanderley Pereira de Oliveira[2], Mônica Lopes Aguiar[1]

[1] Department of Chemical Engineering, Federal University of São Carlos, Rod. Washington Luiz, km 235, SP310, São Carlos - SP, 13565-905, Brazil;

[2] Faculty of Pharmaceutical Science of Ribeirão Preto, University of São Paulo, Av. do Café s/no, CEP: 14040-903, Bairro Monte Alegre, Ribeirão Preto, SP, Brazil

[*]*Corresponding author*: gugs_cardoso@ufsj.edu.br

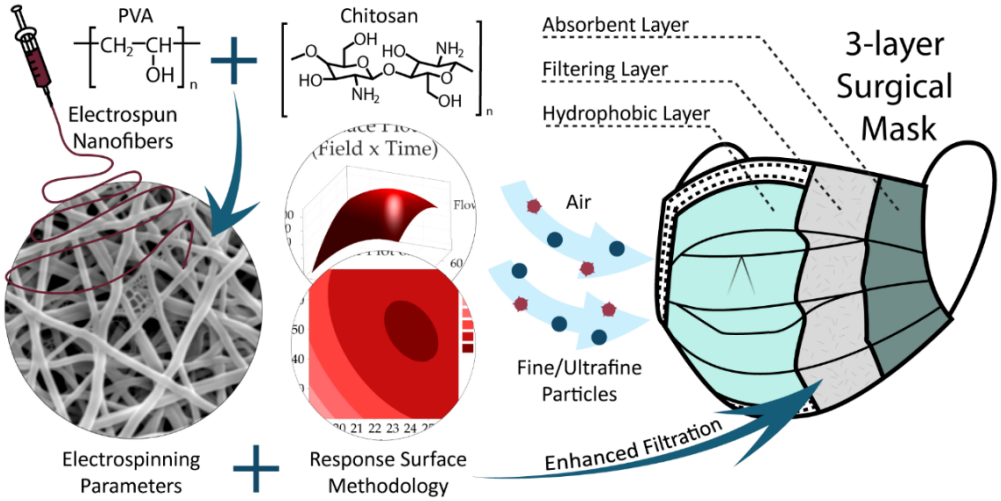

Abstract: Disposable surgical masks have emerged as a solution to the increasing demand for protection against fine/ultrafine particulate matter. This was prompted by the SARS-CoV-2 pandemic and the escalating levels of air pollution in major cities. However, as non-degradable polymers, surgical masks are discarded into the environment and become pollutants. This study produced biodegradable nanofibers via electrospinning, using polyvinyl alcohol (PVA) and chitosan (CS) as substitutes for traditional polymers in a three-layer commercial surgical mask (CSM). Electrospinning production parameters were modeled using response surface methodology and optimized using the desirability method. Then, the air filtration properties, including quality factor (Qf), collection efficiency (η), pressure drop (ΔP) and permeability (K1), were compared with CSM. The main objective was to produce electrospun mats with filtration of fine/ultrafine particles similar to those obtained for the CSM (η: 42.84–67.80% and ΔP: 29.3–32.2 Pa). Subtle variations in production parameters significantly affected the material, with the electric field being the most relevant parameter. The optimized samples OEV(↓K1) and OEV(↓Qf) presented the highest η values (96.27 and 96.58%, respectively), matching the N95 filtration efficiency and complying with international regulations. Their optimal experimental sets were, respectively, 25.01 and 23.39 kV of tension applied for the electrical field, 0.92 and 1.17-mL h-1 of flow rate, and 24.87 and 27.93 min of production time. Notably, nanofibers were more effective than the CSM in capturing particles close to the nanoscale range, such as airborne viruses and fine/ultrafine air pollution. The PVA/CS electrospun membranes are becoming promising alternatives to substitute non-degradable polymers in surgical masks.

Keywords: polyvinyl alcohol; chitosan; electrospinning; nanofibers; response surface; optimization; biodegradable; air filters; *Lippia sidoides*; essential oil.

Published in: Environmental Science: Nano (Royal Society of Chemistry) **DOI:** 10.1039/D3EN00182B

4.1 Introduction

The world's major cities are currently facing significant challenges posed by climate change, resulting in detrimental effects on respiratory health and increased levels of air pollution.[1–4] Among the pollutants of concern are ground-level ozone, nitrogen dioxide,[5] and fine and ultrafine particles[6] originating from fuel combustion, biomass burning, and industrial emissions.[7] Modern indoor lifestyles pose a significant risk of overexposure to particulate matter under 2.5 µm ($PM_{2.5}$ or fine) and 0.1 µm ($PM_{0.1}$ or ultrafine).[8,9] These tiny particles can penetrate and harm organ tissues, triggering oxidative stress, inflammatory responses, and apoptosis,[10] with $PM_{0.1}$ being more harmful than $PM_{2.5}$.[11] While regulations can potentially reduce particulate matter in the air,[12] it is alarming that many countries lack proper legislation targeting fine and ultrafine particles.

This concern regarding fine/ultrafine particles has come to the forefront due to the COVID-19 pandemic.[13] The rapid spread and contamination of the SARS-CoV-2 were caused by the high airborne transmissibility of the virus,[14–16] continuously reinflating the pandemic.[17–19] Mutations on the virus' spikes resulted in higher infectiveness with host cells[20–22] and increased interaction between the spike proteins and solid surfaces.[23] SARS-CoV-2 can attach to particles under $PM_{2.5}$ and even $PM_{0.1}$, forming aerosols close to the nanoscale range.[24–26] Even though the primary transmission mode is direct transmission through droplets, it is believed that lesser aerosols are still capable of causing infection.[23,26–28]

Any form of facial protection significantly reduces the transmission of viruses and the inhalation of pollutants. Face masks play a crucial role in filtering particle pollutants and airborne viruses,[29–32] with N95 and FFP2 masks proving effective against SARS-CoV-2[33,34] and Influenza.[33–36] However, the reliability of cloth masks,[37,38] surgical masks, and even high protective facemasks can vary due to factors like poor fit and inadequate filtration,[37,39] particularly for tiny particles. Thus, it is important to note that even reliable masks cannot guarantee complete immunity. Therefore, surgical masks must effectively defend against aerosols and bioaerosols in the micro and nanoscale range.

Moreover, surgical mask production uses non-degradable polymers, such as polyester, polypropylene, polycarbonate, and polyacrylonitrile.[40] As disposable Personal Protective Equipment, surgical masks are discarded into the environment, aggravating pollution and ecological damage. Under sunlight and in marine habitats, disposable masks release microplastics that can act as pollutant carriers.[41–44] Several studies have investigated microplastics' ability to absorb and carry antibiotics,[45] heavy metals,[46,47] and hydrophobic organic chemicals.[48] Microplastics have been discovered suspended in the air,[49,50] and these airborne microplastics travel long distances[51] affecting the climate[52,53] and the environments where they settle[54,55]. Inhaling these tiny plastic particles can harm lung cells and tissue,[56,57] highlighting the need to mitigate its impact on human health and the environment.

Aligned with the air pollution crisis are respiratory outbreaks, which are expected to occur more frequently.[58] Therefore, developing biodegradable and disposable masks with low cost and reliable efficiency is a promising research subject and a societal demand.[59–61] Bacterial biosynthesis of degradable air filters has already been investigated for cellulose[62] and polyvinyl alcohol (PVA) with chitosan (CS),[63] which have

shown promising results for air filtration, over 95% collection efficiency for $PM_{2.5}$. However, electrospun nanofibers are more effective in filtering tiny particles and aerosols close to the nanoscale range.[24,64–69] The small fiber size diameter can improve the collection mechanisms for particle capture at this size range.[70,71] Biodegradable electrospun nanofibers of polylactic acid (PLA) was successfully used to capture tiny particles between 300 and 500 nm, above 99% collection efficiency.[72] PLA electrospun fibers were also associated with cotton layers to produce efficient masks against bacterial collection.[73] While electrospinning of natural polymers presents challenges,[74–76] progress has been made using modified materials, such as cellulose acetate[77] and blends like PVA/CS.[78–80]

PVA/CS is a blend broadly explored as a biomaterial for food packaging,[81] drug delivery,[82] tissue regeneration, and wound dressing.[79,83,84] It also shows promising properties for air filtration,[80] as demonstrated in our previous study.[78] In this study, we evaluated the air filtration efficiency of electrospun nanofibers using NaCl nanoparticles to simulate aerosols and bioaerosols at the nanoscale size.[24,64,65,77,85,86] It produced biodegradable nanofibers mats made of PVA and CS at several experimental conditions and functionalized them with *Lippia sidoides* essential oil to provide biocidal activity.[87–89] The nanofibers were tested as substitutes for conventional filter media of three-layer surgical masks and optimized by the Response Surface Methodology (RSM)[67,90–93] and Desirability Method (DM)[94–99] to evaluate changes in electrospinning parameters. RSM is responsible for creating a mathematical model that represents the influence of electrospinning production parameters on the responses of air filtration performance. Conversely, DM is a multi-response optimization method capable of combining the response surfaces generated by RSM into an optimum point that best satisfies all the RSM models.

4.2 Materials & Methods

4.2.1 Materials

This study used PVA, with a molecular weight of 85.500 g/mol and a degree of hydrolysis of 89.5% (Vetec Química Fina, Duque de Caxias/RJ, Brazil), and CS, with a degree of deacetylation of 68.5% (Polymar, Fortaleza/CE, Brazil). The analytical-grade glacial acetic acid at 99.0% (LabSynth, Diadema/SP, Brazil) was used to solubilize the polymers. The *Lippia sidoides* essential oil (Produtos Naturais LTDA, Horizonte/CE, Brazil) was used as an additive to provide biocidal activity.[87,88]

4.2.2 Precursor Solution & Electrospinning Process

The solution employed in this study follows the steps described in Mata e*t al*.[78] The concentration of PVA and CS was set at 6.0:1.0 (6.0 % of PVA and 1.0 % of CS). The polymers were previously weighted and dissolved in an aqueous 70% acetic acid solution. The solution was heated to 90 °C for three hours under magnetic stirring and cooled in ambient air. After cooling, 5% (w/w: in weight – solid basis) of *Lippia sidoides* essential oil was added while maintaining the solution under magnetic stirring.

Next, the solution was electrospun, varying the following parameters: electrical field (20 to 25 kV), feed flow rate (0.5 to 1.0 $mL.h^{-1}$), and processing time (30 to 60 min).

A three-layer commercial surgical mask (CSM) was used as the reference for comparison. Initially, the filtering layer, the middle layer of the CSM, was removed. Subsequently, the outer layer of the CSM was utilized as a support for the electrospun fibers. These fibers were produced using the experimental parameters outlined in **Table 4.1**. The objective was to create electrospun mats that could replace the middle layer of the three-layer surgical mask, which acts as the filtering layer. Then compare the results with those obtained with the original CSM.

Table 4.1: Samples produced via electrospinning with parameters selected according to the Central Composite Design in two replicates (A and B).

Sample	Point Type	Field (kV)	Flow Rate ($mL.h^{-1}$)	Time (min)	Sample	Point Type	Field (kV)	Flow Rate ($mL.h^{-1}$)	Time (min)
OE 1	Level	20.00	0.50	30.00	OE 11	Axial	22.50	0.33	45.00
OE 2	Level	25.00	0.50	30.00	OE 12	Axial	22.50	1.17	45.00
OE 3	Level	20.00	1.00	30.00	OE 13	Axial	22.50	0.75	19.77
OE 4	Level	25.00	1.00	30.00	OE 14	Axial	22.50	0.75	70.23
OE 5	Level	20.00	0.50	60.00	OE 15	Center	22.50	0.75	45.00
OE 6	Level	25.00	0.50	60.00	OE 16	Center	22.50	0.75	45.00
OE 7	Level	20.00	1.00	60.00	OE 17	Center	22.50	0.75	45.00
OE 8	Level	25.00	1.00	60.00	OE 18	Center	22.50	0.75	45.00
OE 9	Axial	18.29	0.75	45.00	OE 19	Center	22.50	0.75	45.00
OE 10	Axial	26.70	0.75	45.00	OE 20	Center	22.50	0.75	45.00

4.2.3 Nanofiber Characterization

The structural morphology of the electrospun fibers was analyzed by scanning electron microscopy (SEM). First, 5 × 5 mm samples of the electrospun nanofiber mat were coated with carbon and gold in a Bal-Tec SCD Sputter Coater model-050 (Fürstentum/Liechtenstein) under a pressure of 0.1 mbar. SEM photomicrographs were obtained using a JEOL model JSM 6610LV (Tokyo, Japan).

4.2.4 Permeability & Filtration Efficiency

When studying masks, pressure drop ($\Delta \boldsymbol{P}$) is used to measure breathability. As pressure drop is intrinsically related to the permeability constant ($\boldsymbol{K_1}$), by applying Darcy's Law (Equation 1), it was possible to obtain the constant of permeability ($\boldsymbol{K_1}$) by linear regression. Therefore, the optimization of $\boldsymbol{K_1}$ will also improve breathability. Permeability studies were conducted for all the filter membranes by passing clean air through them. Superficial velocity was varied from 0.1 to 2.0 $L.h^{-1}$ in twenty steps to study the pressure drop of the filters.

$$\frac{\Delta P}{L} = \frac{\mu}{K_1} v_s \qquad (1)$$

where ΔP is the Pressure Drop; L is the filter media thickness; μ is the fluid viscosity (*i.e.*, air); and v_s is the surface velocity. The fiber mat's layer thickness (L) was measured using an optical microscope (Olympus BX60, Olympus Co., Shinjuku, Tokyo, Japan) at magnifications of x10, x20, and x40. The technique of electric particle mobility was used to obtain the filters' collection efficiency (η). Equation 2 exemplifies the filters' collection efficiency calculation. This method calculates the difference between the number of particles projected through the filter media and those ejected from it. To simulate the new coronavirus (SARS-CoV-2), sodium chloride (NaCl) nanoparticles[24,65] were used, with the flow rate set at 1.5 $L.h^{-1}$ and a filtration area of 5.2 cm^2 for each sample[63,85,100]. NaCl nanoparticles ranged from 7 to 250 nm, a broader range that includes fine and ultrafine particulate matter and many respiratory viruses such as SARS-CoV-2 (60 to 140 nm)[13] and H1N1 Influenza (80 to 120 nm)[101–103].

$$\eta = \frac{C_0 - C_f}{C_0} . 100 \qquad (2)$$

where C_0 and C_f are the concentration of nanoparticles before and after the filter media, respectively.

From the experimental results of η, and the corresponding ΔP, the Quality Factor (Q_f) was calculated, which measures the overall performance of the filter media (Equation 3):

$$Q_f = \frac{-\ln(1 - \eta)}{\Delta P} \qquad (3)$$

Filtering efficiency and permeability of the filter media coated with nanofibers were determined on the filtration modulus available in the Laboratory of Environmental Control I (DEQ/UFSCar), as described in **Figure 5.1**. The filtration modulus consists of an air compressor (Shultz Acworth, GA, USA), an air filter for air purification, a nanoparticle generator (Model 3079, TSI, Shoreview, MN, USA), a diffusion dryer (Norgren IMI, Birmingham, UK), a neutralizer of krypton and americium (Model 3054, TSI, Shoreview, MN, USA), and a filter support device. The module apparatus is attached to an electrostatic classifier, a Scanning Mobility Particle Sizer spectrometer (SMPS - Model 3080, TSI, Shoreview, MN, USA), and an ultrafine particle counter (Model 3776, TSI, Shoreview, MN, USA)[104].

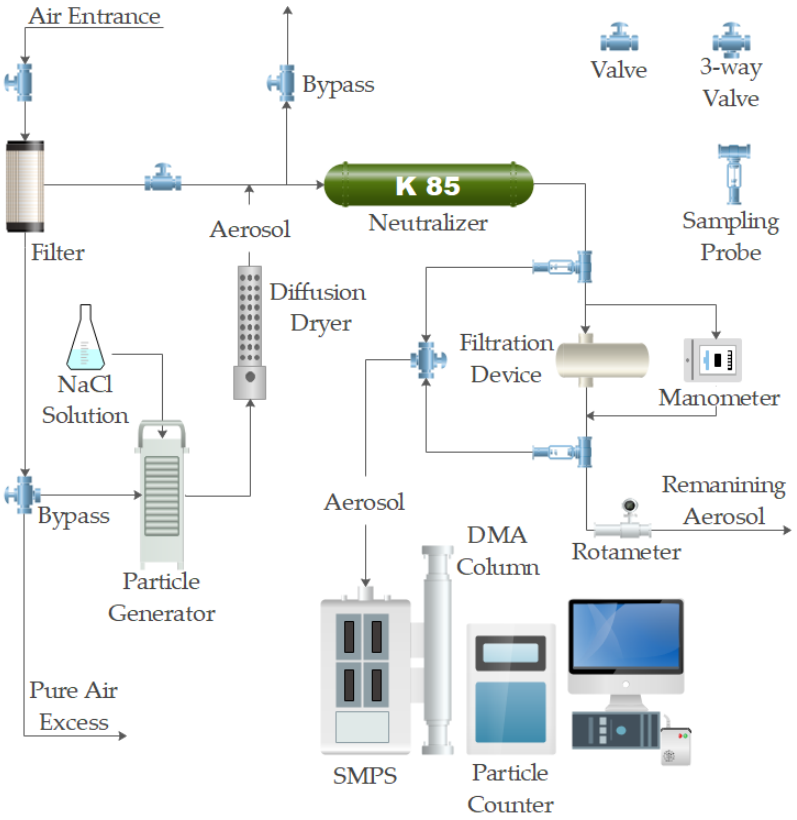

Figure 5.1: Experimental apparatus to evaluate filter media collection efficiency of the Laboratory of Environmental Control I (DEQ/UFSCar).

4.2.5 Response Surface Methodology & Desirability Method

A Central Composite Design (CCD) is a typical factorial design used in the Response Surface Methodology (RSM), as shown in **Figure 4.2**. This design expands the center points with external points to the model, called axial or star points.[90] CCD is more accurate and does not require a three-level factorial experiment to construct a second-order quadratic model.[105]

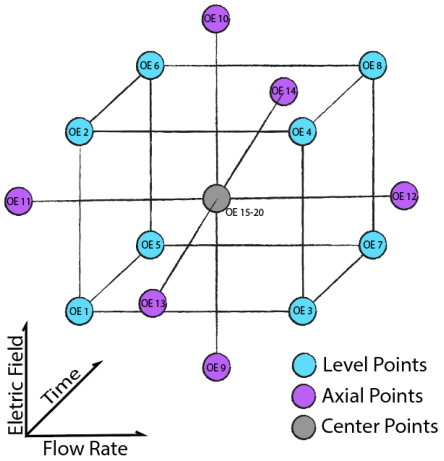

Figure 4.2: Model of the 2^3 (three factors with two levels each) Central Composite Design (CCD) utilized in this study for the Response Surface Methodology (RSM). This CCD is rotational with $\alpha = 1.68$ (constant variance at the same radius inside the model).

In this study, three factors were used, the Electric Field (kV), Flow Rate (mL.h^{-1}), and Time (min). Factors are the axis for each dimension of the cubic CCD. They had two levels each and six repetitions of the center point. All the samples used to construct the model are defined in Table 1. The responses analyzed were global filtration efficiency ($\boldsymbol{\eta}$), the permeability constant in Darcy's law ($\boldsymbol{K_1}$), and overall filtration performance with the quality factor ($\boldsymbol{Q_f}$). The CCD model was generated and analyzed with Minitab®. Data fitting and regression were performed with Excel® and OriginPro® and automatized using PyCharm® (Python 3.10.1). **Appendix C** displays the program.

After treating each response, a response optimization of the models created was performed using the Desirability Method (DM) with four sets of parameters. These sets served as the basis to electrospun new fibers, validate the model, and find an optimum combination of parameters. It is worth mentioning that this study was performed in replicate (runs), repeating the evaluation of the sample to create a more accurate model, as described in Table 1. It was referred to as "runs" because, unlike blocks, this study did not evaluate any nuisance factors that may interfere with the investigation (*e.g.*, chamber humidity and temperature).

4.3 Results & Discussion

4.3.1 Fibers Characterization

Some samples were analyzed under SEM to observe the morphological structures in the fibers' mats. **Figure 4.3** exhibits typical SEM photomicrographs.

CS is known for its harsh properties in producing fibers via electrospinning,[74] and adding PVA and essential oil appears to help its spinnability. At concentrations lower than 2%, chitosan does not present enough structural entanglement to produce fibers,[106] while above 2%, the viscosity increases to the point where the electrospinning process becomes inviable.[107] The electrospun nanofibers exhibited a smooth and uniform surface without any beads.

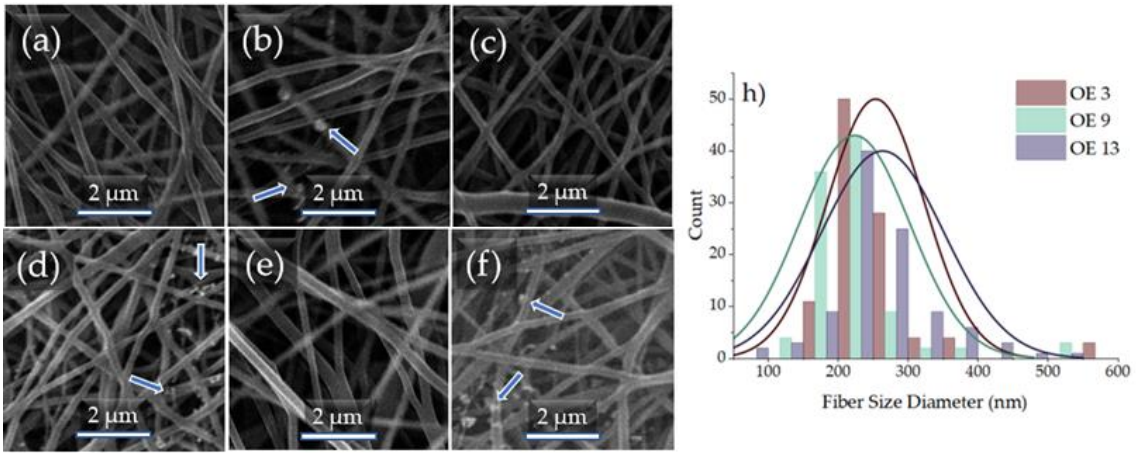

Figure 5.3: Typical SEM photomicrographs of the nanofibers mats before and after the air filtration, respectively, for samples: OE 3 (a) and (b); OE 9 c) and d); and OE 13 (e) and (f). Blue arrows show the aggregates of NaCl nanoparticles retained over the fiber mats after the filtration (magnification 10kx). The nanofiber size distribution is presented in (h).

Since the electrospun fibers were produced using the same mother solution, chemical variations from one fiber to another were not expected. Therefore, it is possible to observe that even minor variations in the physical production parameters can lead to significant changes in the morphology of the fibers. As a result, the filtration efficiency and pressure drop of the electrospun filters are also affected. Thus, further research is required to differentiate the effects of chemical and physical changes on the electrospun mats.

4.3.2 Filtration Performance

Figure 4.4a shows the pressure drop data as a function of the surface filter velocity. **Figure 4.4b** shows the data on the collection efficiency per nanoparticle size for nanofiber membranes at the level points of the CCD (Replicate A). Additional samples (OE 9 to 20) and samples for replicate B are described in **Figure 4.S1** and **Figure 4.S2**. **Table 4.2** summarizes the data of permeability ($\boldsymbol{K_1}$), collection efficiency ($\boldsymbol{\eta}$), quality factor ($\boldsymbol{Q_f}$), and pressure drop ($\Delta\boldsymbol{P}$) obtained for all electrospun nanofiber membranes.

Table 4.2: Summary of data for both air filtration replicates (A and B), obtained for the electrospun samples produced using the parameters in the Central Composite Design (CCD). $\boldsymbol{K_1}$ is the permeability constant, $\boldsymbol{\eta}$ is the collection efficiency, $\Delta\boldsymbol{P}$ is the pressure drop at a filtration velocity of 4.8 cm.s^{-1}. $\boldsymbol{Q_f}$ is the quality factor, and $\boldsymbol{L}$ is the mat's thickness.

Samples (Replicate A)	K_1 (μm^2)	η (%)	ΔP (Pa)	Q_f (Pa^{-1})	Samples (Replicate B)	K_1 (μm^2)	η (%)	ΔP (Pa)	Q_f (Pa^{-1})	L (μm)
Mask	816.55	67.80	32.2	0.035	Mask	909.14	42.84	29.3	0.019	345.01 ± 10.18
OE 1	18.03	94.10	122.9	0.023	OE 1	11.63	79.51	189.2	0.008	30.32 ± 13.34
OE 2	7.79	82.64	171.8	0.010	OE 2	6.43	99.16	208.7	0.023	17.69 ± 1.38
OE 3	70.22	70.93	33.1	0.046	OE 3	37.63	63.87	64.4	0.016	32.33 ± 3.10
OE 4	11.60	89.05	117.0	0.022	OE 4	4.78	99.84	287	0.022	17.90 ± 3.54
OE 5	26.54	88.80	107.5	0.020	OE 5	26.81	82.90	102.3	0.017	37.31 ± 11.65
OE 6	7.20	85.67	394.7	0.005	OE 6	5.40	99.80	538.1	0.011	37.79 ± 10.51
OE 7	14.41	98.40	253.0	0.016	OE 7	14.41	94.90	247.2	0.012	46.93 ± 5.13
OE 8	1.60	99.99	1793.3	0.006	OE 8	1.83	99.99	1604.4	0.006	37.47 ± 15.56
OE 9	8.84	94.45	70.2	0.041	OE 9	17.52	67.12	36.7	0.030	8.35 ± 1.55
OE 10	3.97	99.65	559.3	0.010	OE 10	3.35	99.98	654.2	0.013	27.93 ± 3.69
OE 11	35.54	94.68	158.0	0.018	OE 11	35.55	90.32	120.5	0.019	55.68 ± 2.61
OE 12	4.35	99.90	398.4	0.017	OE 12	4.35	99.82	358.3	0.017	20.07 ± 3.91
OE 13	30.30	97.65	102.1	0.037	OE 13	30.30	82.25	79.2	0.022	31.30 ± 4.79
OE 14	5.22	99.51	419.2	0.013	OE 14	8.58	91.23	260.7	0.009	29.20 ± 4.92
OE 15	9.82	98.66	332.7	0.013	OE 15	7.55	99.94	428.5	0.017	41.82 ± 10.83
OE 16	6.77	99.60	333.0	0.017	OE 16	8.62	96.63	255.9	0.013	29.64 ± 2.88
OE 17	4.90	99.88	317.6	0.021	OE 17	6.59	96.54	211.1	0.016	18.46 ± 6.08
OE 18	4.07	99.90	312.5	0.022	OE 18	4.23	99.64	303.8	0.018	17.23 ± 1.32
OE 19	7.22	97.66	210.2	0.018	OE 19	5.64	99.27	265.9	0.018	19.95 ± 3.31
OE 20	7.59	99.62	267.1	0.021	OE 20	6.44	99.99	323.1	0.028	27.21 ± 7.25

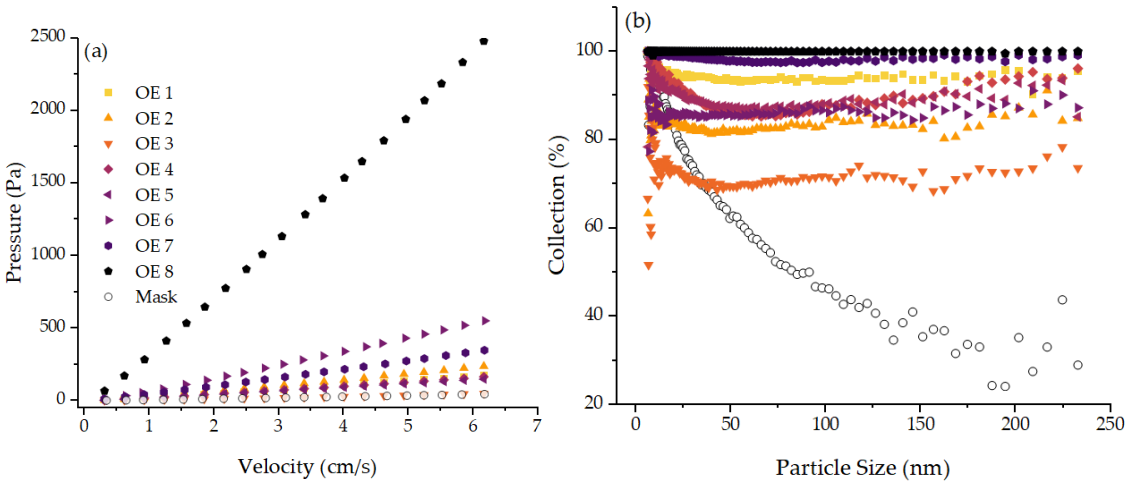

Figure 4.4: (a) Pressure drops by filtration velocity for the surgical masks coated with the electrospun nanofibers membranes, and **(b)** fractional collection efficiency curves for the surgical mask. The exposed samples are the mask and the level points used for the CCD (replicate A). The diameter distribution ranged from 7 to 250 nm, evaluated with a surface velocity of 4.8 cm.s^{-1}.

Electrospun samples presented a wide range of $\boldsymbol{\eta}$, $\boldsymbol{K_1}$ and $\boldsymbol{Q_f}$. A higher-pressure drop indicates sinuous pore channels through the fiber mats, which means that a longer path to cross the filtering membrane. Collection mechanisms, such as direct and inertial impaction, tend to rise during the crossing, improving the collection efficiency. In contrast, low-pressure drops mean fewer air flow obstacles caused by straightforward preferential channels, decreasing the collection efficiency.

Most of the samples had better filtration performances when compared with the surgical mask. The decline in the collection efficiency curve for particles between 7 and 60 nm, particularly for the CSM sample, can be responsible for the most penetrating particle size (MPPS). While particles smaller than the MPPS are dominated by the Brownian diffusion mechanism, the interception mechanism is more influential for larger particles.[108–110]

Nanometer-sized particles (*i.e.*, less than 100 nm) can easily pass through the pores of the nanofiber mat. The predominant collection effects at the nanoscale are the Brownian diffusion and the electrostatic attraction when the fibers' electrical field bounds low-mass particles.[70] These effects are relevant for air filtration since diffusion is the primary filtration mechanism for retaining airborne viruses and small pollution particles.[71] Particles between 100 and 250 nm are large enough to be dominated by diffusive forces and too small to be effectively collected by impaction,[86,100,111] therefore, the collection efficiency tends to be less effective in this particle size range in filters with lower pressure drops.

Nevertheless, most electrospun nanofibers samples showed better filtration efficiency for nanoaerosols larger than 25 nm than the commercial surgical mask. Residual electrical charges from the electrospinning seem to increase the nanoparticle collection efficiency of the nanofiber membranes. Leung & Sun[24,65] observed that polyvinylidene fluoride (PVDF) fiber mats could retain electrical charges for several months after production. Additionally, more particulate matter proximity and contact

with the nanofibers induce stronger electrostatic attraction since nanoparticle removal is a dynamic process of adsorption and desorption.[112]

The overall performance, as measured by the quality factor, presented better results than the CSM, with higher $\boldsymbol{Q_f}$ values for some samples (OE 3, 9, and 13). For velocities close to those in this study (5 cm.s^{-1}), quality factors around 0.02 Pa^{-1} are considered satisfactory[113] since theoretical analysis expects quality factors below 0.01 Pa^{-1} for fibers with a mean diameter of 1 µm.[114]

Bortolassi *et al.*[86] obtained $\boldsymbol{Q_f}$ between 0.04 and 0.06 Pa^{-1}, using electrospun polyacrylonitrile (PAN), while Gao *et al.*[115] obtained values lower than 0.0231 Pa^{-1} for electrospun PAN composites. Bonfim *et al*. [64,85] reported quality factors higher than 0.02 Pa^{-1} using samples with different concentrations of electrospun polyethylene terephthalate (PET) from recycled soft drink bottles.

A considerable difference was also observed in the surgical mask's permeability constant range (816.55 to 909.14 µm²) and the electrospun nanofibers samples (1.60 to 37.63 µm²). The explanation for these permeability values is linked to the filters' thickness (**Figure 4.5**). Electrospun samples' thickness ranged from 8 to 55 µm, while the CSM presented a fiber mat of 345 µm, 7 to 35 times higher than the electrospun samples. A thicker but permissive filter does not necessarily increase the filter's capability to retain particles. In other words, an increase in permeability can cause a decrease in collection efficiency, even with a thicker mat. Although the pressure drop was higher for the filter coated with the electrospun nanofiber mats, some samples got similar values to the mask, indicating that it is possible to improve this property by manipulating the permeability.

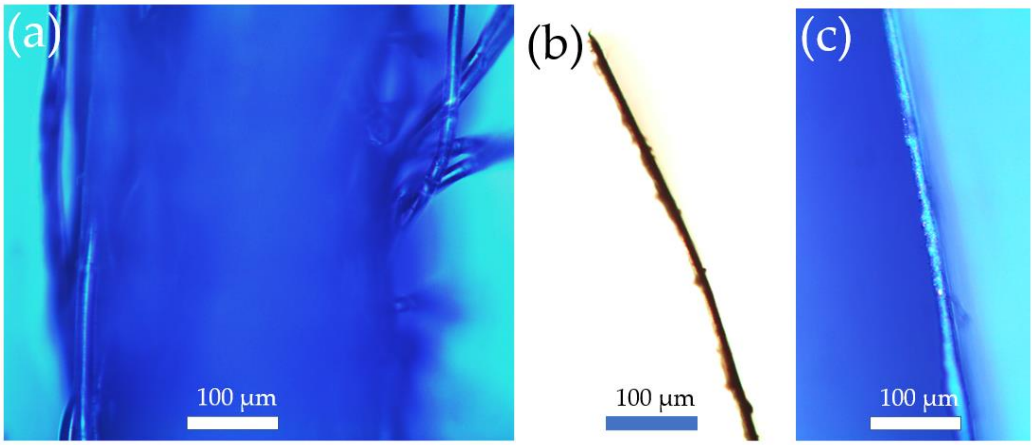

Figure 4.5: Microscope analysis of the thickness for (a) the Commercial Surgical Mask (CSM) filtering layer, with 345 µm and for the electrospun nanofibers without the support: (b) OE 18, with 17 µm; and (c) OE 19, with 20 µm.

4.3.3 Response Surface Methodology

A Central Composite Design was built after analyzing the response data described in Table 2 (*i.e.*, collection efficiency, permeability constant, and quality factor). The Equation models are expressed in the supplementary material (**Table S1**).

From the Pareto charts shown in **Figure 4.6**, it was possible to observe the influence of each parameter and their binary combined effects on the CCD responses. The electrical field was relevant for all the responses, particularly the collection efficiency. Even the quadratic effect of the electrical field (E×E) showed high significance for $\boldsymbol{\eta}$, representing a second-order influence for this parameter. As previously discussed, the primary mechanism of nanoparticle retention is the Brownian diffusion and the collection by electrostatic interaction between the aerosol particle and the fiber residual electrical charge.[70] This phenomenon explains the electrical field's strong influence on collection efficiency, consistent with the literature. Medeiros *et al*.[116] showed that the electrical field was the most influential parameter on zein/poly ethylene oxide fibers, controlling the presence or absence of beads. Changes in the electrical field during the electrospinning process also cause fiber deposition and size distribution variations.[117–119] Even the electrical field direction and the current type used to generate it (*i.e.*, alternate or direct) can influence the nanofibers' morphology.[91,120]

It is worth mentioning that the statistical significance does not mean a positive influence of the respective parameter in each response. For instance, the flow rate combined with the time presents statistical relevance for the permeability (p-value lesser than 0.05). However, this binary effect had a negative influence, as seen in the CCD model equation in the supplementary material (Table S1, Equation S2). This relation makes sense since more time of production and higher flow rate means more material has been squeezed through the needle and deposited over the collector, leading to thicker and denser nanofiber mats with tortuous pore channels. The linear effect of the flow rate does not present a statistical influence on the responses, while its quadratic effect and the binary interaction with other parameters have presented.

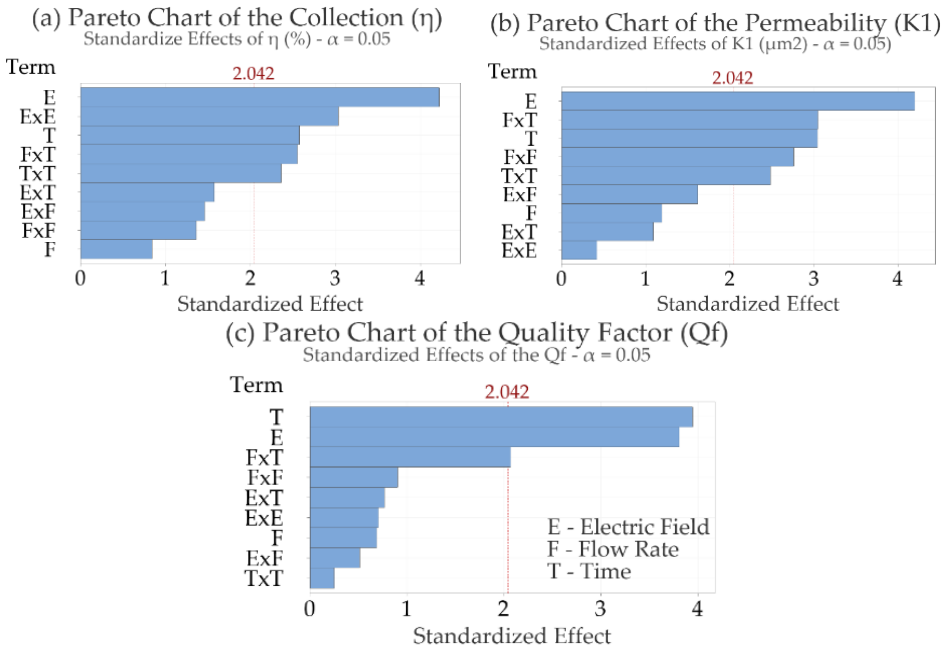

Figure 4.6: Pareto charts for (a) permeability constant ($\boldsymbol{K_1}$); (b) collection efficiency ($\boldsymbol{\eta}$); and (c) quality factor ($\boldsymbol{Q_f}$), showing the parameters and their binary and quadratic interaction for each response. Parameters that have crossed the reference line (in red) presented a statistical significance (p-value less than 0.05).

The resulting contour and surface response plots for the collection efficiency (**η**) are shown in **Figure 4.7**. The same graphs were constructed for the other responses, permeability constant (K_1) and quality factor (Q_f) and are included in the supplementary material as **Figure 4.S3** and **Figure 4.S4**, respectively.

Electrospinning Time and the Electrical Field parameters showed an optimized zone for the collection efficiency plot. An electrospinning time between 50 and 60 min and electrical fields around 23 kV appear to promote better filtration efficiency. Higher flow rates follow the same trend since they reduce permeability, which is undesirable. The overlap curves can optimize the parameters to improve filtration at an acceptable permeability and pressure drop, maintaining the mask's breathability.

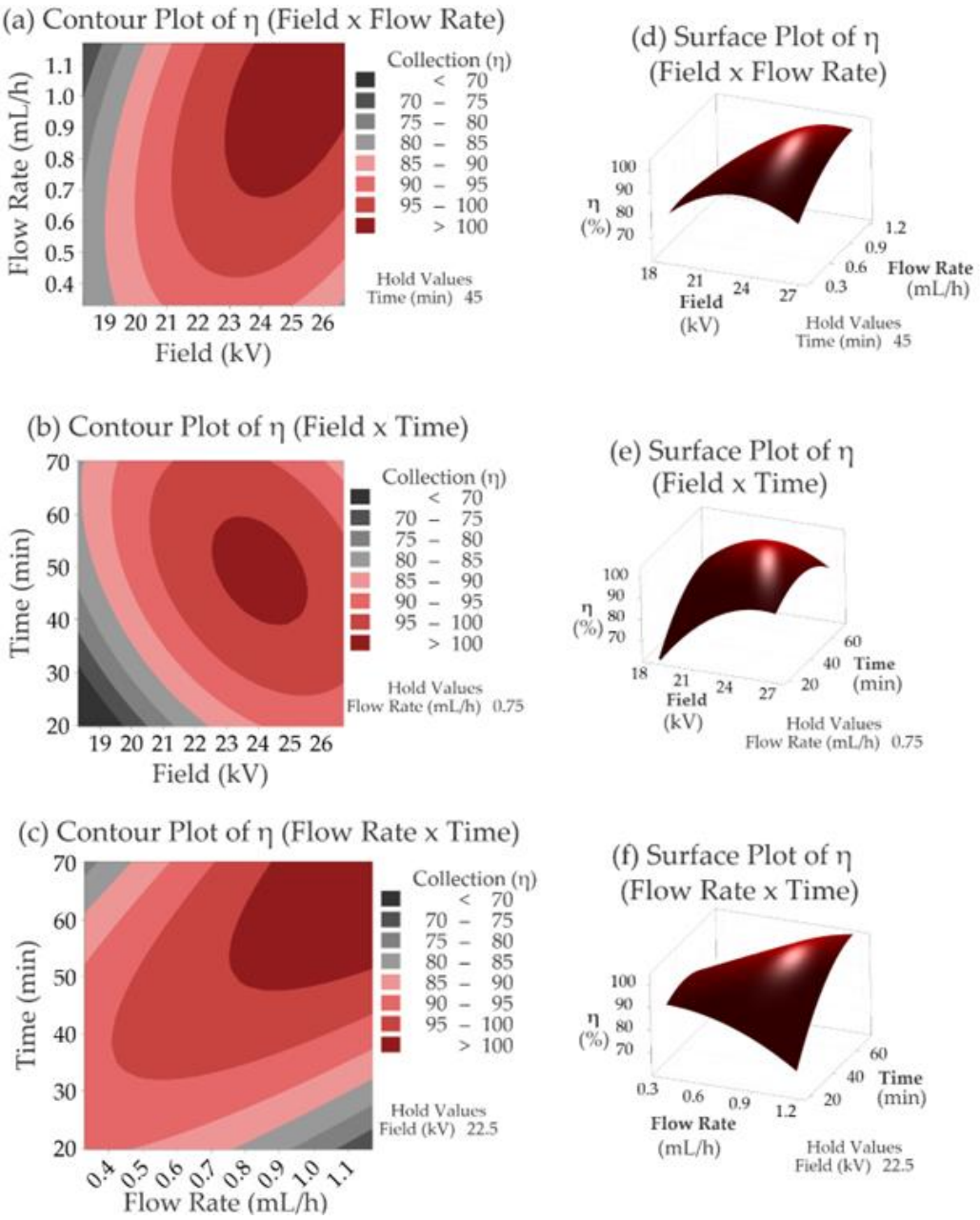

Figure 4.7: Contour plots for collection efficiency response (**η**), taking into consideration the interaction of the parameters: **(a)** electric field × flow rate; **(b)** electric field × time; and **(c)** flow rate × time. Images (d), (e) and (f) show the surface response plots for the same parameter combinations.

4.3.4 Validation & Optimization

Using the Desirability Method (DM) for multiple responses, the nanofiber mats were optimized to validate the Response Surface Methodology. The optimization objectives for each response ($\boldsymbol{Q_f}$, $\boldsymbol{K_1}$, and $\boldsymbol{\eta}$) were varied to ensure the produced fibers comply with international regulations (further discussed in section 3.5).

After optimizing each response individually, DM converts all responses into an individual desirability function ranging from 0 to 1. When the parameter is placed in a target point (maximum, minimum, or a specified value), the desirability function will approximate to 1. The desirability value diminishes as the response value moves away from the target point.[121] The idea is to convert the different response optimizations into individual desirability functions and combine them into a global desirability function. The global desirability function will find sets of parameter values that maximize (or minimize) all the system responses.

The first step was equally optimizing all the responses ($\boldsymbol{Q_f}$, $\boldsymbol{K_1}$, and $\boldsymbol{\eta}$). However, the values obtained for the global desirability were too low (0.5530), as shown in the supplementary material (Figure S5). It shows how the target point found to combine all the responses deviates from the ideal target points from each response individually.

The next step was changing the importance of each response. The importance is the individual contribution of each response to the global desirability model (ranging from 0.1 to 10). We maximized the importance of two responses and reduced the importance of the other response to a minimum. So, we obtained four sets for the parameters, namely:

- OEV(-) for the parameters equally optimized, without changes in importance;
- OEV($\downarrow \boldsymbol{K_1}$) for minimizing the effect of $\boldsymbol{K_1}$ and maximizing the $\boldsymbol{Q_f}$ and the $\boldsymbol{\eta}$ importance;
- OEV($\downarrow \boldsymbol{\eta}$) for diminishing the effect of $\boldsymbol{\eta}$ and maximizing the $\boldsymbol{Q_f}$ and the $\boldsymbol{K_1}$ importance;
- OEV($\downarrow \boldsymbol{Q_f}$) for reducing the effect of $\boldsymbol{Q_f}$ and maximizing the $\boldsymbol{\eta}$ and the $\boldsymbol{K_1}$ importance.

The global desirability for OEV($\downarrow \boldsymbol{K_1}$) was 0.6212, for OEV($\downarrow \boldsymbol{\eta}$) was 0.8237, and for OEV($\downarrow \boldsymbol{Q_f}$) was 0.5350. These graphs are shown in the supplementary material (Figures S6, S7, and S8, respectively).

New nanofibers mats were produced using the parameters configurations for each set obtained by the desirability method. They were tested under the air filtration system described in **Figure 4.1**, and the results are shown in **Figure 4.8**. The parameters conditions and the values obtained are presented in **Table 4.3**.

It is worth mentioning that another way to improve global desirability is by using the weight of the responses before the responses' optimization. Weight is the curvature behavior during the optimization of each response. We did not change the pattern values for the weight.

All the validation samples exhibited superior collection efficiency compared to the CSM. It demonstrates the possibility of achieving more efficient filters than the CSM using natural and biodegradable polymers. Samples OEV(-), OEV($\downarrow \boldsymbol{K_1}$) and OEV($\downarrow \boldsymbol{Q_f}$)

presented a quality factor very close to the higher value of the CSM. Sample OEV(↓$\boldsymbol{\eta}$) showed an unexpected performance, with a $\boldsymbol{Q_f}$ of 0.066, almost double when compared with the CSM and higher than the range of $\boldsymbol{Q_f}$ predicted for the sample (0.022 - 0.051).

Table 4.3: Optimum estimated ranges and obtained values for the different samples of the validation process, compared with the surgical mask. D represents the desirability value obtained for each optimization. Pressure drop ($\Delta \boldsymbol{P}$) evaluation was performed at a filtration velocity of 4.8 cm.s^{-1}.

Sample Response	Commercial Surgical Mask (CSM)	OEV(-) D: 0.5530	OEV(↓Q_f) D: 0.5350	OEV(↓K_1) D: 0.6212	OEV(↓η) D: 0.8237
Optimum Electric Field (kV)	-	24.32	23.39	25.01	21.52
Optimum Flow Rate (mL.h^{-1})	-	1.17	1.17	0.92	1.17
Optimum time (min)	-	20.79	27.93	24.87	19.77
Q_f Prediction Range (Pa^{-1})	-	0.016 - 0.046	0.017 - 0.038	0.017 - 0.034	0.022 - 0.051
Q_f Obtained (Pa^{-1})	0.019 - 0.035	0.033	0.031	0.028	0.066
η Prediction Range (%)	-	64.77 - 94.53	73.66 - 95.15	83.65 - 100.68	49.77 - 78.77
η Obtained (%)	42.84 - 67.80	90.18	96.58	96.27	72.82
K_1 Prediction Range (µm^2)	-	22.3 - 64.2	21.05 - 51.26	4.37 - 28.32	43.03 - 85.81
K_1 Obtained (µm^2)	816.55 - 909.14	14.54	12.25	12.21	53.93
ΔP (Pa)	29.3 - 32.2	70.0	108.1	118.5	19.6
L (µm)	345.01 ± 10.18	13.63 ± 3.05	18.44 ± 4.74	19.36 ± 5.19	14.04 ± 3.70

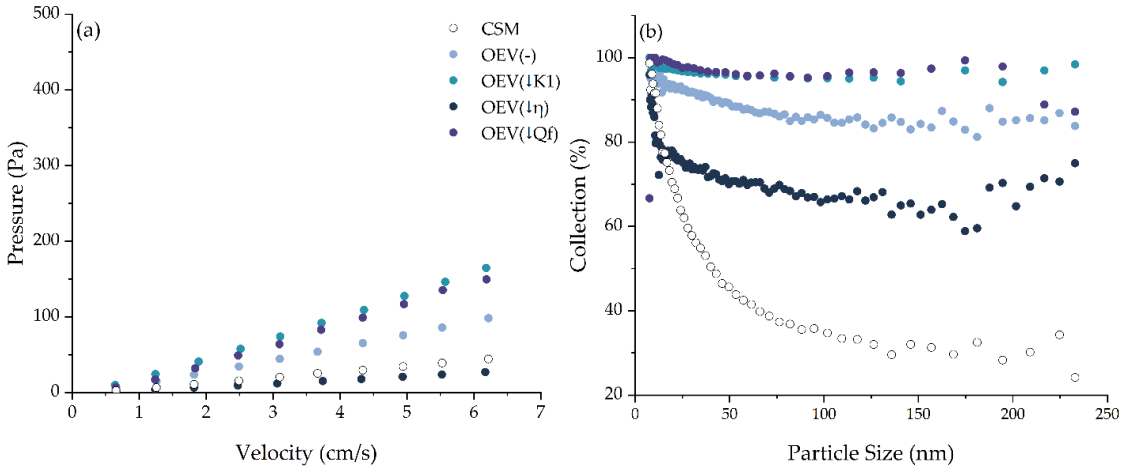

Figure 4.8: (a) Pressure drop by filtration velocity and (b) Fractional efficiency curves for the commercial surgical mask (CSM) and the validation samples. The diameter distribution ranged from 7 to 250 nm, evaluated at a filtration velocity of 4.8 cm.s^{-1}.

However, the collection efficiency of OEV(↓$\boldsymbol{\eta}$) was the lowest among the validation samples (72.82%). It is indicative that the $\boldsymbol{Q_f}$ calculation prioritizes reducing

the pressure drop (19.6Pa) at the expense of collection efficiency. This reasoning makes sense, as the $\boldsymbol{Q_f}$ calculus measures the overall performance as a filter, taking into account the trade-off between retention capacity ($\boldsymbol{\eta}$) and energetic expenditure ($\Delta \boldsymbol{P}$). It aims to find a balance between these factors rather than focusing solely on individual properties. Therefore, the sample OEV($\downarrow \boldsymbol{\eta}$) demonstrates the best overall performance as a filter. At the same pace, the samples OEV($\downarrow \boldsymbol{K_1}$) and OEV($\downarrow \boldsymbol{Q_f}$) achieved high collection efficiencies (96.27% and 96.58%) but at the expense of higher pressure drops (118.5 Pa and 108.1 Pa). As one of the goals of this study is to ensure compliance of the electrospun fibers with international regulations, it was necessary to reduce the filter performance in order to increase the collection efficiency required by the legislation.

4.3.5 Legislation Accordance

A comparison was made using international legislation for surgical masks, as shown in **Table 4.4**. It used Brazilian legislation (ABNT NBR 15052 2021),[122] United States legislation (ASTM F2100 2019),[123], and European legislation (EN 14683 2019).[124] As a comparative basis, in addition to CSM, other samples of commercial masks were tested in the filtration efficiency module described in Figure 1. Homemade masks made of Oxford fabric (HH-1) and cotton fabric (HH-2), three-layer polypropylene surgical masks (SM-1, SM-2, and SM-3), and N95 masks (N95-1, N95-2, and N95-3) from different brands were also included in the testing.

All the commercial and validation samples comply with the regulation for the pressure drop, with some differences between the samples and their classes. Samples OEV($\downarrow \boldsymbol{K_1}$) and OEV($\downarrow \boldsymbol{Q_f}$) presented higher filtration efficiency than required for the mask legislations (≥ 95%) at levels 0 and 1 (Brazilian), level 1 (United States), and Type I (Europe Union). They also have higher pressure drops than the majority of commercial samples. Even though sample OEV($\downarrow \boldsymbol{Q_f}$) presented slightly better performance than OEV($\downarrow \boldsymbol{K_1}$), both samples presents suitable properties as a biodegradable alternative for the surgical mask.

Among the commercial samples, only sample N95-3 could meet the regulatory standards for collection efficiency. Those findings highlight that even highly efficient commercial samples often fall short of regulatory standards. Improvements in the production process and increased oversight may be necessary to encourage these brands to enhance the quality of their materials.

As our study was conducted at a low airflow rate, further investigation is needed to fully comply the electrospun samples with the technical standards outlined in **Table 4.4**. Our research team is currently addressing these issues in ongoing studies. Other material properties, such as mechanical strength and hydrophobicity, must be improved before conducting experiments at higher airflow rates and velocities. These are common hindrances for electrospinning of natural and biodegradable polymers,[125–128] which has been the focus of the research community.[129–137]

Table 4.4: Comparison between the optimized samples and some legislations about mask properties from Brazil (ABNT NBR 2021), the United States (ASTM F2100 2019), and Europe Union (EN 14683 2019). The filtration area was 5.2 cm².

Technical Standard/Sample	Pressure Drop ($Pa.cm^{-2}$)	Collection Efficiency (%)
ABNT NBR 15052 (2021)	Levels 0 and 1: <49.03 Levels 2 and 3: < 58.84	Levels 0 and 1: ≥ 95 Levels 2 and 3: ≥ 98
ASTM F2100 (2019)	Level 1: <49.03 Levels 2 and 3: < 58.84	Level 1: ≥ 95 Levels 2 and 3: ≥ 98
EN 14683* (2019)	Types I and II: < 40 Type IIR: < 60	Type I: ≥ 95 Types II and IIR: ≥ 98
OEV(-)	13.46	90.18
OEV($\downarrow \boldsymbol{K_1}$)	22.78	96.27
OEV($\downarrow \boldsymbol{\eta}$)	3.77	72.82
OEV($\downarrow \boldsymbol{Q_f}$)	20.79	96.58
HH-1	8.11	25.85
HH-2	10.52	46.13
SM-1	8.23	59.89
SM-2	11.88	62.08
SM-3	22.71	76.77
N95-1	17.11	82.15
N95-2	11.19	92.11
N95-3	16.35	95.49

* Technical Standard EN 14683 does not define a filtration efficiency for particles, only for bacterial filtration efficiency.

4.4 Conclusion

Using the Response Surface Methodology (RSM), a mathematical model was constructed to relate the electrospinning process parameters (electric field, flow rate, and production time) to the responses in air filtration of fine and ultrafine particles (quality factor, permeability constant, and collection efficiency). It was observed from the RSM analysis that the electrical field had a significant influence on all parameters, leading to an increase in collection efficiency and a decrease in the permeability constant. The Desirability Method (DM) was subsequently employed to identify parameter sets that optimize the electrospun fibers to meet international regulations.

Validation samples were electrospun using the sets of parameters derived from the DM. Among the optimized samples, OEV($\downarrow \boldsymbol{K_1}$) and OEV($\downarrow \boldsymbol{Q_f}$) presented the best collection efficiency for tiny particles (96.27 and 96.58%), even higher than the N95 masks used as the basis for comparison (82.15, 92.11, and 95.49%). The parameter set for OEV($\downarrow \boldsymbol{K_1}$) and OEV($\downarrow \boldsymbol{Q_f}$) was, respectively: 25.01 and 23.39 kV for the tension applied for the electrical field; 0.92 and 1.17 $mL.h^{-1}$ of flow rate; and 24.87 and 27.93 min of time production. Both samples complied with the legislation presented.

Although the electrospun nanofibers still require some improvements, such as mechanical resistance and hydrophobicity, these results demonstrated that biodegradable materials are strong candidates for replacing traditional polymers used in face mask production. Nanofiber mats made from PVA/CS and essential oil have demonstrated that they could be as efficient as surgical masks and even N95 in the filtration of tiny particles as associated viruses and pollution particulate matter. The optimization also showed that minor adjustments to the parameter's conditions could significantly improve the nanofiber mats' filtration efficiency and permeability. Using statistical designs such as RSM and DM, it is also possible to tailor the material production and manipulate the fiber's properties to meet specific requirements, such as higher efficiency or changes in permeability and quality factor values.

Author Contributions: Conceptualization, G.C.M., M.S.M. and W.P.O.; data curation, G.C.M.; formal analysis, G.C.M; funding acquisition, W.P.O. and M.L.A. investigation, G.C.M. and M.S.M.; methodology, G.C.M., M.S.M. and W.P.O..; project administration, M.L.A.; resources, W.P.O. and M.L.A.; software, G.C.M.; supervision, W.P.O. and M.L.A.; validation, G.C.M. and M.S.M.; visualization, G.C.M., M.S.M. and W.P.O.; writing—original draft preparation, G.C.M.; writing—review and editing, G.C.M., W.P.O. and M.L.A.; All authors have read and agreed to the published version of the manuscript.

Funding: This research was funded by Coordination for the Improvement of Higher Education Personnel (CAPES) grant number 88887.505019/2020-00, the National Council for Scientific and Technological Development (CNPq), grant number 424792/2018-4 and the Foundation of Research Support of São Paulo State (FAPESP) grant number 2018/26069-0.

Acknowledgments: This research was funded by Coordination for the Improvement of Higher Education Personnel (CAPES) grant number 88887.505019/2020-00, the National Council for Scientific and Technological Development (CNPq), grant number 424792/2018-4, and the Foundation of Research Support of São Paulo State (FAPESP) grant number 2018/26069-0. The authors acknowledge the financial support of the CAPES, CNPq, and FAPESP. We also would like to thank the personnel and staff from the Environmental Control Laboratory of the Federal University of São Carlos (LCA/UFSCar), the Laboratory of P&D in Pharmaceutical Process of the University of São Paulo (LAPROFAR/USP), the Chemistry Department of the Faculty of Philosophy, Science, and Letters of the University of São Paulo (FFCLRP/USP) and the Laboratory of Electronic Microscopy of the Department of Materials Engineering of the University of São Paulo (EESC/USP).

Conflicts of Interest: The authors declare no conflict of interest.

4.5 References

1. Carozzi, F. & Roth, S. Dirty density: Air quality and the density of American cities. *Journal of Environmental Economics and Management* **118**, 102767 (2023).
2. Lu, X. *et al.* Progress of Air Pollution Control in China and Its Challenges and Opportunities in the Ecological Civilization Era. *Engineering* **6**, 1423–1431 (2020).
3. Nguyen, L. S. P. *et al.* Trans-boundary air pollution in a Southeast Asian megacity: Case studies of the synoptic meteorological mechanisms and impacts on air quality. *Atmospheric Pollution Research* **13**, 101366 (2022).
4. Rodrigues, V. *et al.* Assessing air pollution in European cities to support a citizen centered approach to air quality management. *Science of The Total Environment* **799**, 149311 (2021).
5. Sicard, P. *et al.* Trends in urban air pollution over the last two decades: A global perspective. *Science of The Total Environment* **858**, 160064 (2023).
6. de Jesus, A. L. *et al.* Ultrafine particles and PM2.5 in the air of cities around the world: Are they representative of each other? *Environment International* **129**, 118–135 (2019).
7. Abdillah, S. F. I. & Wang, Y.-F. Ambient ultrafine particle (PM0.1): Sources, characteristics, measurements and exposure implications on human health. *Environmental Research* **218**, 115061 (2023).
8. Kadam, V. V., Wang, L. & Padhye, R. Electrospun nanofibre materials to filter air pollutants – A review: *Journal of Industrial Textiles* (2016) doi:10.1177/1528083716676812.
9. Marval, J. & Tronville, P. Ultrafine particles: A review about their health effects, presence, generation, and measurement in indoor environments. *Building and Environment* **216**, 108992 (2022).

10. Zhang, J. *et al.* Adverse effects of exposure to fine particles and ultrafine particles in the environment on different organs of organisms. *Journal of Environmental Sciences* **135**, 449–473 (2024).
11. Chen, R. *et al.* Beyond PM2.5: The role of ultrafine particles on adverse health effects of air pollution. *Biochimica et Biophysica Acta (BBA) - General Subjects* **1860**, 2844–2855 (2016).
12. Presto, A. A., Saha, P. K. & Robinson, A. L. Past, present, and future of ultrafine particle exposures in North America. *Atmospheric Environment: X* **10**, 100109 (2021).
13. Zhu, N. *et al.* A Novel Coronavirus from Patients with Pneumonia in China, 2019. *New England Journal of Medicine* (2020) doi:10.1056/NEJMoa2001017.
14. Morawska, L. *et al.* Size distribution and sites of origin of droplets expelled from the human respiratory tract during expiratory activities. *Journal of Aerosol Science* **40**, 256–269 (2009).
15. Morawska, L. & Cao, J. Airborne transmission of SARS-CoV-2: The world should face the reality. *Environment International* **139**, 105730 (2020).
16. Wang, W., Kang, S., Zhou, W. & Vikesland, P. J. Environmental routes of virus transmission and the application of nanomaterial-based sensors for virus detection. *Environ. Sci.: Nano* **10**, 393–423 (2023).
17. Dash, P. *et al.* Sequence analysis of Indian SARS-CoV-2 isolates shows a stronger interaction of mutant receptor-binding domain with ACE2. *International Journal of Infectious Diseases* **104**, 491–500 (2021).
18. El-Shabasy, R. M. *et al.* Three waves changes, new variant strains, and vaccination effect against COVID-19 pandemic. *International Journal of Biological Macromolecules* **204**, 161–168 (2022).
19. Xu, Z., Liu, K. & Gao, G. F. Omicron variant of SARS-CoV-2 imposes a new challenge for the global public health. *Biosafety and Health* (2022) doi:10.1016/j.bsheal.2022.01.002.
20. Faria, N. R. *et al.* Genomics and epidemiology of the P.1 SARS-CoV-2 lineage in Manaus, Brazil. *Science* **372**, 815–821 (2021).
21. Iacobucci, G. Covid-19: New UK variant may be linked to increased death rate, early data indicate. *BMJ* **372**, n230 (2021).
22. Tegally, H. *et al.* Detection of a SARS-CoV-2 variant of concern in South Africa. *Nature* **592**, 438–443 (2021).
23. Castaño, N. *et al.* Fomite Transmission, Physicochemical Origin of Virus–Surface Interactions, and Disinfection Strategies for Enveloped Viruses with Applications to SARS-CoV-2. *ACS Omega* **6**, 6509–6527 (2021).
24. Leung, W. W. F. & Sun, Q. Charged PVDF multilayer nanofiber filter in filtering simulated airborne novel coronavirus (COVID-19) using ambient nano-aerosols. *Separation and Purification Technology* **245**, 116887 (2020).
25. Tian, Y. *et al.* Study on the Collection Efficiency of Bioaerosol Nanoparticles by Andersen-Type Impactors. *J Biomed Nanotechnol* 319–326 (2022).
26. Lee, B. U. Minimum Sizes of Respiratory Particles Carrying SARS-CoV-2 and the Possibility of Aerosol Generation. *International Journal of Environmental Research and Public Health* **17**, 6960 (2020).
27. Kwon, T., Osterrieder, N., Gaudreault, N. N. & Richt, J. A. Fomite Transmission of SARS-CoV-2 and Its Contributing Factors. *Pathogens* **12**, 364 (2023).
28. Asadi, S. *et al.* Influenza A virus is transmissible via aerosolized fomites. *Nat Commun* **11**, 4062 (2020).
29. Ganczak, M., Pasek, O., Duda – Duma, Ł., Świstara, D. & Korzeń, M. Use of masks in public places in Poland during SARS-Cov-2 epidemic: a covert observational study. *BMC Public Health* **21**, 393 (2021).
30. Ippolito, M. *et al.* Medical masks and Respirators for the Protection of Healthcare Workers from SARS-CoV-2 and other viruses. *Pulmonology* **26**, 204–212 (2020).
31. Selvaranjan, K., Navaratnam, S., Rajeev, P. & Ravintherakumaran, N. Environmental challenges induced by extensive use of face masks during COVID-19: A review and potential solutions. *Environmental Challenges* **3**, 100039 (2021).
32. Oliveira, A. E. de *et al.* Physical Barrier against COVID-19: Materials to Inhibit or Eliminate the Virus. in *Living with COVID-19* (Jenny Stanford Publishing, 2021).
33. Cheng, Y. *et al.* Face masks effectively limit the probability of SARS-CoV-2 transmission. *Science* **372**, 1439–1443 (2021).
34. Lindsley, W. G., Blachere, F. M., Law, B. F., Beezhold, D. H. & Noti, J. D. Efficacy of face masks, neck gaiters and face shields for reducing the expulsion of simulated cough-generated aerosols. *Aerosol Science and Technology* **55**, 449–457 (2021).
35. Booth, M. C., Clayton, M., Crook, B. & Gawn, J. M. Effectiveness of surgical masks against influenza bioaerosols. *Journal of Hospital Infection* **84**, 22–26 (2013).
36. Suess, T. *et al.* The role of facemasks and hand hygiene in the prevention of influenza transmission in households: results from a cluster randomised trial; Berlin, Germany, 2009-2011. *BMC Infect Dis* **12**, 26 (2012).
37. Aydin, O. *et al.* Performance of fabrics for home-made masks against the spread of COVID-19 through droplets: A quantitative mechanistic study. *Extreme Mechanics Letters* **40**, 100924 (2020).
38. Crilley, L. R. *et al.* Non-woven materials for cloth-based face masks inserts: relationship between material properties and sub-micron aerosol filtration. *Environ. Sci.: Nano* **8**, 1603–1613 (2021).
39. Morais, F. G. *et al.* Filtration efficiency of a large set of COVID-19 face masks commonly used in Brazil. *Aerosol Science and Technology* **0**, 1–21 (2021).
40. Aragaw, T. A. Surgical face masks as a potential source for microplastic pollution in the COVID-19 scenario. *Marine Pollution Bulletin* **159**, 111517 (2020).
41. Anastopoulos, I. & Pashalidis, I. Single-use surgical face masks, as a potential source of microplastics: Do they act as pollutant carriers? *Journal of Molecular Liquids* **326**, 115247 (2021).
42. Fadare, O. O. & Okoffo, E. D. Covid-19 face masks: A potential source of microplastic fibers in the environment. *Science of The Total Environment* **737**, 140279 (2020).
43. Ma, M., Xu, D., Zhao, J. & Gao, B. Disposable face masks release micro particles to the aqueous environment after simulating sunlight aging: Microplastics or non-microplastics? *Journal of Hazardous Materials* **443**, 130146 (2023).
44. Pfohl, P. *et al.* Environmental Degradation of Microplastics: How to Measure Fragmentation Rates to Secondary Micro- and Nanoplastic Fragments and Dissociation into Dissolved Organics. *Environ. Sci. Technol.* **56**, 11323–11334 (2022).
45. Li, J., Zhang, K. & Zhang, H. Adsorption of antibiotics on microplastics. *Environmental Pollution* **237**, 460–467 (2018).
46. Godoy, V., Blázquez, G., Calero, M., Quesada, L. & Martín-Lara, M. A. The potential of microplastics as carriers of metals. *Environmental Pollution* **255**, 113363 (2019).

47. Oz, N., Kadİzade, G. & Yurtsever, M. Investigation of heavy metal adsorption on microplastics. *Applied Ecology and Environmental Research* **17**, 7301–7310 (2019).
48. Hartmann, N. B. *et al.* Microplastics as vectors for environmental contaminants: Exploring sorption, desorption, and transfer to biota. *Integrated Environmental Assessment and Management* **13**, 488–493 (2017).
49. Shao, L. *et al.* Airborne microplastics: A review of current perspectives and environmental implications. *Journal of Cleaner Production* **347**, 131048 (2022).
50. Akhbarizadeh, R. *et al.* Suspended fine particulate matter (PM2.5), microplastics (MPs), and polycyclic aromatic hydrocarbons (PAHs) in air: Their possible relationships and health implications. *Environmental Research* **192**, 110339 (2021).
51. Brahney, J. *et al.* Constraining the atmospheric limb of the plastic cycle. *Proceedings of the National Academy of Sciences* **118**, e2020719118 (2021).
52. Aeschlimann, M., Li, G., Kanji, Z. A. & Mitrano, D. M. Potential impacts of atmospheric microplastics and nanoplastics on cloud formation processes. *Nat. Geosci.* **15**, 967–975 (2022).
53. Revell, L. E., Kuma, P., Le Ru, E. C., Somerville, W. R. C. & Gaw, S. Direct radiative effects of airborne microplastics. *Nature* **598**, 462–467 (2021).
54. Allen, D. *et al.* Temporal Archive of Atmospheric Microplastic Deposition Presented in Ombrotrophic Peat. *Environ. Sci. Technol. Lett.* **8**, 954–960 (2021).
55. Brahney, J., Hallerud, M., Heim, E., Hahnenberger, M. & Sukumaran, S. Plastic rain in protected areas of the United States. *Science* **368**, 1257–1260 (2020).
56. Amato-Lourenço, L. F. *et al.* Presence of airborne microplastics in human lung tissue. *Journal of Hazardous Materials* **416**, 126124 (2021).
57. Goodman, K. E., Hare, J. T., Khamis, Z. I., Hua, T. & Sang, Q.-X. A. Exposure of Human Lung Cells to Polystyrene Microplastics Significantly Retards Cell Proliferation and Triggers Morphological Changes. *Chem. Res. Toxicol.* **34**, 1069–1081 (2021).
58. Singh, S. *et al.* How an outbreak became a pandemic: a chronological analysis of crucial junctures and international obligations in the early months of the COVID-19 pandemic. *The Lancet* **398**, 2109–2124 (2021).
59. Babaahmadi, V., Amid, H., Naeimirad, M. & Ramakrishna, S. Biodegradable and multifunctional surgical face masks: A brief review on demands during COVID-19 pandemic, recent developments, and future perspectives. *Science of The Total Environment* **798**, 149233 (2021).
60. Bian, Y., Zhang, C., Wang, H. & Cao, Q. Degradable nanofiber for eco-friendly air filtration: Progress and perspectives. *Separation and Purification Technology* **306**, 122642 (2023).
61. Souzandeh, H., Wang, Y., Netravali, A. N. & Zhong, W.-H. Towards Sustainable and Multifunctional Air-Filters: A Review on Biopolymer-Based Filtration Materials. *Polymer Reviews* **59**, 651–686 (2019).
62. Sun, B. *et al.* In Situ Biosynthesis of Biodegradable Functional Bacterial Cellulose for High-Efficiency Particulate Air Filtration. *ACS Sustainable Chem. Eng.* **10**, 1644–1652 (2022).
63. Wang, Z. *et al.* Antibacterial and environmentally friendly chitosan/polyvinyl alcohol blend membranes for air filtration. *Carbohydrate Polymers* **198**, 241–248 (2018).
64. Bonfim, D. P. F., Cruz, F. G. S., Bretas, R. E. S., Guerra, V. G. & Aguiar, M. L. A Sustainable Recycling Alternative: Electrospun PET-Membranes for Air Nanofiltration. *Polymers* **13**, 1166 (2021).
65. Leung, W. W. F. & Sun, Q. Electrostatic charged nanofiber filter for filtering airborne novel coronavirus (COVID-19) and nano-aerosols. *Separation and Purification Technology* **250**, 116886 (2020).
66. Li, H.-W., Wu, C.-Y., Tepper, F., Lee, J.-H. & Lee, C. N. Removal and retention of viral aerosols by a novel alumina nanofiber filter. *Journal of Aerosol Science* **40**, 65–71 (2009).
67. Matulevicius, J. *et al.* Design and Characterization of Electrospun Polyamide Nanofiber Media for Air Filtration Applications. *Journal of Nanomaterials* **2014**, e859656 (2014).
68. Thakur, V. K. *Nanocellulose Polymer Nanocomposites: Fundamentals and Applications*. (John Wiley & Sons, 2014).
69. Xia, T., Bian, Y., Zhang, L. & Chen, C. Relationship between pressure drop and face velocity for electrospun nanofiber filters. *Energy and Buildings* **158**, 987–999 (2018).
70. Konda, A. *et al.* Aerosol Filtration Efficiency of Common Fabrics Used in Respiratory Cloth Masks. *ACS Nano* **14**, 6339–6347 (2020).
71. Das, O. *et al.* The need for fully bio-based facemasks to counter coronavirus outbreaks: A perspective. *Science of The Total Environment* **736**, 139611 (2020).
72. Wang, L. *et al.* Biodegradable and high-performance multiscale structured nanofiber membrane as mask filter media via poly(lactic acid) electrospinning. *Journal of Colloid and Interface Science* **606**, 961–970 (2022).
73. Patil, N. A. *et al.* Needleless electrospun phytochemicals encapsulated nanofibre based 3-ply biodegradable mask for combating COVID-19 pandemic. *Chemical Engineering Journal* **416**, 129152 (2021).
74. Geng, X., Kwon, O.-H. & Jang, J. Electrospinning of chitosan dissolved in concentrated acetic acid solution. *Biomaterials* **26**, 5427–5432 (2005).
75. Meli, L., Miao, J., Dordick, J. S. & Linhardt, R. J. Electrospinning from room temperature ionic liquids for biopolymer fiber formation. *Green Chem.* **12**, 1883–1892 (2010).
76. Zhang, B. *et al.* Chitosan nanostructures by in situ electrospinning for high-efficiency PM2.5 capture. *Nanoscale* **9**, 4154–4161 (2017).
77. Almeida, D. S. *et al.* Biodegradable CA/CPB electrospun nanofibers for efficient retention of airborne nanoparticles. *Process Safety and Environmental Protection* **144**, 177–185 (2020).
78. Mata, G. C. da, Morais, M. S., Oliveira, W. P. de & Aguiar, M. L. Composition Effects on the Morphology of PVA/Chitosan Electrospun Nanofibers. *Polymers* **14**, 4856 (2022).
79. Morais, M. S., Bonfim, D. P. F., Aguiar, M. L. & Oliveira, W. P. Electrospun Poly (Vinyl Alcohol) Nanofibrous Mat Loaded with Green Propolis Extract, Chitosan and Nystatin as an Innovative Wound Dressing Material. *Journal of Pharmaceutical Innovation* 1–15 (2022) doi:10.1007/s12247-022-09681-7.
80. Vu, T. H. N., Morozkina, S. N. & Uspenskaya, M. V. Study of the Nanofibers Fabrication Conditions from the Mixture of Poly(vinyl alcohol) and Chitosan by Electrospinning Method. *Polymers* **14**, 811 (2022).

81. Panda, P. K., Sadeghi, K. & Seo, J. Recent advances in poly (vinyl alcohol)/natural polymer based films for food packaging applications: A review. *Food Packaging and Shelf Life* **33**, 100904 (2022).
82. Duru Kamaci, U. & Peksel, A. Fabrication of PVA-chitosan-based nanofibers for phytase immobilization to enhance enzymatic activity. *International Journal of Biological Macromolecules* **164**, 3315–3322 (2020).
83. Abbas, W. A., Sharafeldin, I. M., Omar, M. M. & Allam, N. K. Novel mineralized electrospun chitosan/PVA/TiO2 nanofibrous composites for potential biomedical applications: computational and experimental insights. *Nanoscale Advances* **2**, 1512–1522 (2020).
84. Rieger, K. A., Birch, N. P. & Schiffman, J. D. Designing electrospun nanofiber mats to promote wound healing – a review. *J. Mater. Chem. B* **1**, 4531–4541 (2013).
85. Bonfim, D. P. F., Cruz, F. G. S., Guerra, V. G. & Aguiar, M. L. Development of Filter Media by Electrospinning for Air Filtration of Nanoparticles from PET Bottles. *Membranes* **11**, 293 (2021).
86. Bortolassi, A. C. C. *et al.* Efficient nanoparticles removal and bactericidal action of electrospun nanofibers membranes for air filtration. *Mater Sci Eng C Mater Biol Appl* **102**, 718–729 (2019).
87. Baldim, I., Paziani, M. H., Grizante Barião, P. H., Kress, M. R. von Z. & Oliveira, W. P. Nanostructured Lipid Carriers Loaded with Lippia sidoides Essential Oil as a Strategy to Combat the Multidrug-Resistant Candida auris. *Pharmaceutics* **14**, 180 (2022).
88. Baldim, I., Tonani, L., von Zeska Kress, M. R. & Pereira Oliveira, W. Lippia sidoides essential oil encapsulated in lipid nanosystem as an anti-Candida agent. *Industrial Crops and Products* **127**, 73–81 (2019).
89. Rathod, N. B., Kulawik, P., Ozogul, F., Regenstein, J. M. & Ozogul, Y. Biological activity of plant-based carvacrol and thymol and their impact on human health and food quality. *Trends in Food Science & Technology* **116**, 733–748 (2021).
90. Bhattacharya, S. *Central Composite Design for Response Surface Methodology and Its Application in Pharmacy*. *Response Surface Methodology in Engineering Science* (IntechOpen, 2021). doi:10.5772/intechopen.95835.
91. He, H., Wang, Y., Farkas, B., Nagy, Z. K. & Molnar, K. Analysis and prediction of the diameter and orientation of AC electrospun nanofibers by response surface methodology. *Materials & Design* **194**, 108902 (2020).
92. Breig, S. J. M. & Luti, K. J. K. Response surface methodology: A review on its applications and challenges in microbial cultures. *Materials Today: Proceedings* **42**, 2277–2284 (2021).
93. Yördem, O. S., Papila, M. & Menceloğlu, Y. Z. Effects of electrospinning parameters on polyacrylonitrile nanofiber diameter: An investigation by response surface methodology. *Materials & Design* **29**, 34–44 (2008).
94. Souza, C., Bott, R. & Oliveira, W. Optimization of the extraction of flavonoids compounds from herbal material using experimental design and multi-response analysis. *LATIN AMERICAN JOURNAL OF PHARMACY* **26**, 682 (2007).
95. Das, D., Das, S. & Ishtiaque, S. M. Optimal design of nonwoven air filter media: Effect of fibre shape. *Fibers Polym* **15**, 1456–1461 (2014).
96. Costa, N. R., Lourenço, J. & Pereira, Z. L. Desirability function approach: A review and performance evaluation in adverse conditions. *Chemometrics and Intelligent Laboratory Systems* **107**, 234–244 (2011).
97. Jeong, I.-J. & Kim, K.-J. An interactive desirability function method to multiresponse optimization. *European Journal of Operational Research* **195**, 412–426 (2009).
98. Souza, A. M. de *et al.* Application of the desirability function for the development of new composite eco-efficiency indicators for concrete. *Journal of Building Engineering* **40**, 102374 (2021).
99. Varatharajulu, M. *et al.* Evaluation of Desirability Function Approach and Genetic Algorithm optimization of drilling characteristics on Duplex 2205. *Materials Today: Proceedings* **22**, 589–600 (2020).
100. Bortolassi, A. C. C., Guerra, V. G. & Aguiar, M. L. Characterization and evaluate the efficiency of different filter media in removing nanoparticles. *Separation and Purification Technology* **175**, 79–86 (2017).
101. Vajda, J., Weber, D., Brekel, D., Hundt, B. & Müller, E. Size distribution analysis of influenza virus particles using size exclusion chromatography. *Journal of Chromatography A* **1465**, 117–125 (2016).
102. Scheuch, G. Breathing Is Enough: For the Spread of Influenza Virus and SARS-CoV-2 by Breathing Only. *Journal of Aerosol Medicine and Pulmonary Drug Delivery* **33**, 230–234 (2020).
103. Jilani, T. N., Jamil, R. T. & Siddiqui, A. H. H1N1 Influenza. in *StatPearls* (StatPearls Publishing, 2022).
104. de Barros, P. M., Rodrigues Cirqueira, S. S. & Aguiar, M. L. Evaluation of the Deposition of Nanoparticles in Fibrous Filter. *Materials Science Forum* **802**, 174–179 (2014).
105. Granato, D. & Ares, G. *Mathematical and Statistical Methods in Food Science and Technology*. (John Wiley & Sons, 2014).
106. Homayoni, H., Ravandi, S. A. H. & Valizadeh, M. Electrospinning of chitosan nanofibers: Processing optimization. *Carbohydrate Polymers* **77**, 656–661 (2009).
107. Bhattarai, N., Edmondson, D., Veiseh, O., Matsen, F. A. & Zhang, M. Electrospun chitosan-based nanofibers and their cellular compatibility. *Biomaterials* **26**, 6176–6184 (2005).
108. Balgis, R. *et al.* Synthesis and evaluation of straight and bead-free nanofibers for improved aerosol filtration. *Chemical Engineering Science* **137**, 947–954 (2015).
109. Kravtsov, A., Brnig, H., Zhandarov, S. & Beyreuther, R. The electret effect in polypropylene fibers treated in a corona discharge. in (2000). doi:10.1002/1098-2329(200024)19:4<312::AID-ADV7>3.0.CO;2-X.
110. Lv, D. *et al.* Green Electrospun Nanofibers and Their Application in Air Filtration. *Macromolecular Materials and Engineering* **303**, 1800336 (2018).
111. Zhu, M. *et al.* Electrospun Nanofibers Membranes for Effective Air Filtration. *Macromolecular Materials and Engineering* **302**, 1600353 (2017).
112. Zhu, M. *et al.* A novel cellulose acetate/poly (ionic liquid) composite air filter. *Cellulose* **27**, 3889–3902 (2020).
113. Leung, W. W.-F., Hung, C.-H. & Yuen, P.-T. Effect of face velocity, nanofiber packing density and thickness on filtration performance of filters with nanofibers coated on a substrate. *Separation and Purification Technology* **71**, 30–37 (2010).
114. Bucher, T. M., Tafreshi, H. V. & Tepper, G. C. Modeling performance of thin fibrous coatings with orthogonally layered nanofibers for improved aerosol filtration. *Powder Technology* **249**, 43–53 (2013).
115. Gao, H. *et al.* A low filtration resistance three-dimensional composite membrane fabricated via free surface electrospinning for effective PM2.5 capture. *Environ. Sci.: Nano* **4**, 864–875 (2017).

116. Medeiros, G. B. *et al.* Experimental design to evaluate properties of electrospun fibers of zein/poly (ethylene oxide) for biomaterial applications. *Journal of Applied Polymer Science* **138**, 50898 (2021).
117. Bellan, L. M. & Craighead, H. G. Control of an electrospinning jet using electric focusing and jet-steering fields. *Journal of Vacuum Science & Technology B: Microelectronics and Nanometer Structures Processing, Measurement, and Phenomena* **24**, 3179–3183 (2006).
118. Mamtha, V., Narasimha Murthy, H. N., Authade, P. & Sridhar, R. Study of Electrospun fiber diameter using ANSOFT and ANSYS. *Materials Today: Proceedings* **5**, 21529–21537 (2018).
119. Sahay, R., Thavasi, V. & Ramakrishna, S. Design Modifications in Electrospinning Setup for Advanced Applications. *Journal of Nanomaterials* **2011**, e317673 (2011).
120. Ura, D. P. *et al.* The Role of Electrical Polarity in Electrospinning and on the Mechanical and Structural Properties of As-Spun Fibers. *Materials* **13**, 4169 (2020).
121. Lee, D.-H., Jeong, I.-J. & Kim, K.-J. A desirability function method for optimizing mean and variability of multiple responses using a posterior preference articulation approach. *Quality and Reliability Engineering International* **34**, 360–376 (2018).
122. ABNT NBR 15052. Máscara de uso odonto-médico-hospitalar - Requisitos e métodos de ensaio. https://www.abntcatalogo.com.br/pnm.aspx?Q=UEQyTEsvQUVVYmV2WWVNVU9KS1Y4WHRzY2JLV2c0QkZKVStpMGtMMVNWbz0= (2021).
123. ASTM F2100. Standard Specification for Performance of Materials Used in Medical Face Masks. https://www.astm.org/f2100-21.html (2019).
124. EN 14683. Medical face masks - Requirements and test methods. *Scandia Gear - Maritime Outfitters since 1974* https://www.scandiagear.com/quality/norms-and-standards/personal-protection/en14683-2019/ (2019).
125. Mele, E. Electrospinning of natural polymers for advanced wound care: towards responsive and adaptive dressings. *J. Mater. Chem. B* **4**, 4801–4812 (2016).
126. Vineis, C. & Varesano, A. 14 - Natural polymer-based electrospun fibers for antibacterial uses. in *Electrofluidodynamic Technologies (EFDTs) for Biomaterials and Medical Devices* (eds. Guarino, V. & Ambrosio, L.) 275–294 (Woodhead Publishing, 2018). doi:10.1016/B978-0-08-101745-6.00014-1.
127. Soares, R. M. D., Siqueira, N. M., Prabhakaram, M. P. & Ramakrishna, S. Electrospinning and electrospray of bio-based and natural polymers for biomaterials development. *Materials Science and Engineering: C* **92**, 969–982 (2018).
128. Chagas, P. A. M. *et al.* Bilayered electrospun membranes composed of poly(lactic-acid)/natural rubber: A strategy against curcumin photodegradation for wound dressing application. *Reactive and Functional Polymers* **163**, 104889 (2021).
129. Nadaf, A. *et al.* Recent update on electrospinning and electrospun nanofibers: current trends and their applications. *RSC Advances* **12**, 23808–23828 (2022).
130. Al-Abduljabbar, A. & Farooq, I. Electrospun Polymer Nanofibers: Processing, Properties, and Applications. *Polymers* **15**, 65 (2023).
131. Majumder, S., Hassan Sagor, M. M. & Tarik Arafat, M. Functional electrospun polymeric materials for bioelectronic devices: a review. *Materials Advances* **3**, 6753–6772 (2022).
132. Medeiros, G. B., Lima, F. de A., de Almeida, D. S., Guerra, V. G. & Aguiar, M. L. Modification and Functionalization of Fibers Formed by Electrospinning: A Review. *Membranes* **12**, 861 (2022).
133. Rashid, T. U., Gorga, R. E. & Krause, W. E. Mechanical Properties of Electrospun Fibers—A Critical Review. *Advanced Engineering Materials* **23**, 2100153 (2021).
134. Selatile, K., Ray, S. S., Ojijo, V. & Sadiku, R. E. Morphological, Thermal, and Mechanical Properties of Electrospun Recycled Poly(ethylene terephthalate)/Graphene Oxide Composite Nanofiber Membranes. *ACS Omega* **6**, 21005–21015 (2021).
135. Can-Herrera, L. A., Oliva, A. I., Dzul-Cervantes, M. a. A., Pacheco-Salazar, O. F. & Cervantes-Uc, J. M. Morphological and Mechanical Properties of Electrospun Polycaprolactone Scaffolds: Effect of Applied Voltage. *Polymers* **13**, 662 (2021).
136. Sharpe, J. M., Lee, H., Hall, A. R., Bonin, K. & Guthold, M. Mechanical Properties of Electrospun, Blended Fibrinogen: PCL Nanofibers. *Nanomaterials (Basel)* **10**, 1843 (2020).
137. Nauman, S., Lubineau, G. & Alharbi, H. F. Post Processing Strategies for the Enhancement of Mechanical Properties of ENMs (Electrospun Nanofibrous Membranes): A Review. *Membranes (Basel)* **11**, 39 (2021).

4.6 Supplementary Material

Table 4.S1: Regression equation models obtained by the Central Composite Desing, analyzed with the Response Surface Methodology, for the responses of Collection (η), Permeability Constant (K1), and Quality Factor (Q_F).

Response		Model	p-value	Equation
η (%)	=	-275 + 29.44 Field (kV) - 93.6 Flow Rate (mL/h) + 2.11 Time (min) - 0.602 Field (kV)*Field (kV) - 26.9 Flow Rate (mL/h)*Flow Rate (mL/h) - 0.01300 Time (min)*Time (min) + 3.88 Field (kV)*Flow Rate (mL/h) - 0.0697 Field (kV)*Time (min) + 1.131 Flow Rate (mL/h)*Time (min)	0.000	(S1)
K1 (μm²)	=	141 - 6.8 Field (kV) + 98.1 Flow Rate (mL/h) - 2.20 Time (min) + 0.117 Field (kV)*Field (kV) + 76.9 Flow Rate (mL/h)*Flow Rate (mL/h) + 0.01924 Time (min)*Time (min) - 6.06 Field (kV)*Flow Rate (mL/h) + 0.0680 Field (kV)*Time (min) - 1.901 Flow Rate (mL/h)*Time (min)	0.000	(S2)
Q_F	=	0.044 - 0.00568 Field (kV) + 0.1029 Flow Rate (mL/h) + 0.00125 Time (min) + 0.000140 Field (kV)*Field (kV) - 0.0180 Flow Rate (mL/h)*Flow Rate (mL/h) - 0.000001 Time (min)*Time (min) - 0.00138 Field (kV)*Flow Rate (mL/h) - 0.000034 Field (kV)*Time (min) - 0.000921 Flow Rate (mL/h)*Time (min)	0.002	(S3)

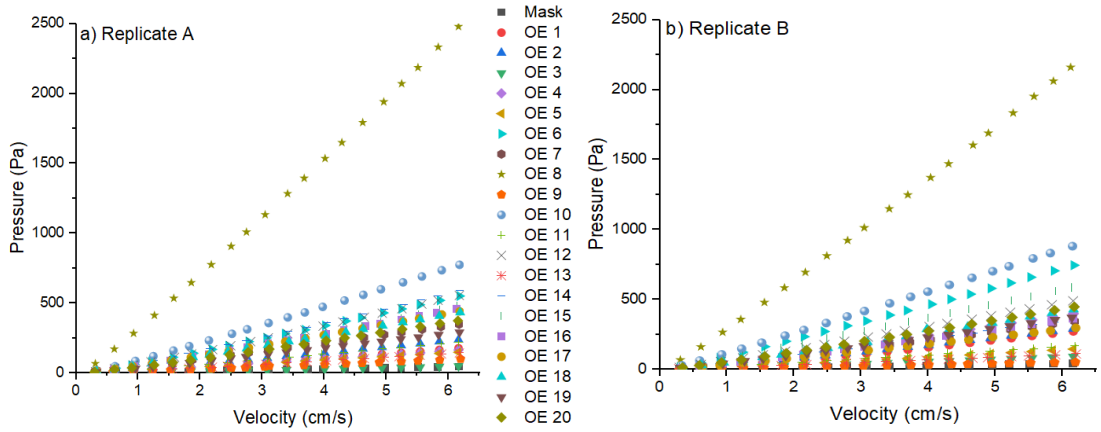

Figure 4.S1: Pressure drop per surface velocity for all the samples of both replicates in the CCD model (A and B).

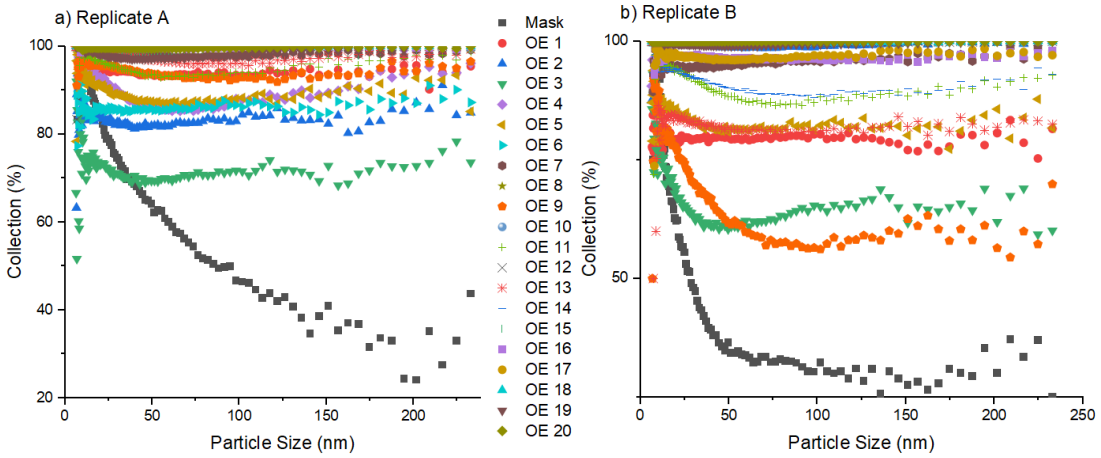

Figure 4.S2: Fractional efficiency curve for all samples of both replicates in the CCD model (A and B).

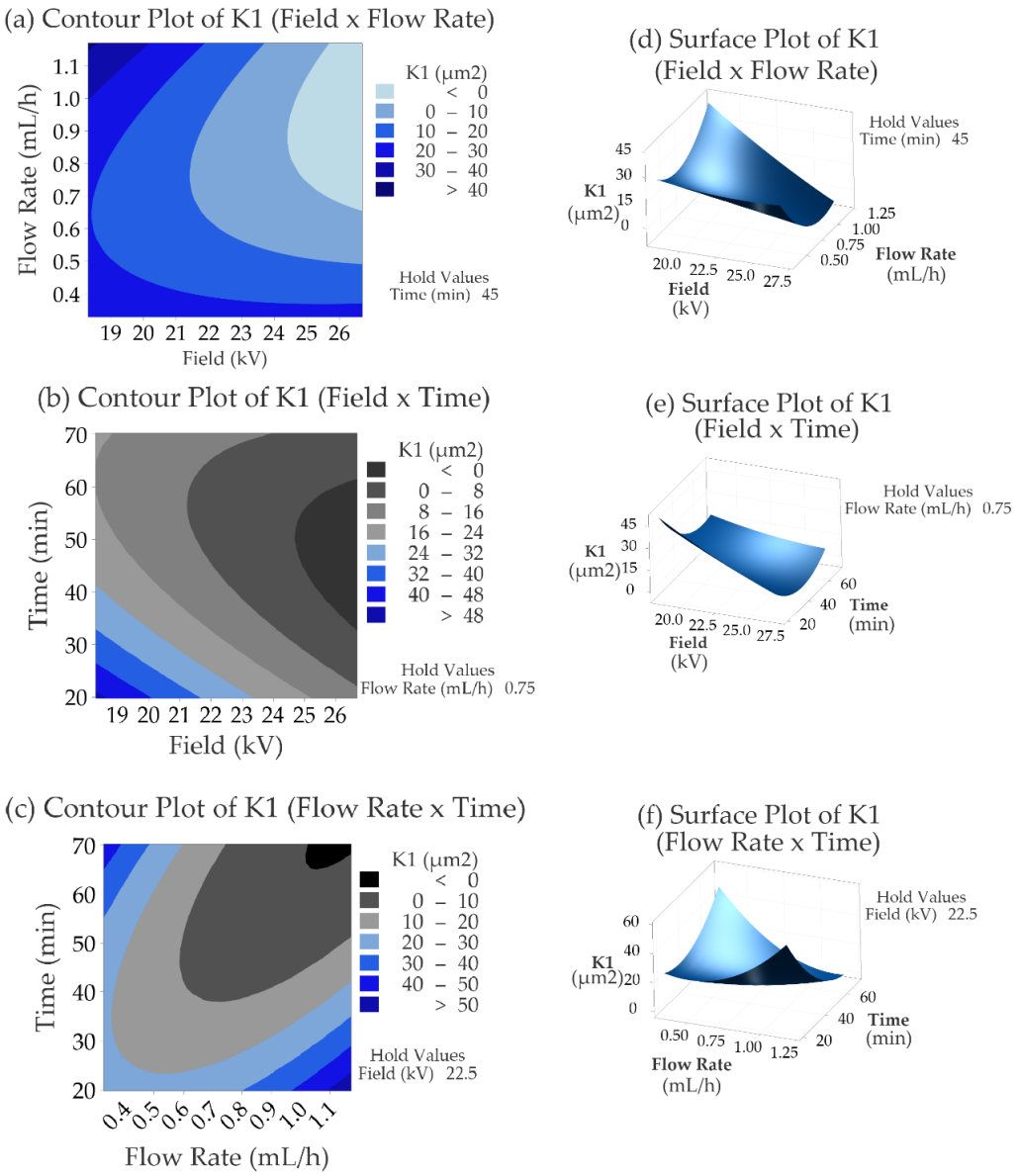

Figure 4.S3: Contour plots for the Permeability Constant (K1) response, taking into consideration the interaction of the parameters: **(a)** electric field × flow rate; **(b)** electric field × time; and **(c)** flow rate × time. (d), (e), and (f) show the surface plot for the same parameter combinations, respectively.

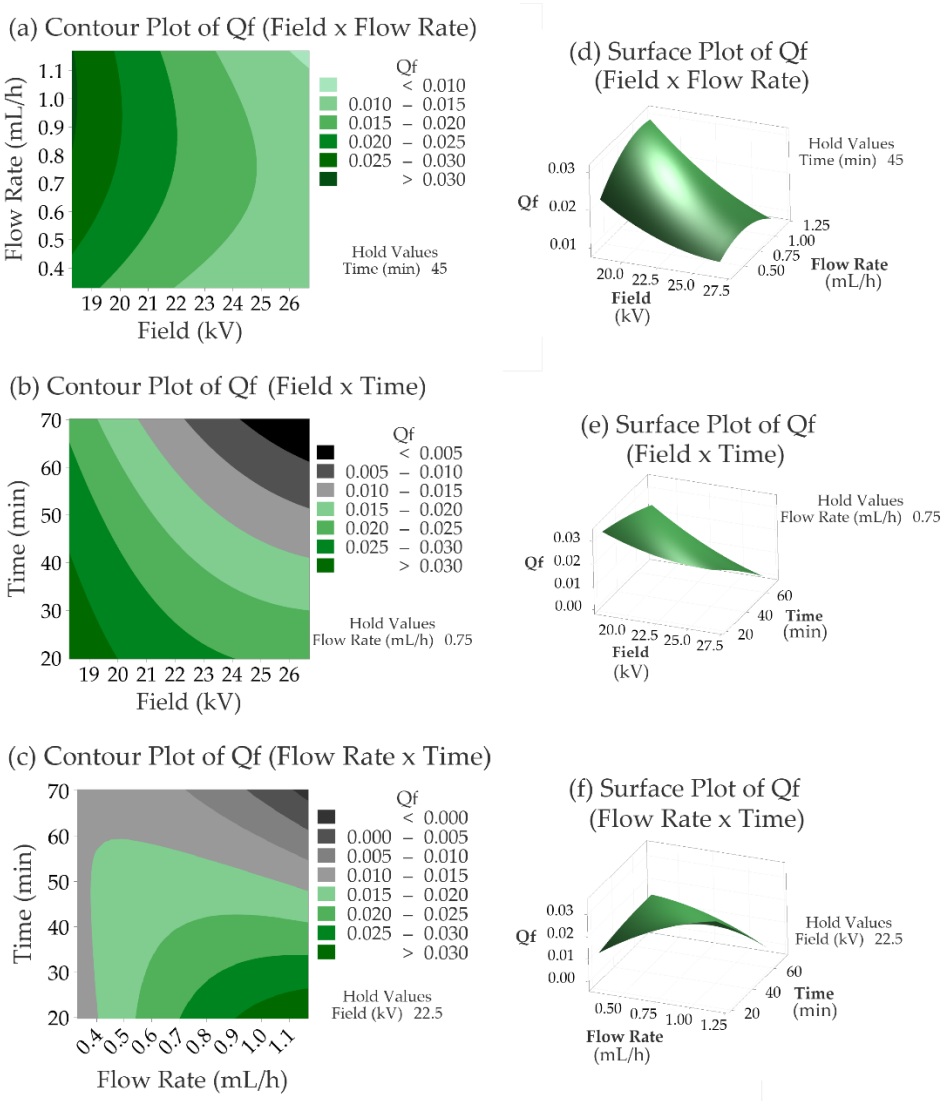

Figure 4.S4: Contour plots for Quality Factor (Q_F) response, taking into consideration the interaction of the parameters: **(a)** electric field × flow rate; **(b)** electric field × time; and **(c)** flow rate × time. (d), (e) and (f) show the surface plot for the same parameter combinations.

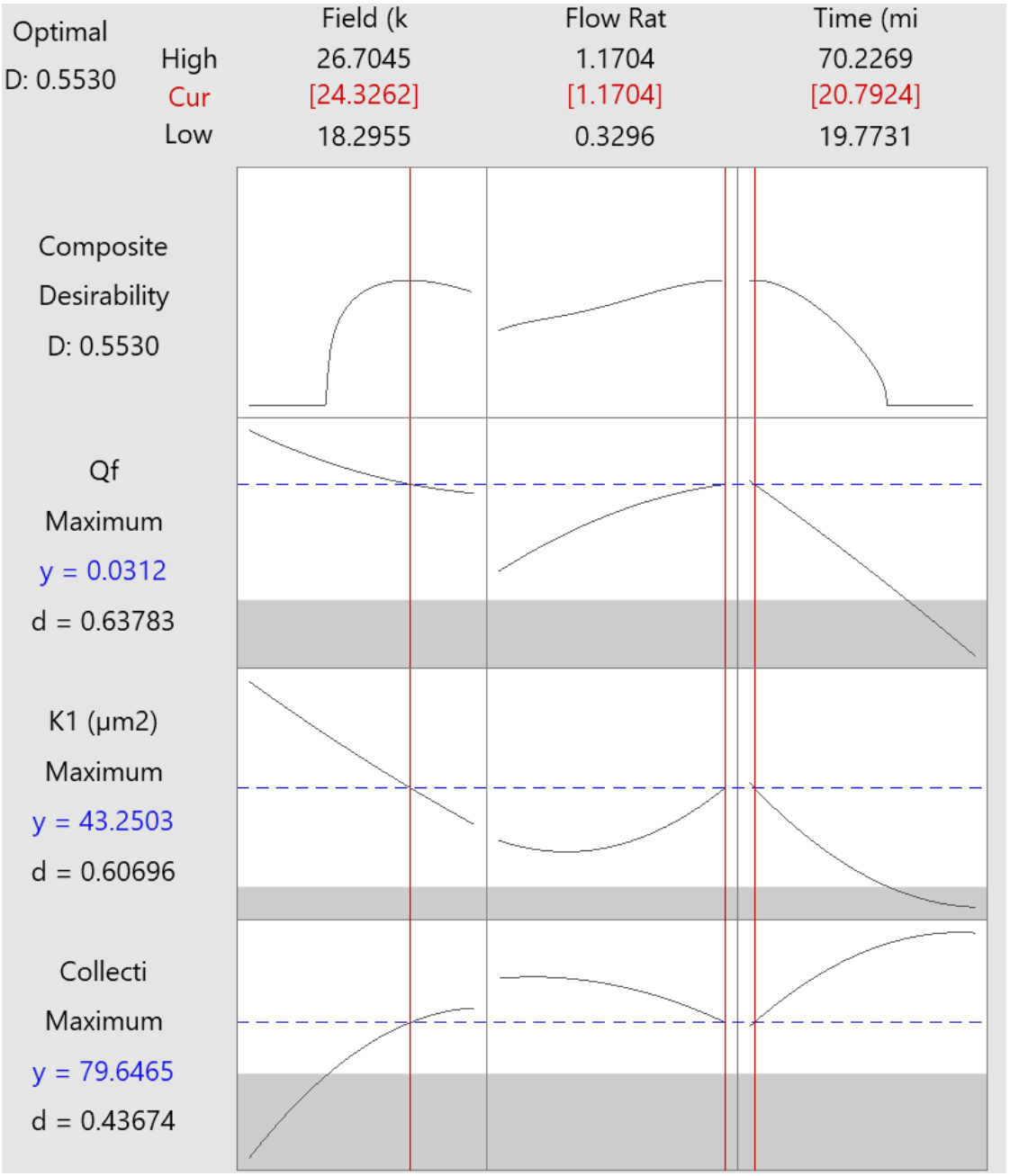

Figure 4.S5: Desirability evaluation, holding the same importance parameters for each response in 1.

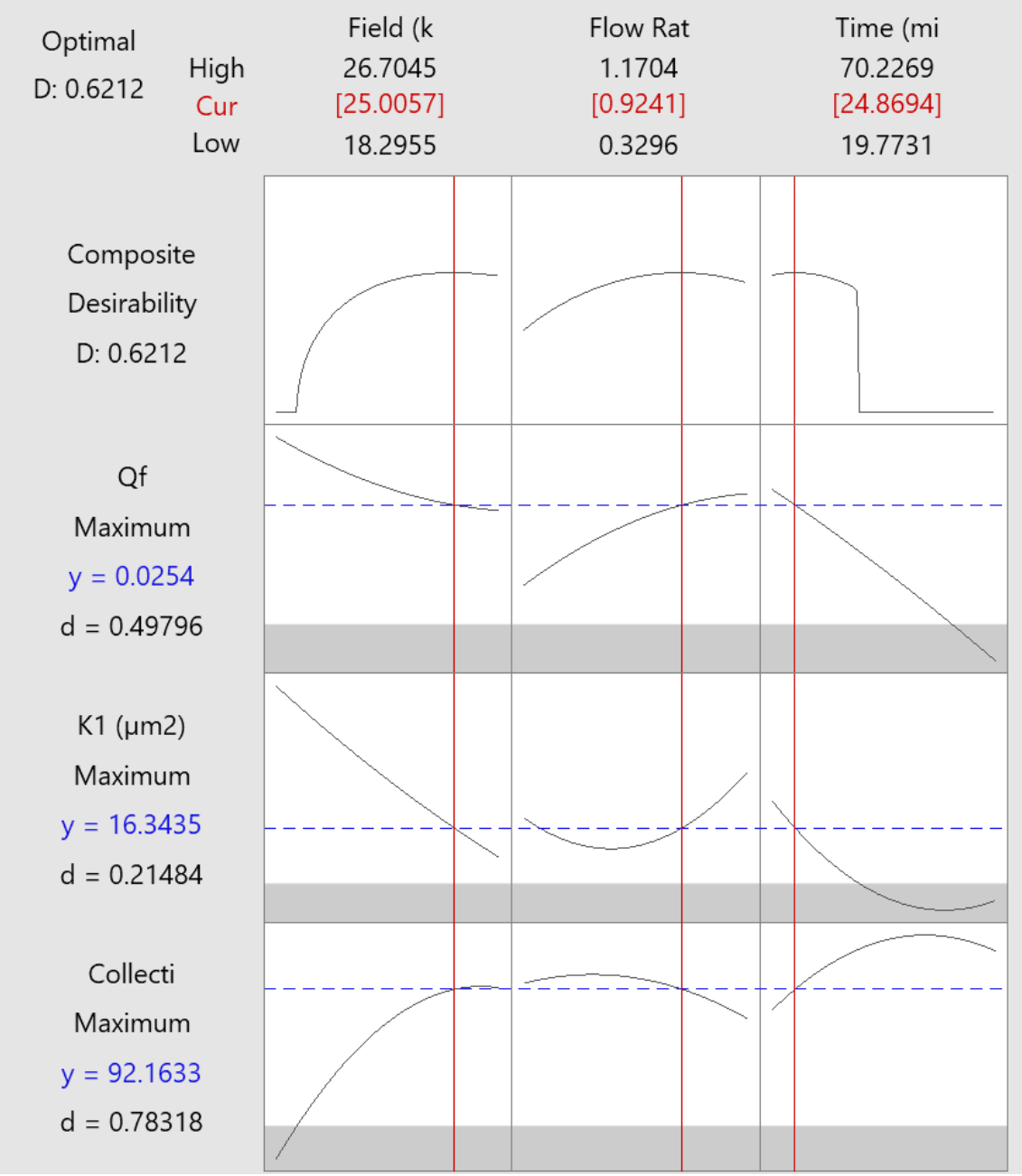

Figure 4.S6: Desirability evaluation, holding the same importance parameters for Quality Factor (Q_F) and Collection Efficiency (η) at the maximum value (10), and decreasing the importance of the Permeability Constant (K1) to the minimum value (0.1).

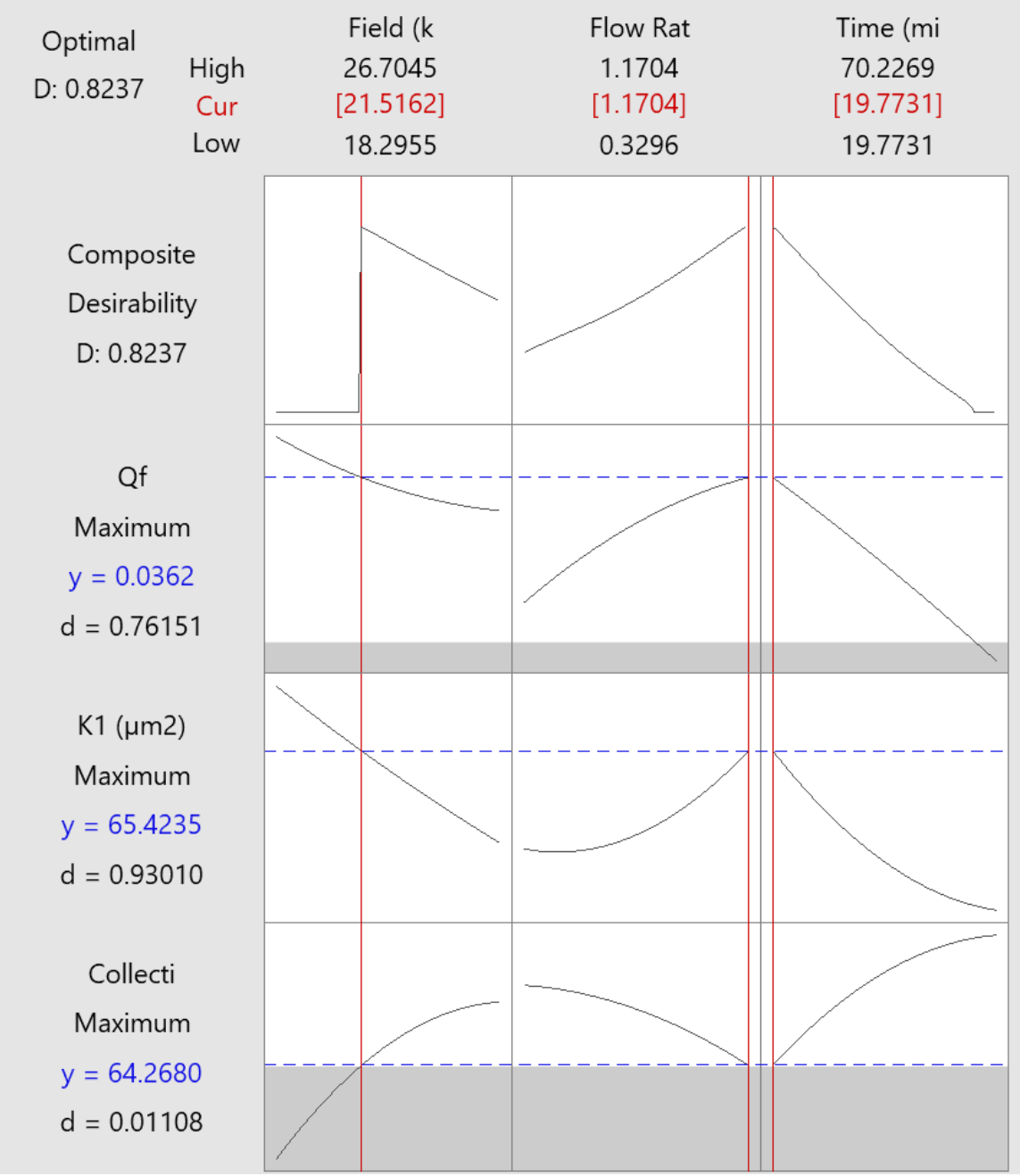

Figure 4.S7: Desirability evaluation, holding the same importance parameters for Quality Factor (Q_F) and Permeability Constant (K1) at the maximum value (10), and decreasing the importance of the Collection Efficiency (η) to the minimum value (0.1).

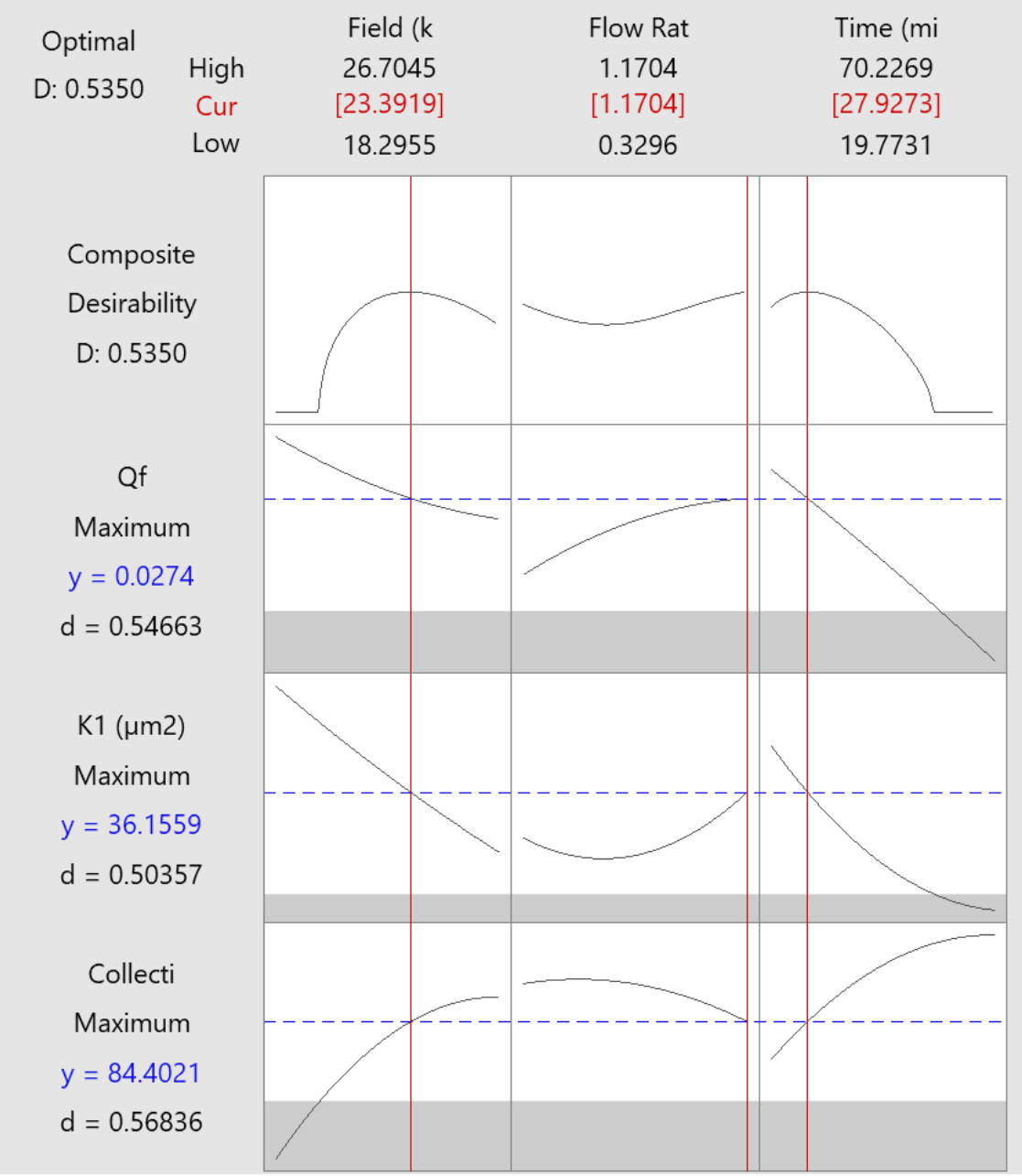

Figure 4.S8: Desirability evaluation, holding the same importance parameters for Collection Efficiency (η) and Permeability Constant (K1) at the maximum value (10) and decreasing the importance of the Quality Factor (Q_F) to the minimum value (0.1).

V

SPIDER-NETS IN AIR FILTRATION I

V - SPIDER-NETS IN AIR FILTRATION I

Spider-Nets in PVA/Chitosan Electrospun Nanofibers and their Influence on Nanoparticles Air Filtration

Gustavo Cardoso Mata[1,*], Maria Sirlene Morais[2], Wanderley Pereira Oliveira[2], Mônica Lopes Aguiar[1,*]

[1] Department of Chemical Engineering, Federal University of São Carlos, Rod. Washington Luiz, km 235, SP310, São Carlos - SP, 13565-905, Brazil;

[2] Faculty of Pharmaceutical Science of Ribeirão Preto, University of São Paulo, Av. do Café s/nº, CEP: 14040-903, Bairro Monte Alegre, Ribeirão Preto, SP, Brazil

[*]*Corresponding authors*: gugs_cardoso@ufsj.edu.br/mlaguiar@ufscar.br

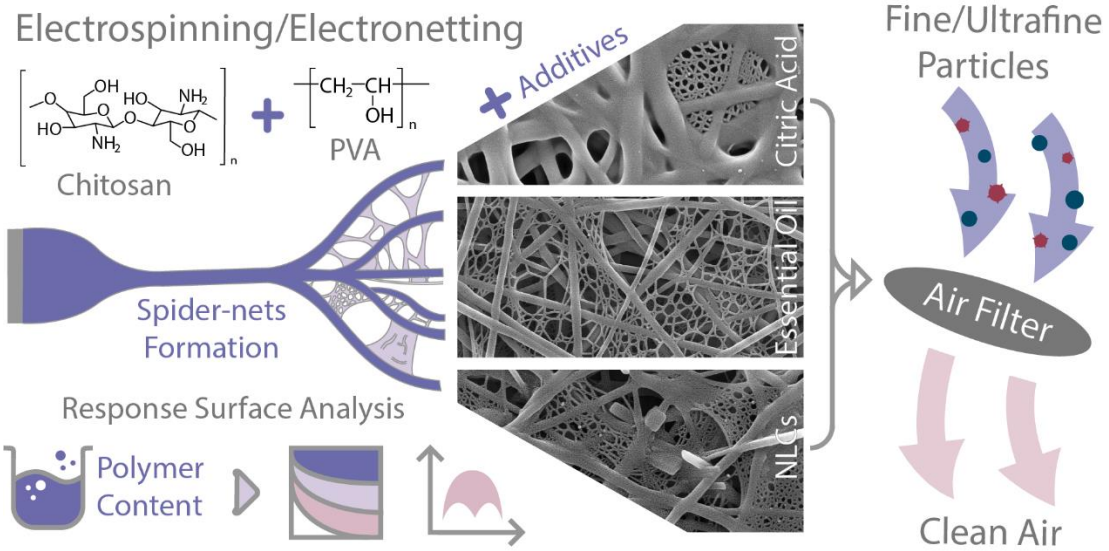

Abstract: "Spider-nets" or "nano-nets", are unique nanometric web-like structures formed between electrospun fibers. Due to their distinct properties, spider-nets have found applications in various fields, including sensors, tissue scaffolds, and water treatment, with potential applications for air filtration of tiny particulate matter. However, the predominant exploration of spider-nets in synthetic polymers raises concerns about environmental pollution, especially from microplastics. This study investigates the formation process of spider-nets in blends of polyvinyl alcohol (PVA) and chitosan (CS), emphasizing the influence of electrospinning/electronetting parameters on the air filtration of fine/ultrafine particles. A Multilevel Factorial Design was used to construct mathematical models representing the influence of polymer content on the fiber mat properties. By controlling the PVA:CS ratio, we could regulate spider-net porosity and coverage, preventing fiber fusion and film formation. It tested samples with the addition of citric acid (Cit), cetyltrimethylammonium bromide (CTAB), and pure and encapsulated *Lippia sidoides* essential oil (EO). Additives completely altered spider-net framework and improved air filtration performance, with the EO sample displaying the highest collection efficiency (99.6%), followed by the Cit sample (99.3%). Both samples complied with the strictest worldwide legislations for face masks, with collection efficiency above 98.0% and pressure drops lower than 40 $Pa.cm^{-2}$. Production parameters were an electrical field of 23.4 kV and a flow rate of 1.17 $mL.h^{-1}$ over 28 minutes. Spider-nets present a significant enhancement for materials in nanoparticles air filtration, establishing the electronetting of natural and biodegradable fibers as a promising alternative for ecological and efficient air filters.

Keywords: *Spider-net; Nano-nets; Electrospinning; Air Filtration; Nanofibers; PVA; Chitosan.*

Submitted to: Environmental Science: Nano (Royal Society of Chemistry)

5.1 Introduction

"Spider-nets",[1–3] also known as "nano-nets",[4] are rare nanostructures with Steiner-like geometry that forms while producing nanofibers via the electrospinning technique. These ultra-low thickness nanowebs have diameters below 50 nm, one-tenth of the diameter of standard electrospun fibers,[5] reaching diameters as small as 20 nm.[6] The production of spider-net structures is an advanced electrohydrodynamic technique based on electrospinning and has already acquired a name: electronetting.[4,7]

Some areas have been explored for the application of spider-nets. For instance, Li *et al.* used gold probes and polyamide-6/nitrocellulose spider-net membranes as sensors to detect trace amounts of lead.[8] Nylon-6 nano-nets also exhibited high sensitivity to formaldehyde[9] and L-ascorbic acid,[10] with remarkably low detection limits of approximately 50 ppb. Electronetting was also employed for tissue scaffolds,[11–14] purification of lithium-ion batteries,[15] and water treatment[16,17] for the removal of arsenic and organic dyes from water.[18]

Another potential application of spider-nets is air filtration. The production of filtering media has gained attention due to the COVID-19 pandemic,[19–27] along with the increasing air pollution in major urban centers worldwide.[28–32] Particulate matter can cause numerous health issues, such as asthma,[33–36] cardiovascular diseases[37,38], and interfere with fetal development.[39] In particular, tiny particles and ultrafine powders ($PM_{0.3}$>) can surpass traditional barriers,[20,40,41] penetrating and harming the lung tissue.[42,43] The tiny pores formed by the spider-net present a tool to enhance the containment of these fine/ultrafine particles, preventing their passage through the fibrous mat.[44,45] The spider-nets tightly intertwine the nanofibers, improving the mechanical strength of the air filters without compromising their efficiency.[45–48]

Li *et al*. noted that the cotton fibers coated with polyvinyl alcohol (PVA), produced by electronetting increased the collection efficiency from 74.6% to 98.1%.[46] Zhang *et al*. tested air filtration against ripple-like fibers of polyamide 6 (PA-6) with the presence of spider-nets, obtaining a high efficiency of 99.9% with a low air resistance of 95 Pa.[49] Liu *et al*. recently observed that increasing the coverage of spider-nets from 25% to 100% over the electrospun fiber mat also increased the collection efficiency, from 67.9% to 95.1%.[45] All the studies above tested air filtration of particles ranging between 0.3 and 0.5 µm in diameter.

Spider-nets were majorly explored in synthetic polymers such as polyvinylidene fluoride (PVDF), polyacrylonitrile (PAN), polyurethane (PU)[45,50] and poly(m-phenylene isophthalamide).[15,51,52] However, these polymers could end up in the environment, releasing microplastics[53–57] that act as pollutant carriers for antibiotics,[58] heavy metals,[59,60] and hydrophobic organic chemicals.[61] Spider-nets were also observed in natural and biodegradable polymers such as gelatin,[62] silk,[63] polyvinyl alcohol (PVA),[46,64] and PVA blended with chitosan.[65] Even though the production and manipulation of natural and biodegradable nanofibers through electrospinning are still a challenge,[66–72] the application of spider-nets in air filtration using natural and biodegradable polymers has not been fully explored, creating a promising field of study.

This paper tested the electronetting technique to produce spider-net web structures using the biodegradable polymers PVA and chitosan for air filtration of fine and ultrafine particles below the size range of previous studies ($PM_{0.3}$>).Different additives were also tested to observe their influence on the spider-net structure, such as cetyltrimethylammonium bromide (CTAB), citric acid (Cit), pure essential oil of *Lippia sidoides* (EO), and the essential oil encapsulated in Nanostructured Lipid Carriers (NLCs).[73] We studied the morphology of the fiber mat resulting from electrospinning/electronetting and tested its air filtration efficiency against particulate matter between 7 and 250 nm. The results proved promising, opening a window for the applications of spider-nets and the production of efficient and biodegradable filtering media.

5.2 Methodology

5.2.1 Materials

The polymers employed in this research consisted of polyvinyl alcohol (PVA) with a molecular weight of 85,500 $g.mol^{-1}$ and a hydrolysis degree of 89.5% (Vetec Química Fina, Duque de Caxias/RJ, Brazil) and chitosan (CS) with a deacetylation degree of 68.5% (Polymar, Fortaleza/CE, Brazil). As the solvent, it was utilized analytical-grade glacial acetic acid (G) at 99.0% purity (LabSynth, Diadema/SP, Brazil). The additives included citric acid (LabSynth, Diadema/SP, Brazil) and Cetyltrimethylammonium Bromide at 98% purity (CTAB, Sigma Aldrich, Saint Louis/MO, United States). Additional additives encompassed the pure *Lippia Sidoides* essential oil (Produtos Naturais LTDA, Horizonte/CE, Brazil) and the oil encapsulated as a Nanostructured Lipid Carriers (NLC).

The NLCs loaded with *L. sidoides* essential oil were prepared using the hot homogenization method followed by ultrasonication, as described by Baldim *et al*.[74,75] Two distinct NLCs were produced: one cationic (NLC_{Cat}) – constituted by 6% w/w of the solid lipid precirol (Gatefosse, France), 1% w/w of the liquid lipid oleic acid, 3% w/w of the essential oil, 1% of the cationic surfactant CTAB, and 3% w/w of poloxamer 188®; and one anionic (NLC_{An})[76,77] - consisting by 5.2% (w/w) of a mixture (1:1) of carnauba wax + beeswax as the solid lipid, 1% w/w of oleic acid as the liquid lipid, 2% w/w of the *L. sidoides* essential oil, and 2.8% w/w of anionic surfactant sodium dodecyl sulfate.[75] Water was added to adjust the total weight percentage to 100% (q.s.p. 100% w/w). The encapsulation of *L. sidoides* essential oil into NLCs aimed to slow the release of the EOs from the electrospun nanofibers and to evaluate its effects on spider-net formation.

5.2.2 Electrospinning of PVA/CS Compositions

The polymer solutions were individually prepared, with PVA concentrations ranging from 6% to 12% (w/v) and CS from 1% to 4% (w/v), as outlined in **Table 5.1**. The polymers were weighed and dissolved in a water/glacial acetic acid system (30:70) under constant magnetic stirring for 3 h at temperatures between 80 and 90°C until complete

dissolution and then mixed to create solutions in different proportions, maintaining the ratio of 3:1 for PVA to CS.

Table 5.1: Compositions after the mixture of PVA and Chitosan solutions. Their mixture proportion was maintained at the ratio of 3 parts of PVA solution to 1 parts of CS solution.

Polyvinyl Alcohol Content (%)	Chitosan Content (%)			
	1	2	3	4
6	4.5/0.25	4.5/0.50	4.5/0.75	4.5/1.00
8	6.0/0.25	6.0/0.50	6.0/0.75	6.0/1.00
10	7.5/0.25	7.5/0.50	7.5/0.75	7.5/1.00
12	9.0/0.25	9.0/0.50	9.0/0.75	9.0/1.00

5.2.3 Electrospinning Setup for Air Filtration

The electrospinning setup comprised a high-voltage generator with a continuous current source (Electrotest HIPOT CC, Model EH6005C, Instrutemp, São Paulo/SP, Brazil), an infusion pump (Harvard Apparatus, Model Elite I/W PROGR SINGLE, Holliston/MA, USA), and a stainless-steel rotating cylinder as the drum collector.

Uniform electrospinning conditions were applied across the experimental runs with the compositions presented in **Table 7.1**. These samples were also electrospun under optimal production parameters for the composition, as described in our previous study,[78] being an electrical field of 23.4 kV, a flow rate of 1.17 mL/h, and a production time of 28 min. It used a 5 mL plastic syringe with a metallic needle having a 0.55 mm opening. The metallic drum collector, covered with aluminium foil, was positioned 10 cm away from the needle tip and rotated at a speed of 595 rpm. Subsequently, the electrospun nanofibers were exposed to ambient air overnight to allow the remaining acetic acid to volatilize. The electrospinning process maintained the temperature and relative humidity at approximately 22 °C and 40%, respectively.

For the electrospinning of the samples with additives, one of the compositions of **Table 7.1** was taken as the basis for the following tests. It was chosen sample 6.0/1.00 (PVA at 6% and chitosan at 1.00%). 5% (w/w—dry basis) of each additive: CTAB, Cit, EO, and NLCs, was added and compared with the original sample.[65]

5.2.4 Filtration Tests

Filtration tests were conducted at the Laboratory of Environmental Control in the Department of Chemical Engineering at the University of São Carlos (UFSCar). All filtration steps, details, and equipment were the same as those described in Mata *et al*.,[78] and were shown in the Supplementary Material (**Figure S5.1**). This study investigated the collection efficiency (η) of NaCl nanoparticles[79] with diameters between 7 and 250 nm,[80–84] using a filtration area of 5.2 cm^2, and 1.5 $L.min^{-1}$ of flow rate, or 4.8

cm.s^{-1} of surface velocity. The pressure drop ($\boldsymbol{\Delta P}$) was tested in air flow rates between 0.2 and 2.0 L.min^{-1}, as described by Bonfim *et al.*[85,86]

Since the permeability is explicitly related to the microstructural parameters of fibrous porous media,[85] the empirical porosity (**ε**) of the filter media was calculated following Ergun's Equation, as shown below (**Equation 5.1**):

$$\frac{\Delta \boldsymbol{P}}{\boldsymbol{L}} = \frac{\mathbf{150}.\boldsymbol{\mu}.\boldsymbol{v_s}.(\mathbf{1}-\boldsymbol{\varepsilon})^{\mathbf{2}}}{\boldsymbol{\varepsilon}^{\mathbf{3}}.\boldsymbol{d_f}} + \frac{\mathbf{1.75}.(\mathbf{1}-\boldsymbol{\varepsilon}).\boldsymbol{\rho_g}.\boldsymbol{v_s^2}}{\boldsymbol{\varepsilon}^{\mathbf{3}}.\boldsymbol{d_f}} \qquad \textbf{(5.1)}$$

where μ is the gas viscosity; $\boldsymbol{v_s}$ is the superficial air filtration velocity; $\boldsymbol{\rho_g}$ is the gas density; and $\boldsymbol{d_f}$ is the average diameter of the fiber. Porosity was theoretically determined to assess the void fraction between fibers.

5.2.5 Morphological Analysis & Data Treatment

The morphology of the electrospun nanofibers was analysed from photomicrographs obtained by scanning electron microscopy (SEM). Electrospun nanofiber mat samples of 5×5 mm were coated with gold in a Bal-Tec SCD Sputter Coater model-050 (Fürstentum/Liechtenstein) under a pressure of 0.1 mbar. The SEM photomicrographs were obtained with two SEM equipment: a Carl Zeiss scanning electron microscope mod EVO 50 (Cambridge/United Kingdom); and a model SEM FEI Inspect F50 with FEG electron source with ETD and vCD detectors (Eindhoven/Netherlands). To identify which images are from each equipment, the SEM images were labeled with a symbol in the left inferior corner: a rhombus for the Carl Zeiss EVO 50; and a hexagon for the FEI Inspect F50. It used magnifications between 5 and 50 kX. The fiber mat's layer thickness ($\boldsymbol{L}$) was measured using an optical microscope (Olympus BX60, Olympus Co., Shinjuku, Tokyo, Japan) at magnifications of x10, and x20.

To calculate the spider-net coverage over the electrospun mat, its area was determined and compared with the total area of the SEM images from each sample, as exemplified in **Figure 5.1**. In cases of different spider-net superposition – when their layers overlap at different depths – the spider-net area was counted only once (**Figure 5.1 c)**). Internal layers are difficult to define, leading to estimation errors.

The diameter distribution of the electrospun nanofibers was determined by image analysis from SEM micrographs using ImageJ® software. Fiber mats thickness was measured with Image-Pro Plus 7.0®. Graphs were constructed using OriginPro® 2021, and images using Adobe Illustrator CC® 2019. The filtration data were treated using Excel® and PyCharm® (Python 3.11.4).

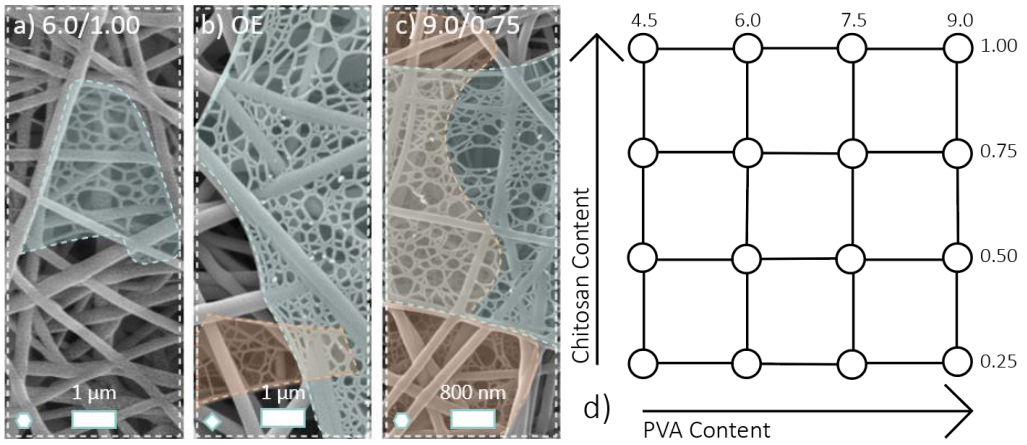

Figure 5.1: a) to **c)** Exemplification of spider-net coverage measurement using SEM images. The sum of all spider-net coverage areas (green) was divided by the total area of the SEM images (white) for each sample. The orange area shows spider-net structures at depth, which is deeper than the superficial layer shown in green; **d)** Multilevel factorial design, with 4^2, 2 factors (PVA and CS content), and 4 levels each.

5.2.6 Multilevel Factorial Desing

This study used a multilevel factorial design, with a general 4^2-factorial design, being two factors with four levels each. It was used Minitab® to evaluate the composition effects (**Table 5.1**) on the air filtration (collection efficiency), the fiber mat thickness, and the spider-net coverage on the electrospun mat. The regression model, denoted as $\hat{y}$, adopts a polynomial structure where $\boldsymbol{x_i}$ denotes the factors, $\boldsymbol{x_i^2}$ denotes the quadratic terms resulting from the interaction of each factor with itself, and $\boldsymbol{x_i x_j}$ represents the interaction between distinct factors. **Equation 5.2** illustrates the regression model utilized, where $\hat{y}$ represents the variable analyzed, while $\boldsymbol{\beta_{ij}}$ is the constant coefficient for each term. **Figure 5.1**, **d)** exemplifies a scheme of the model.

$$\hat{y} = \boldsymbol{\beta_0} + \boldsymbol{\beta_1 x_1} + \boldsymbol{\beta_2 x_2} + \boldsymbol{\beta_{11} x_1^2} + \boldsymbol{\beta_{22} x_2^2} + \boldsymbol{\beta_{12} x_1 x_2} \qquad \textbf{(5.2)}$$

5.3 Results & Discussion

5.3.1 PVA/Chitosan Blends

For the first observation, it fixed the chitosan content and varied the PVA concentration, as shown in **Figure 5.2**. As expected, 1% of pure CS does not yield fibers at electrical fields below 40 kV (**Figure 5.2 a)**).[87] The blend of PVA and CS enabled the electrospinning of CS at 1% and induced the formation of spider-nets that increased its coverage with the rise in PVA concentration. The sample with PVA at 4.5% exhibits a condensate spider-net with pores under 50 nm unevenly distributed along the fiber mat. In contrast, PVA at 6.0% displays a sparse yet well-distributed structure alongside the fiber mat. At higher contents (PVA 7.5 and 9.0%), the spider-net appears denser with

smaller pores, forming thin film layers and aggregates with fiber fusion, as seen in **Figure 5.2 d)** and **e)**.

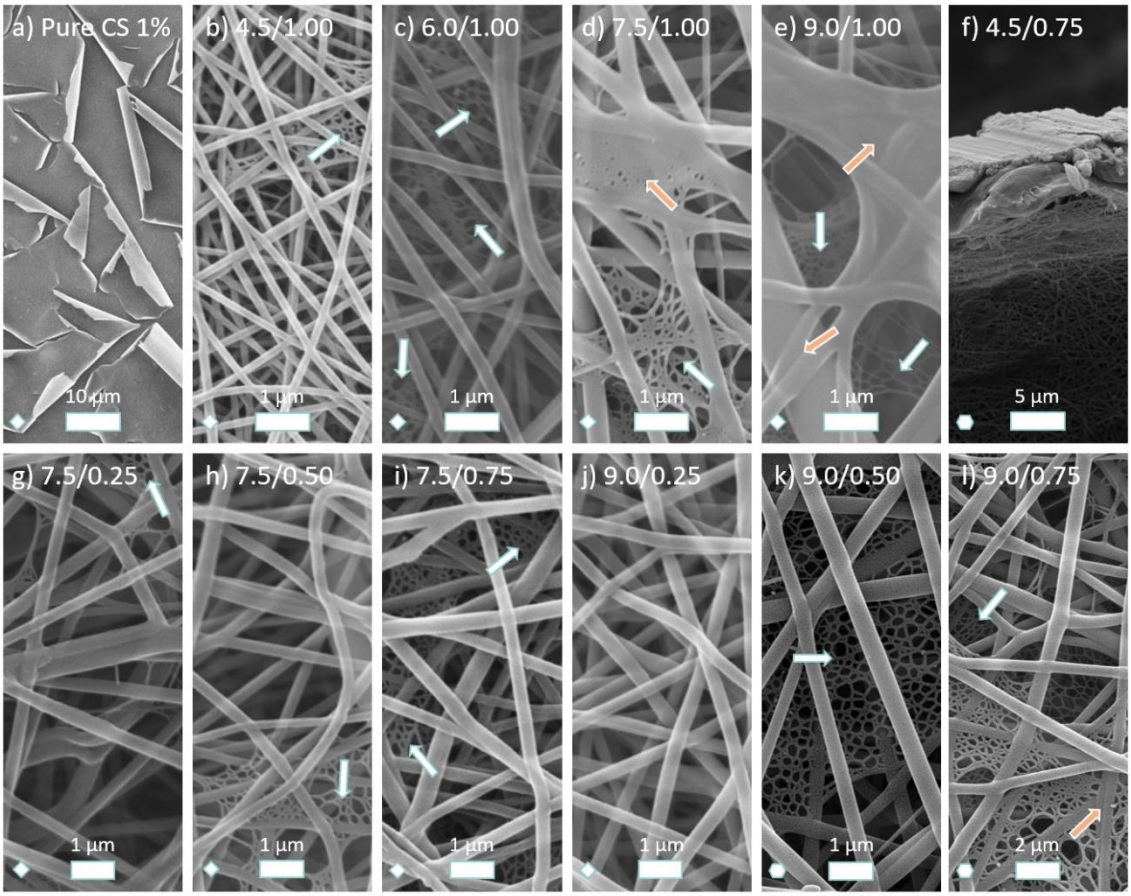

Figure 5.2: The SEM photomicrographs depict a series of samples with fixed chitosan (CS) content at 1.00%, while the polyvinyl alcohol (PVA) content varied as follows: **a)** 0% or pure chitosan (CS); **b)** 4.5%; **c)** 6.0%; **d)** 7.5%; and **e)** 9.0%. Panel **f)** presents a scale comparison between the nanofibers and the thickness of the aluminum foil on which the nanofibers were electrospun. Additionally, the series with 7% PVA includes **g)** CS at 0.25%, **h)** CS at 0.50%, and **i)** 0.75%, while the series with PVA 9% includes **j)** CS at 0.25%; **k)** CS at 0.50%; and **l)** 0.75%. White arrows indicate the presence of spider-net structures, while orange arrows indicate films or fiber fusion.

From the conductivity data (supplementary material, **Table S5.1**), it is observed that solutions with the lowest conductivity (PVA 9.0/0.50 to PVA 9.0/1.00) exhibit a higher presence of spider-nets (**Figure 5.2**, **k)** and **e)**), diverging with the literature describes.[2,45,64] However, they also tended to form films and fiber fusion. It is also possible that the increase in concentration, reduced the conductivity threshold for spider-net formation,[47] balancing the effect of decreased conductivity. It could be stated that by varying the CS content, the coverage and distribution of spider-nets in the polymeric matrix also vary. At the same time, PVA influences pore sizes, inducing the formation of films instead of spider-nets at high concentrations. Average fiber size distribution and SEM images from the samples described in **Table 5.1** are shown in the supplementary material (**Table S5.2** and **Figure S5.2**, respectively).

5.3.2 Spider-nets Formation

The electric field appears to be crucial for the formation of spider-nets.[88,89] As depicted in **Figure 5.3 a)**, a high electric field increases the residual charges in the polymeric solution, polarizing the molecules on the pendant droplet surface and creating instabilities at the apex of the Taylor cone (**I**).[47,90,91] Those instabilities, influenced by viscoelastic properties and interfacial surface tensions, favor the formation of droplets of polymeric solution through electrospraying,[92] competing with electrospinning. During the flight, the droplets undergo different forces, including an intense electrical field that stretches and distorts the droplet into a thin film, which travels alongside the electrospun fiber toward the collector (**II**).[44,93] The charges present on the highly electrified thin film and the charges in the "wet" flighting nanofiber start to attract each other,[2,3] creating protrusions on the fiber and distorting the thin film towards the neighboring nanofiber (**III**).[94,95]

Conversely, as the solvent in the thin film evaporates, a phase separation occurs, resulting in polymer-rich and solvent-rich phases (**IV**). The polymer-rich phase solidifies the polymer, forming a nucleation point on the thin film. As the solvent evaporates, polymer molecules in the fiber and the thin film gather, ultimately creating spider-net structures with Steiner-tree geometry after the disappearance of the solvent-rich phase (**V**).[6,47] The entire process of film deformation, rapid phase separation, and spider-net formation could occur within milliseconds.[4,62]

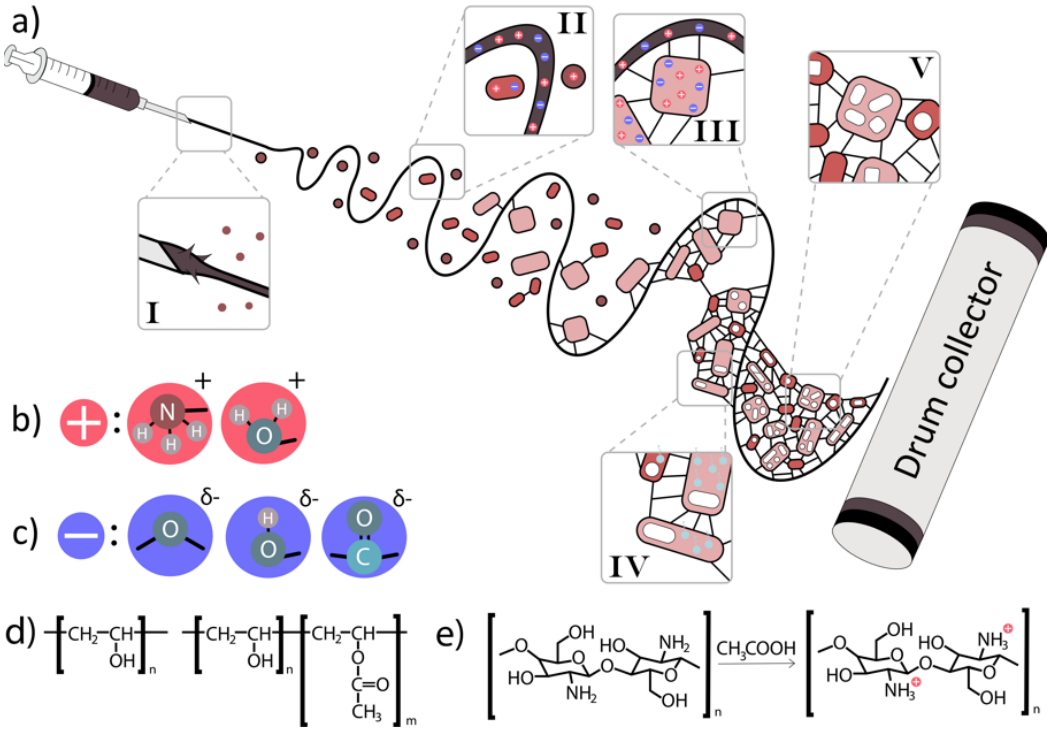

Figure 5.3: a) spider-net formation process: I. Taylor cone instability, leading to multijetting and electrospraying; II. stretching of electrosprayed droplets in thin films; III. Thin films bond with vicinal fibers; IV. Solvent evaporation and polymer phase enrichment, forming pores; and V. Spider-net formation. Radical structures of: **b)** the positive charges; **c)** the negative charges. **d)** Structures of polyvinyl alcohol completely and partially hydrolyzed; **e)** protonation of chitosan with acetic acid.

Conductivity, aligned with the electrical field, emerges as the driving force behind spider-net formation by helping to create the instabilities in the Taylor cone, favoring the electrospraying.[6,47] Consequently, raising the ionic charge of the polymeric solution might improve spider-net coverage over the fiber mat. Studies have indicated that adding acid[1] or salt[2,44] can induce spider-net formation, supporting the hypothesis regarding the influence of ionic species in spider-net formation. For the solution of PVA/CS, N, and O present on their molecular structures work as receivers of ions H^+ due to the high acetic acid content (70%),[96,97] as shown in **Figures 5.3**, **b)** to **e)**. They act as the ionic charges responsible for the spider-nets formation.

5.3.3 Air Filtration of Nanoparticles

Samples in **Table 5.1** had their filtration properties tested against nanoparticles with measurement of their pressure drops (**Figure 5.4**). The filtration data is shown in **Table 5.2**.

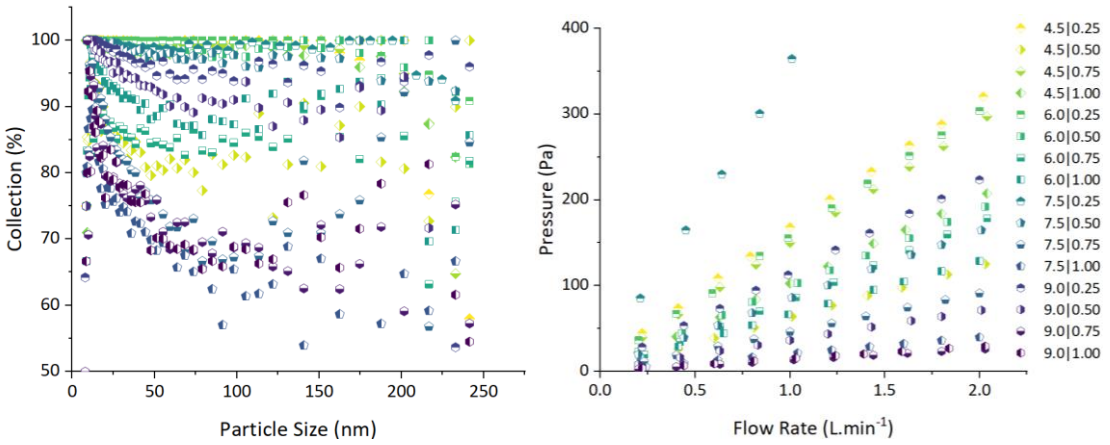

Figure 5.4: On the left, the fractional collection efficiencies from the samples of the Multilevel Factorial Desing. On the right, their respective pressure drops. Geometric symbols represent the PVA content, while the coloration position of the symbol indicates the CS content.

Many samples presented quality factors above 0.02 Pa^{-1}. Those values are satisfactory for the air velocities used in this study,[98] considering that theoretical analysis expects quality factors below 0.01 Pa^{-1} for fibers with a mean diameter of 1 µm.[99] Bonfim et al.[85,86] observed quality factors exceeding 0.02 Pa^{-1} when utilizing samples with varying concentrations of electrospun polyethylene terephthalate (PET) sourced from recycled soft drink bottles. Bortolassi et al.[81] reported achieving Qf values ranging from 0.04 to 0.06 Pa^{-1} using electrospun polyacrylonitrile (PAN), while Gao et al.[79] found values below 0.0231 Pa^{-1} for electrospun PAN composites.

The overall observation is that all the samples exhibited very low porosity, suggesting a stacked fiber mat configuration. Among the air filtration samples, 9.0/0.75 and 9.0/1.00 had also the highest porosity, explaining their low pressure drops and collection efficiencies. Larger porosities allow for higher flow rates, thereby increasing

the filter permeability.[100] Additionally, these samples had high fiber diameters, as indicated in **Table S5.2**, which could potentially increase filter porosity. These characteristics led samples 9.0/0.75 and 9.0/1.00 to have the highest quality factors (0.68 and 0.59, respectively), indicating that the quality factor calculation prioritizes low pressure drop over collection efficiency.[78]

Table 5.2: Filtration properties of Multilevel Factorial Desing samples described in **Table 5.1**. Pressure drop (ΔP) was measured at 1.5 L.min^{-1} of flow rate.

Sample	Pressure Drop (Pa)	Thickness (µm)	Porosity	Spider-net Coverage (%)	Collection Efficiency (%)	Quality Factor (Pa^{-1})
4.5/0.25	245.0	11.80	0.113	1.20	99.80	0.025
4.5/0.50	95.1	19.46	0.167	0.00	83.71	0.019
4.5/0.75	225.8	15.54	0.126	2.98	98.15	0.018
4.5/1.00	152.3	11.95	0.129	3.98	97.17	0.023
6.0/0.25	239.1	20.20	0.123	5.71	99.93	0.030
6.0/0.50	146.3	14.56	0.125	6.97	98.65	0.029
6.0/0.75	133.2	15.47	0.132	2.64	85.31	0.014
6.0/1.00	99.5	11.12	0.136	10.13	90.38	0.023
7.5/0.25	574.3	20.64	0.089	13.58	98.96	0.008
7.5/0.50	128.5	19.72	0.143	3.29	98.19	0.031
7.5/0.75	70.4	17.28	0.156	15.05	78.48	0.022
7.5/1.00	30.3	12.48	0.166	38.12	71.47	0.041
9.0/0.25	174.5	44.87	0.159	0.77	96.72	0.020
9.0/0.50	55.2	20.89	0.161	57.67	92.53	0.047
9.0/0.75	20.5	9.73	0.199	75.10	75.36	0.068
9.0/1.00	22.9	10.83	0.172	48.51	74.33	0.059

Samples collection efficiency was satisfactory, above 96% for half of the samples. Samples 4.5/0.25 and 6.0/0.25 presented the best collection efficiency, 99.8% and 99.9% respectively, however, at the expense of high pressure drops. A greater pressure drop signifies tortuous pore channels within the fiber mats, resulting in a longer path for the air through the filtration membrane. This elongated path enhances collection mechanisms like direct and inertial impaction, thus increasing collection efficiency. Conversely, lower pressure drops indicate fewer airflow obstructions due to direct preferential channels, leading to decreased collection efficiency.

Samples with higher collection efficiency had also lower porosity values. The lower porosity values could also be related to the thickness of the fiber mats, another indication of stacked fiber layers. Except for sample 9.0/0.25, all the other samples had thicknesses around 10 to 20 µm. The thin fiber mats shows a low depth on the fibers,

which is unexpected for samples with high collection efficiencies, such as 4.5/0.25 and 6.0/0.50, for example.

At first glance, it seems that the increase in spider-net coverage is also leading to low-pressure drops and, consequently, lower collection efficiencies. However, those decreases are also related to the increase in the fiber size diameter (**Table S5.2**) and the increases in porosity. The relation between the spider-nets and the air filtration properties will be explored in the next sections.

5.3.4 Multilevel Factorial Desing

Although many studies have examined how electrospinning parameters impact the morphology of nanofibers, the traditional approach is still expensive and time-consuming.[101] The numerous parameters and variables influencing the electrospinning process require a large number of experiments to properly understand the interactions between them. The statistical design of experiments (DoE) has emerged as an efficient and reliable tool for investigating the relationships between parameters.[102] **Figure 5.5** shows the influence of the PVA and CS content in the responses Collection efficiency, Spider-net Coverage, Porosity, and Thickness. **Figure S5.3** shows the surface plots from each response, a different perspective of the models shown in **Figure 5.5**.

From the Pareto charts (**Figure S5.4**), it is possible to observe that the collection efficiency and the thickness of the fiber mat have a significant influence on the chitosan content. This does not necessarily imply a positive influence, as can be seen in the model equations and ANOVA analysis (**Table S5.3** to **S5.7**). As the chitosan content increases, both responses diminish. However, when the PVA content rises, the collection efficiency diminishes.

The analysis of the DoE suggests that the formation of spider-nets could increase the porosity of the fiber mat and reduce its thickness, which is beneficial for the pressure drop but detrimental to the collection efficiency. Overall, the presence of spider-nets also increases the quality factor of the fiber mats, as fibers with higher spider-net coverage also exhibit higher quality factor values (**Table 5.2**).

Upon analyzing the Contour Plots, it is evident that the spider-net coverage correlates with the porosity of the fibers. In the main effects plot (**Figure S5.5**), they exhibit similar influences from both PVA and CS. Therefore, it can be inferred that the high solid content increases the porosity of the fiber mats and the spider-net presence. Additionally, the fiber diameter (**Table S5.2**) appears to follow the same trend.

While the collection efficiency is compromised by high porosity and low thickness, the presence of spider-nets on the fiber mat doesn't necessarily hinder the collection of fine and ultrafine particles. The polymer solid content in the solutions may be the primary factor in increasing porosity and reducing thickness. The following sections will address this issue by keeping the solid content constant and varying the spider-net coverage through the use of additives.

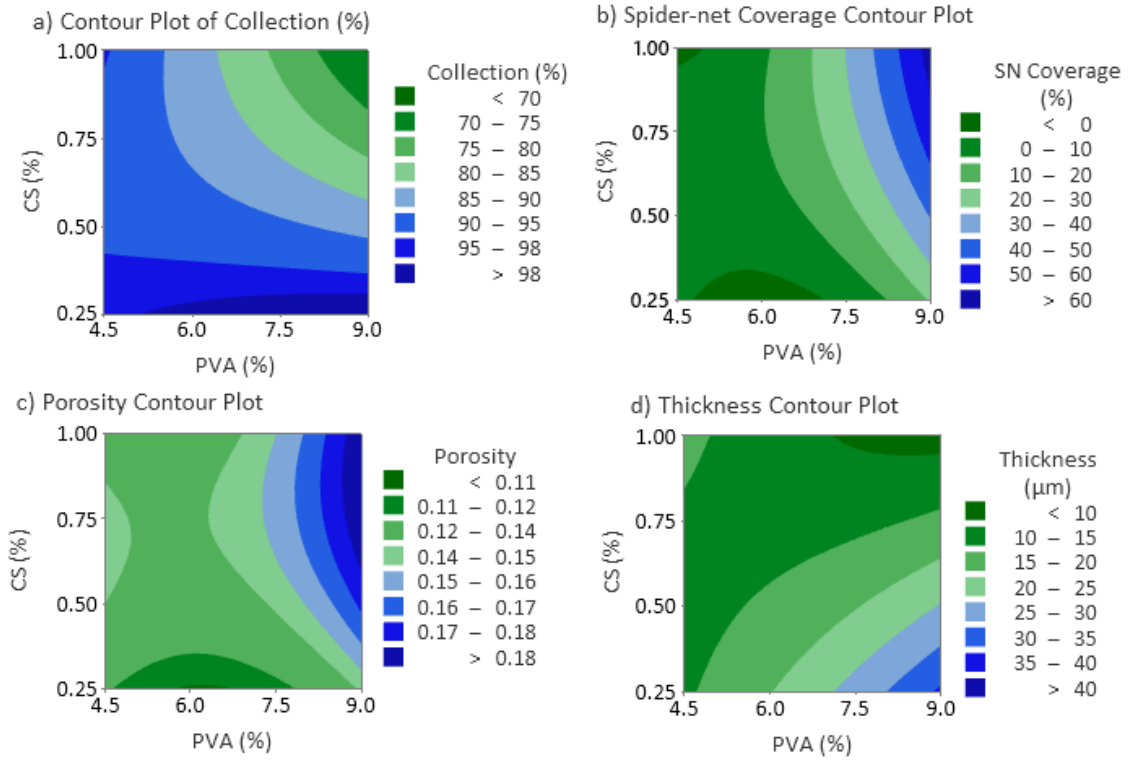

Figure 5.5: Contour plots generated by the samples defined on the Multilevel Factorial Design, showing the influence of the polymer content in each air filtration response.

5.3.5 Additive Influence on the Spider-nets

To assess the influence of different additives on the spider-net framework, we selected sample 6.0/1.00 (PVA 6.0% and CS 1.00%) from **Table 5.1**. Sample 6.0/1.00 was chosen because it exhibited well-defined spider-net structures and fiber mats free from thin films, fiber fusion, beads, or aggregates. Although sample 9.0/0.50 (PVA 9.0% and CS 0.50%) showed similar spider-net structures, sample 6.0/1.00 had a higher CS content, which is a preferable property, to confer biocidal activity for the fiber mat.[103,104] CS is hydrophobic, and in higher contents normally leads to agglomeration and fiber fusion, a characteristic not observed in 6.0/1.00.[105,106] Additionally, sample 9.0/0.50 had a larger average fiber diameter than 6.0/1.00 (**Table S5.2**), which could potentially interfere with the air filtration studies.[107–109]

The SEM images of the fibers with additives are presented in **Figure 5.6**. It was added citric acid (Cit), cetyltrimethylammonium bromide (CTAB), essential oil of *Lippia sidoides* in pure form (EO) and encapsulated as a Nanostructured Lipid Carrier (NLC). NLCs used two different surfactants in its composition, one cationic (NLC_{Cat}) and one anionic (NLC_{An}).

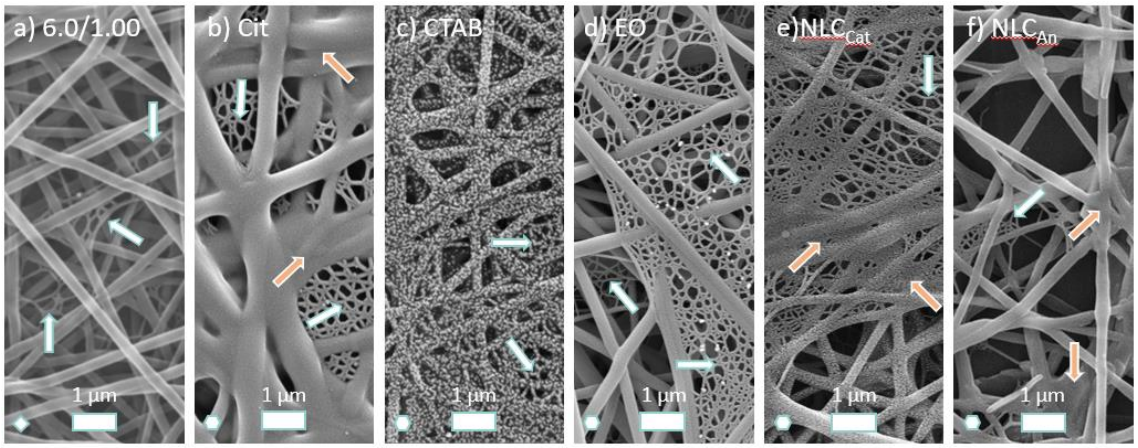

Figure 5.6: SEM image from the samples with the basis composition of **a)** PVA 6.0% and CS 1.00% and with 5% (w/w) addition of **b)** citric acid; **c)** cetyltrimethylammonium bromide; **d)** pure *Lippia sidoides* essential oil; and the essential oil encapsulated as **e)** a cationic nanostructured lipid carrier; and **f)** an anionic nanostructured lipid carrier.

Notably, even a minor additive addition in sample 6.0/1.00, 5% – w/w total solid content, had a profound effect, causing significant alterations in the distribution of spider-nets, their porous sizes, and the average fiber size of the samples (refer to **Table 5.2**). The addition of citric acid appeared to induce crosslinking between chains, a behavior previously reported[110] and similar to the effect observed with formic acid.[46,64] Citric acid addition also resulted in fiber fusion and aggregation.

The CTAB sample distorted SEM imaging. This phenomenon is attributed to interactions between CTAB and the gold particles used to coat the samples. This cationic property of CTAB is well-known and has been explored in the synthesis of gold nanoparticles.[111–113] The same effect was observed in sample NLC_{Cat}, with less intensity due to the low CTAB concentration in NLC_{Cat}.

The sample with pure essential oil produced the most favorable spider-net structure. It is possible that the addition of essential oil reduced the solution's hygroscopicity, leading to improvements in spider-net formation and preventing fiber fusion and film formation, as observed in samples with NLCs. Both samples contain surfactants that may interfere with spider-net formation by retaining water on the fibers or diminishing the surface tension. We excluded the sample NLC_{An} in the following steps due to its poor morphological structure, excessive fiber fusion, and aggregations, and undesirable characteristics for air filtration.

5.3.6 Spider-nets in Air Filtration

The additive influence and its impact on spider-net morphology were also investigated for air filtration, as shown in **Figure 5.7**. For comparison, **Table 5.3** shows the filtration data from the additive samples.

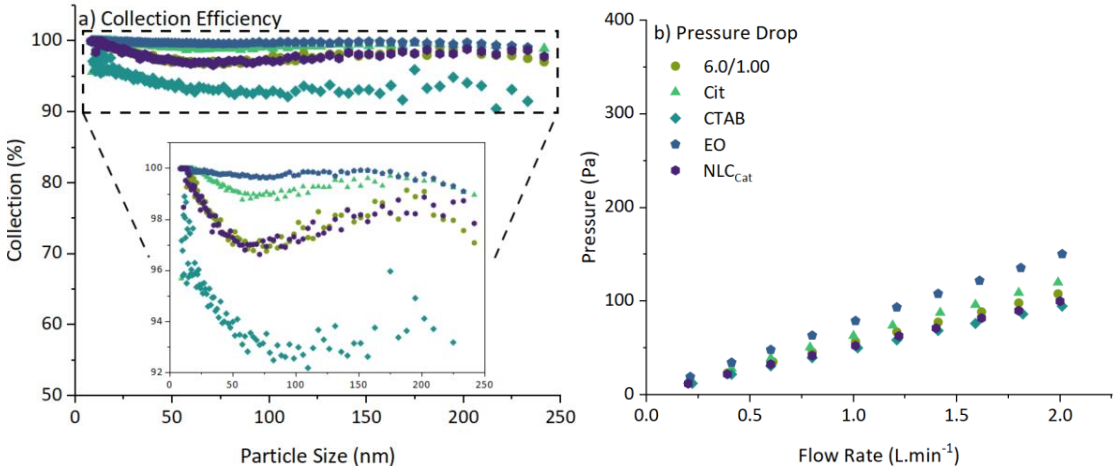

Figure 5.7: a) Collection efficiency and **b)** Pressure drop of the sample PVA 6% and CS 1.00% with and without different additives.

Table 5.3: Filtration properties of the additive samples. Pressure drop (ΔP) was measured at 1.5 L.min^{-1} of flow rate.

Sample	Pressure Drop (Pa)	Fiber Mat Thickness (µm)	Porosity	Fiber size (nm)	Spider-net Coverage (%)	Collection Efficiency (%)	Quality Factor (Pa^{-1})
6.0/1.00	99.5	11.12	0.136	204.4 ± 32.2	10.13	90.38	0.023
Cit	92.6	20.72	0.142	347.6 ± 113.7	8.18	99.26	0.053
CTAB	74.4	13.66	0.157	208.8 ± 58.0	-	93.74	0.040
EO	117.3	11.19	0.119	249.1 ± 65.7	63.31	99.64	0.048
NLC$_{Cat}$	76.8	10.63	0.113	437.0 ± 151.9	33.65	97.56	0.048

All the samples exhibited higher collection efficiencies and quality factors than the original sample, 6.0/1.00. Sample EO had a slightly higher pressure drop, along with the highest collection efficiency and spider-net coverage with large and porous spider-net structures. Sample NLC$_{Cat}$ presented considerable spider-net coverage, with many film fusions instead of large pores. Due to the CTAB gold particle interaction, it was not possible to evaluate the spider-net coverage of the sample. Cit sample was expected to have higher spider-net coverage; however, most of these spider-nets were in deeper layers, covered by fibers and film fusions.

When comparing samples 6.0/1.00 and sample EO, it is possible to observe the influence of the spider-net on the collection efficiency performance. They had slightly different porosity values (0.136 and 0.119, respectively), very similar thickness (11.12 and 11.19 µm), close average nanofiber diameter sizes (204.4 and 249.1 nm), but very

different spider-nets coverage (10.13 and 63.31%). As seen in the inset of **Figure 5.7**, sample 6.0/1.0 presents a decrescent curvature in its collection efficiency, particularly for nanosized particles (> 100 nm), a curvature not seen in sample EO. Therefore, the spider-nets presence could be the factor that increased the nanoparticle filtration.

Nanoparticles can easily traverse the nanofiber mat's pores, affecting the collection efficiency. The decrease observed in the collection of nanoparticles may account for the most penetrating particle size (MPPS). Particles smaller than the MPPS are primarily affected by Brownian diffusion. At the nanoscale, the primary mechanisms governing particle collection are Brownian diffusion and electrostatic attraction, particularly when the fibers' electric field attracts low-mass particles.[114] Larger particles are predominantly influenced by mechanisms such as interception and inertial impaction,[115–117] while particles ranging from 100 to 250 nm are sufficiently large to be primarily influenced by diffusive forces and too small to be efficiently collected by impaction.[81,82,118]

As classical filtration theory dictates, increasing the fiber diameter reduces the porosity and pressure drop.[118,119] However, the opposite trend was observed from sample 6.0/1.00 to EO. Despite being a highly porous structure, the significant presence of spider-net appears to reduce the pathway for the passing air. Where there previously existed an open pore between fibers, there is now a spider-net covering this pore, along with its own smaller pores formed by tiny nanofibers. This occurrence enhances the air-fiber contact and, consequently, the exposure of transiting nanoparticles to the electric field of these nanofibers, increasing the nanoparticles air filtration.

Three main rationales can clarify how the presence of spider-nets contributes to enhancing air filtration in electrospun mats. The first one explains that the enhanced capabilities of spider-nets for air filtration occur due to their significant slip effect, which takes place during the air transition from the continuous flow regime to the molecular regime.[120,121] At fiber diameters close to the mean free path of air molecules (66 nm), the gas velocity is non-zero at the fiber surface, causing the molecules to "slip", consequently reducing the drag force on the airflow.[122,123] These properties can overcome the intrinsic limitation in the trade-off between filtration efficiency and pressure drop present in conventional filters,[124] increasing the potential of spider nets in air filtration of nanoparticles, without high costs in pressure drop. The evidence of how the spider-net had influenced the air filtration trade-off is the quality factor, which had more than doubled from sample 6.0/1.00 to sample EO (0.023 and 0.048, respectively).

Spider-nets could also enhance the traditional retention mechanisms of particles, as our second rationale will explore. Spider-nets' minute pores can improve sieving and inertial impact captures, retaining particulate matter of different sizes over the spider-net web.[44,45,49] The different mechanisms can compete among themselves, depending on the particle diameter.[116] Particles between 100 and 1000 nm are predominantly affected by Brownian motion diffusion, the same mechanism responsible for virus capture.[125] Mechanical collection is also a relevant mechanism for this range of

sizes.[84] Nanometric particles (below 100 nm) can effortlessly pass through the mat's pores, being more affected by electrostatic capture mechanisms.

The third rationale concerns the charge retention on the spider-nets. Liu *et al*. studied the charge retention between PVDF electrospun mats with and without spider-nets, observing that the spider-nets help increase the charge retained in the fibers,[45] keeping those charges for several months.[83,84] Electrostatic attraction plays a predominant role in the retention of fine and ultrafine particles such as $PM_{0.1}$ and viruses,[126] with many techniques using the electrical field to bind and capture low-mass particles.[114,127–130] The nanoscale fibers possess high surface energy and surface reactivity,[1,131,132] enhancing the interaction between fiber and particle during the dynamic process of adsorption and desorption,[133] and consequently increasing the fine/ultrafine particle collection.

5.3.7 Legislation Accordance

We compared the samples in this study with three international mask regulations: United States legislations (ASTM F2100 and NIOSH 42 CFR 84);[134,135] European legislation (EN 14683);[136] and Brazilian legislation (ABNT NBR 15052).[137] The results are shown in **Table 5.4**.

Table 5.4: Comparison between the samples with the best filtration performance and some legislations about mask properties from Brazil (ABNT NBR 2021), the United States (ASTM F2100 2019), and the Europe Union (EN 14683 2019). The filtration area was 5.2 cm².

Technical Standard/Sample	Pressure Drop ($Pa.cm^{-2}$)	Collection Efficiency (%)
ABNT NBR 15052 (2021)	Levels 0 and 1: <49.03	Levels 0 and 1: ≥ 95
	Levels 2 and 3: < 58.84	Levels 2 and 3: ≥ 98
ASTM F2100 (2019)	Level 1: <49.03	Level 1: ≥ 95
	Levels 2 and 3: < 58.84	Levels 2 and 3: ≥ 98
EN 14683* (2019)	Types I and II: < 40	Type I: ≥ 95
	Type IIR: < 60	Types II and IIR: ≥ 98
NIOSH 42 CFR 84 (1996)	-	N95: ≥ 95 N99: ≥ 99
6.0/0.50	28.13	98.65
7.5/0.50	24.71	98.19
Cit	17.81	99.26
EO	22.56	99.64

* Technical Standard EN 14683 does not define a filtration efficiency for particles, only for bacterial filtration efficiency.

Almost all the samples have their pressure drop complying with the European legislation, the strictest regulation for face masks. The exceptions were sample 7.5/0.25, which does not comply with any regulation, and samples 4.25/0.25, 4.5/075, and 6.0/25 which complied with type IIR from the European legislation. Samples 4.5/0.25, 4.5/0.75, 4.5/1.00, 6.0/0.25, 9.0/0.25, and NLC_{Cat} complied with the lower levels for collection efficiency for all the regulations (>95%).

Samples described in **Table 5.4** complied with the higher levels of all the regulations, reaching N98 filtration capabilities (>98%) and showing the potential of natural and biodegradable polymers for air filtration purposes. Samples Cit and EO had higher air filtration efficiencies (>99%) with the lowest pressure drops, being classified as N99, meaning that even with greater fiber diameter sizes, the high spider-net coverage was capable of increasing collection efficiency with a low cost in pressure drops. Sample EO had an even better performance, considering that its thickness was lower than both samples 6.0/0.50 and 7.0/0.50.

5.4 Conclusion

The use of spider-net in air filtration opens a new window for nanomaterial control and materials enhancement, particularly for natural and biodegradable polymers. In this study, we investigated the influence of the electrospinning and electronetting technique on the formation of "spider-nets" or "nano-nets" structures and its impact on air filtration for fine/ultrafine particles. Our findings reveal that adjusting the concentrations of PVA and CS polymers allows for the adaptation of pore morphology and spider-net coverage. Furthermore, the introduction of additives like CTAB, citric acid, and essential oils of *Lippia sidoides* can modify the structures of spider-nets, increasing their coverage and changing their morphology.

Fiber mats with additives demonstrated their potential for air filtration. Many samples in our study complied with lower levels of international regulation for the air filtration of face masks. Samples 6.0/0.50, 7.5/0.50, Cit, and EO achieve the highest levels for the standard regulations, with collection efficiency above 98%. Sample EO displayed the highest collection efficiency among the additive samples with excellent quality factor (99.64%, and 0.048, respectively), followed by the sample with citric acid (99.26%, and 0.053), showing that the additives and the spider-net coverage had a prominent effect on the air filtration of nanoparticles. In future studies, we suggest proper investigation of the spider-nets influence on other material properties, such as mechanical strength and hydrophobicity.

Author contributions

Conceptualization, G. C. M., M. S. M., and W. P. O.; data curation, G. C. M.; formal analysis, G. C. M; funding acquisition, W. P. O. and M. L. A.; investigation, G. C. M. and M. S. M.; methodology, G. C. M., M. S. M. and W. P. O.; project administration, M. L. A.; resources, W. P. O. and M. L. A.; software, G. C. M.; supervision, W. P. O. and M. L. A.; validation, G. C. M. and M. S. M.; visualization, G. C. M., M. S. M. and

W. P. O.; writing—original draft preparation, G. C. M.; writing—review and editing, G. C. M., W. P. O. and M. L. A. All authors have read and agreed to the published version of the manuscript.

Funding: This research was funded by Coordination for the Improvement of Higher Education Personnel (CAPES) grant number 88887.505019/2020-00, the National Council for Scientific and Technological Development (CNPq), grants number 424792/2018-4 scholarship grant number 140704/2023-0 and the Foundation of Research Support of São Paulo State (FAPESP) grant number 2018/26069-0.

Acknowledgements

This research was funded by Coordination for the Improvement of Higher Education Personnel (CAPES) grant number 88887.505019/2020-00, the National Council for Scientific and Technological Development (CNPq), grant number 424792/2018-4 and scholarship grant number 140704/2023-0, and the Foundation of Research Support of São Paulo State (FAPESP) grant number 2018/ 26069-0. The authors acknowledge the financial support of CAPES, CNPq, and FAPESP. We also would like to thank the personnel and staff from the Environmental Control Laboratory of the Federal University of São Carlos (LCA/ UFSCar), the Laboratory of P&D in Pharmaceutical Process of the University of São Paulo (LAPROFAR/USP), the Chemistry Department of the Faculty of Philosophy, Science, and Letters of the University of São Paulo (FFCLRP/USP) and the Laboratory of Electronic Microscopy of the Department of Materials Engineering of the University of São Paulo (EESC/USP).

Conflicts of interest

There are no conflicts to declare.

5.5 Chapter References

1 J. Matulevicius, L. Kliucininkas, D. Martuzevicius, E. Krugly, M. Tichonovas and J. Baltrusaitis, Design and Characterization of Electrospun Polyamide Nanofiber Media for Air Filtration Applications, *Journal of Nanomaterials*, 2014, **2014**, e859656.

2 N. A. M. Barakat, M. A. Kanjwal, F. A. Sheikh and H. Y. Kim, Spider-net within the N6, PVA and PU electrospun nanofiber mats using salt addition: Novel strategy in the electrospinning process, *Polymer -London-*, 2009, **50**, 4389–4396.

3 H. R. Pant, M. P. Bajgai, K. T. Nam, Y. A. Seo, D. R. Pandeya, S. T. Hong and H. Y. Kim, Electrospun nylon-6 spider-net like nanofiber mat containing TiO2 nanoparticles: A multifunctional nanocomposite textile material, *Journal of Hazardous Materials*, 2011, **185**, 124–130.

4 B. Ding, C. Li, Y. Miyauchi, O. Kuwaki and S. Shiratori, Formation of novel 2D polymer nanowebs via electrospinning, *Nanotechnology*, 2006, **17**, 3685.

5 B. Robert and G. Nallathambi, A concise review on electrospun nanofibres/nanonets for filtration of gaseous and solid constituents (PM2.5) from polluted air, *Colloid and Interface Science Communications*, 2020, **37**, 100275.

6 X. Wang, B. Ding, G. Sun, M. Wang and J. Yu, Electro-spinning/netting: A strategy for the fabrication of three-dimensional polymer nano-fiber/nets, *Progress in Materials Science*, 2013, **58**, 1173–1243.

7 S. Yang, X. Wang, B. Ding, J. Yu, J. Qian and G. Sun, Controllable fabrication of soap-bubble-like structured polyacrylic acid nano-nets via electro-netting, *Nanoscale*, 2011, **3**, 564–568.

8 Y. Li, Y. Si, X. Wang, B. Ding, G. Sun, G. Zheng, W. Luo and J. Yu, Colorimetric sensor strips for lead (II) assay utilizing nanogold probes immobilized polyamide-6/nitrocellulose nano-fibers/nets, *Biosens Bioelectron*, 2013, **48**, 244–250.

9 X. Wang, Y. Si, J. Wang, B. Ding, J. Yu and S. S. Al-Deyab, A facile and highly sensitive colorimetric sensor for the detection of formaldehyde based on electro-spinning/netting nano-fiber/nets, *Sensors and Actuators B: Chemical*, 2012, **163**, 186–193.

10 Y. Wen, Y. Li, Y. Si, X. Wang, F. Li, J. Yu and B. Ding, Ready-to-use strip for l-ascorbic acid visual detection based on polyaniline/polyamide 66 nano-fibers/nets membranes, *Talanta*, 2015, **144**, 1146–1154.

11 R. Nirmala, H.-S. Kang, M. H. El-Newehy, R. Navamathavan, H.-M. Park and H. Y. Kim, Human Osteoblast Cytotoxicity Study of Electrospun Polyurethane/Calcium Chloride Ultrafine Nanofibers, *Journal of Nanoscience and Nanotechnology*, 2011, **11**, 4749–4756.

12 R. Nirmala, R. Navamathavan, H.-S. Kang, M. H. El-Newehy and H. Y. Kim, Preparation of polyamide-6/chitosan composite nanofibers by a single solvent system via electrospinning for biomedical applications, *Colloids and Surfaces B: Biointerfaces*, 2011, **83**, 173–178.

13 R. Nirmala, H.-M. Park, R. Navamathavan, H.-S. Kang, M. H. El-Newehy and H. Y. Kim, Lecithin blended polyamide-6 high aspect ratio nanofiber scaffolds via electrospinning for human osteoblast cell culture, *Materials Science and Engineering: C*, 2011, **31**, 486–493.

14 C. Tian, F. Wu, W. Jiao, X. Liu, X. Yin, Y. Si, J. Yu and B. Ding, Antibacterial and antiviral N-halamine nanofibrous membranes with nanonet structure for bioprotective applications, *Composites Communications*, 2021, **24**, 100668.

15 K. Xiao, Y. Zhai, J. Yu and B. Ding, Nanonet-structured poly(m-phenylene isophthalamide)–polyurethane membranes with enhanced thermostability and wettability for high power lithium ion batteries, *RSC Adv.*, 2015, **5**, 55478–55485.

16 Y. Chen, N. Tang, W. Zhu, S. Liu and Y. Zhang, Biomimetic nanonet membranes with UV-driven self-cleaning performance for water remediation, *Journal of Membrane Science*, 2023, **687**, 122047.

17 J. Zhou, X. Li, T. Hou, X. Zhang and B. Yang, Biodegradable, biomimetic, and nanonet-engineered membranes enable high-flux and highly-efficient oil/water separation, *Journal of Hazardous Materials*, 2022, **434**, 128858.

18 H. R. Pant, H. J. Kim, M. K. Joshi, B. Pant, C. H. Park, J. I. Kim, K. S. Hui and C. S. Kim, One-step fabrication of multifunctional composite polyurethane spider-web-like nanofibrous membrane for water purification, *Journal of Hazardous Materials*, 2014, **264**, 25–33.

19 N. Zhu, D. Zhang, W. Wang, X. Li, B. Yang, J. Song, X. Zhao, B. Huang, W. Shi, R. Lu, P. Niu, F. Zhan, X. Ma, D. Wang, W. Xu, G. Wu, G. F. Gao and W. Tan, A Novel Coronavirus from Patients with Pneumonia in China, 2019, *New England Journal of Medicine*, , DOI:10.1056/NEJMoa2001017.

20 O. Aydin, B. Emon, S. Cheng, L. Hong, L. P. Chamorro and M. T. A. Saif, Performance of fabrics for home-made masks against the spread of COVID-19 through droplets: A quantitative mechanistic study, *Extreme Mechanics Letters*, 2020, **40**, 100924.

21 Y. Feng, T. Marchal, T. Sperry and H. Yi, Influence of wind and relative humidity on the social distancing effectiveness to prevent COVID-19 airborne transmission: A numerical study, *Journal of Aerosol Science*, 2020, **147**, 105585.

22 S. N. Shankar, C. T. Witanachchi, A. F. Morea, J. A. Lednicky, J. C. Loeb, Md. M. Alam, Z. H. Fan, A. Eiguren-Fernandez and C.-Y. Wu, SARS-CoV-2 in residential rooms of two self-isolating persons with COVID-19, *Journal of Aerosol Science*, 2022, **159**, 105870.

23 L. Morawska and J. Cao, Airborne transmission of SARS-CoV-2: The world should face the reality, *Environment International*, 2020, **139**, 105730.

24 W. Wang, S. Kang, W. Zhou and P. J. Vikesland, Environmental routes of virus transmission and the application of nanomaterial-based sensors for virus detection, *Environ. Sci.: Nano*, 2023, **10**, 393–423.

25 V. C. Thi Le, S. Yoon, E. Kang, M. Sheraz, T. Uk Han, A. Anus, H. Duy Mai, S. Choi and S. Kim, A capture and inactivation system against pathogens in indoor air using copper nanoparticle decorated melamine sponge hybrid air filters, *Environmental Science: Advances*, 2022, **1**, 356–364.

26 L. R. Crilley, A. A. Angelucci, B. Malile, C. J. Young, T. C. VandenBoer and J. I. L. Chen, Non-woven materials for cloth-based face masks inserts: relationship between material properties and sub-micron aerosol filtration, *Environ. Sci.: Nano*, 2021, **8**, 1603–1613.

27 J. Wang, L. Hou, Z. Yao, W. Dou, G. Li and L. Zhang, Antifouling sandwich-structured electrospun nanofibrous membranes by integrating fluffy and hydrophobic layers for long-term airborne particulate matter segregation, *Environ. Sci.: Nano*, 2021, **8**, 3322–3330.

28 F. Carozzi and S. Roth, Dirty density: Air quality and the density of American cities, *Journal of Environmental Economics and Management*, 2023, **118**, 102767.

29 X. Lu, S. Zhang, J. Xing, Y. Wang, W. Chen, D. Ding, Y. Wu, S. Wang, L. Duan and J. Hao, Progress of Air Pollution Control in China and Its Challenges and Opportunities in the Ecological Civilization Era, *Engineering*, 2020, **6**, 1423–1431.

30 L. S. P. Nguyen, J. Hian-Wui Chang, S. M. Griffith, T. T. Hien, S. Soon-Kai Kong, H. N. Le, H.-Y. Huang, G.-R. Sheu and N.-H. Lin, Trans-boundary air pollution in a Southeast Asian megacity: Case studies of the synoptic meteorological mechanisms and impacts on air quality, *Atmospheric Pollution Research*, 2022, **13**, 101366.

31 V. Rodrigues, C. Gama, A. Ascenso, K. Oliveira, S. Coelho, A. Monteiro, E. Hayes and M. Lopes, Assessing air pollution in European cities to support a citizen centered approach to air quality management, *Science of The Total Environment*, 2021, **799**, 149311.

32 J. da M. Singer, C. D. S. de André, P. A. de André, F. M. M. Rocha, D. Waked, A. M. Vaz, G. F. Gois, M. de F. Andrade, M. M. Veras, P. H. N. Saldiva and L. V. Barrozo, Assessing socioeconomic bias of exposure to urban air pollution: an autopsy-based study in São Paulo, Brazil, *The Lancet Regional Health – Americas*, , DOI:10.1016/j.lana.2023.100500.

33 P. E. Pfeffer, I. S. Mudway and J. Grigg, Air Pollution and Asthma: Mechanisms of Harm and Considerations for Clinical Interventions, *Chest*, 2021, **159**, 1346–1355.

34 J. Q. Koenig, Air pollution and asthma, *Journal of Allergy and Clinical Immunology*, 1999, **104**, 717–722.

35 D. Singh, I. Gupta and A. Roy, The association of asthma and air pollution: Evidence from India, *Economics & Human Biology*, 2023, **51**, 101278.

36 R.-R. Duan, K. Hao and T. Yang, Air pollution and chronic obstructive pulmonary disease, *Chronic Diseases and Translational Medicine*, 2020, **6**, 260–269.

37 S. Rajagopalan, S. G. Al-Kindi and R. D. Brook, Air Pollution and Cardiovascular Disease: JACC State-of-the-Art Review, *Journal of the American College of Cardiology*, 2018, **72**, 2054–2070.

38 M. Dastoorpoor, Z. Sekhavatpour, K. Masoumi, M. J. Mohammadi, H. Aghababaeian, N. Khanjani, B. Hashemzadeh and M. Vahedian, Air pollution and hospital admissions for cardiovascular diseases in Ahvaz, Iran, *Science of The Total Environment*, 2019, **652**, 1318–1330.

39 D. Kim, Z. Chen, L.-F. Zhou and S.-X. Huang, Air pollutants and early origins of respiratory diseases, *Chronic Diseases and Translational Medicine*, 2018, **4**, 75–94.

40 M. Ippolito, F. Vitale, G. Accurso, P. Iozzo, C. Gregoretti, A. Giarratano and A. Cortegiani, Medical masks and Respirators for the Protection of Healthcare Workers from SARS-CoV-2 and other viruses, *Pulmonology*, 2020, **26**, 204–212.

41 C. J. Kähler and R. Hain, Fundamental protective mechanisms of face masks against droplet infections, *Journal of Aerosol Science*, 2020, **148**, 105617.

42 R. Chen, B. Hu, Y. Liu, J. Xu, G. Yang, D. Xu and C. Chen, Beyond PM2.5: The role of ultrafine particles on adverse health effects of air pollution, *Biochimica et Biophysica Acta (BBA) - General Subjects*, 2016, **1860**, 2844–2855.

43 J. Zhang, Z. Chen, D. Shan, Y. Wu, Y. Zhao, C. Li, Y. Shu, X. Linghu and B. Wang, Adverse effects of exposure to fine particles and ultrafine particles in the environment on different organs of organisms, *Journal of Environmental Sciences*, 2024, **135**, 449–473.

44 N. Wang, X. Wang, B. Ding, J. Yu and G. Sun, Tunable fabrication of three-dimensional polyamide-66 nano-fiber/nets for high efficiency fine particulate filtration, *J. Mater. Chem.*, 2012, **22**, 1445–1452.

45 H. Liu, S. Zhang, L. Liu, J. Yu and B. Ding, High-Performance PM0.3 Air Filters Using Self-Polarized Electret Nanofiber/Nets, *Advanced Functional Materials*, 2020, **30**, 1909554.

46 X. W. Li, H. Y. Kong and J. H. He, Study on highly filtration efficiency of electrospun polyvinyl alcohol micro-porous webs, *Indian J Phys*, 2015, **89**, 175–179.

47 S. Zhang, K. Chen, J. Yu and B. Ding, Model derivation and validation for 2D polymeric nanonets: Origin, evolution, and regulation, *Polymer*, 2015, **74**, 182–192.

48 H. R. Pant, M. P. Bajgai, K. T. Nam, K. H. Chu, S.-J. Park and H. Y. Kim, Formation of electrospun nylon-6/methoxy poly(ethylene glycol) oligomer spider-wave nanofibers, *Materials Letters*, 2010, **64**, 2087–2090.

49 S. Zhang, H. Liu, F. Zuo, X. Yin, J. Yu and B. Ding, A Controlled Design of Ripple-Like Polyamide-6 Nanofiber/Nets Membrane for High-Efficiency Air Filter, *Small*, 2017, **13**, 1603151.

50 D. Kimmer, P. Slobodian, D. Petráš, M. Zatloukal, R. Olejník and P. Sáha, Polyurethane/multiwalled carbon nanotube nanowebs prepared by an electrospinning process, *Journal of Applied Polymer Science*, 2009, **111**, 2711–2714.

51 S. Zhang, H. Liu, X. Yin, Z. Li, J. Yu and B. Ding, Tailoring Mechanically Robust Poly(m-phenylene isophthalamide) Nanofiber/nets for Ultrathin High-Efficiency Air Filter, *Sci Rep*, 2017, **7**, 40550.

52 S. Zhang, H. Liu, J. Yu, W. Luo and B. Ding, Microwave structured polyamide-6 nanofiber/net membrane with embedded poly(m-phenylene isophthalamide) staple fibers for effective ultrafine particle filtration, *J. Mater. Chem. A*, 2016, **4**, 6149–6157.

53 I. Anastopoulos and I. Pashalidis, Single-use surgical face masks, as a potential source of microplastics: Do they act as pollutant carriers?, *Journal of Molecular Liquids*, 2021, **326**, 115247.

54 O. O. Fadare and E. D. Okoffo, Covid-19 face masks: A potential source of microplastic fibers in the environment, *Science of The Total Environment*, 2020, **737**, 140279.

55 M. Ma, D. Xu, J. Zhao and B. Gao, Disposable face masks release micro particles to the aqueous environment after simulating sunlight aging: Microplastics or non-microplastics?, *Journal of Hazardous Materials*, 2023, **443**, 130146.

56 P. Pfohl, M. Wagner, L. Meyer, P. Domercq, A. Praetorius, T. Hüffer, T. Hofmann and W. Wohlleben, Environmental Degradation of Microplastics: How to Measure Fragmentation Rates to Secondary Micro- and Nanoplastic Fragments and Dissociation into Dissolved Organics, *Environ. Sci. Technol.*, 2022, **56**, 11323–11334.

57 D. P. Mesquita, C. Quintelas and E. C. Ferreira, Fate and occurrence of microplastics in wastewater treatment plants, *Environ. Sci.: Adv.*, , DOI:10.1039/D3VA00167A.

58 J. Li, K. Zhang and H. Zhang, Adsorption of antibiotics on microplastics, *Environmental Pollution*, 2018, **237**, 460–467.

59 V. Godoy, G. Blázquez, M. Calero, L. Quesada and M. A. Martín-Lara, The potential of microplastics as carriers of metals, *Environmental Pollution*, 2019, **255**, 113363.

60 N. Oz, G. Kadİzade and M. Yurtsever, Investigation of heavy metal adsorption on microplastics., *Applied Ecology and Environmental Research*, 2019, **17**, 7301–7310.

61 N. B. Hartmann, S. Rist, J. Bodin, L. H. Jensen, S. N. Schmidt, P. Mayer, A. Meibom and A. Baun, Microplastics as vectors for environmental contaminants: Exploring sorption, desorption, and transfer to biota, *Integrated Environmental Assessment and Management*, 2017, **13**, 488–493.

62 X. Wang, B. Ding, J. Yu and J. Yang, Large-scale fabrication of two-dimensional spider-web-like gelatin nano-nets via electro-netting, *Colloids and Surfaces B: Biointerfaces*, 2011, **86**, 345–352.

63 J. Ayutsede, M. Gandhi, S. Sukigara, H. Ye, C. Hsu, Y. Gogotsi and F. Ko, Carbon Nanotube Reinforced Bombyx mori Silk Nanofibers by the Electrospinning Process, *Biomacromolecules*, 2006, **7**, 208–214.

64 N. Wang, Y. Si, J. Yu, H. Fong and B. Ding, Nano-fiber/net structured PVA membrane: Effects of formic acid as solvent and crosslinking agent on solution properties and membrane morphological structures, *Materials & Design*, 2017, **120**, 135–143.

65 G. C. da Mata, M. S. Morais, W. P. de Oliveira and M. L. Aguiar, Composition Effects on the Morphology of PVA/Chitosan Electrospun Nanofibers, *Polymers*, 2022, **14**, 4856.

66 E. Mele, Electrospinning of natural polymers for advanced wound care: towards responsive and adaptive dressings, *J. Mater. Chem. B*, 2016, **4**, 4801–4812.

67 P. A. M. Chagas, R. Schneider, D. M. dos Santos, A. J. G. Otuka, C. R. Mendonça and D. S. Correa, Bilayered electrospun membranes composed of poly(lactic-acid)/natural rubber: A strategy against curcumin photodegradation for wound dressing application, *Reactive and Functional Polymers*, 2021, **163**, 104889.

68 G. B. Medeiros, P. R. de Souza, K. M. Retamiro, C. V. Nakamura, E. C. Muniz and E. Corradini, Experimental design to evaluate properties of electrospun fibers of zein/poly (ethylene oxide) for biomaterial applications, *Journal of Applied Polymer Science*, 2021, **138**, 50898.

69 M. S. Morais, D. P. F. Bonfim, M. L. Aguiar and W. P. Oliveira, Electrospun Poly (Vinyl Alcohol) Nanofibrous Mat Loaded with Green Propolis Extract, Chitosan and Nystatin as an Innovative Wound Dressing Material, *Journal of Pharmaceutical Innovation*, 2022, 1–15.

70 E. Abdelhakeem, S. Monir, M. H. M. Teaima, K. O. Rashwan and M. El-Nabarawi, State-of-the-Art Review of Advanced Electrospun Nanofiber Composites for Enhanced Wound Healing, *AAPS PharmSciTech*, 2023, **24**, 246.

71 C. Vineis and A. Varesano, in *Electrofluidodynamic Technologies (EFDTs) for Biomaterials and Medical Devices*, eds. V. Guarino and L. Ambrosio, Woodhead Publishing, 2018, pp. 275–294.

72 R. M. D. Soares, N. M. Siqueira, M. P. Prabhakaram and S. Ramakrishna, Electrospinning and electrospray of bio-based and natural polymers for biomaterials development, *Materials Science and Engineering: C*, 2018, **92**, 969–982.

73 E. B. Souto, I. Baldim, W. P. Oliveira, R. Rao, N. Yadav, F. M. Gama and S. Mahant, SLN and NLC for topical, dermal, and transdermal drug delivery, *Expert Opinion on Drug Delivery*, 2020, **17**, 357–377.

74 I. Baldim, L. Tonani, M. R. von Zeska Kress and W. Pereira Oliveira, Lippia sidoides essential oil encapsulated in lipid nanosystem as an anti-Candida agent, *Industrial Crops and Products*, 2019, **127**, 73–81.

75 I. Baldim, M. H. Paziani, P. H. Grizante Barião, M. R. von Z. Kress and W. P. Oliveira, Nanostructured Lipid Carriers Loaded with Lippia sidoides Essential Oil as a Strategy to Combat the Multidrug-Resistant Candida auris, *Pharmaceutics*, 2022, **14**, 180.

76 C.-Y. Chen, Y.-H. Lee, S.-H. Chang, Y.-F. Tsai, J.-Y. Fang and T.-L. Hwang, Oleic acid-loaded nanostructured lipid carrier inhibits neutrophil activities in the presence of albumin and alleviates skin inflammation , *IJN*, 2019, **14**, 6539–6553.

77 R. Chitas, C. Nunes, S. Reis, P. Parreira and M. C. L. Martins, How Charge, Size and Protein Corona Modulate the Specific Activity of Nanostructured Lipid Carriers (NLC) against Helicobacter pylori, *Pharmaceutics*, 2022, **14**, 2745.

78 G. C. da Mata, M. S. Morais, W. P. de Oliveira and M. L. Aguiar, Sustainable surgical masks: optimizing fine/ultrafine particle filtration using PVA/chitosan electrospun nanofibers, *Environ. Sci.: Nano*, 2023, **10**, 2185–2200.

79 H. Gao, Y. Yang, O. Akampumuza, J. Hou, H. Zhang and X. Qin, A low filtration resistance three-dimensional composite membrane fabricated via free surface electrospinning for effective PM2.5 capture, *Environ. Sci.: Nano*, 2017, **4**, 864–875.

80 D. S. Almeida, L. D. Martins, E. C. Muniz, A. P. Rudke, R. Squizzato, A. Beal, P. R. de Souza, D. P. F. Bonfim, M. L. Aguiar and M. L. Gimenes, Biodegradable CA/CPB electrospun nanofibers for efficient retention of airborne nanoparticles, *Process Safety and Environmental Protection*, 2020, **144**, 177–185.

81 A. C. C. Bortolassi, S. Nagarajan, B. de Araújo Lima, V. G. Guerra, M. L. Aguiar, V. Huon, L. Soussan, D. Cornu, P. Miele and M. Bechelany, Efficient nanoparticles removal and bactericidal action of electrospun nanofibers membranes for air filtration, *Mater Sci Eng C Mater Biol Appl*, 2019, **102**, 718–729.

82 A. C. C. Bortolassi, V. G. Guerra and M. L. Aguiar, Characterization and evaluate the efficiency of different filter media in removing nanoparticles, *Separation and Purification Technology*, 2017, **175**, 79–86.

83 W. W. F. Leung and Q. Sun, Electrostatic charged nanofiber filter for filtering airborne novel coronavirus (COVID-19) and nano-aerosols, *Separation and Purification Technology*, 2020, **250**, 116886.

84 W. W. F. Leung and Q. Sun, Charged PVDF multilayer nanofiber filter in filtering simulated airborne novel coronavirus (COVID-19) using ambient nano-aerosols, *Separation and Purification Technology*, 2020, **245**, 116887.

85 D. P. F. Bonfim, F. G. S. Cruz, R. E. S. Bretas, V. G. Guerra and M. L. Aguiar, A Sustainable Recycling Alternative: Electrospun PET-Membranes for Air Nanofiltration, *Polymers*, 2021, **13**, 1166.

86 D. P. F. Bonfim, F. G. S. Cruz, V. G. Guerra and M. L. Aguiar, Development of Filter Media by Electrospinning for Air Filtration of Nanoparticles from PET Bottles, *Membranes*, 2021, **11**, 293.

87 X. Geng, O.-H. Kwon and J. Jang, Electrospinning of chitosan dissolved in concentrated acetic acid solution, *Biomaterials*, 2005, **26**, 5427–5432.

88 C. Wang, T. Hashimoto and Y. Wang, Extension Rate and Bending Instability of Electrospinning Jets: the Role of the Electric Field, *Macromolecules*, 2021, **54**, 7193–7209.

89 C. Wang, J. Wang, L. Zeng, Z. Qiao, X. Liu, H. Liu, J. Zhang and J. Ding, Fabrication of Electrospun Polymer Nanofibers with Diverse Morphologies, *Molecules*, 2019, **24**, 834.

90 A. Mirek, P. Korycka, M. Grzeczkowicz and D. Lewińska, Polymer fibers electrospun using pulsed voltage, *Materials & Design*, 2019, **183**, 108106.

91 C. G. Reyes and J. P. F. Lagerwall, Disruption of Electrospinning due to Water Condensation into the Taylor Cone, *ACS Applied Materials & Interfaces*, 2020, **12**, 26566–26576.

92 S. Haider and A. Haider, *Electrospinning and Electrospraying - Techniques and Applications*, 2019.

93 J. M. Deitzel, J. Kleinmeyer, D. Harris and N. C. Beck Tan, The effect of processing variables on the morphology of electrospun nanofibers and textiles, *Polymer*, 2001, **42**, 261–272.

94 R. P. A. Hartman, D. J. Brunner, D. M. A. Camelot, J. C. M. Marijnissen and B. Scarlett, JET BREAK-UP IN ELECTROHYDRODYNAMIC ATOMIZATION IN THE CONE-JET MODE, *Journal of Aerosol Science*, 2000, **31**, 65–95.

95 H.-H. Kim, J.-H. Kim and A. Ogata, Time-resolved high-speed camera observation of electrospray, *Journal of Aerosol Science*, 2011, **42**, 249–263.

96 N. B. Halima, Poly(vinyl alcohol): review of its promising applications and insights into biodegradation, *RSC Adv.*, 2016, **6**, 39823–39832.

97 V. F. Medina, C. S. Griggs, B. Petery, J. Mattei-Sosa, L. Gurtowski, S. A. Waisner, J. Blodget and R. Moser, Fabrication, Characterization, and Testing of Graphene Oxide and Hydrophilic Polymer Graphene Oxide Composite Membranes in a Dead-End Flow System, *Journal of Environmental Engineering*, 2017, **143**, 04017072.

98 W. W.-F. Leung, C.-H. Hung and P.-T. Yuen, Effect of face velocity, nanofiber packing density and thickness on filtration performance of filters with nanofibers coated on a substrate, *Separation and Purification Technology*, 2010, **71**, 30–37.

99 T. M. Bucher, H. V. Tafreshi and G. C. Tepper, Modeling performance of thin fibrous coatings with orthogonally layered nanofibers for improved aerosol filtration, *Powder Technology*, 2013, **249**, 43–53.

100 B. Xiao, W. Wang, X. Zhang, G. Long, J. Fan, H. Chen and L. Deng, A novel fractal solution for permeability and Kozeny-Carman constant of fibrous porous media made up of solid particles and porous fibers, *Powder Technology*, 2019, **349**, 92–98.

101 E. Hadipour-Goudarzi, N. Hemmatinejad and M. A. Shokrgozar, Fabrication and DOE Optimization of Electrospun Chitosan/Gelatin/PVA Nanofibers for Skin Tissue Engineering, *Macromolecular Materials and Engineering*, 2023, **308**, 2200562.

102 J. Bae, H. Kim, S. Park, K. S. Kim and H. Choi, Parametrization Study of Electrospun Nanofiber Including LiCl Using Response Surface Methodology (RSM) for Water Treatment Application, *Applied Sciences*, 2020, **10**, 7295.

103 R. Belalia, S. Grelier, M. Benaissa and V. Coma, New Bioactive Biomaterials Based on Quaternized Chitosan, *J. Agric. Food Chem.*, 2008, **56**, 1582–1588.

104 P. Fernandez-Saiz, J. M. Lagaron and M. J. Ocio, Optimization of the biocide properties of chitosan for its application in the design of active films of interest in the food area, *Food Hydrocolloids*, 2009, **23**, 913–921.

105 P. Lu and Y. Xia, Maneuvering the Internal Porosity and Surface Morphology of Electrospun Polystyrene Yarns by Controlling the Solvent and Relative Humidity, *Langmuir*, 2013, **29**, 7070–7078.

106 B. Zaarour, L. Zhu, C. Huang and X. Jin, Controlling the Secondary Surface Morphology of Electrospun PVDF Nanofibers by Regulating the Solvent and Relative Humidity, *Nanoscale Research Letters*, 2018, **13**, 285.

107 S. Zhang, N. A. Rind, N. Tang, H. Liu, X. Yin, J. Yu and B. Ding, in *Electrospinning: Nanofabrication and Applications*, eds. B. Ding, X. Wang and J. Yu, William Andrew Publishing, 2019, pp. 365–389.

108 J. Payen, P. Vroman, M. Lewandowski, A. Perwuelz, S. Callé-Chazelet and D. Thomas, Influence of fiber diameter, fiber combinations and solid volume fraction on air filtration properties in nonwovens, *Textile Research Journal*, 2012, **82**, 1948–1959.

109 P. Bulejko, O. Krištof, M. Dohnal and T. Svěrák, Fine/ultrafine particle air filtration and aerosol loading of hollow-fiber membranes: A comparison of mathematical models for the most penetrating particle size and dimensionless permeability with experimental data, *Journal of Membrane Science*, 2019, **592**, 117393.

110 A. E. de Oliveira, M. Aguiar and V. Guerra, Improved filter media with PVA/citric acid/Triton X-100 nanofibers for filtration of nanoparticles from air, *Polymer Bulletin*, , DOI:10.1007/s00289-020-03431-w.

111 M. Lu, H. Zhu, M. Lin, F. Wang, L. Hong, J.-F. Masson and W. Peng, Comparative study of block copolymer-templated localized surface plasmon resonance optical fiber biosensors: CTAB or citrate-stabilized gold nanorods, *Sensors and Actuators B: Chemical*, 2021, **329**, 129094.
112 J. M. Gisbert-González, M. V. Oliver-Pardo, F. J. Sarabia, V. Climent, J. M. Feliu and E. Herrero, On the behavior of CTAB/CTAOH adlayers on gold single crystal surfaces, *Electrochimica Acta*, 2021, **391**, 138947.
113 J. He, S. Unser, I. Bruzas, R. Cary, Z. Shi, R. Mehra, K. Aron and L. Sagle, The facile removal of CTAB from the surface of gold nanorods, *Colloids and Surfaces B: Biointerfaces*, 2018, **163**, 140–145.
114 A. Konda, A. Prakash, G. A. Moss, M. Schmoldt, G. D. Grant and S. Guha, Aerosol Filtration Efficiency of Common Fabrics Used in Respiratory Cloth Masks, *ACS Nano*, 2020, **14**, 6339–6347.
115 R. Balgis, C. W. Kartikowati, T. Ogi, L. Gradon, L. Bao, K. Seki and K. Okuyama, Synthesis and evaluation of straight and bead-free nanofibers for improved aerosol filtration, *Chemical Engineering Science*, 2015, **137**, 947–954.
116 A. Kravtsov, H. Brnig, S. Zhandarov and R. Beyreuther, 2000.
117 D. Lv, M. Zhu, Z. Jiang, S. Jiang, Q. Zhang, R. Xiong and C. Huang, Green Electrospun Nanofibers and Their Application in Air Filtration, *Macromolecular Materials and Engineering*, 2018, **303**, 1800336.
118 M. Zhu, J. Han, F. Wang, W. Shao, R. Xiong, Q. Zhang, H. Pan, Y. Yang, S. K. Samal, F. Zhang and C. Huang, Electrospun Nanofibers Membranes for Effective Air Filtration, *Macromolecular Materials and Engineering*, 2017, **302**, 1600353.
119 K. Aruchamy, A. Mahto and S. K. Nataraj, Electrospun nanofibers, nanocomposites and characterization of art: Insight on establishing fibers as product, *Nano-Structures & Nano-Objects*, 2018, **16**, 45–58.
120 X. Zhao, S. Wang, X. Yin, J. Yu and B. Ding, Slip-Effect Functional Air Filter for Efficient Purification of PM2.5, *Sci Rep*, 2016, **6**, 35472.
121 Z. Quan, Y. Zu, Y. Wang, M. Zhou, X. Qin and J. Yu, Slip effect based bimodal nanofibrous membrane for high-efficiency and low-resistance air purification, *Separation and Purification Technology*, 2021, **275**, 119258.
122 D. Shou, L. Ye and J. Fan, Gas transport properties of electrospun polymer nanofibers, *Polymer*, 2014, **55**, 3149–3155.
123 C.-H. Hung and W. W.-F. Leung, Filtration of nano-aerosol using nanofiber filter under low Peclet number and transitional flow regime, *Separation and Purification Technology*, 2011, **79**, 34–42.
124 P. Li, C. Wang, Y. Zhang and F. Wei, Air filtration in the free molecular flow regime: a review of high-efficiency particulate air filters based on carbon nanotubes, *Small*, 2014, **10**, 4543–4561.
125 O. Das, R. E. Neisiany, A. J. Capezza, M. S. Hedenqvist, M. Försth, Q. Xu, L. Jiang, D. Ji and S. Ramakrishna, The need for fully bio-based facemasks to counter coronavirus outbreaks: A perspective, *Science of The Total Environment*, 2020, **736**, 139611.
126 S. Zhang, N. Wang, Q. Zhang, R. Guan, Z. Qu, L. Sun and J. Li, The Rise of Electroactive Materials in Face Masks for Preventing Virus Infections, *ACS Appl. Mater. Interfaces*, 2023, **15**, 48839–48854.
127 F. de A. Lima, G. B. Medeiros, P. A. M. Chagas, M. L. Aguiar and V. G. Guerra, Aerosol Nanoparticle Control by Electrostatic Precipitation and Filtration Processes—A Review, *Powders*, 2023, **2**, 259–298.
128 G. B. Medeiros, F. de A. Lima, D. S. de Almeida, V. G. Guerra and M. L. Aguiar, Modification and Functionalization of Fibers Formed by Electrospinning: A Review, *Membranes*, 2022, **12**, 861.
129 F. de A. Lima and V. G. Guerra, Influence of wire spacing and plate spacing on electrostatic precipitation of nanoparticles: An approach involving electrostatic shielding and diffusion charging, *Particuology*, 2023, **80**, 127–139.
130 F. M. O. da Silva, L. G. M. da Silva, A. C. A. Justi, M. V. Rodrigues and M. L. Aguiar, Use of hybrid filters to optimize the process of the filtration in cement particles, *Heliyon*, , DOI:10.1016/j.heliyon.2023.e21808.
131 V. K. Thakur, *Nanocellulose Polymer Nanocomposites: Fundamentals and Applications*, John Wiley & Sons, 2014.
132 T. Xia, Y. Bian, L. Zhang and C. Chen, Relationship between pressure drop and face velocity for electrospun nanofiber filters, *Energy and Buildings*, 2018, **158**, 987–999.
133 M. Zhu, Q. Cao, B. Liu, H. Guo, X. Wang, Y. Han, G. Sun, Y. Li and J. Zhou, A novel cellulose acetate/poly (ionic liquid) composite air filter, *Cellulose*, 2020, **27**, 3889–3902.
134 ASTM F2100, Standard Specification for Performance of Materials Used in Medical Face Masks, https://www.astm.org/f2100-21.html, (accessed 19 February 2023).
135 NIOSH guide to the selection and use of particulate respirators certified under 42 CFR 84., , DOI:10.26616/NIOSHPUB96101.
136 EN 14683, EN 14683, https://www.scandiagear.com/quality/norms-and-standards/personal-protection/en14683-2019/, (accessed 19 February 2023).
137 ABNT NBR 15052, Máscara de uso odonto-médico-hospitalar - Requisitos e métodos de ensaio, https://www.abntcatalogo.com.br/pnm.aspx?Q=UEQyTEsvQUVVYmV2WWVNVU9KS1Y4WHRzY2JLV2c0QkZKVStpMGtMMVNWbz0=, (accessed 21 February 2023).

4.6 Supplementary Materials

Methodology of Permeability & Filtration Efficiency

Permeability analyses were performed on each of the filter membranes by directing purified air through them. The flow rate ranged from 0.1 to 2.0 $L.h^{-1}$ in ten increments to assess the filters' pressure differential (**Equation S5.1**).

$$\frac{\Delta P}{L} = \frac{\mu}{K_1} v_s \qquad \textbf{(S5.1)}$$

where **ΔP** is the Pressure Drop; **L** is the filter media thickness; **μ** is the fluid viscosity (*i.e.*, air); and $\mathbf{v_s}$ is the surface velocity. The thickness of the fiber mat layer (L) was determined utilizing an optical microscope (Olympus BX60, Olympus Co., Shinjuku, Tokyo, Japan) at magnifications of x10, and x20. The electric particle mobility technique was employed to determine the collection efficiency (**η**) of the filters. **Equation S5.2** illustrates the calculation process for the filters' collection efficiency. This approach involves comparing the number of particles passing through the filter media with those expelled from it. Sodium chloride (NaCl) nanoparticles were utilized,[1,2] with a surface velocity maintained at 1.5 $L.h^{-1}$ and a filtration area of 5.2 cm^2 for each sample.[3–5] The NaCl nanoparticles ranged from 7 to 250 nm.

$$\eta = \frac{C_0 - C_f}{C_0} . 100 \qquad \textbf{(S5.2)}$$

where $\mathbf{C_0}$ and $\mathbf{C_f}$ are the concentration of nanoparticles before and after the filter media, respectively.

Using the experimental results of **η** and the corresponding **ΔP**, we calculated the Quality Factor ($\mathbf{Q_f}$), which serves as a metric for assessing the overall performance of the filter media (as shown in **Equation S5.3**):

$$Q_f = \frac{-\ln(1-\eta)}{\Delta P} \qquad \textbf{(S5.3)}$$

Filtering efficiency and permeability of the filter media coated with nanofibers were determined on the filtration modulus available in the Laboratory of Environmental Control I (DEQ/UFSCar), as described in **Figure 5.1**. The filtration modulus consists of an air compressor (Shultz Acworth, GA, USA), an air filter for air purification, a nanoparticle generator (Model 3079, TSI, Shoreview, MN, USA), a diffusion dryer (Norgren IMI, Birmingham, UK), a neutralizer of krypton and americium (Model 3054, TSI, Shoreview, MN, USA), and a filter support device. The module apparatus is attached to an electrostatic classifier, a Scanning Mobility Particle Sizer spectrometer (SMPS - Model 3080, TSI, Shoreview, MN, USA), and an ultrafine particle counter (Model 3776, TSI, Shoreview, MN, USA)[6].

Table S5.1: Electrical conductivity ($\mu S.cm^{-1}$) of pure solution of chitosan (CS) and polyvinyl alcohol (PVA) and in mixtures of both. (Copyright © 2022 Gustavo C. Mata et al.). [8]

Chitosan (CS) content (%)	Polyvinyl alcohol (PVA) content (%)				
	0.0	4.5	6.0	7.5	9.0
0.00	-	238.06	231.99	249.75	286.41
0.25	519.92	312.98	254.31	247.65	278.89
0.50	826.48	326.97	301.87	300.82	180.51
0.75	1176.31	347.91	363.20	350.97	195.31
1.00	1505.96	445.97	396.27	369.77	211.83

Table S5.2: Fiber diameter distribution (nm) for the different compositions of electrospun fibers obtained from the samples described in **Table 4.1**. (Copyright © 2022 Gustavo C. Mata et al.). [8]

Chitosan Content (%)	**Polyvinyl Alcohol (PVA) Content (%)**			
	4.5	**6.0**	**7.5**	**9.0**
0.25	153.1 ± 31.2	214.8 ± 38.7	240.9 ± 76.8	282.4 ± 40.2
0.50	193.4 ± 40.5	234.0 ± 34.4	242.3 ± 62.6	398.8 ± 65.5
0.75	159.3 ± 27.8	229.1 ± 39.9	286.2 ± 87.1	261.8 ± 66.6
1.00	162.4 ± 21.2	204.4 ± 32.2	376.7 ± 89.0	416.4 ± 101.8

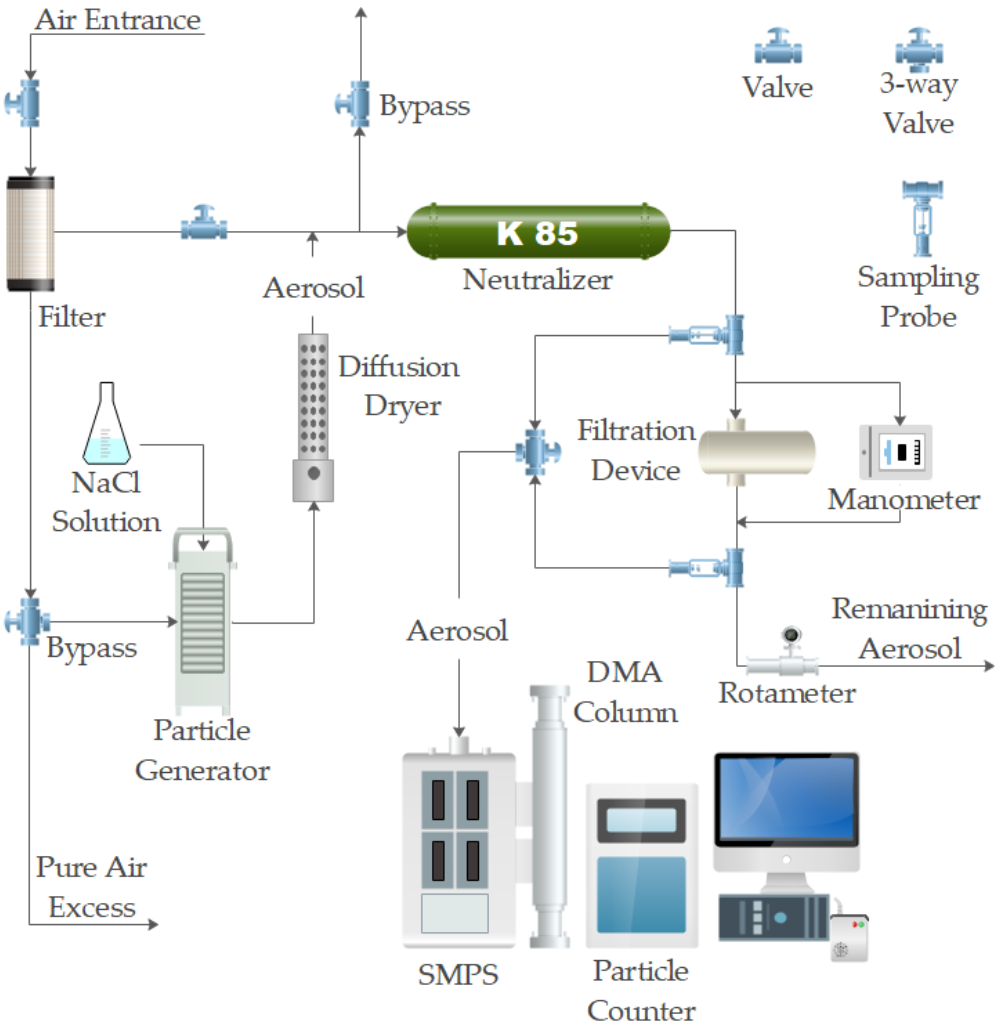

Figure S5.1: Experimental apparatus to evaluate filter media collection efficiency of the Laboratory of Environmental Control I (DEQ/UFSCar).[7]

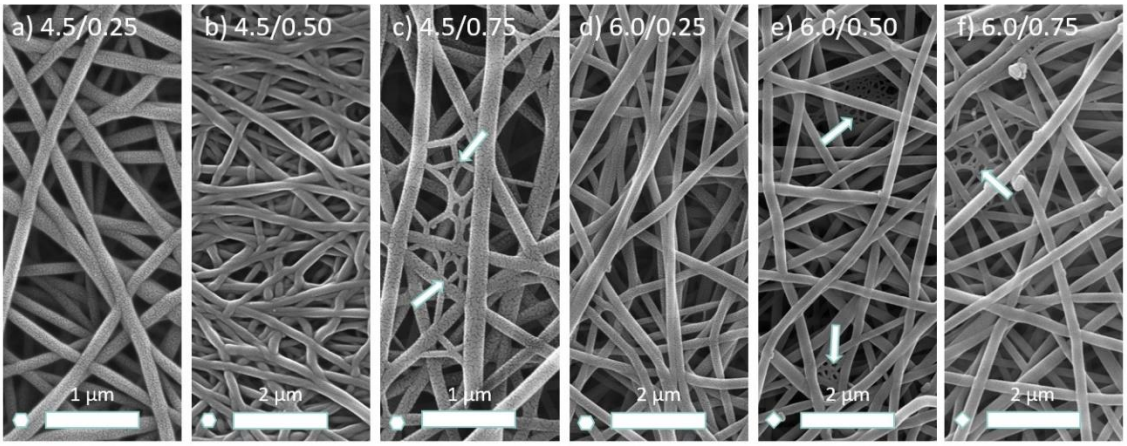

Figure S5.2: SEM images of electrospun samples in the series of PVA 4.5% and 6.0% with CS: **a)** and **d)** at 0.25%; **b)** and **e)** at 0.50%; and **c)** and **f)** at 0.75%, respectively.

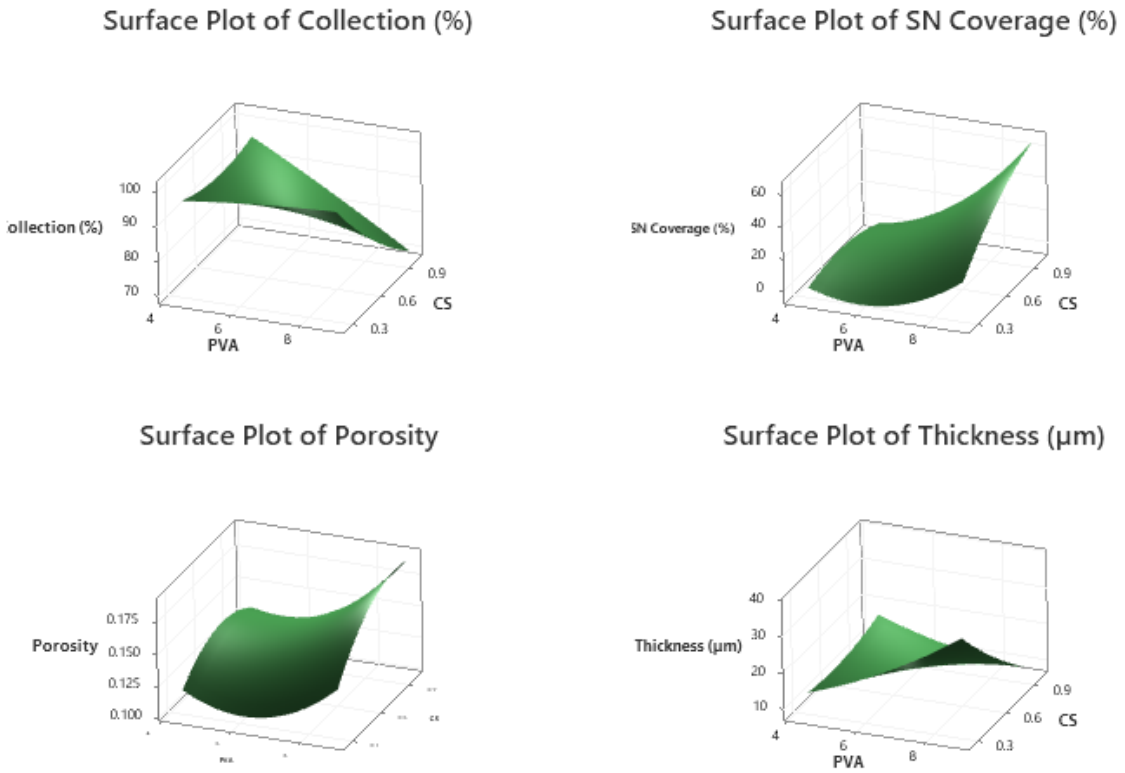

Figure S5.5: Surface plots showing the behavior of the PVA and chitosan content in each of the responses studied.

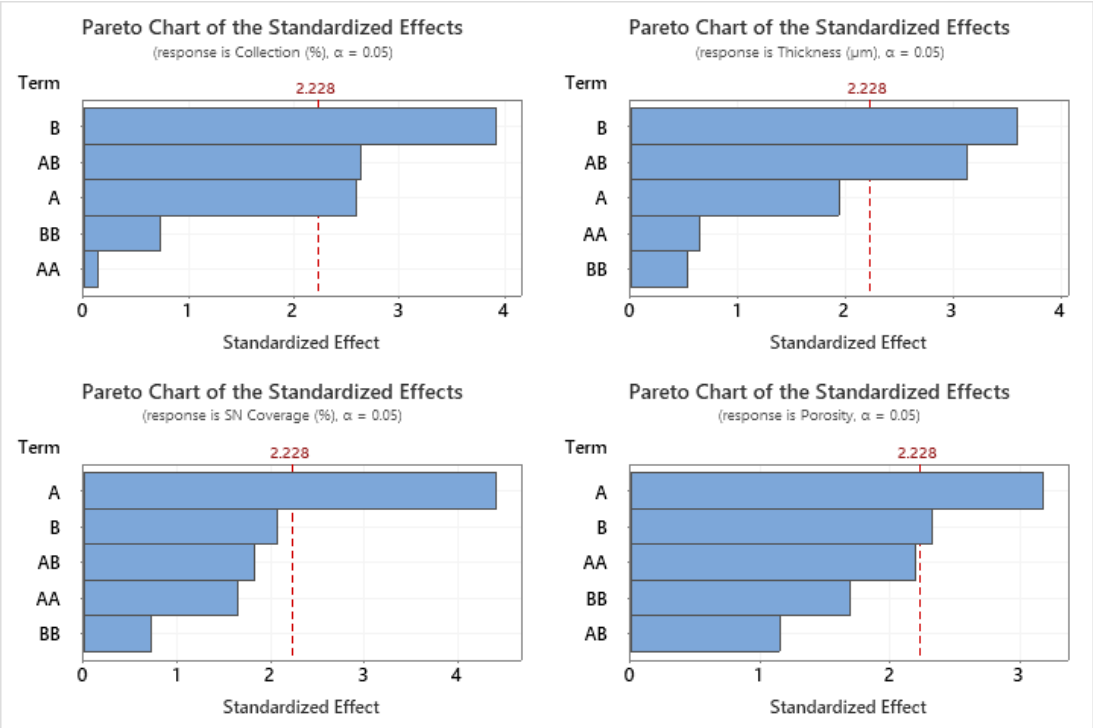

Figure S5.3: Pareto charts showing the relevance of each factor in the responses of this study. Term A represents the PVA Content, while term B is the chitosan content.

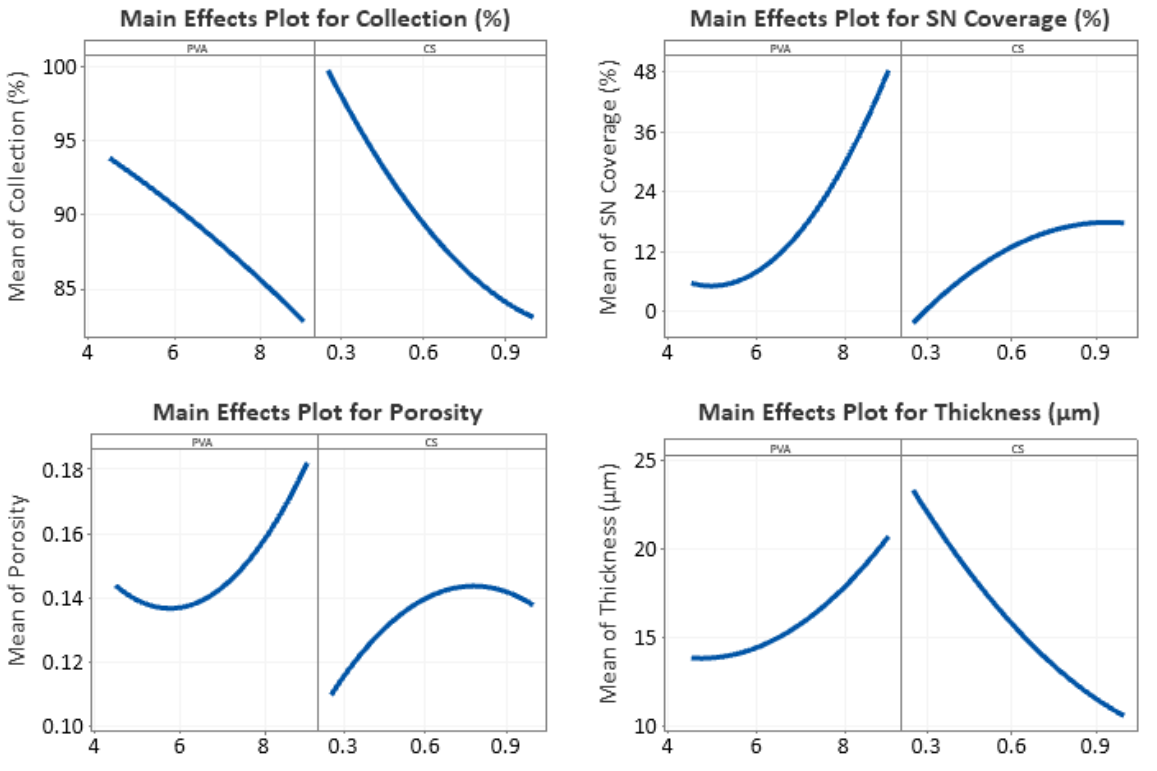

Figure S5.4: Main effect plots showing the individual influence of each parameter in the respective response.

Table S5.3: Models generated by Response Surface Analysis of the Multilevel Factorial Desing.

Response		Model	p-Value
Collection (%)	=	84.3 + 4.45 PVA + 14.8 CS - 0.100 PVA*PVA + 18.4 CS*CS - 8.88 PVA*CS	0.008
SN Coverage (%)	=	96.0 - 34.8 PVA - 15.6 CS + 2.63 PVA*PVA - 41.7 CS*CS + 13.99 PVA*CS	0.008
Porosity	=	0.2580 - 0.0574 PVA + 0.115 CS + 0.00437 PVA*PVA - 0.1216 CS*CS + 0.01099 PVA*CS	0.016
Thickness (µm)	=	0.1 + 1.93 PVA + 28.3 CS + 0.377 PVA*PVA + 11.3 CS*CS - 8.80 PVA*CS	0.011

Table S5.4: ANOVA analysis of the response model for fiber mat Collection Efficiency.

Analysis of Variance					
Source	DF	Adj SS	Adj MS	F-Value	P-Value
Model	5	1183.99	236.798	5.92	0.008
Linear	2	885.14	442.572	11.07	0.003
PVA	1	269.42	269.415	6.74	0.027
CS	1	615.73	615.729	15.40	0.003
Square	2	21.91	10.953	0.27	0.766
PVA*PVA	1	0.81	0.813	0.02	0.889
CS*CS	1	21.09	21.093	0.53	0.484
2-Way Interaction	1	276.94	276.939	6.93	0.025
PVA*CS	1	276.94	276.939	6.93	0.025
Error	10	399.71	39.971		
Total	15	1583.70			

Table S5.5: ANOVA analysis of the response model for the fiber mat Spider-net Coverage.

Analysis of Variance					
Source	DF	Adj SS	Adj MS	F-Value	P-Value
Model	5	6251.8	1250.4	6.07	0.008
Linear	2	4894.4	2447.2	11.89	0.002
PVA	1	4008.1	4008.1	19.47	0.001
CS	1	886.3	886.3	4.3	0.065
Square	2	669.8	334.9	1.63	0.245
PVA*PVA	1	561	561	2.72	0.13
CS*CS	1	108.8	108.8	0.53	0.484
2-Way Interaction	1	687.6	687.6	3.34	0.098
PVA*CS	1	687.6	687.6	3.34	0.098
Error	10	2058.9	205.9		
Total	15	8310.7			

Table S5.6: ANOVA analysis of the response model for the fiber mat Porosity.

Analysis of Variance					
Source	DF	Adj SS	Adj MS	F-Value	P-Value
Model	5	0.007895	0.001579	4.91	0.016
Linear	2	0.004997	0.002498	7.77	0.009
PVA	1	0.003253	0.003253	10.12	0.010
CS	1	0.001744	0.001744	5.42	0.042
Square	2	0.002473	0.001237	3.85	0.058
PVA*PVA	1	0.001549	0.001549	4.82	0.053
CS*CS	1	0.000925	0.000925	2.88	0.121
2-Way Interaction	1	0.000425	0.000425	1.32	0.277
PVA*CS	1	0.000425	0.000425	1.32	0.277
Error	10	0.003216	0.000322		
Total	15	0.011110			

Table S5.7: ANOVA analysis of the response model for the fiber mat Thickness.

Analysis of Variance					
Source	DF	Adj SS	Adj MS	F-Value	P-Value
Model	5	757.49	151.497	5.43	0.011
Linear	2	465.78	232.888	8.35	0.007
PVA	1	104.63	104.627	3.75	0.081
CS	1	361.15	361.148	12.95	0.005
Square	2	19.44	9.722	0.35	0.714
PVA*PVA	1	11.53	11.533	0.41	0.535
CS*CS	1	7.91	7.910	0.28	0.606
2-Way Interaction	1	272.27	272.267	9.77	0.011
PVA*CS	1	272.27	272.267	9.77	0.011
Error	10	278.81	27.881		
Total	15	1036.30			

References

1 W. W. F. Leung and Q. Sun, Electrostatic charged nanofiber filter for filtering airborne novel coronavirus (COVID-19) and nano-aerosols, *Separation and Purification Technology*, 2020, **250**, 116886.

2 W. W. F. Leung and Q. Sun, Charged PVDF multilayer nanofiber filter in filtering simulated airborne novel coronavirus (COVID-19) using ambient nano-aerosols, *Separation and Purification Technology*, 2020, **245**, 116887.

3 Z. Wang, F. Yan, H. Pei, J. Li, Z. Cui and B. He, Antibacterial and environmentally friendly chitosan/polyvinyl alcohol blend membranes for air filtration, *Carbohydrate Polymers*, 2018, **198**, 241–248.

4 D. P. F. Bonfim, F. G. S. Cruz, V. G. Guerra and M. L. Aguiar, Development of Filter Media by Electrospinning for Air Filtration of Nanoparticles from PET Bottles, *Membranes*, 2021, **11**, 293.

5 A. C. C. Bortolassi, V. G. Guerra and M. L. Aguiar, Characterization and evaluate the efficiency of different filter media in removing nanoparticles, *Separation and Purification Technology*, 2017, **175**, 79–86.

6 P. M. de Barros, S. S. Rodrigues Cirqueira and M. L. Aguiar, Evaluation of the Deposition of Nanoparticles in Fibrous Filter, *Materials Science Forum*, 2014, **802**, 174–179.

7 G. C. da Mata, M. S. Morais, W. P. de Oliveira and M. L. Aguiar, Sustainable surgical masks: optimizing fine/ultrafine particle filtration using PVA/chitosan electrospun nanofibers, *Environ. Sci.: Nano*, 2023, **10**, 2185–2200.

8 G. C. da Mata, M. S. Morais, W. P. de Oliveira and M. L. Aguiar, Composition Effects on the Morphology of PVA/Chitosan Electrospun Nanofibers, *Polymers*, 2022, **14**, 4856.

VI

SPIDER-NETS IN AIR FILTRATION II

VI - SPIDER-NETS IN AIR FILTRATION II

Electrospinning Parameters for Air Filtration with Spider-net Structures

Gustavo Cardoso Mata[1], Maria Sirlene Morais[2], Wanderley Pereira Oliveira[2], Mônica Lopes Aguiar[1]

[1] Department of Chemical Engineering, Federal University of São Carlos, Rod. Washington Luiz, km 235, SP310, São Carlos - SP, 13565-905, Brazil;

[2] Faculty of Pharmaceutical Science of Ribeirão Preto, University of São Paulo, Av. do Café s/nº, CEP: 14040-903, Bairro Monte Alegre, Ribeirão Preto, SP, Brazil

[*] *Corresponding authors*: gugs_cardoso@ufsj.edu.br/mlaguiar@ufscar.br

Abstract: Spider-nets, intricate structures formed between electrospun nanofibers, have garnered significant interest due to their unique morphology and potential applications in various fields. However, many aspects of its formation and the electrospinning parameters behind it, still unclear. This study investigates the influence of electrospinning parameters on spider-net structures and their impact on nanoparticle air filtration. Materials utilized included polyvinyl alcohol (PVA), chitosan (CS), and essential oil of *Lippia sidoides*. The formation of spider-nets, observed mainly in polymers with added salts, is affected by the solution's conductivity. By controlling electrospinning conditions and collector types, spider-net coverage can be enhanced, thereby improving nanoparticle filtration efficiency without significant increases in pressure drop. Scanning Electron Microscopy (SEM) analysis revealed that drum collectors facilitate higher spider-net coverage compared to flat plate collectors. Solvent tests demonstrated that acetic acid induces spider-net formation, while water impedes it. Air filtration tests showed that spider-net presence increases collection efficiency, albeit with slightly higher pressure drops. The best sample was 6.0/1.0/EO, with 99.64% collection efficiency and 117.3 Pa of pressure drop. It was produced using 23.4 kV of electric tension, with 1.17 $mL.h^{-1}$ of flow rate, during 28min. The study concludes that manipulating fiber charges, collector types, and solvent compositions can effectively control spider-net formation, offering new possibilities for biodegradable materials with enhanced functionalities and applications.

Keywords: *SARS-CoV-2; air filters; electrospinning; bioaerosols; antimicrobial, antiviral, biocide.*

Submitted to: Nano Life (World Scientific Publishing Co.).

6.1 Introduction

Spider-nets are unique structures formed between electrospun nanofibers. They present a peculiar spider web-like morphology, with its internal fibrils with diameters of less than 60 nm. The phenomena of spider-net formation were already observed in polymers with salt addition,[1] being the salt content a crucial factor.[2] Salts ionic species raise the polymer solutions' conductivity by dispersing charges, generating more hydrogen bonds between the chains.[3] Barakat *et al.* observed a threshold to the spider-net formation, disappearing at high conductivities.[2]

Spider-nets unique properties had attracted attention of the scientific community, aiming to explore its potential applications. Spider-net had already been applied for tissue scaffolds,[4–7] purification of lithium-ion batteries,[8] and water treatment.[9–11] The use of spider-nets for air filtration is still in its early stages, with plenty of room for research.

The main goal of this study is to understand the influence of the electrospinning parameters on the spider-net structures, and its influence on the air filtration of nanoparticles. The control of those structures is a promising technique to raise the nanoparticle filtration without significant increases in efficiency and pressure drop.

6.2 Methodology

6.2.1 Materials

The polymers used to produce the electrocpun nanofibers were polyvinyl alcohol (PVA) with a molecular weight of 85,500 $g.mol^{-1}$ and a hydrolysis degree of 89.5% (Vetec Química Fina, Duque de Caxias/RJ, Brazil) and chitosan (CS) with a deacetylation degree of 68.5% (Polymar, Fortaleza/CE, Brazil). Analytical-grade glacial acetic acid (G) at 99.0% purity (LabSynth, Diadema/SP, Brazil) was used as the solvent. The additives included the pure *Lippia Sidoides* essential oil (Produtos Naturais LTDA, Horizonte/CE, Brazil).

6.2.2 Solution and electrospinning parameters

Both polymers were weighed and dissolved in a mixture in proportion of 70:30 of glacial acetic acid for deionized water, under constant magnetic stirring for 3 h at temperatures between 80 and 90°C until complete dissolution and then mixed to create solutions with 6.0% of PVA and 1.0% of chitosan (6.0/1.00). This concentration is an optimum proportion find in our previous study[12]. It was also tested the composition of 7.5% of PVA and 0.25% of chitosan (sample 7.5/0.25).

The electrospinning apparatus is composed by a high-voltage generator with a continuous current source (Electrotest HIPOT CC, Model EH6005C, Instrutemp, São Paulo/SP, Brazil), an infusion pump (Harvard Apparatus, Model Elite I/W PROGR SINGLE, Holliston/MA, USA), a stainless-steel rotating cylinder as the drum collector and a copper plate as flat collector. The samples were also electrospun under optimal production parameters for the composition, as described in our previous study,[13] being

an electrical field of 23.4 kV, a flow rate of 1.17 mL/h, and a production time of 28 min. Drum rotation speed was 595 rpm and the needle tip to collector distance was set in 10 cm.

The nanofiber collection area was set at 196 cm² to standardize electrospinning between tests on a flat plate collector and a rotating drum collector. The sides of the drum collector were covered with polyethylene vinyl acetate (EVA) layers as insulators to trap the electric field lines in a specific area, a technique adapted from Nguyen *et al*.[14] For the flat plate collector, the collection area was a square with a size of 14 x 14 cm², with the needle tip pointing towards the center of the square. The electrical conductivity of the samples were determined in a Metrohm 912 bench-top conductometer (Metrohm AG, Herisau, Switzerland) in triplicate.

6.2.3 Morphological and Surface Analysis

Scanning Electron Microscopy (SEM) was used to investigate the nanofibers surface morphology of electrospun nanofibers. Electrospun nanofiber mat samples of 5×5 mm were coated with gold in a Bal-Tec SCD Sputter Coater model-050 (Fürstentum/Liechtenstein) under a pressure of 0.1 mbar. SEM photomicrographs were obtained with three different SEM equipment: a Carl Zeiss scanning electron microscope mod EVO 50 (Cambridge/United Kingdom); a SEM FEI Inspect F50 with FEG electron source with ETD and vCD detectors (Eindhoven/Netherlands); and a JEOL model JSM 6610LV (Tokyo, Japan). To identify the source of each image, SEM images were labeled with a symbol in the lower left corner: a rhombus for the Carl Zeiss EVO 50; a hexagon for the FEI Inspect F50; and a circle for the JSM 6610LV. It used magnifications between 5 and 20 kX.

To accurately measure the diameter distribution of the electrospun nanofibers, image analysis was conducted using SEM micrographs with ImageJ® software. The thickness of the fiber mats was measured using Image-Pro Plus 7.0®. Graphs were constructed using OriginPro® 2021, and images were created with Adobe Illustrator CC® 2019. Filtration data were analyzed using Excel® and PyCharm® (Python 3.11.4).

6.2.4 Air Filtration Tests

Air filtration tests were performed by the passage of clean air with superficial velocity ranging from 0.2 to 2.0 $L.h^{-1}$, to evaluate the filter's pressure drop.

$$\frac{\Delta \boldsymbol{P}}{\boldsymbol{L}} = \frac{\boldsymbol{\mu}}{\boldsymbol{K_1}} \boldsymbol{v_s} \qquad \textbf{(1)}$$

where $\Delta \boldsymbol{P}$ is the Pressure Drop; $\boldsymbol{L}$ is the filter media thickness; $\boldsymbol{\mu}$ is the fluid viscosity (*i.e.*, air); and $\boldsymbol{v_s}$ is the surface velocity. Fiber mat's layer thickness ($\boldsymbol{L}$) was measured

using an optical microscope (Olympus BX60, Olympus Co., Shinjuku, Tokyo, Japan) at magnifications of x10, and x20. The filters' collection efficiency ($\boldsymbol{\eta}$) was used with the electric particle mobility technique. **Equation 6.2** exemplifies the filters' collection efficiency calculation. This method uses the difference between the number of sodium chloride (NaCl) nanoparticles[15,16] before the filter media and those ejected from it. The flow rate was set at 1.5 L.h^{-1} and a filtration area of 5.2 cm² for each sample[17–19]. NaCl nanoparticles ranged from 7 to 250 nm.

$$\boldsymbol{\eta = \frac{C_0 - C_f}{C_0} . 100} \qquad \textbf{(6.2)}$$

where $\boldsymbol{C_0}$ and $\boldsymbol{C_f}$ are the concentration of nanoparticles before and after the filter media, respectively.

From the data results of $\boldsymbol{\eta}$, and $\boldsymbol{\Delta P}$, the Quality Factor ($\boldsymbol{Q_f}$) was calculated, measuring the overall performance of the filter media (**Equation 6.3**):

$$\boldsymbol{Q_f = \frac{-\ln(1-\eta)}{\Delta P}} \qquad \textbf{(6.3)}$$

The filtering efficiency and permeability of the filter media coated with nanofibers were assessed using the filtration setup available at the Laboratory of Environmental Control I (DEQ/UFSCar), as illustrated in **Figure 6.1**.

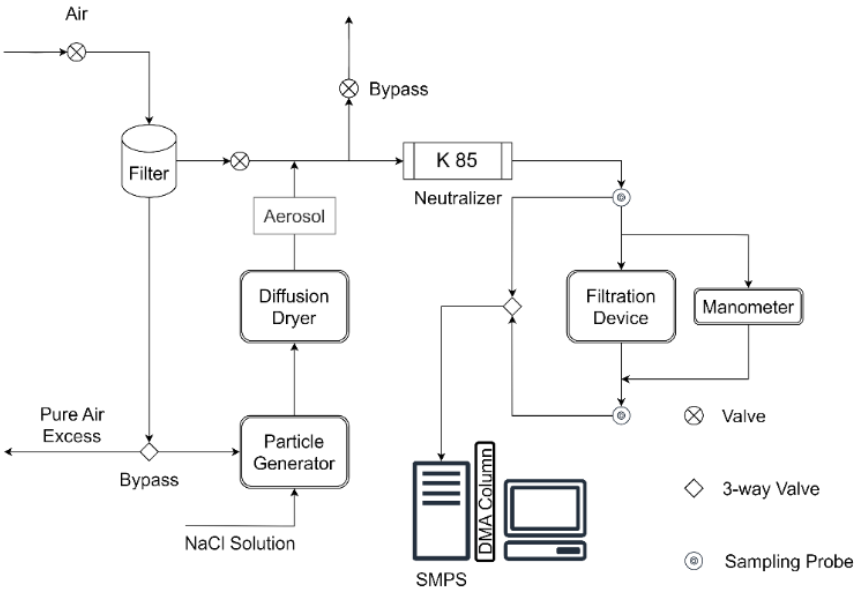

Figure 6.1: Experimental apparatus to evaluate filter media collection efficiency of the Laboratory of Environmental Control I (DEQ/UFSCar).

This filtration system comprises an air compressor (Shultz Acworth, GA, USA), an air purification filter, a nanoparticle generator (Model 3079, TSI, Shoreview, MN, USA), a diffusion dryer (Norgren IMI, Birmingham, UK), a krypton and americium neutralizer (Model 3054, TSI, Shoreview, MN, USA), and a filter support device. Additionally, the setup includes an electrostatic classifier, a Scanning Mobility Particle Sizer spectrometer (SMPS - Model 3080, TSI, Shoreview, MN, USA), and an ultrafine particle counter (Model 3776, TSI, Shoreview, MN, USA).[20]

6.3 Results & Discussion

6.3.1 Morphology analysis

The morphology of electrospun fibers can be influenced by the type of collectors used,[21–23] although the impact of the collector on spider-net formation has not been previously documented. To explore this influence, it tested several solutions and produced nanofibers using both a drum collector and a flat plate (**Figure 6.2**, **a)** to **d)**. We maintained a consistent collection area of 196 cm² to ensure uniform fiber packaging. Our observations reveal that the samples produced with a rotative drum exhibited a higher coverage of spider-nets compared to those electrospun over a flat plate. This finding is supported by most of the studies referenced in our research, which demonstrate the presence of spider-nets primarily using a metal roller or a rotative drum,[1,3–5,10,24–35] as opposed to a flat plate collector.[36] Additionally, some studies either do not specify the type of collector used,[2,6,8,11,31,37–41] or their electrospinning design do not align with the conditions discussed above.[7,42]

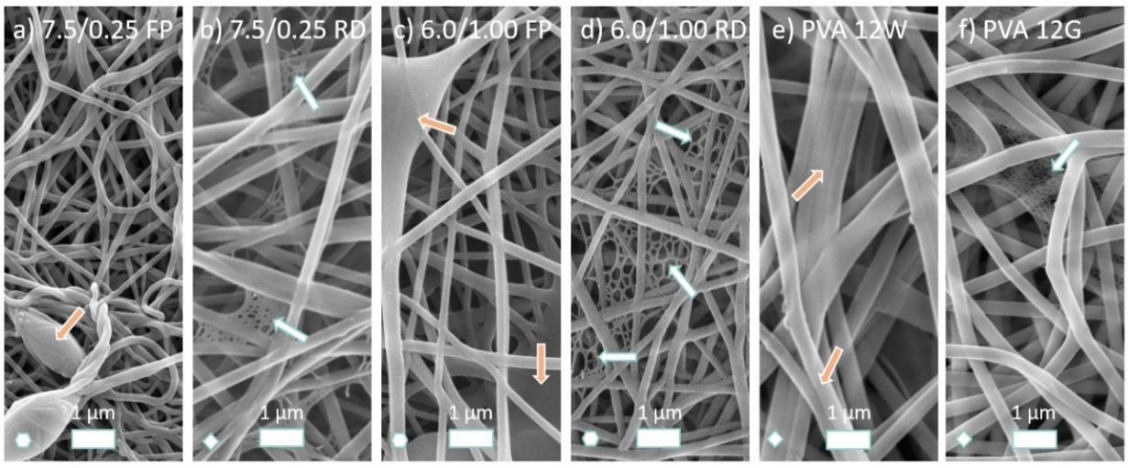

Figure 6.2: SEM images of fibers produced using a flat plate collector (FP) and a rotating drum collector (RD), where **a)** and **b)** represent a sample with 7.5% PVA and 0.25% CS, and **c)** and **d)** illustrate a sample with 6% PVA and 1.00% CS. Images **e)** and **f)** showcase samples with pure PVA at 12%, using water (W) and acetic acid (G) as solvents, respectively. White arrows indicate the presence of spider-net structures, while orange arrows indicate films, beads or fiber fusion.

The following reasoning can explain the mechanism behind the enhanced spider-net formation facilitated by the rotating drum. Upon deposition onto the collector, fibers and their associated charges become anchored at specific points on the drum surface, establishing a fixed charge orientation relative to the drum surface. As the drum rotates, these fixed charges undergo variations in their relative direction, consequently altering their orientation within the electric field direction.[43,44] This rotation of charges may generate a local magnetic field[45] and induce a current within the electrospun mat, thereby augmenting charge retention in the fiber mat.[26] These additional forces during deposition potentially bolster spider-net formation by subjecting charges to stress and increasing their mutual attraction. **Figure 6.3** illustrates this mechanism. The speed rotation could also improve spider-net formation. The rotational movement accelerates the solvent evaporation, facilitating the transition between the solvent phase to the polymer enrichment phase that forms the spider-nets.

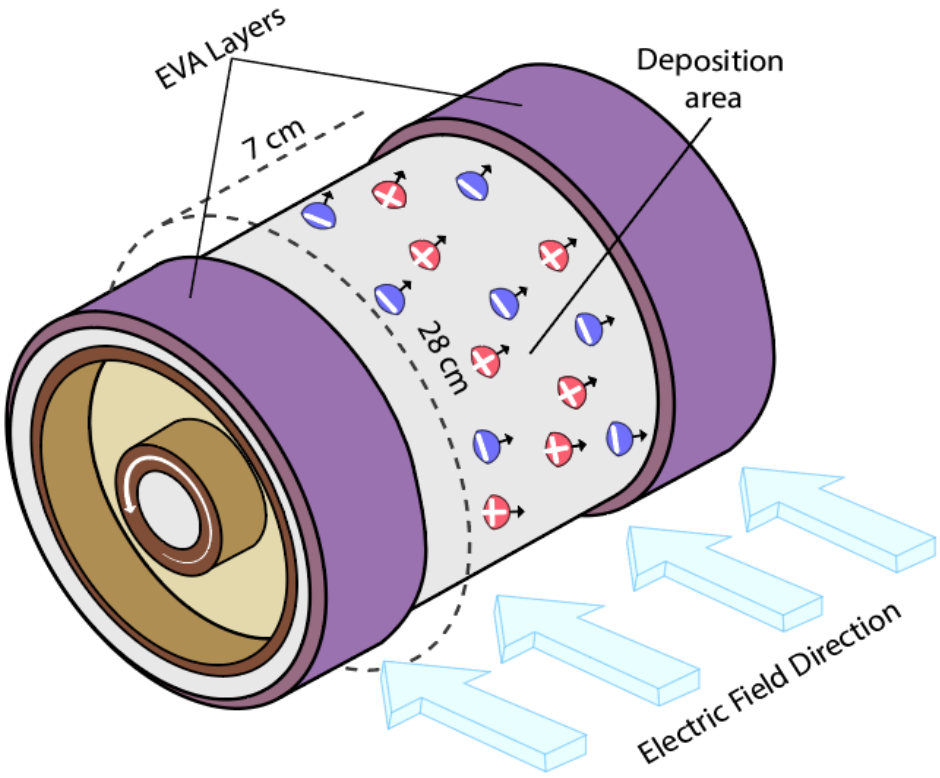

Figure 6.3: Schematic illustrating the rotating drum with a controlled area for fiber deposition used in the electrospinning/electronetting of PVA/chitosan samples. It demonstrates the influence of the electrical field on the rotating drum and the resulting charge orientation due to drum rotation.

6.3.2 Solvent Tests

We tested samples with pure PVA at 12% using only water (PVA 12W) and acetic acid at 70% (PVA 12G), as shown in **Figure 6.2**, **e)** and **f)**. Electrospun nanofibers from aqueous PVA formulation did not exhibit spider-nets, as previously reported.[46] The sample with acetic acid exhibits a minor presence of those structures, but they appear more "fragile" than those with chitosan addition. Other researchers have found similar

results. Li *et al*. produced PVA at 12% using formic acid as the solvent, obtaining similar structures scattered throughout the polymeric matrix.[27] In Wang et al.'s study, formic acid and water were employed as solvents for PVA with a 10% content. Solely utilizing formic acid resulted in a high spider-net coverage across the electrospun mat. When a 1:1 mixture of water and acetic acid was used, the resulting fibers exhibited smaller sizes compared to the previous samples. However, this alteration led to a decreased coverage and distribution of spider-nets.[32]

The primary distinction between acetic and formic acids as solvents lies in spider-nets' coverage. Acetic acid is commonly used in the production process to hydrolyze polyvinyl acetate, producing PVA. Once PVA is formed, it is generally stable and does not readily react with acetic acid. It appears that the acetal formation between hydroxyl groups in PVA and the aldehyde group in formic acid can react under acidic conditions,[32] creating crosslinking between chains and consequently enhancing spider-nets' coverage.

Water appears to hinder the formation of spider-nets. In this study and in the cases mentioned above, water impeded the formation of spider-nets. During the elongation step, hygroscopic polymers such as PVA tend to absorb moisture from the air.[47,48] The condensation of water releases latent heat, prompting the fibers to expel the solvent prematurely, turning the system into a thermodynamically unstable phase,[49] and thereby preventing the solidification of the fibers.[50] For instance, the excess humidity retained between the polymer chains leads to fiber fusion and the formation of thin film layers.[10] As a result, changing the composition of the binary solution, specifically the water-acetic acid ratio, also influences the solubility of the polymers on the fiber during the flight, interfering in the separation of phases.[47,50,51]

Zhang *et al*. produced polyacrylic acid (PAA) nanofibers using water and ethyl alcohol, varying the solvent content. By changing the proportion of solvents, they observed that an increase in the water proportion leads to the formation of thin films instead of spider-nets. In systems with ethyl alcohol/water ratios of 1:1, 1:3, and 0:1, no phase separation occurred, forming non-porous films. They deduced that an increase in the proportion of water in the solutions resulted in a deterioration of phase separation, disrupting PAA spider-nets.[52]

Additional tests were conducted with 7% PVA using different solvents and additives, but none resulted in the formation of spider-nets. It corroborates the hypothesis that concentration is crucial in spider-net formation. The nanofiber size distribution of the PVA 7% samples and the SEM images and are presented in **Figures 6.4** and **6.5**, respectively. They also show that using water as the solvent for PVA tends to increase the average fiber size distribution, following the literature.[32,46,52]

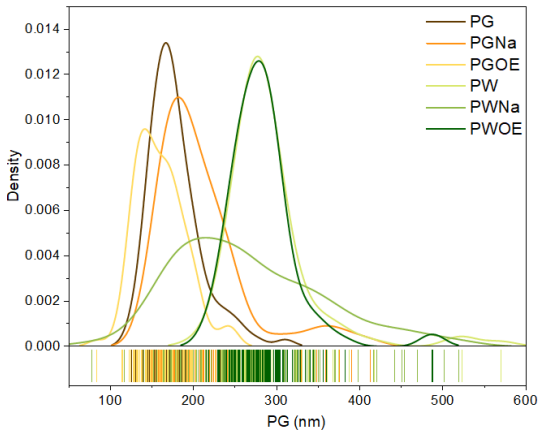

Figure 6.4: Fiber diameter distribution for the PVA 7% series test samples described above.

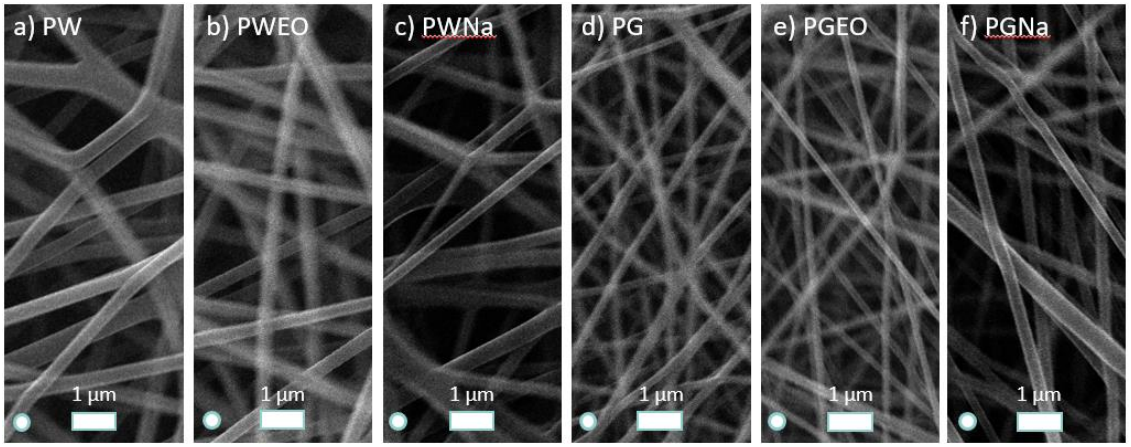

Figure 6.5: Sem images of electrospun samples with PVA at 7% content, being: **a)** pure PVA with water as solvent; **b)** PVA and water with 5% addition (basis weight) of *Lippia sidoides* essential oil; **c)** PVA and water with 5% addition of NaCl; **d)** pure PVA with acetic acid as solvent; **e)** PVA and acetic acid with 5% addition (basis weight) of *Lippia sidoides* essential oil; and **f)** PVA and acetic acid with 5% addition of NaCl.

6.3.3 Spider-nets in Air Filtration of Nanoparticles

Samples 6.0/1.0 and EO were produced using both collectors, a rotative drum (RD) and a flat plate (FP), and they were tested for air filtration (**Figure 6.6**). Deposition area was kept constant at 196 cm², as shown in **Figure 6.3**, to ensure uniform fiber deposition over the RD and FP collectors. All the samples tested exhibited high collection efficiency, exceeding 97%. However, the electric field lines in FP samples tend to accumulate in a specific area,[53] leading to fiber layer packaging, thickening the FP electrospun fiber mats. Consequently, the collection efficiency (η) increases at the expense of high-pressure drops (ΔP).

When comparing only the samples collected using the rotating drum (RD), the sample with additive demonstrated a higher collection efficiency despite having an increased average fiber size diameter. As previously reported,[26] spider-nets slightly increased the pressure drop for the RD samples. This indicates that the enhanced spider-

net coverage observed in the 6.0/1.00 sample led to an increase in the collection efficiency, despite the increase in fiber size due to the additive. However, this improvement was accompanied by a slight increase in pressure drop.

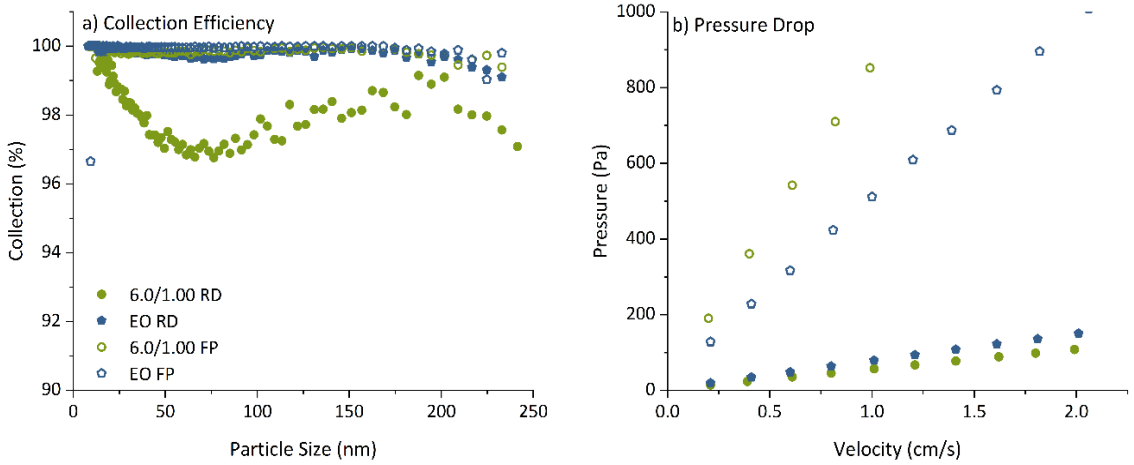

Figure 6.6: a) Collection efficiency and **b)** pressure drop of the sample PVA 6% and CS 1.00% with (EO) and without (6.0/1.00) essential oil addition. The tests used a rotative drum (RD) and a flat plate (FP).

Samples using pure PVA at 7% and 12% with different solvents (*i.e.*, acetic acid and water) were also tested for air filtration (**Figure 6.7**). However, due to its high viscosity, electrospun sample PVA 12G does not provide sufficient coverage for effective air filtration tests. It was observed that the samples with water exhibited a very low-pressure drop (approx. 30 Pa) at the expense of low collection efficiencies. Nevertheless, the increase in PVA content also improved the collection efficiency from 68.65% to 84.53%. Sample PVA 7G demonstrated high collection efficiency but had the highest pressure drop among the samples produced with a rotating drum, even with the lowest average fiber diameter (**Table 6.1**). This behavior could be attributed to the inadequate cavity structures formed in the PVA 7G fiber mat[34] (**Figure 6.5**), as the theory dictates, the cavity volume is inversely proportional to the pressure drop.[28,54] The complex and tortuous pore nets prolong the path and time for the air to traverse the fiber mat, enhancing particle contact, capture and increasing the pressure drop.[13] In contrast, as observed in PVA 7W and 12W, highly porous structures allow air penetration, resulting in low collection efficiency and pressure drops.

From the conductivity data, it seems that the low conductivity increased the presence of spider-nets. Charges generated by the acetic acid induce spider-net formation. Also, it seems that the chitosan can improve the structure leading to a robust spider-nets network. Researchers reported that salt addition [10] or acids [24] could induce spider-nets formation, corroborating the hypothesis that the role of ionic species is composed by the acetic acid addition. N and O present on the structures of CS and PVA work as receivers of ions H^+ due to the high acetic acid content (70%), as shown in **Figures 6.8**, **a)** and **b)**. The ionic species interaction between vicinal fibers by hydrogen

bonds during the fiber deposition leads to the generation of spider-net-like structures [24], as in **Figure 6.8**, **c)**.

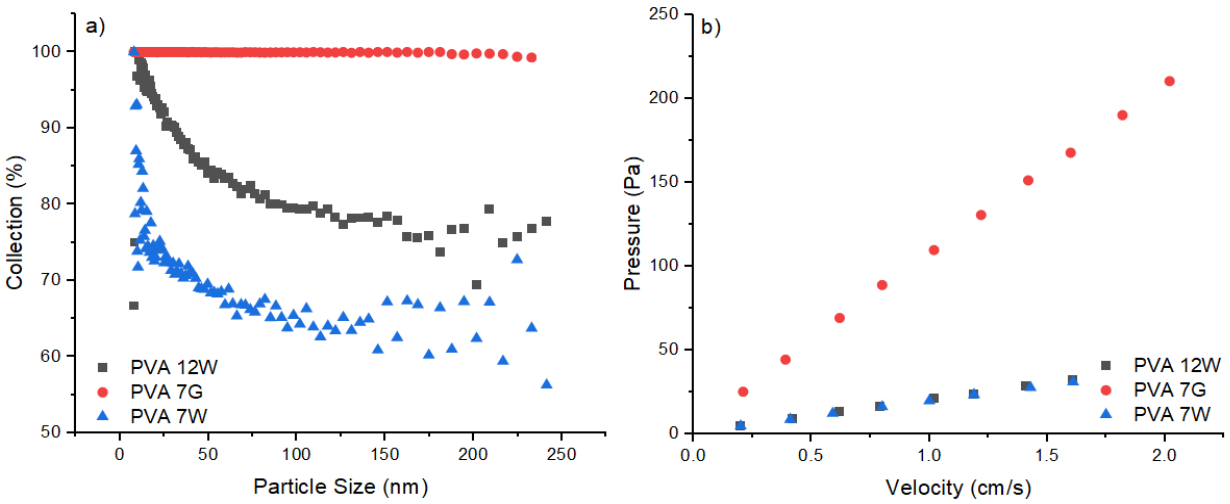

Figure 6.7: a) collection efficiency and **b)** pressure drop for the PVA samples with different solvents.

Table 6.1: Conductivity, fiber diameter, collection efficiency, pressure drop were and Quality Factor evaluated for samples tested in the air filtration. The experiments were conducted at an air velocity of 1.5 L.min^{-1}, covering an evaluation area of 5.2 cm².

Sample	Conductivity ($\mu S.cm^{-1}$)	Fiber Size (nm)	Collection efficiency (%)	Pressure Drop (Pa)	Quality Factor (Q_f)
PVA 7W	180.04 ± 8.4	291.5 ± 55.0	68.65	29.3	0.040
PVA 7G	238.06 ± 6.9	117.9 ± 31.6	99.73	160	0.037
PVA 12W	263.4 ± 4.5	567.4 ± 57.7	84.53	30.2	0.062
PVA 12G	459.3 ± 3.1	372.5 ± 120.1	-	-	-
6.0/1.00 (RD)	689.0 ± 14.7	204.4 ± 31.2	97.65	84.1	0.045
6.0/1.00 (FP)	"	288.72 ± 48.4	99.70	1387.4	0.004
6.0/1.00/EO (RD)	599.1 ± 48.8	249.1 ± 65.7	99.64	117.3	0.048
6.0/1.00/EO (FP)	"	301.88 ± 39.98	99.86	744.4	0.009

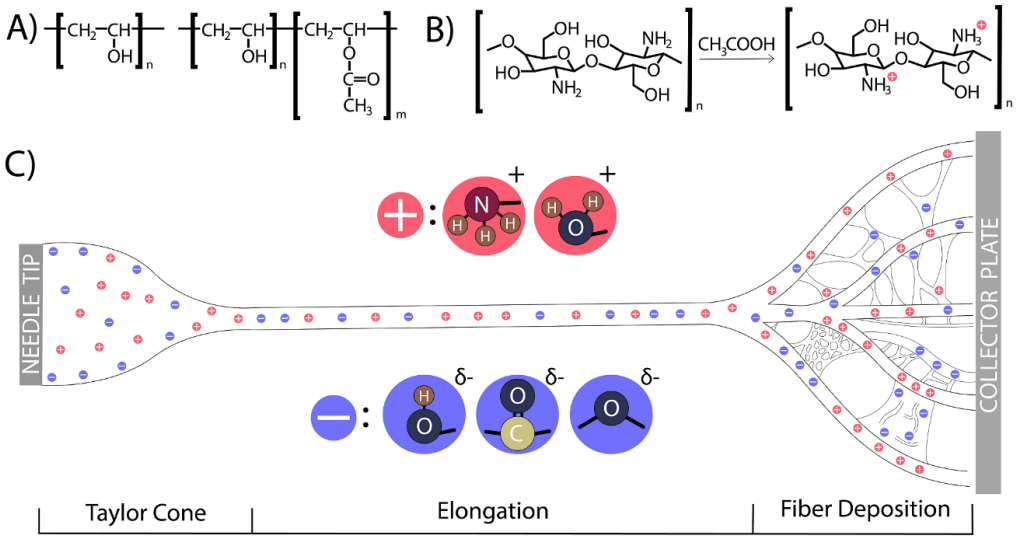

Figure 6.8: a) Structures of polyvinyl alcohol completely hydrolyzed and partially hydrolyzed; **b)** protonation of chitosan with acetic acid; **c)** Spider-net structure formation scheme. Charges between fibers force interchain interaction, generating spider-nets. The ion-like structures can be positive and negative in PVA and CS.

6.4 Conclusion

Spider-net structures were successfully obtained in fibers of PVA and CS. By manipulating the retaining charges onto the fibers, the spider-nets can be controlled and improved with additives like essential oils. The electrical field and collector type are also relevant since the material rotation inside the electrical field helps the spider-net formation. A rotating drum can also improve the spider-net formation, as our study observed. Additionally, the choice of solvents, such as water and acetic acid, proves effective in controlling spider-net formation and the diameter of electrospun mat fibers. The control and formation of spider-nets are a promising technique, with potential for natural polymers such as PVA and chitosan. This improvement could lead to new biodegradable materials with new functionalities and applications.

Author contributions

Conceptualization, G. C. M., M. S. M., and W. P. O.; data curation, G. C. M.; formal analysis, G. C. M; funding acquisition, W. P. O. and M. L. A.; investigation, G. C. M. and M. S. M.; methodology, G. C. M., M. S. M. and W. P. O.; project administration, M. L. A.; resources, W. P. O. and M. L. A.; software, G. C. M.; supervision, W. P. O. and M. L. A.; validation, G. C. M. and M. S. M.; visualization, G. C. M., M. S. M. and W. P. O.; writing—original draft preparation, G. C. M.; writing—review and editing, G. C. M., W. P. O. and M. L. A. All authors have read and agreed to the published version of the manuscript.

Funding: This research was funded by Coordination for the Improvement of Higher Education Personnel (CAPES) grant number 88887.505019/2020-00, the National Council for Scientific and Technological Development (CNPq), grants number 424792/2018-4 scholarship grant number 140704/2023-0 and the Foundation of Research Support of São Paulo State (FAPESP) grant number 2018/26069-0.

Acknowledgements

This research was funded by Coordination for the Improvement of Higher Education Personnel (CAPES) grant number 88887.505019/2020-00, the National Council for Scientific and Technological Development (CNPq), grant number 424792/2018-4 and scholarship grant number 140704/2023-0, and the Foundation of Research Support of São Paulo State (FAPESP) grant number 2018/ 26069-0. The authors acknowledge the financial support of CAPES, CNPq, and FAPESP. We also would like to thank the personnel and staff from the Environmental Control Laboratory of the Federal University of São Carlos (LCA/ UFSCar), the Laboratory of P&D in Pharmaceutical Process of the University of São Paulo (LAPROFAR/USP), the Chemistry Department of the Faculty of Philosophy, Science, and Letters of the University of São Paulo (FFCLRP/USP) and the Laboratory of Electronic Microscopy of the Department of Materials Engineering of the University of São Paulo (EESC/USP).

Conflicts of interest

There are no conflicts to declare.

6.6 Chapter References

1 R. Nirmala, H.-S. Kang, M. H. El-Newehy, R. Navamathavan, H.-M. Park and H. Y. Kim, Human Osteoblast Cytotoxicity Study of Electrospun Polyurethane/Calcium Chloride Ultrafine Nanofibers, *Journal of Nanoscience and Nanotechnology*, 2011, **11**, 4749–4756.

2 R. Nirmala, R. Navamathavan, H.-S. Kang, M. H. El-Newehy and H. Y. Kim, Preparation of polyamide-6/chitosan composite nanofibers by a single solvent system via electrospinning for biomedical applications, *Colloids and Surfaces B: Biointerfaces*, 2011, **83**, 173–178.

3 R. Nirmala, H.-M. Park, R. Navamathavan, H.-S. Kang, M. H. El-Newehy and H. Y. Kim, Lecithin blended polyamide-6 high aspect ratio nanofiber scaffolds via electrospinning for human osteoblast cell culture, *Materials Science and Engineering: C*, 2011, **31**, 486–493.

4 C. Tian, F. Wu, W. Jiao, X. Liu, X. Yin, Y. Si, J. Yu and B. Ding, Antibacterial and antiviral N-halamine nanofibrous membranes with nanonet structure for bioprotective applications, *Composites Communications*, 2021, **24**, 100668.

5 K. Xiao, Y. Zhai, J. Yu and B. Ding, Nanonet-structured poly(m-phenylene isophthalamide)–polyurethane membranes with enhanced thermostability and wettability for high power lithium ion batteries, *RSC Adv.*, 2015, **5**, 55478–55485.

6 Y. Chen, N. Tang, W. Zhu, S. Liu and Y. Zhang, Biomimetic nanonet membranes with UV-driven self-cleaning performance for water remediation, *Journal of Membrane Science*, 2023, **687**, 122047.

7 J. Zhou, X. Li, T. Hou, X. Zhang and B. Yang, Biodegradable, biomimetic, and nanonet-engineered membranes enable high-flux and highly-efficient oil/water separation, *Journal of Hazardous Materials*, 2022, **434**, 128858.

8 H. R. Pant, H. J. Kim, M. K. Joshi, B. Pant, C. H. Park, J. I. Kim, K. S. Hui and C. S. Kim, One-step fabrication of multifunctional composite polyurethane spider-web-like nanofibrous membrane for water purification, *Journal of Hazardous Materials*, 2014, **264**, 25–33.

9 W. Liu, M. Graham, E. A. Evans and D. H. Reneker, Poly(meta-phenylene isophthalamide) nanofibers: Coating and post processing, *Journal of Materials Research*, 2002, **17**, 3206–3212.

10 N. A. M. Barakat, M. A. Kanjwal, F. A. Sheikh and H. Y. Kim, Spider-net within the N6, PVA and PU electrospun nanofiber mats using salt addition: Novel strategy in the electrospinning process, *Polymer -London-*, 2009, **50**, 4389–4396.

11 H. R. Pant, M. P. Bajgai, C. Yi, R. Nirmala, K. T. Nam, W. Baek and H. Y. Kim, Effect of successive electrospinning and the strength of hydrogen bond on the morphology of electrospun nylon-6 nanofibers, *Colloids and Surfaces A: Physicochemical and Engineering Aspects*, 2010, **370**, 87–94.

12 G. C. da Mata, M. S. Morais, W. P. de Oliveira and M. L. Aguiar, Composition Effects on the Morphology of PVA/Chitosan Electrospun Nanofibers, *Polymers*, 2022, **14**, 4856.

13 G. C. da Mata, M. S. Morais, W. P. de Oliveira and M. L. Aguiar, Sustainable surgical masks: optimizing fine/ultrafine particle filtration using PVA/chitosan electrospun nanofibers, *Environ. Sci.: Nano*, 2023, **10**, 2185–2200.

14 D.-N. Nguyen, Y. Hwang and W. Moon, Electrospinning of well-aligned fiber bundles using an End-point Control Assembly method, *European Polymer Journal*, 2016, **77**, 54–64.

15 W. W. F. Leung and Q. Sun, Electrostatic charged nanofiber filter for filtering airborne novel coronavirus (COVID-19) and nano-aerosols, *Separation and Purification Technology*, 2020, **250**, 116886.

16 W. W. F. Leung and Q. Sun, Charged PVDF multilayer nanofiber filter in filtering simulated airborne novel coronavirus (COVID-19) using ambient nano-aerosols, *Separation and Purification Technology*, 2020, **245**, 116887.

17 Z. Wang, F. Yan, H. Pei, J. Li, Z. Cui and B. He, Antibacterial and environmentally friendly chitosan/polyvinyl alcohol blend membranes for air filtration, *Carbohydrate Polymers*, 2018, **198**, 241–248.

18 D. P. F. Bonfim, F. G. S. Cruz, V. G. Guerra and M. L. Aguiar, Development of Filter Media by Electrospinning for Air Filtration of Nanoparticles from PET Bottles, *Membranes*, 2021, **11**, 293.

19 A. C. C. Bortolassi, V. G. Guerra and M. L. Aguiar, Characterization and evaluate the efficiency of different filter media in removing nanoparticles, *Separation and Purification Technology*, 2017, **175**, 79–86.

20 P. M. de Barros, S. S. Rodrigues Cirqueira and M. L. Aguiar, Evaluation of the Deposition of Nanoparticles in Fibrous Filter, *Materials Science Forum*, 2014, **802**, 174–179.

21 M. A. A. D. Prá, R. M. Ribeiro-do-Valle, M. Maraschin and B. Veleirinho, Effect of collector design on the morphological properties of polycaprolactone electrospun fibers, *Materials Letters*, 2017, **193**, 154–157.
22 D. H. Kang and H. W. Kang, Advanced electrospinning using circle electrodes for freestanding PVDF nanofiber film fabrication, *Applied Surface Science*, 2018, **455**, 251–257.
23 G. B. Medeiros, F. de A. Lima, D. S. de Almeida, V. G. Guerra and M. L. Aguiar, Modification and Functionalization of Fibers Formed by Electrospinning: A Review, *Membranes*, 2022, **12**, 861.
24 J. Matulevicius, L. Kliucininkas, D. Martuzevicius, E. Krugly, M. Tichonovas and J. Baltrusaitis, Design and Characterization of Electrospun Polyamide Nanofiber Media for Air Filtration Applications, *Journal of Nanomaterials*, 2014, **2014**, e859656.
25 H. R. Pant, M. P. Bajgai, K. T. Nam, Y. A. Seo, D. R. Pandeya, S. T. Hong and H. Y. Kim, Electrospun nylon-6 spider-net like nanofiber mat containing TiO2 nanoparticles: A multifunctional nanocomposite textile material, *Journal of Hazardous Materials*, 2011, **185**, 124–130.
26 H. Liu, S. Zhang, L. Liu, J. Yu and B. Ding, High-Performance PM0.3 Air Filters Using Self-Polarized Electret Nanofiber/Nets, *Advanced Functional Materials*, 2020, **30**, 1909554.
27 X. W. Li, H. Y. Kong and J. H. He, Study on highly filtration efficiency of electrospun polyvinyl alcohol micro-porous webs, *Indian J Phys*, 2015, **89**, 175–179.
28 S. Zhang, H. Liu, F. Zuo, X. Yin, J. Yu and B. Ding, A Controlled Design of Ripple-Like Polyamide-6 Nanofiber/Nets Membrane for High-Efficiency Air Filter, *Small*, 2017, **13**, 1603151.
29 S. Zhang, H. Liu, X. Yin, Z. Li, J. Yu and B. Ding, Tailoring Mechanically Robust Poly(m-phenylene isophthalamide) Nanofiber/nets for Ultrathin High-Efficiency Air Filter, *Sci Rep*, 2017, **7**, 40550.
30 S. Zhang, H. Liu, J. Yu, W. Luo and B. Ding, Microwave structured polyamide-6 nanofiber/net membrane with embedded poly(m-phenylene isophthalamide) staple fibers for effective ultrafine particle filtration, *J. Mater. Chem. A*, 2016, **4**, 6149–6157.
31 X. Wang, B. Ding, J. Yu and J. Yang, Large-scale fabrication of two-dimensional spider-web-like gelatin nano-nets via electro-netting, *Colloids and Surfaces B: Biointerfaces*, 2011, **86**, 345–352.
32 N. Wang, Y. Si, J. Yu, H. Fong and B. Ding, Nano-fiber/net structured PVA membrane: Effects of formic acid as solvent and crosslinking agent on solution properties and membrane morphological structures, *Materials & Design*, 2017, **120**, 135–143.
33 B. Ding, T. Ogawa, J. Kim, K. Fujimoto and S. Shiratori, Fabrication of a super-hydrophobic nanofibrous zinc oxide film surface by electrospinning, *Thin Solid Films*, 2008, **516**, 2495–2501.
34 Y. Yang, S. Zhang, X. Zhao, J. Yu and B. Ding, Sandwich structured polyamide-6/polyacrylonitrile nanonets/bead-on-string composite membrane for effective air filtration, *Separation and Purification Technology*, 2015, **152**, 14–22.
35 B. Liu, S. Zhang, X. Wang, J. Yu and B. Ding, Efficient and reusable polyamide-56 nanofiber/nets membrane with bimodal structures for air filtration, *Journal of Colloid and Interface Science*, 2015, **457**, 203–211.
36 N. Wang, X. Wang, B. Ding, J. Yu and G. Sun, Tunable fabrication of three-dimensional polyamide-66 nano-fiber/nets for high efficiency fine particulate filtration, *J. Mater. Chem.*, 2012, **22**, 1445–1452.
37 B. Ding, C. Li, Y. Miyauchi, O. Kuwaki and S. Shiratori, Formation of novel 2D polymer nanowebs via electrospinning, *Nanotechnology*, 2006, **17**, 3685.
38 Y. Li, Y. Si, X. Wang, B. Ding, G. Sun, G. Zheng, W. Luo and J. Yu, Colorimetric sensor strips for lead (II) assay utilizing nanogold probes immobilized polyamide-6/nitrocellulose nano-fibers/nets, *Biosens Bioelectron*, 2013, **48**, 244–250.
39 X. Wang, Y. Si, J. Wang, B. Ding, J. Yu and S. S. Al-Deyab, A facile and highly sensitive colorimetric sensor for the detection of formaldehyde based on electro-spinning/netting nano-fiber/nets, *Sensors and Actuators B: Chemical*, 2012, **163**, 186–193.
40 Y. Wen, Y. Li, Y. Si, X. Wang, F. Li, J. Yu and B. Ding, Ready-to-use strip for l-ascorbic acid visual detection based on polyaniline/polyamide 66 nano-fibers/nets membranes, *Talanta*, 2015, **144**, 1146–1154.
41 H. R. Pant, M. P. Bajgai, K. T. Nam, K. H. Chu, S.-J. Park and H. Y. Kim, Formation of electrospun nylon-6/methoxy poly(ethylene glycol) oligomer spider-wave nanofibers, *Materials Letters*, 2010, **64**, 2087–2090.
42 D. Kimmer, P. Slobodian, D. Petráš, M. Zatloukal, R. Olejník and P. Sáha, Polyurethane/multiwalled carbon nanotube nanowebs prepared by an electrospinning process, *Journal of Applied Polymer Science*, 2009, **111**, 2711–2714.
43 H. Xie, M. Sun, X. Fan, Z. Lin, W. Chen, L. Wang, L. Dong and Q. He, Reconfigurable magnetic microrobot swarm: Multimode transformation, locomotion, and manipulation, *Science Robotics*, 2019, **4**, eaav8006.
44 T. Xu, J. Zhang, M. Salehizadeh, O. Onaizah and E. Diller, Millimeter-scale flexible robots with programmable three-dimensional magnetization and motions, *Science Robotics*, 2019, **4**, eaav4494.
45 J. Xu, X. Liu, Z. Zhang, L. Wang, R. Tan and D. Zhang, Controllable generation of nanofibers through a magnetic-field-assisted electrospinning design, *Materials Letters*, 2019, **247**, 19–24.
46 A. E. de Oliveira, M. Aguiar and V. Guerra, Improved filter media with PVA/citric acid/Triton X-100 nanofibers for filtration of nanoparticles from air, *Polymer Bulletin*, , DOI:10.1007/s00289-020-03431-w.
47 P. Lu and Y. Xia, Maneuvering the Internal Porosity and Surface Morphology of Electrospun Polystyrene Yarns by Controlling the Solvent and Relative Humidity, *Langmuir*, 2013, **29**, 7070–7078.
48 S. Alswid and M. Issa, Study The Effect of Conditions of The Electro Spinning Cabin (Humidity) on Electro-spun PolyVinyl Alcohol (PVA) Nano-fibers, *Al-Nahrain Journal for Engineering Sciences*, 2017, **20**, 520–525.
49 B. Barua and M. C. Saha, Influence of humidity, temperature, and annealing on microstructure and tensile properties of electrospun polyacrylonitrile nanofibers, *Polymer Engineering & Science*, 2018, **58**, 998–1009.
50 C. G. Reyes and J. P. F. Lagerwall, Disruption of Electrospinning due to Water Condensation into the Taylor Cone, *ACS Applied Materials & Interfaces*, 2020, **12**, 26566–26576.
51 B. Zaarour, L. Zhu, C. Huang and X. Jin, Controlling the Secondary Surface Morphology of Electrospun PVDF Nanofibers by Regulating the Solvent and Relative Humidity, *Nanoscale Research Letters*, 2018, **13**, 285.
52 S. Zhang, K. Chen, J. Yu and B. Ding, Model derivation and validation for 2D polymeric nanonets: Origin, evolution, and regulation, *Polymer*, 2015, **74**, 182–192.
53 R. Sahay, V. Thavasi and S. Ramakrishna, Design Modifications in Electrospinning Setup for Advanced Applications, *Journal of Nanomaterials*, 2011, **2011**, e317673.

54 K.-T. Park and J. Hwang, Filtration and inactivation of aerosolized bacteriophage MS2 by a CNT air filter fabricated using electro-aerodynamic deposition, *Carbon*, 2014, **75**, 401–410.

VII

MECHANICAL PROPERTIES

VII - MECHANICAL PROPERTIES

Sustainable Surgical Masks II: Mechanical Properties Enhancement of Electrospun PVA/Chitosan Nanofibers

Gustavo Cardoso da Mata[1, *], Maria Sirlene Morais[2], Guilherme José Aguilar[3], Delia Rita Tapia-Blácido[3], Wanderley Pereira de Oliveira[2], Mônica Lopes Aguiar[1]

[1] Department of Chemical Engineering, Federal University of São Carlos, Rod. Washington Luiz, km 235, SP310, São Carlos - SP, 13565-905, Brazil;
[2] Faculty of Pharmaceutical Science of Ribeirão Preto, University of São Paulo, Av. do Café s/nº, CEP: 14040-903, Bairro Monte Alegre, Ribeirão Preto, SP, Brazil
[3] Faculty of Philosophy, Sciences and Letters of Ribeirão Preto, University of São Paulo, Av. do Café s/nº, CEP: 14040-903, Bairro Monte Alegre, Ribeirão Preto, SP, Brazil
[*] *Corresponding author*: gugs_cardoso@ufsj.edu.br

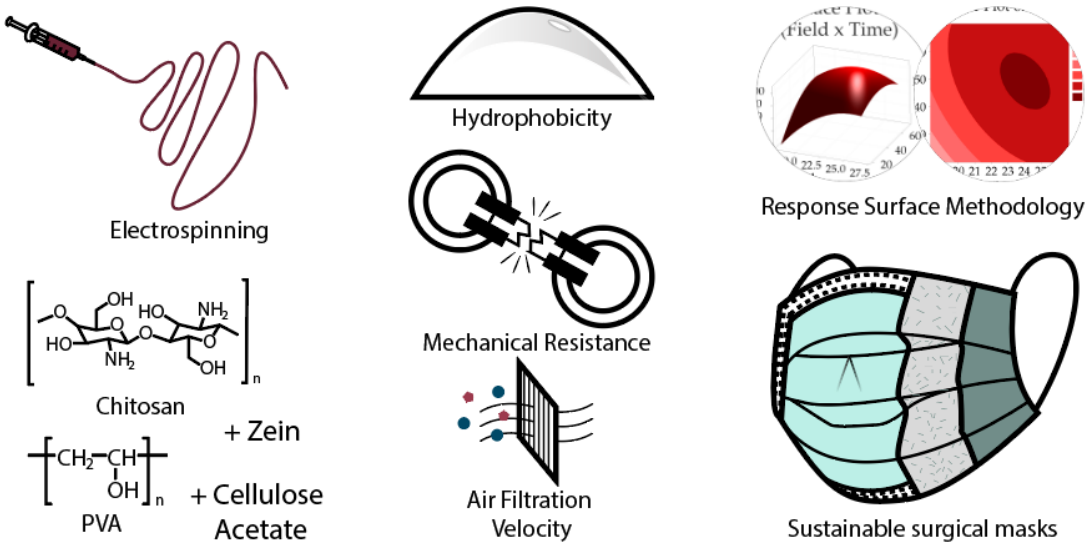

Abstract: One of the consequences of the COVID-19 outbreak was the high generation and consumption of plastic products, particularly facemasks. As non-biodegradable polymers, disposable facemasks end up becoming microplastics, which damage the environment and public health. This study aims to enhance the properties of polyvinyl alcohol (PVA) and chitosan (CS) electrospun nanofibers to produce resilient and hydrophobic disposable surgical masks, using natural and biodegradable polymers. Cellulose acetate (CA) and zein (ZN) were added to enhance its mechanical resistance and hydrophobicity, respectively. The effects of these additions were investigated using Response Surface Methodology (RSM), with the additives content as the variables and mechanical and air filtration properties as the responses. Electrospinning parameters were set at an electrical potential of 23.4 kV and a flow rate of 1.17 $mL.h^{-1}$ over 28 minutes. The addition of ZN and CA slightly changed the average nanofiber sizes, ranging between 150 and 230 nm, close to sample without additives, MR00, which had an average size of 183 nm. Mechanical properties showed improvement, with stress tension increasing by up to 21% compared to MR00. Additionally, hydrophobicity increased, from 38.9° for MR00 to 100.1° for sample MR04. Mathematical models constructed with RSM were optimized to produce new samples. It was possible to increase hydrophobicity, elongation, and pressure drop while maintaining high collection efficiencies of up to 99%. Although mechanical resistance decreased, the models remain useful for optimizing these properties individually. Those results show the potential of natural polymers as substitutes for synthetic polymers, particularly in air filtration of nanoparticles.

Keywords: *Air filters; electrospinning; mechanical properties; contact angle; PVA; chitosan.*
To be submitted to: Journal of Cleaner Production (Elsevier)

7.1 Introduction

Today, it is possible to see the pollution caused by the COVID-19 pandemic through the many disposable materials tossed into the environment. Even though COVID-19 has come to an end, the use of disposable masks remains a significant research topic, not only due to the anticipation of new pandemics but also because of the threat of air pollution in major cities.[1–8] The widespread and necessary use of protective facemasks,[9–16] particularly the disposable ones, has made them pollutants, ending up in the environment.[17–19] Under sunlight and in aggressive conditions, such as marine water, those masks degrade, releasing micro and nano plastics.[20–23] Those micro and nanoplastics travel long distances through air[24–27] and water,[28–31] carrying antibiotics,[32] heavy metals[33,34] and hydrophobic organic chemicals,[35] affecting the climate and the environments where they settle.[36–40]

Many synthetic polymers are used to produce disposable face masks, such as polypropylene, polyurethane, polyacrylonitrile, and polyester.[41–43] Recently, the research community has encouraged a transition from synthetic to natural and biodegradable polymers. Ecofriendly polymers such as polylactic acid (PLA) produced by electrospinning technique have already been used as air filters to capture particles between 300 and 500 nm, achieving collection efficiencies of up to 99%.[44] PLA was also tested with cotton layers to improve bacterial collection.[45] Liu *et al*.[46] and Zhang *et al*.[47] obtained similar collection efficiency results for the same particle range; however, they used synthetic polymers such as polyvinylidene difluoride (PVDF) and polyamide-6 (PA-6), respectively, indicating that natural and biodegradable polymers can achieve the same filtration efficiency as synthetic polymers.

A specific problem in discardable surgical masks is its capability to filtrate fine and ultrafine particles. Tiny aerosols can infiltrate through the pores of the mat like projectiles or be carried by airflow, particularly droplets ranging between 0.3 to 2 µm.[48] Particles with enough momentum can breach the fabric pores. With higher energy, it is more likely that the particle will cross the electrospun fiber mat. Shear stress and surface tension may force the particles to traverse through the interfiber spaces,[49] potentially reaching the respiratory tract.[50] Those particles penetrates and harms the lung tissue,[51,52] causing health issues such cardiovascular diseases,[53,54] and asthma.[55–58]

Natural fibers also prove to be effective for particles smaller than 300 nm. Oliveira et al.[59] tested the air filtration of nanoparticles using PVA combined with citric acid and Triton X-100, achieving collection efficiencies of 94%.[59] In our previous study,[60] PVA was blended with chitosan (CS), resulting in collection efficiencies of up to 96%. For comparison, Almeida et al.[61] tested cellulose acetate (CA) nanofibers loaded with cetylpyridinium bromide, achieving similar collection efficiency (>99%) for fine/ultrafine particles compared to Bonfim et al.,[62,63] who used electrospun filters of polyethylene terephthalate (PET) from recycled soft drink bottles.

However, natural and biodegradable nanofibers present a disadvantage compared to synthetic polymers. They are a challenge to electrospin,[64–66] often

hydrophilic, and generally lack mechanical resistance, limiting their range of applications. PVA/CS blends have shown promising properties,[66–69] with applications in food packaging,[70] drug delivery (82),[71] tissue regeneration, and wound dressing.[72–74] However, it is still necessary to improve their mechanical resistance and hydrophobicity without compromising their eco-friendly nature.

There are still some other options for natural polymers that could address this issue. CA has been used to enhance the mechanical resistance of electrospun nanofibers made from both synthetic and natural polymers, such as polyacrylate, nylon,[75] and CS,[76] and has also shown compatibility with PVA.[77] Zein (ZN), a prolamine originating from corn protein, is one of the few natural hydrophobic polymers and has already been used to increase the hydrophobicity of nanofibers, being electrospun in blends with PVA,[78] CS,[79,80] CA,[81] silk,[82] and collagen.[83]

In this study, we tested the addition of ZN and CA to increase the mechanical properties of the electrospun fiber mat and tested it against fine/ultrafine particles with different air filtration velocities. It also intend to evaluate the capability of PVA/CS electrospun fiber mats to resist higher air filtration velocities without a loss of filtration efficiency in sustainable and discardable surgical facemasks. A Central Composite Design (CCD) with Response Surface Methodology (RSM)[84–87] was used to construct a model that represents the properties of the electrospun fiber mats. The Desirability method (DM),[88–93] a multiresponse optimization technique, was employed to optimize the addition of Zein and Cellulose Acetate, aiming to control the fiber mat properties of air filtration, mechanical resistance and hydrophobicity.

7.2 Materials & Methods

7.2.1 Materials

This study used PVA (polyvinyl alcohol) with molecular weight of 85,500 $g.mol^{-1}$ and a degree of hydrolysis ranging between 86.5% and 89.5% (Vetec Química Fina, Duque de Caxias/RJ, Brazil), and CS (Chitosan) with a degree of deacetylation of 68.5% (Polymar, Fortaleza/CE, Brazil). Additionally, zein (ZN) from corn protein with ± 40 kDa (Sigma Aldrich, Saint Louis/MA, USA) and cellulose acetate (CA) with ± 30 kDa (Sigma Aldrich, Saint Louis/MA, USA) were employed as additives. Analytical-grade glacial acetic acid at 99.0% purity (LabSynth, Diadema/SP, Brazil) was used for polymer solubilization. *Lippia sidoides* essential oil (EO) (Produtos Naturais LTDA, Horizonte/CE, Brazil) was added as an additive to confer biocidal activity[94,95].

7.2.2 Precursor Solution & Electrospinning Process

A mother solution was prepared using 6% (w/v) of PVA and 1% (w/v) of CS, using acetic acid (70%) as the solvent. This mixture was heated to 90 °C and stirred magnetically for 3 hours, following the procedure outlined in Mata et al. (2022)[67].

Subsequently, 20 mL aliquots were extracted to add ZN and CA, yielding samples as specified in **Table 7.1**. Following each addition, the samples were heated to 50 °C for one hour to dissolve the additives. The solutions were then cooled in ambient air. Post-cooling, 5% (w/w: based on weight – solid basis) of *Lippia sidoides* essential oil was added while maintaining the solutions under magnetic stirring.

Table 7.1: Polyvinyl alcohol and chitosan (PVA/CS) samples produced *via* electrospinning technique, with addition of different contents of zein (ZN) and cellulose acetate (CA), according to the central composite design. CA and ZN were added by weight (w/w – solid basis), the percentage is related to the total solid content of PVA and CS.

RunOrder	PtType	Zein (%)	Cellulose Acetate (%)
MR00	Control	-	-
MR01	Level	2.000	2.000
MR02	Level	5.000	2.000
MR03	Level	2.000	5.000
MR04	Level	5.000	5.000
MR05	Axial	1.379	3.500
MR06	Axial	5.621	3.500
MR07	Axial	3.500	1.379
MR08	Axial	3.500	5.621
MR09	Center	3.500	3.500
MR10	Center	3.500	3.500
MR11	Center	3.500	3.500
MR12	Center	3.500	3.500
MR13	Center	3.500	3.500

The samples described in **Table 7.1** were then electrospun, according with the optimal parameters previously obtained in Mata *et al*. (2023)[60]. The parameters were 23.4 kV of electric potential, 1.17 mL.h^{-1} of flow rate, and 28 minutes of production time. It used a rotating drum as collector with 594 rpm and the distance between needle and collector was set at 10 cm. The samples were then dried overnight, while maintaining humidity levels below 50% throughout both the fiber production and the drying processes. The samples were produced in different substrates, depending on the experiment. Samples for the contact angle measurement were produced using aluminum foil as the substrate. The samples for the mechanical resistance tests were produced on crepe tape (masking tape), as they adhere in the aluminum foil.

Face masks usually consist of three layers of thin non-woven fabric: an outer waterproof layer to repel fluids, a middle filtering layer to prevent particles and pathogen-containing droplets from passing through in either direction, and an inner absorbent layer to capture user droplets [16,36].[42,96] Samples for air filtration were produced on the outer layer of a three-layer commercial surgical mask to proper simulate a surgical mask, with an electrospun fiber acting as the filtering layer[60].

7.2.3 Morphological Analysis

Scanning Electron Microscopy (SEM) was employed to examine the surface morphology of electrospun nanofibers. Samples of electrospun nanofiber mats measuring 5×5 mm were gold-coated using a Bal-Tec SCD Sputter Coater model-050 (Fürstentum/Liechtenstein) at a pressure of 0.1 mbar. SEM images were captured using a JEOL model JSM 6610LV (Tokyo, Japan) at magnifications ranging from 2.5 to 20 kX.

7.2.4 Mechanical Properties & Water Contact Angle Mesurements

To perform the mechanical resistance tests, a TX Plus Texturometer (TA Instruments, USA) with crosshead speed of 2 $mm.s^{-1}$ was used. The tests were performed using the nanofibers mats described in **Table 7.1**, with measurements of 80 x 6 mm and initial grip separation of 60 mm, following the ASTM D 828-97 method,[97] adapted by Aguilar & Tápia-Blácido (2023).[98] The maximum tensile strength, elongation at break, and Young's Modulus of the nanofiber mats were directly derived from the stress-strain curves using Texture Expert V.1.22 software (SMS, Surrey, U.K.). They were performed in the Faculty of Philosophy, Sciences and Letters of Ribeirão Preto, University of São Paulo (USP). An electronic micrometer (ZAAS Precision) to measure the thickness of the electrospun mats at 30 randomly chosen points was used. The average thickness, along with the fiber mat's known area and mass, was used to calculate the apparent density (g/cm^3) of the filters. This density reflects the average of at least six separate measurements.

Water Contact Angle (WCA) of the samples was measured using an Optical Tensiometer Biolin Theta, model Attention C 201 (Västra Frölunda/Sweden), with 120 measurements each. Data were obtained and treated with the software Biolin Theta Console®. They were performed at the Chemistry Institute of São Carlos (USP/SC).

7.2.5 Permeability & Air Filtration

Permeability and pressure drop tests were evaluated using the passage of clean air, varying the flow rate in seven steps from 1.5 to 10.5 $L.min^{-1}$. Using Darcy's Law (**Equation 7.1**) it was possible to obtain the permeability constant (K_1).

$$\frac{\boldsymbol{\Delta P}}{\boldsymbol{L}} = \frac{\mu}{\boldsymbol{K_1}} . \boldsymbol{v_s} \qquad \textbf{(7.1)}$$

where $\boldsymbol{\Delta P}$ (Pa) is the pressure drop; $\boldsymbol{L}$ (m) is the filter media thickness; $\boldsymbol{\mu}$ (Pa.s) is the fluid viscosity (*i.e.*, air); and v_s ($m.s^{-1}$) is the surface velocity of the crossing fluid.

Filters collection efficiency**,** $\boldsymbol{\eta}$ (**Equation 7.2**) was measured using the electric particle mobility technique. The system calculates the difference of particles projected on the fiber mats against the particles ejected from it. Sodium chloride (NaCl) nanoparticles ranging from 7 to 250 nm[99,100] were used, with the volumetric flow varying from 1.5 $L.h^{-1}$ to 12 $L.min^{-1}$ and a filtration area of 5.2 cm^2 for each sample[62,101,102].

$$\eta = \frac{C_0 - C_f}{C_0} . 100 \qquad (7.2)$$

where C_0 and C_f are the concentration of nanoparticles before and after the filter media, respectively. Based on the experimental findings of η and the corresponding ΔP, we derived the quality factor (Q_f), which assesses the overall efficiency of the filter media using **Equation 7.3**:

$$Q_f = \frac{-ln(1-\eta)}{\Delta P} \qquad (7.3)$$

As permeability directly correlates with the microstructural parameters of fibrous porous media,[63] the empirical porosity (ε) of the filter media was determined using Ergun's Equation, as depicted below (**Equation 7.4**):

$$\frac{\Delta P}{L} = \frac{150 . \mu . v_s . (1-\varepsilon)^2}{\varepsilon^3 . d_f} + \frac{1.75 . (1-\varepsilon) . \rho_g . v_s^2}{\varepsilon^3 . d_f} \qquad (7.4)$$

where μ is the gas viscosity; v_s is the superficial air filtration velocity; ρ_g is the gas density; and d_f is the average diameter of the fiber. Porosity was theoretically determined to assess the void fraction between fibers. The filtering efficiency and permeability of nanofiber-coated filter media were evaluated using the filtration setup available at the Laboratory of Environmental Control I (DEQ/UFSCar), depicted in **Figure 7.1**.

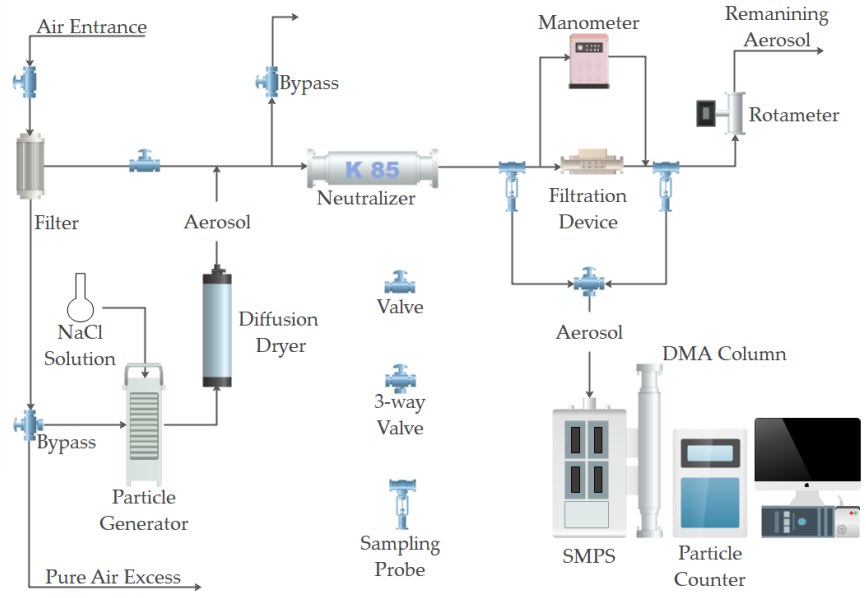

Figure 7.1: Experimental setup for assessing the collection efficiency of filter media at the Laboratory of Environmental Control I (DEQ/UFSCar).

This setup comprises an air compressor (Shultz, Acworth, GA, USA), an air purifier, a nanoparticle generator (Model 3079, TSI, Shoreview, MN, USA), a diffusion dryer (Norgren IMI, Birmingham, UK), a krypton and americium neutralizer (Model 3054, TSI, Shoreview, MN, USA), and a filter support device. Additionally, the setup is equipped with an electrostatic classifier, a scanning mobility particle sizer spectrometer (SMPS – Model 3080, TSI, Shoreview, MN, USA), and an ultrafine particle counter (Model 3776, TSI, Shoreview, MN, USA).[60,103]

7.2.6 Response Surface Analysis & Validation

The central composite design (CCD) represents a common factorial design employed in RSM, as illustrated in **Figure 7.2**. This design extends the center points with additional external points known as axial or star points[84]. CCD offers improved accuracy and does not necessitate a three-level factorial experiment for constructing a second-order quadratic model[104].

In this study, two factors were examined: the ZN and CA contents. These factors serve as the axes for each dimension of the cubic central composite design (CCD). Each factor had two levels, and the center point was repeated five times. **Figure 7.2** outlines all the samples used in constructing the model. The analyzed responses included global filtration efficiency ($\boldsymbol{\eta}$), the pressure drop ($\boldsymbol{\Delta P}$), the contact angle ($\boldsymbol{\theta}$), the Young Modulus ($\boldsymbol{E}$), and the tension ($\boldsymbol{\sigma}$).

Upon processing each response, we conducted an optimization of the generated models using the desirability method (DM), utilizing many sets of parameters, depending on the study velocity. These sets were found in electrospinning fresh fibers, validating the model, and identifying the optimal parameter combination. Notably, this study underwent replication (runs), where the sample evaluation was repeated to establish a more precise model. These iterations were termed "runs" as the study did not assess any extraneous factors, unlike blocks, which could potentially interfere with the investigation, such as chamber humidity and temperature.

The regression model utilized to derive the $\hat{y}$ model follows a polynomial sequence format, where $\boldsymbol{x_i}$ denotes the individual factors, $\boldsymbol{x_i^2}$ represents the quadratic terms of each factor (*i.e.*, self-interaction), and $\boldsymbol{x_i x_j}$ denotes the interaction between different factors[67]. **Equation 7.4** depicts the regression model employed.

$$\hat{y} = \boldsymbol{\beta_0} + \boldsymbol{\beta_1 x_1} + \boldsymbol{\beta_2 x_2} + \boldsymbol{\beta_{11} x_1^2} + \boldsymbol{\beta_{22} x_2^2} + \boldsymbol{\beta_{12} x_1 x_2} \qquad \textbf{(7.4)}$$

where $\hat{y}$ represents the variable analyzed, while $\boldsymbol{\beta_{ij}}$ is the constant coefficient for each term. The CCD model was created and analyzed using Minitab®, with data fitting and regression carried out in Excel® and OriginPro®. Automation was achieved using PyCharm® (Python 3.10.1).

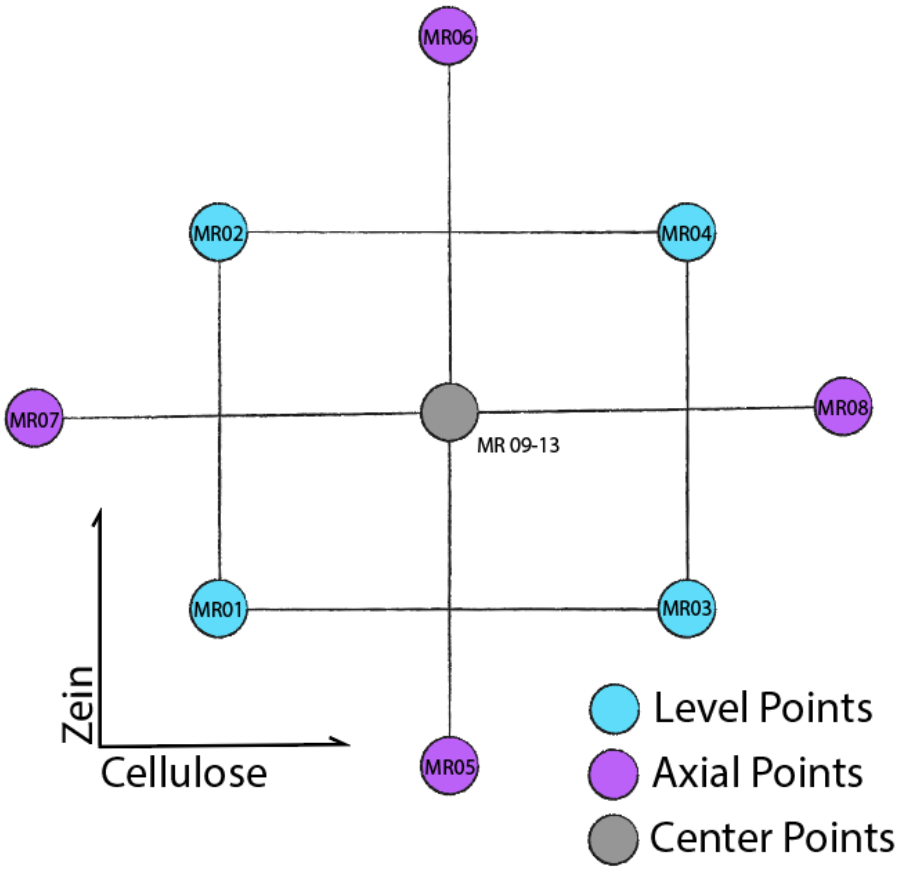

Figure 7.2: The design employed in this study for the RSM was a 2^2 CCD, featuring two factors with two levels each. This CCD is characterized as rotational, with a constant variance of $\alpha = 1.414$ maintained at the same radius within the model.

7.3 Results & Discussion

7.3.1 Morphological Analysis

From the SEM analysis (**Figure 7.3**), is possible to understand the superficial characteristics of the samples described in **Table 7.1**. **Figure 7.4** and **Table 7.2** shows the influence of zein (ZN) and cellulose acetate (CA) in the fiber diameters, fiber mat porosity and permeability.

Fiber size distribution was maintained between 150 and 230 nm for all the samples. ZN has the capability to improve spinning continuity by weakening hydrogen bonds between polymer molecules, resulting in a narrow diameter distribution,[105] as observed in our study. In general, all the samples presented very similar shapes, indicating that the addition of ZN and CA had minimal influence on the fiber morphology and diameter sizes. It was possible to observe minimal fibers in many samples, as can be seen in samples MR03 and MR10 (**Figure 7.3 d)** and **k)**, respectively) which it believe to be spider-net structures.[46,106,107] They appeared damaged, possibly due to the high-energy beam used in the SEM analysis (25 kV). **Figure S7.1** shows the surface plot, main effect plot and pareto charts for the responses described in **Figure 7.4**. **Tables S7.1**, **S7.2** and **S7.3**, shows their ANOVA data, and **Table 7.5** show the models generated.

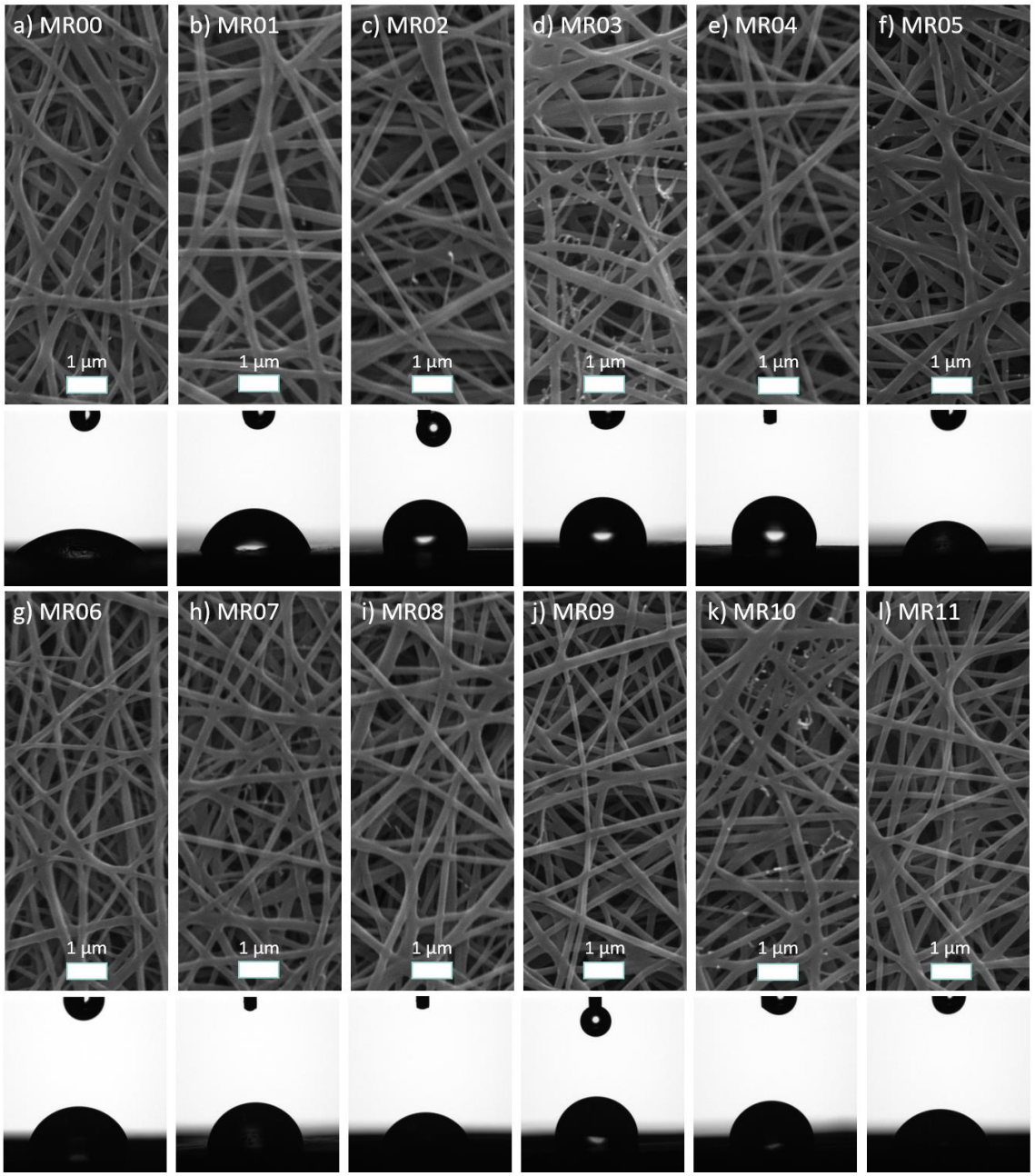

Figure 7.3: Scanning Electron Microscope (SEM) images of some of the samples described in **Table 7.1**, and their respective contact angle, used to construct the Central Composite Design (CCD).

Although the model constructed by the CCD presented a p-value > 0.05 (**Table S7.1**), the contour plot in **Figure 7.4, b)** can provide an estimation of how ZN and CA were altering the nanofiber structure. It seems that the interaction between ZN and CA was capable of reducing the average fiber diameter size, whereas an unbalanced proportion between the polymers tends to increase the fiber diameter size. Lin et al.[83] observed that the increase in zein amount in collagen fibers more than doubled their average diameter, while Liu et al.[108] observed the opposite effect, with ZN reducing the average fiber diameter size of CA electrospun nanofibers by less than half. Same was observed by Deng *et al*.[109] when adding ZN to gelatin fibers.

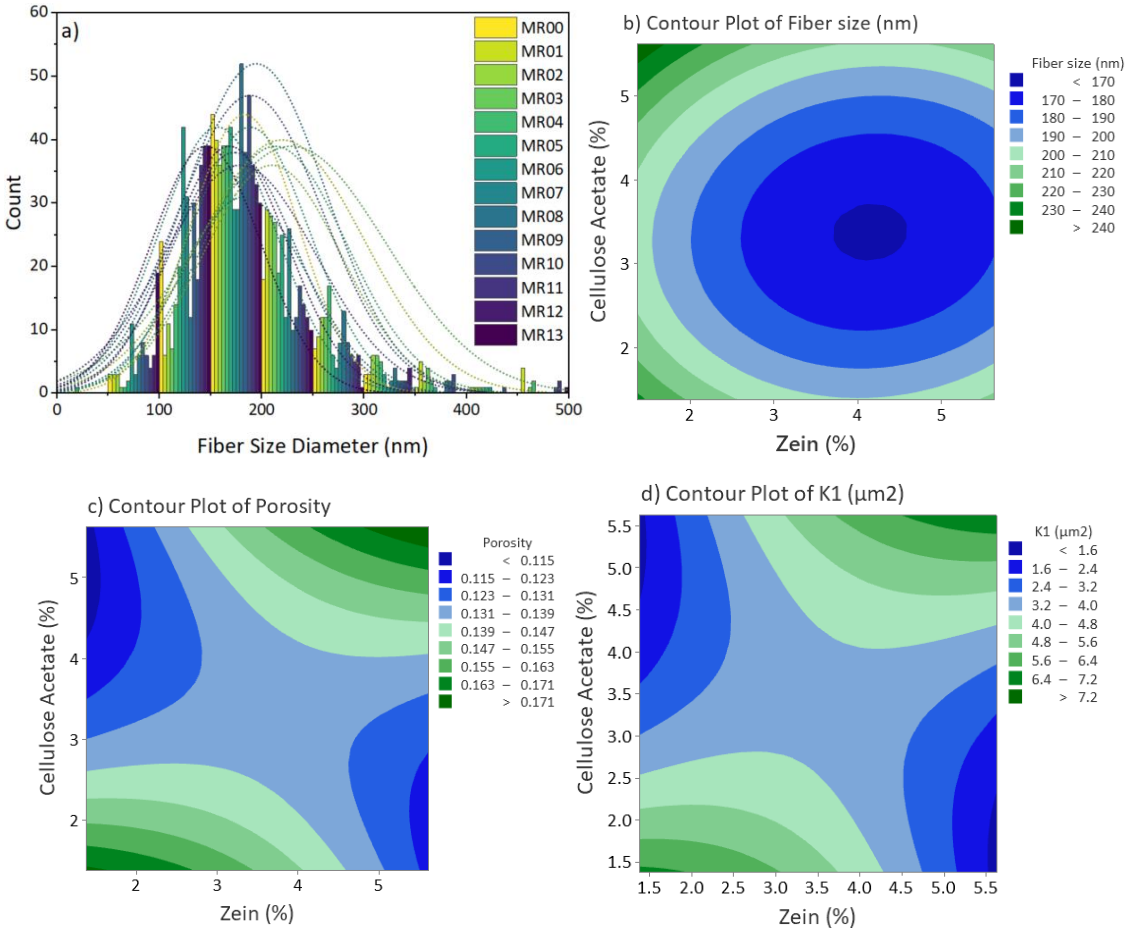

Figure 7.4: a) Fiber size distribution for the samples used to construct the CCD; Contour plot showing the influence of zein and cellulose acetate in the following fiber mat properties: **b)** fiber size diameter (d_f); **c)** porosity (ε); and **d)** permeability (K_1).

Table 7.2: Morphological properties obtained for the analysis of the CCD samples, being: d_f the fiber size diameter; ε the porosity; and K_1 the permeability contant, derived from the Darcy's Law. Data used to obtain ε and K_1 is expressed in **Table 7.3**.

Sample	d_f (nm)	ε	K_1 (µm)
MR00	183.0 ± 52.5	0.155	4.145
MR01	219.7 ± 80.3	0.150	5.071
MR02	209.9 ± 67.8	0.119	2.284
MR03	228.7 ± 92.9	0.122	2.871
MR04	213.0 ± 69.9	0.151	5.462
MR05	189.9 ± 57.0	0.123	2.379
MR06	156.8 ± 57.2	0.139	2.846
MR07	182.7 ± 61.5	0.161	5.356
MR08	194.4 ± 69.1	0.156	5.107
MR09	172.9 ± 60.4	0.135	2.999
MR10	190.2 ± 70.4	0.138	3.331
MR11	178.8 ± 74.4	0.120	2.234
MR12	168.4 ± 56.8	0.133	6.957
MR13	145.6 ± 53.9	0.144	3.221

Increasing the CA content could prevent the bead formation, producing stable fibers. At high ZN contents, the poor entanglement of zein molecules can diminish the overall solution entanglement, disrupting and preventing the fiber formation.[108] Even though zein alone is difficult to stabilize and produce fibers, it can act as a plasticizer enhancing spinnability of other polymers,[108] diminishing the fibers diameters.[109] Zein molecules are capable of weaken the hydrogen bonding between polymer chains, consequently increasing the spinning continuity.[105] Within zein, the groups -OH, $-NH_2$, and -C=O can create hydrogen bonds with the -OH groups present in PVA.[110]

One significant challenge in electrospinning is the tendency of fibers to densely accumulate, leading to reduced porosity and smaller pore sizes. The porosity and pore sizes within electrospun scaffolds primarily rely on the diameter of the fibers and their packing density.[111] As seen in **Figure 7.4**, **c)** and **d)**, ZN and CA appear to have a similar influence on both properties: porosity and permeability. **Table 7.2** shows that all the fibers exhibited low porosity, indicating a densely packed fiber mat. A similar response was observed when adding ZN to collagen fibers,[83] gelatin fibers,[109] and silk fibers,[82] suggesting that ZN addition results in fiber mat packaging and reduced porosity, while simultaneously enhancing the mechanical resistance of the electrospun fiber mats.[111]

7.3.2 Mechanical Resistance

Figure 7.5 shows the mechanical properties of the samples used to construct the Central Composite Design (CCD). Same data is presented in **Table S7.5**. The samples thickness presented close values, ranging between 14 to 18 µm. Despite the variability in Stress, Elongation, and Young's Modulus data, several samples exhibited values higher than that of sample MR00, indicating that even small additions of both Zein (ZN) and cellulose acetate (CA) were able to influence the original mechanical strength. For instance, sample MR08 had the highest Stress Tension value and ranked among the highest values for Young's Modulus.

The values of mechanical resistance obtained for the PVA/CS fibers were considerable for natural polymers, up to 12.4 MPa (Sample MR08), since electrospinning of natural polymers is already a challenge.[64–66] Chitosan electrospinning is particularly problematic,[112–114] and the increase in chitosan content tends to diminish the fiber mat tensile strength.[115] Chen *et al*. [115] produced chitosan nanofibers, obtaining tensile strength values of 0.5 MPa. Ojha *et al*.[116] produced chitosan core-sheath fibers using polyethylene oxide (PEO) as sheath, obtaining 4 MPa of tensile strength for a electrospun mat of 0.12 µm of thickness. When combined with PEO, chitosan electrospun were able to gain up to 8.9 MPa of mechanical strength.[117]

Blending CS with PVA it is already known to improve its mechanical resistance.[69,118] MR08 tensile strength was slightly higher than pure cellulose acetate electrospun fibers (12.1 MPa),[119] and more than double than PVA electrospun nanofibers (5.8 MPa).[120] The addition of chitosan to PVA membranes disrupts the formation of PVA crystallites, leading to a less uniform structure and a filamentous

matrix with increased porosity.[121] It could be caused by the interaction of -OH groups, from PVA, with the -NH groups, from chitosan.[69] Charernsriwilaiwat *et al.*[114] produced blends with CS and PVA varying the polymers' proportion, obtaining tension values between 1.5 and 8.9 MPa. It shows that the addition of essential oil of *Lippia sidoides* also help to increase the fiber mat mechanical properties.

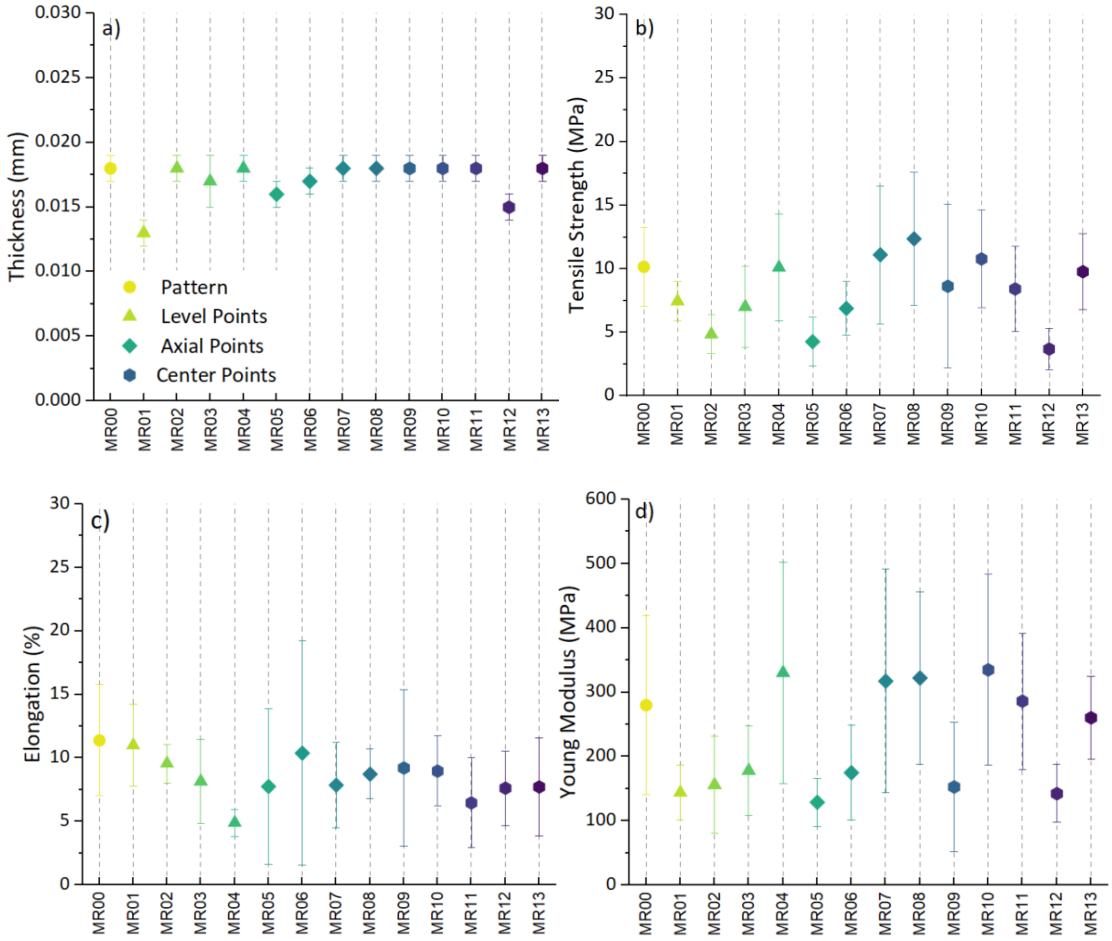

Figure 7.5: Mechanical resistance for the samples described in the Central composite Design (CCD), being: **a)** Fiber Mat Thickness; **b)** Mechanical Strength; **c)** Elongation; and **d)** Young Modulus.

The mechanical strength of electrospun fibers of combined natural polymers were also comparable of those produced with synthetic polymers. Kim *et al.*[122] produced electrospun fibers of the synthetic polymer polyurethane (PU) obtaining tensile strength between 6.7 MPa to pure PU and up to 8.1 MPa for PU with addition of fly ash. Yang *et al.*[107] obtained values between 3.2 and 14.3 MPa for electrospun composites of polyamide-6 (PA-6) and polyacrylonitrile (PAN). Nylon-6 had tensile strengths between 7.2 and 10.4 MPa.[123,124] To better understand the behavior induced by each additive, **Figure 7.6** illustrates the Contour Plots of the responses obtained from the models generated using Response Surface Methodology (RSM).

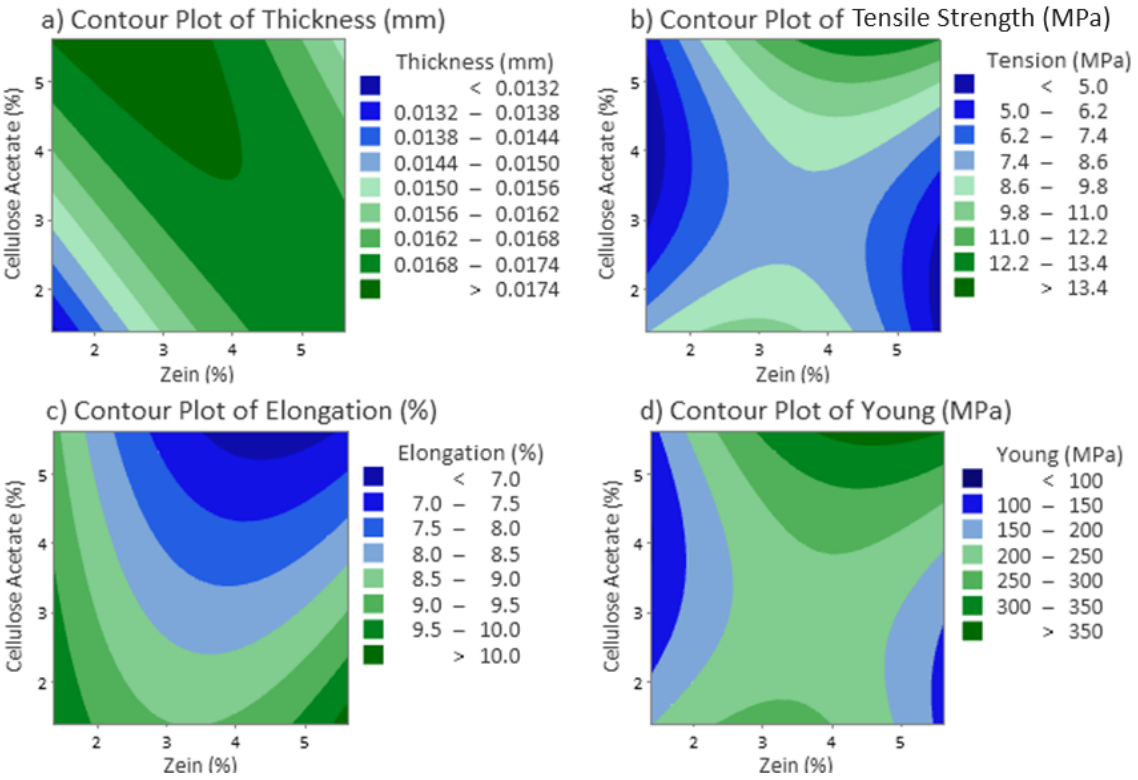

Figure 7.6: Contour plots of each response used to construct the Central composite Design (CCD) for mechanical resistance, showing the influence of the zein (ZN) and cellulose acetate (CA) contents.

Graph **7.6**, **a)** shows that the thickness has a balance influencing the response, since the simultaneously increase or decrease in ZN and CA contents tends to diminish the electrospun mat thickness. Graphs **7.6**, **b)** and **d)** show very similar behaviors, evidence that the ZN and the CA have the similar effect over the Tension and the Young Modulus. It is also possible to observe that the isolated influence of each additive diminishes both properties, with an accentuated effect for the Tension response. In contrast, the combined effect of ZN and CA was able to enhance both properties, showing that electrospun mat gained mechanical resistance caused by their interactions. The combined effect of ZN and CA is also influencing the elongation, however, in the opposite direction. It is decreasing the elongation capacity from the electrospun nanofibers. Lin *et al*.[83] observed that ZN addition to CA electrospun fibers increased its tensile strength while reduced its elongation at break, which leads to a more brittle structure. Therefore, it seems that ZN can structurally reinforce the fibers mechanical resistance at some extent.[108]

Supplementary materials show the pareto charts (**Figure S7.2**) with the statistical significance for the models in the parameters of each response. **Figure S7.3** shows the Main Effects Plot for each mechanical resistance response, and the individual influence for ZN and CA, while **Figure S7.4** shows the respectively Surface Plots. **Tables S7.6** to **S7.9** shows the ANOVA analysis for the Thickness, Tension, Elongation and Young Modulus responses, respectively.

7.3.2 Water Contact Angle (WCA)

Measurement of WCA (Water Contact Angle) stands as one of the pivotal methods employed to understand the hydrophilicity, wettability, hydration, and surface homogeneity of films and fibers.[125] From **Figures 7.3** and **7.7** is possible to observe how the addition of zein and cellulose acetate increased the contact angle. Samples MR02 to MR04 displayed the higher contact angles, reaching 100.16° with the higher contents of both polymers. Those results are promising since a small addition was capable of highly increasing the contact angle, thus, increasing the fiber hydrophobicity higher than some synthetic polymers. Even though polyamide-6 (PA-6) is considered a hydrophilic polymer,[126] it has contact angles close to 50° for its electrospun nanofibers.[127] Many other synthetic polymers have contact angles in the range of this study, such as polyacetal (POM, 76.2°), polymethyl methacrylate (PMMA, 79.7°), polystyrene (PS, 95.5°), and polypropylene (PP, 101.2°).[128]

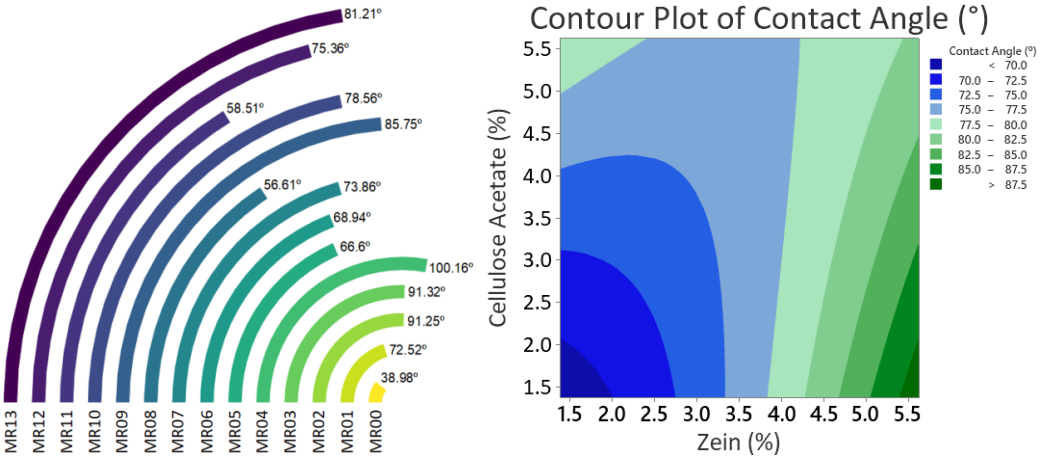

Figure 7.7: On the left, the contact angle obtained from the samples from de Central Composite Design (CCD). On the right, the contact angle Contour Plot, showing the combined influence of cellulose acetate and zein in the contact angle response.

The majority of natural and biodegradable polymers are hydrophilic, therefore, turning those kinds of materials into hydrophobic could be a challenge. Chitosan was already used to increase the hydrophobicity of agarose films, from 66.2 to 97.7°,[129] and in combination with starch.[130,131] Li *et al*.[132] produced layer-by-layer films with chitosan, sodium alginate and ferulic acid, obtaining contact angles up to 82°. Yan *et al*.[69] measured the contact angle of PVA and chitosan films, obtaining values of 22° for the pure PVA and 73° for PVA/chitosan blends, produced in a proportion of 2:1. The high presence of hydroxyl groups on the PVA fibers' surface makes PVA a very hydrophilic material. Blended with chitosan increase the interaction between both polymers, diminishing the hydroxyl groups availability.[132] In our samples, even with a higher proportion of PVA to chitosan (6:1), the zein addition was capable of compensating the PVA excess and increase the fiber's hydrophobicity.

Zein presence had the highest influence on the contact angle, as seen in the Contour Plot (**Figure 7.7**). It is considered a hydrophobic protein,[79] as result of the apolar amino acids of proline and glutamine, main constituents of the zein molecule.[83] Zein has low stability in water tending to collapse into a film,[133] however, it is well dissolved in solutions with high content of acetic acid.[83] Acetic acid also dissolves well the cellulose acetate.[61] Both polymers were already electrospun together, with the cellulose acetate slightly diminishing the contact angle of pristine zein fibers.[81] Cellulose acetate has great stability against wetting, particularly because the presence of acetyl groups, being capable to resist and delay the water penetration.[77] From the Main Effect Plots and Pareto Charts (**Figure S7.5**) it is possible to observe that while the cellulose acetate has a minor effect in increasing the contact angle, the zein has the primary influence in the electrospun mat hydrophobicity. **Table S7.10** shows the ANOVA data for the Contact Angle response.

7.3.3 Air Filtration & Pressure Drop

In our previous study (**Chapter 4**),[60] we tested different electrospinning parameters to optimize the filtration conditions of sustainable surgical masks produced with natural and biodegradable polymers. However we did not take into account the necessity for the surgical masks to resist high air filtration velocities, such as the ones occurring in coughing and sneezing.[134–139] In this study, we intent to address the air filtration velocity, as shown in **Figure 7.8**. CCD samples were tested at different air filtration velocities: 3.0, 4.5, and 6.0 L.min^{-1}, and compared by RSM analysis (**Figure 7.9**) to observe the effects of increasing air filtration velocity on the collection of fine and ultrafine particles. **Table 7.3** shows the filtration data per air filtration velocity.

Table 7.3: Air filtration data for the CCD samples, tested againt different air filtration velocities. $\boldsymbol{\eta}$ represents the collection efficiency, $\boldsymbol{\Delta P}$ the pressure drop and $\boldsymbol{Q_f}$ the quality factor.

Sample	3.0 L.min^{-1}			4.5 L.min^{-1}			6.0 L.min^{-1}		
	$\boldsymbol{\eta}$ (%)	$\boldsymbol{\Delta P}$ (Pa)	$\boldsymbol{Q_f}$ (Pa^{-1})	$\boldsymbol{\eta}$ (%)	$\boldsymbol{\Delta P}$ (Pa)	$\boldsymbol{Q_f}$ (Pa^{-1})	$\boldsymbol{\eta}$ (%)	$\boldsymbol{\Delta P}$ (Pa)	$\boldsymbol{Q_f}$ (Pa^{-1})
MR00	99.67	242.4	0.023	97.37	353.7	0.010	99.33	465.1	0.010
MR01	98.19	161.2	0.024	87.50	239.2	0.008	96.55	312.1	0.010
MR02	99.72	428.7	0.013	93.06	639.1	0.004	98.74	834.5	0.005
MR03	99.57	359.6	0.015	99.42	509.4	0.010	97.35	669.2	0.005
MR04	97.55	193.6	0.019	95.13	280.1	0.010	90.29	360.0	0.006
MR05	99.90	400	0.017	98.78	577.6	0.007	99.09	755.6	0.006
MR06	98.00	360.9	0.010	99.47	517.9	0.010	99.31	680.8	0.007
MR07	99.31	189.9	0.026	95.47	280.2	0.011	95.50	364.0	0.008
MR08	90.21	195.0	0.011	97.58	283.5	0.013	99.28	373.1	0.013
MR09	96.95	371.7	0.009	90.20	526.7	0.004	98.15	696.9	0.005
MR10	95.29	315.8	0.009	91.53	461.5	0.005	97.56	604.8	0.006
MR11	99.02	462.4	0.010	98.18	673.5	0.005	98.78	878.1	0.005
MR12	95.12	128.1	0.023	96.54	188.4	0.017	93.12	247.2	0.011
MR13	98.59	345.5	0.012	99.03	502.2	0.009	97.75	646.9	0.006

As expected, some samples diminished its collection with the increase in the air flow velocity. In others, the collection efficiency from tests at 4.5 L.min^{-1} were lower than tests at 6.0 L.min^{-1}. Overall, many samples presented collection efficiencies between 95.0 and 99.0 %, with sample MR05 presenting the highest collection efficiency for the air filtration velocity of 3.0 L.min^{-1}, and sample MR06 for the velocities of 4.5 and 6.0 L.min^{-1}. The sample with the lowest pressure drop for all the velocities was MR12. To properly understand the influence of ZN and CA in the filtration properties, we constructed Contour Plots for each filtration velocity (**Figure 7.9**).

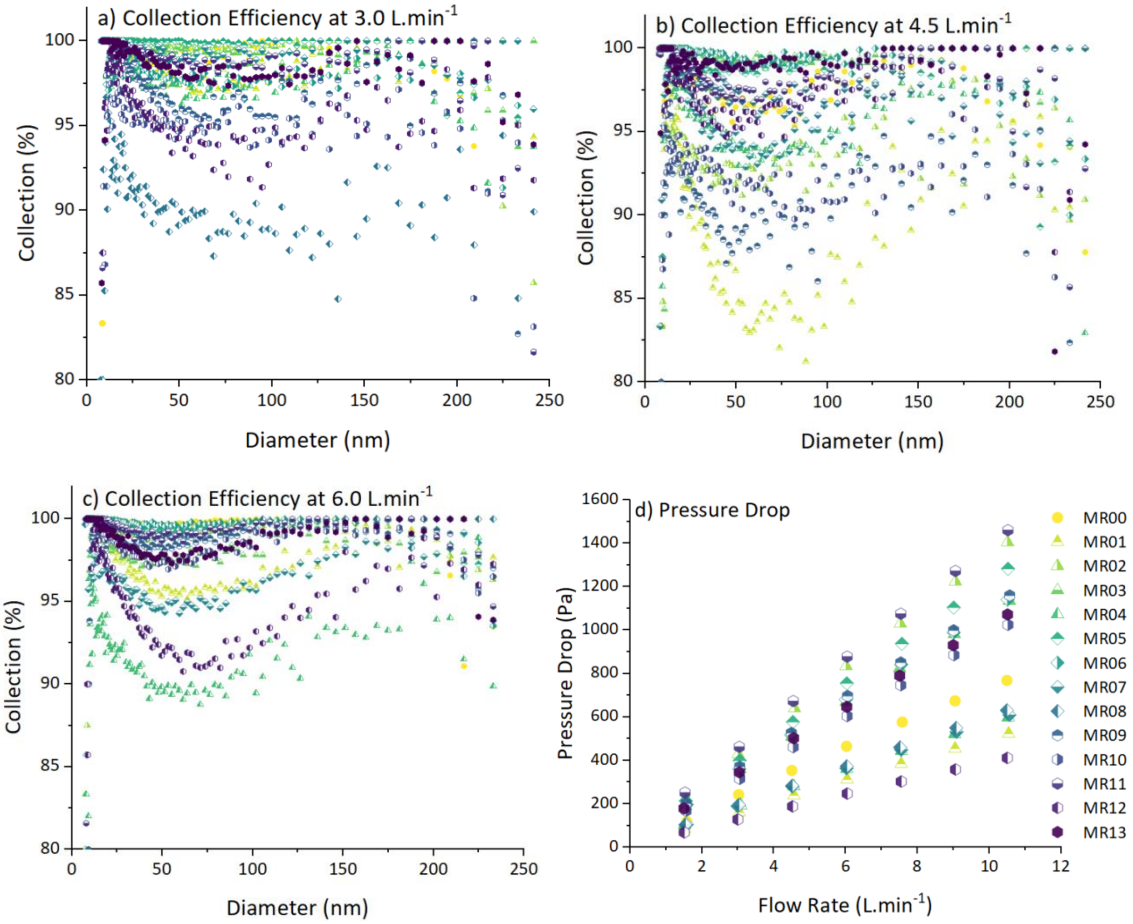

Figure 7.8: Fractional collection efficiency curves for the CCD samples, tested in different velocities, being: **a)** 3.0 L.min^{-1}; **b)** 4.5 L.min^{-1}; and **c)** 6.0 L.min^{-1}; The diameter distribution ranged from 7 to 250 nm, evaluated at a filtration velocity of 4.8 cm s^{-1}. Graph **d)** shows the pressure drop by filtration velocity.

It can be observed that the air filtration velocity had a significant impact on the air filtration models. All models appeared to be quite different from each other, while also showing statistical significance (p-value < 0.05), indicating that the generated models accurately represent the studied behavior (**Table S7.10**). It is also possible that the presented models differed so much due to changes in the collection mechanisms

from one filtration velocity to another. As the air carrying velocity increases, so does the ballistic action of the particles, following the kinetic energy equation (**Equation 7.5**):

$$K = \frac{m.v^2}{2} \qquad (7.5)$$

where K is the kinetic energy, m is the particle mass, and v is the particle velocity.

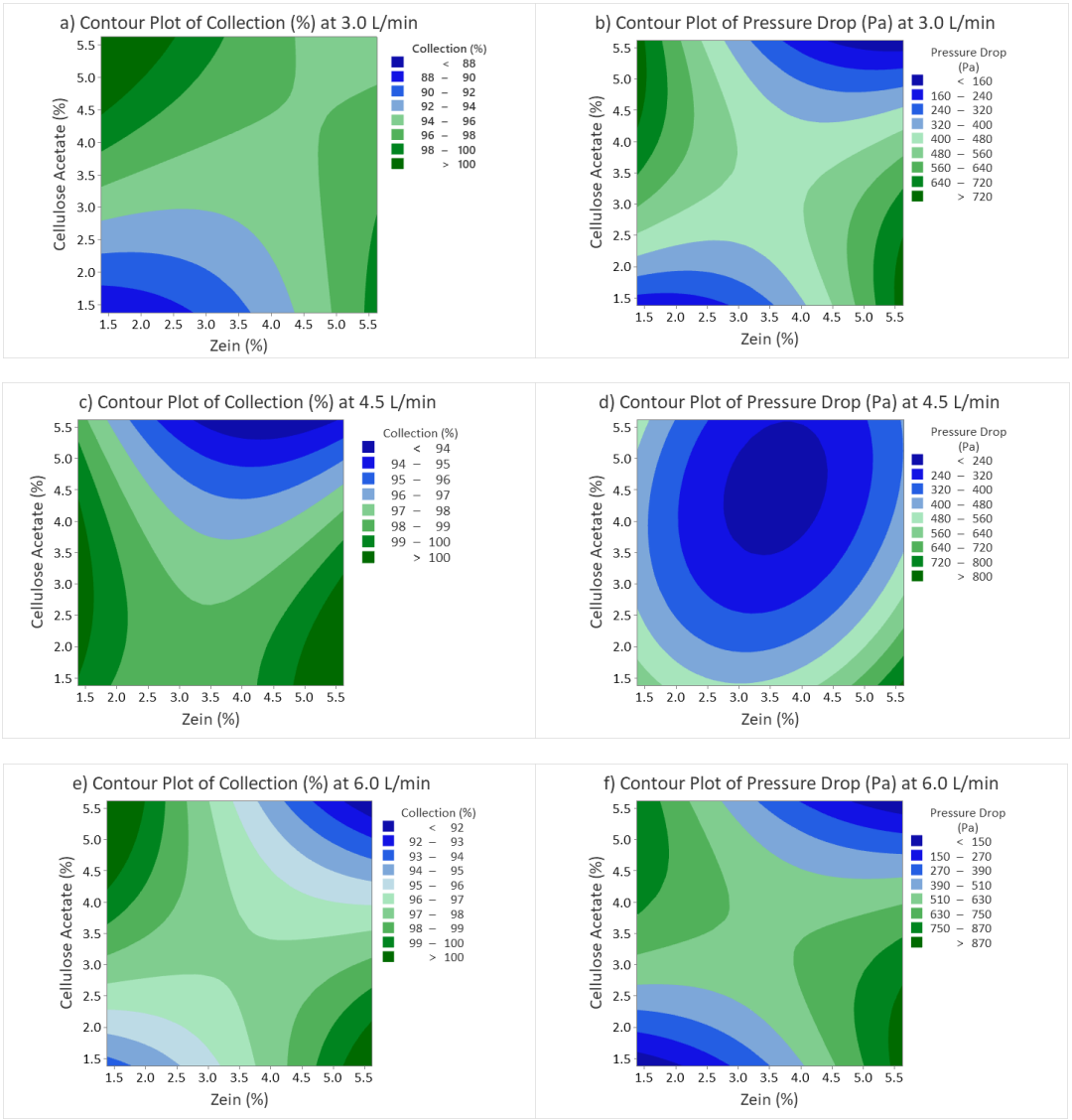

Figure 7.9: Contour plots for the collection efficiency and pressure drop responses, constructed,respectively, for: **a)** and **b)** the velocity of 3.0 L.min^{-1}; **c)** and **d)** the velocity of 4.5 L.min^{-1}; and **e)** and **f)** the velocity of 6.0 L.min^{-1}.

One or another mechanism can dominate over the others, depending on the particle size[140]. Therefore, by doubling the filtration velocity from 3.0 to 6.0 L.min^{-1}, for

instance, there is a quadratic effect on the energy carried by the particle, potentially increasing collection effects by inertial impaction and direct interception, which are relevant for particles above 100 nm,[99] as observed in **Figure 7.8**, **a)** and **c)**.

Nanometric particles (> 100 nm) exhibited similar collection efficiencies overall. The primary capture mechanisms are electrostatic attraction[141] and Brownian diffusion,[142] depending on the surface energy and enhanced surface reactivity of the polymers.[106,143,144] Therefore, we believe that the minor additions of ZN and CA did not cause significant effects on the fiber surface to create stronger interactions between fibers and particles, and consequently increase the filtering efficiency.[145]

As expected by Darcy's Law (**Equation 7.1**), the pressure drop exhibited a linear behavior, increasing with the air filtration velocity. Our intention was to identify a potential filter rupture point, where the filter mat would cease to handle the increasing pressure drop, resulting in an abrupt decrease in its values. Surprisingly, none of the samples tested in this study showed a rupture point within the evaluated air filtration range.

Figures S7.6 to **S7.8** shows the graphs of Surface Plots, Main Effects and Pareto Charts for the collection efficiency and pressure drop responses evaluated in the velocities of 3.0, 4.5 and 6.0 $L.min^{-1}$. **Table S7.10** shows the model equations obtained by the CCD and RSM analysis. **Tables S7.11** to **S7.16** contain the ANOVA analysis of the collection efficiency and pressure drop at the different filtration velocities.

7.3.4 Optimization & Validation

The air filtration samples used in constructing the RSM models were optimized using the Desirability Method (DM). DM utilizes the CCD model equations to optimize the responses individually and then combines the individual solutions into a single desirability function, which ranges from 0 to 1.[60] When the parameter aligns with a target point (maximum, minimum, or a specified value), the desirability function will approach 1. As the response value deviates from the target point, the desirability value decreases.[146] The global desirability function aims to identify sets of parameter values that maximize or minimize all system responses.

To proper address the air filtration tests, three optimizations were made, using the data from each air filtration velocity. Validation samples (MRV) were named according to their filtration velocity, as: MRV (3.0), for the data of 3.0 $L.min^{-1}$; MRV (4.5), for the data of 4.5 $L.min^{-1}$; and MRV (6.0), for the data of 6.0 $L.min^{-1}$ the collection efficiency, the pressure drop, and the three mechanical resistance responses that presented statistical significance (p-value < 0.5), that is the Fiber Mat Thickness; the Stress Tension; and the Young Modulus were optimized. **Figures 7.10** and **7.11** shows the air filtration of the MRV samples. **Table 7.4** and **Table 7.5** shows the optimization data for the mechanical resistance and the air filtration, respectively.

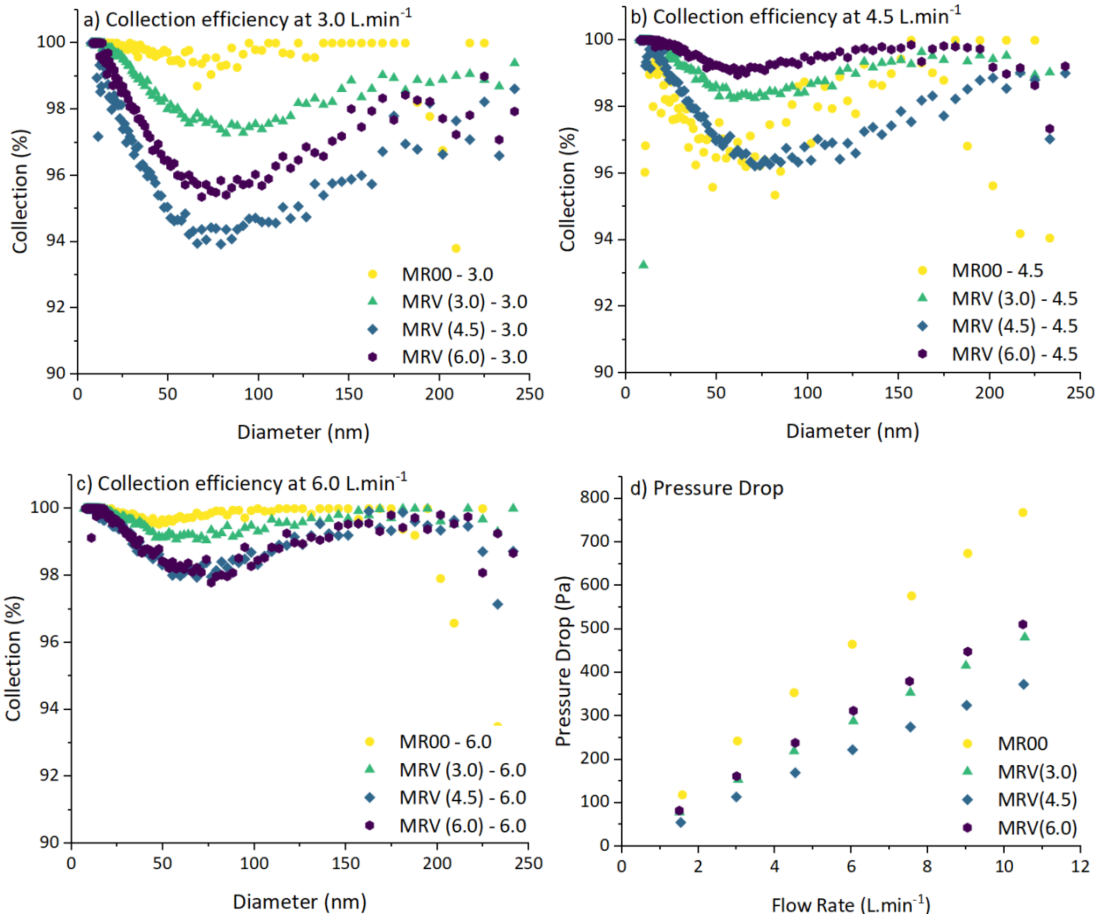

Figure 7.10: Fractional air filtration collection of the optimized samples, per filtration velocity, being: **a)** 3.0 L.min^{-1}; b**)** 4.5 L.min^{-1}; and **c)** 6.0 L.min^{-1}. Graph **d)** shows the pressure drop for the same samples.

From **Figure 7.10**, it is possible to observe that MRV samples slightly decrease air filtration collection, although MRV (3.0) and MRV (6.0) samples exhibited higher collection efficiencies for air filtration at 4.5 L.min^{-1}. This could be a compensation for the high gap between the MR00 pressure drop and the MRV samples, with MRV (4.5) showing the lowest pressure drop. Comparison between air filtration velocities (**Figure 7.11**) shows an increase in air filtration collection for MRV samples with the increase in air filtration velocity. It reinforces our previous observations that air filtration velocity is also increasing other collection phenomena, such as direct interception and inertial impaction.[99]

Mechanical resistance data (**Table 7.4**) shows that the optimization was not capable to converge all the solutions, reducing the Tension and Young Modulus of MRV samples when compared to MR00. Interestingly, the elongation, that was not optimized, increased, surpassing even the CCD samples (MR01 to MR13). The mechanical resistance trade off between Tension and Elongation is amply known, similar to the trade off in ar filtration, between collection efficiency and pressure drop. To increase one of the properties, generally, the other one needs to decrease.

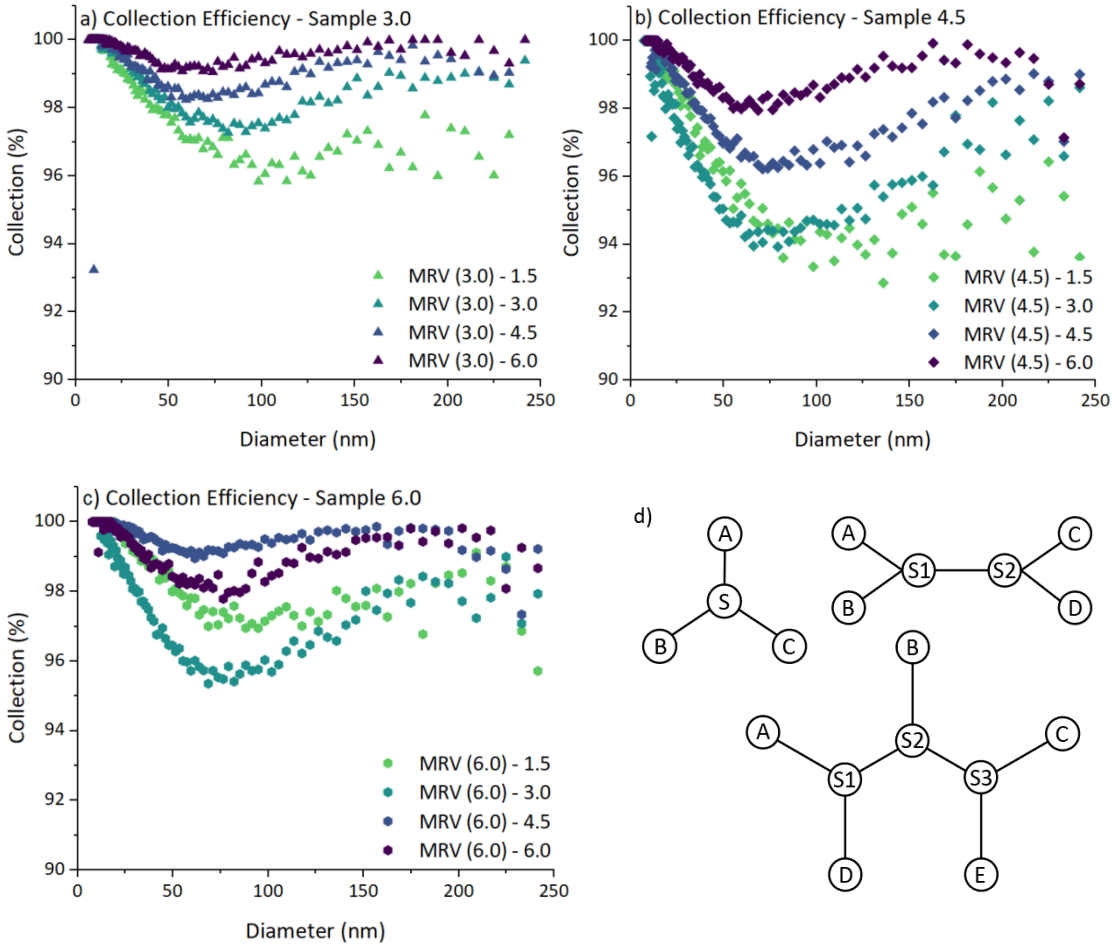

Figure 7.11: Fractional air filtration collection of the optimized samples, per sample in different filtration velocities, being: **a)** MRV (3.0); b**)** MRV (4.5); and **c)** MRV (6.0). Graph **d)** shows the Steiner Tree optimization problem with 3 responses (up left), 4 responses (up right), and 5 responses (down) were A, B, C, D and E are the individual optimum points and S_i is the common solution points.

This behaviour could be responsible by the many optimized responses, each one requiring different conditions and additives contents to improve its propertie value. When generating the models they could favor one or more properties to the detriment of the other, trying to satisfy the maximum possible number of conditions. As we can see, the pressure drop and the contact angle were enhanced in comparison to MR00, in exchange for slight variations in the collection efficiency and thickness, and a decrease in Tension and Young Modulus. As consequence, the quality factors of the validation samples also increased. This optimization problem is known as Steiner Tree,[147,148] depicted in **Figure 7.11**, **d)**. With an increase in the number of responses the number of possible solutions also increase, and the difficulty to attend to all of them.

Although it was not possible to optimize all properties simultaneously, the models constructed by the CCD are still amenable to more targeted optimization, directly favoring one property over another. For example, during the construction of a desirability function that prioritizes mechanical strength at the expense of other parameters. Therefore, the models still prove useful and capable of increasing

mechanical strength, as observed in samples MR07 and MR08. By adjusting optimization parameters such as weight, responsible for the curvature of optimization, and importance, responsible for the contribution of each response to the model, it is possible to improve one or more parameters, depending on the need and applications of each material.

Table 7.4: Mechanical resistance properties of the optimization samples.

Sample / Response	MR00	MRV (3.0) D: 0.6579	MRV (4.5) D: 0.5623	MRV (6.0) D: 0.6053
ZN Content (%)	-	3.66	3.99	3.6974
CA Content (%)	-	5.62	4.93	5.6213
Thickness (mm)	0.017 ± 0.001	0.016 ± 0.001	0.018 ± 0.001	0.017 ± 0.001
Tension (MPa)	10.17 ± 3.11	3.93 ± 0.93	2.74 ± 0.80	3.62 ± 1.07
Elongation (%)	11.39 ± 4.38	19.05 ± 0.53	17.26 ± 26	19.57 ± 4.44
Young Modulus (MPa)	280.10 ± 139.59	56.47 ± 16.63	34.18 ± 10.43	66.38 ± 23.31
Contact Angle (°)	38.98	36.56	65.88	73.14

Table 7.5: Air filtration properties of the optimization samples. $\boldsymbol{\eta}$ represents the collection efficiency, $\boldsymbol{\Delta P}$ the pressure drop and $\boldsymbol{Q_f}$ the quality factor.

Sample	3.0 L.min^{-1}			4.5 L.min^{-1}			6.0 L.min^{-1}		
	$\boldsymbol{\eta}$ (%)	$\boldsymbol{\Delta P}$ (Pa)	$\boldsymbol{Q_f}$ (Pa^{-1})	$\boldsymbol{\eta}$ (%)	$\boldsymbol{\Delta P}$ (Pa)	$\boldsymbol{Q_f}$ (Pa^{-1})	$\boldsymbol{\eta}$ (%)	$\boldsymbol{\Delta P}$ (Pa)	$\boldsymbol{Q_f}$ (Pa^{-1})
MR00	99.67	242.4	0.023	97.37	353.7	0.010	99.33	465.1	0.010
MRV (3.0)	98.30	153.3	0.027	98.65	218.9	0.020	99.42	287.9	0.018
MRV (4.5)	95.49	113.9	0.027	97.39	169.3	0.021	98.69	222.3	0.019
MRV (6.0)	96.75	161.5	0.021	99.41	238.1	0.022	98.74	312.1	0.014

7.4 Conclusions

In this study, with small additions of Zein (ZN) and cellulose acetate (CA), it was possible to modify the chemical and mechanical properties of polyvinyl alcohol (PVA) and chitosan (CS) electrospun membranes. ZN and CA added to PVA/CS nanofibers slightly changed their average fiber diameter, while increasing their mechanical resistance and hydrophobicity. Air filtration tests showed a packed mat with low porosity; however, they also presented lower pressure drops and high collection efficiencies, excellent characteristics for air filters.

The optimization process was capable of improving properties such as the contact angle and reducing the pressure drop; however, it affected the mechanical resistance. Due to the many variables used, the model could not meet all requirements; yet, it could be used to improve one or more responses according to the demand for material properties. Therefore, our study presents a viable and green alternative to traditional non-degradable discardable facemasks, following the ecological trend

worldwide. We also expect that our study can enhance the use of natural polymers, opening up application opportunities for natural and biodegradable materials.

Author contributions

Conceptualization, G. C. M., M. S. M., and W. P. O.; data curation, G. C. M.; formal analysis, G. C. M; funding acquisition, W. P. O. and M. L. A.; investigation, G. C. M. and M. S. M.; methodology, G. C. M., M. S. M. and W. P. O.; project administration, M. L. A.; resources, W. P. O. and M. L. A.; software, G. C. M.; supervision, W. P. O. and M. L. A.; validation, G. C. M. and M. S. M.; visualization, G. C. M., M. S. M. and W. P. O.; writing—original draft preparation, G. C. M.; writing—review and editing, G. C. M., W. P. O. and M. L. A. All authors have read and agreed to the published version of the manuscript.

Funding: This research was funded by Coordination for the Improvement of Higher Education Personnel (CAPES) grant number 88887.505019/2020-00, the National Council for Scientific and Technological Development (CNPq), grants number 424792/2018-4 scholarship grant number 140704/2023-0 and the Foundation of Research Support of São Paulo State (FAPESP) grant number 2018/26069-0.

Acknowledgements

This research was funded by Coordination for the Improvement of Higher Education Personnel (CAPES) grant number 88887.505019/2020-00, the National Council for Scientific and Technological Development (CNPq), grant number 424792/2018-4 and scholarship grant number 140704/2023-0, and the Foundation of Research Support of São Paulo State (FAPESP) grant number 2018/ 26069-0. The authors acknowledge the financial support of CAPES, CNPq, and FAPESP. We also would like to thank the personnel and staff from the Environmental Control Laboratory of the Federal University of São Carlos (LCA/ UFSCar), the Laboratory of P&D in Pharmaceutical Process of the University of São Paulo (LAPROFAR/USP), the Chemistry Department of the Faculty of Philosophy, Science, and Letters of the University of São Paulo (FFCLRP/USP) and the Laboratory of Electronic Microscopy of the Department of Materials Engineering of the University of São Paulo (EESC/USP).

Conflicts of interest

There are no conflicts to declare.

7.5 References

1. Carozzi, F. & Roth, S. Dirty density: Air quality and the density of American cities. *Journal of Environmental Economics and Management* **118**, 102767 (2023).
2. Lu, X. *et al.* Progress of Air Pollution Control in China and Its Challenges and Opportunities in the Ecological Civilization Era. *Engineering* **6**, 1423–1431 (2020).
3. Nguyen, L. S. P. *et al.* Trans-boundary air pollution in a Southeast Asian megacity: Case studies of the synoptic meteorological mechanisms and impacts on air quality. *Atmospheric Pollution Research* **13**, 101366 (2022).
4. Rodrigues, V. *et al.* Assessing air pollution in European cities to support a citizen centered approach to air quality management. *Science of The Total Environment* **799**, 149311 (2021).
5. Sicard, P. *et al.* Trends in urban air pollution over the last two decades: A global perspective. *Science of The Total Environment* **858**, 160064 (2023).
6. de Jesus, A. L. *et al.* Ultrafine particles and PM2.5 in the air of cities around the world: Are they representative of each other? *Environment International* **129**, 118–135 (2019).
7. Abdillah, S. F. I. & Wang, Y.-F. Ambient ultrafine particle (PM0.1): Sources, characteristics, measurements and exposure implications on human health. *Environmental Research* **218**, 115061 (2023).
8. Singh, S. *et al.* How an outbreak became a pandemic: a chronological analysis of crucial junctures and international obligations in the early months of the COVID-19 pandemic. *The Lancet* **398**, 2109–2124 (2021).
9. Ganczak, M., Pasek, O., Duda – Duma, Ł., Świstara, D. & Korzeń, M. Use of masks in public places in Poland during SARS-Cov-2 epidemic: a covert observational study. *BMC Public Health* **21**, 393 (2021).
10. Ippolito, M. *et al.* Medical masks and Respirators for the Protection of Healthcare Workers from SARS-CoV-2 and other viruses. *Pulmonology* **26**, 204–212 (2020).
11. Selvaranjan, K., Navaratnam, S., Rajeev, P. & Ravintherakumaran, N. Environmental challenges induced by extensive use of face masks during COVID-19: A review and potential solutions. *Environmental Challenges* **3**, 100039 (2021).
12. Oliveira, A. E. de *et al.* Physical Barrier against COVID-19: Materials to Inhibit or Eliminate the Virus. in *Living with COVID-19* (Jenny Stanford Publishing, 2021).
13. Cheng, Y. *et al.* Face masks effectively limit the probability of SARS-CoV-2 transmission. *Science* **372**, 1439–1443 (2021).
14. Lindsley, W. G., Blachere, F. M., Law, B. F., Beezhold, D. H. & Noti, J. D. Efficacy of face masks, neck gaiters and face shields for reducing the expulsion of simulated cough-generated aerosols. *Aerosol Science and Technology* **55**, 449–457 (2021).

15. Booth, M. C., Clayton, M., Crook, B. & Gawn, J. M. Effectiveness of surgical masks against influenza bioaerosols. *Journal of Hospital Infection* **84**, 22–26 (2013).
16. Suess, T. *et al.* The role of facemasks and hand hygiene in the prevention of influenza transmission in households: results from a cluster randomised trial; Berlin, Germany, 2009-2011. *BMC Infect Dis* **12**, 26 (2012).
17. Chen, X. *et al.* Used disposable face masks are significant sources of microplastics to environment. *Environmental Pollution* **285**, 117485 (2021).
18. Schmutz, M. *et al.* Cotton and Surgical Masks—What Ecological Factors Are Relevant for Their Sustainability? *Sustainability* **12**, 10245 (2020).
19. Alfarisi, S. *et al.* A Sustainable Approach towards Disposable Face Mask Production Amidst Pandemic Outbreaks. *Sustainability* **14**, 3849 (2022).
20. Anastopoulos, I. & Pashalidis, I. Single-use surgical face masks, as a potential source of microplastics: Do they act as pollutant carriers? *Journal of Molecular Liquids* **326**, 115247 (2021).
21. Fadare, O. O. & Okoffo, E. D. Covid-19 face masks: A potential source of microplastic fibers in the environment. *Science of The Total Environment* **737**, 140279 (2020).
22. Ma, M., Xu, D., Zhao, J. & Gao, B. Disposable face masks release micro particles to the aqueous environment after simulating sunlight aging: Microplastics or non-microplastics? *Journal of Hazardous Materials* **443**, 130146 (2023).
23. Pfohl, P. *et al.* Environmental Degradation of Microplastics: How to Measure Fragmentation Rates to Secondary Micro- and Nanoplastic Fragments and Dissociation into Dissolved Organics. *Environ. Sci. Technol.* **56**, 11323–11334 (2022).
24. Shao, L. *et al.* Airborne microplastics: A review of current perspectives and environmental implications. *Journal of Cleaner Production* **347**, 131048 (2022).
25. Akhbarizadeh, R. *et al.* Suspended fine particulate matter (PM2.5), microplastics (MPs), and polycyclic aromatic hydrocarbons (PAHs) in air: Their possible relationships and health implications. *Environmental Research* **192**, 110339 (2021).
26. Brahney, J. *et al.* Constraining the atmospheric limb of the plastic cycle. *Proceedings of the National Academy of Sciences* **118**, e2020719118 (2021).
27. Ding, J. *et al.* Atmospheric microplastics in the Northwestern Pacific Ocean: Distribution, source, and deposition. *Science of The Total Environment* **829**, 154337 (2022).
28. Kye, H. *et al.* Microplastics in water systems: A review of their impacts on the environment and their potential hazards. *Heliyon* **9**, e14359 (2023).
29. Buckingham, J. W., Manno, C., Waluda, C. M. & Waller, C. L. A record of microplastic in the marine nearshore waters of South Georgia. *Environmental Pollution* **306**, 119379 (2022).
30. Gálvez-Blanca, V. *et al.* Occurrence and size distribution study of microplastics in household water from different cities in continental Spain and the Canary Islands. *Water Research* **238**, 120044 (2023).
31. Garcia, T. M. *et al.* Microplastics in subsurface waters of the western equatorial Atlantic (Brazil). *Marine Pollution Bulletin* **150**, 110705 (2020).
32. Li, J., Zhang, K. & Zhang, H. Adsorption of antibiotics on microplastics. *Environmental Pollution* **237**, 460–467 (2018).
33. Godoy, V., Blázquez, G., Calero, M., Quesada, L. & Martín-Lara, M. A. The potential of microplastics as carriers of metals. *Environmental Pollution* **255**, 113363 (2019).
34. Oz, N., Kadİzade, G. & Yurtsever, M. Investigation of heavy metal adsorption on microplastics. *Applied Ecology and Environmental Research* **17**, 7301–7310 (2019).
35. Hartmann, N. B. *et al.* Microplastics as vectors for environmental contaminants: Exploring sorption, desorption, and transfer to biota. *Integrated Environmental Assessment and Management* **13**, 488–493 (2017).
36. Aeschlimann, M., Li, G., Kanji, Z. A. & Mitrano, D. M. Potential impacts of atmospheric microplastics and nanoplastics on cloud formation processes. *Nat. Geosci.* **15**, 967–975 (2022).
37. Revell, L. E., Kuma, P., Le Ru, E. C., Somerville, W. R. C. & Gaw, S. Direct radiative effects of airborne microplastics. *Nature* **598**, 462–467 (2021).
38. Allen, D. *et al.* Temporal Archive of Atmospheric Microplastic Deposition Presented in Ombrotrophic Peat. *Environ. Sci. Technol. Lett.* **8**, 954–960 (2021).
39. Brahney, J., Hallerud, M., Heim, E., Hahnenberger, M. & Sukumaran, S. Plastic rain in protected areas of the United States. *Science* **368**, 1257–1260 (2020).
40. Wang, Y. *et al.* Airborne hydrophilic microplastics in cloud water at high altitudes and their role in cloud formation. *Environ Chem Lett* **21**, 3055–3062 (2023).
41. Jung, S., Lee, S., Dou, X. & Kwon, E. E. Valorization of disposable COVID-19 mask through the thermo-chemical process. *Chemical Engineering Journal* **405**, 126658 (2021).
42. Aragaw, T. A. Surgical face masks as a potential source for microplastic pollution in the COVID-19 scenario. *Marine Pollution Bulletin* **159**, 111517 (2020).
43. Chua, M. H. *et al.* Face Masks in the New COVID-19 Normal: Materials, Testing, and Perspectives. *Research* **2020**, (2020).
44. Wang, L. *et al.* Biodegradable and high-performance multiscale structured nanofiber membrane as mask filter media via poly(lactic acid) electrospinning. *Journal of Colloid and Interface Science* **606**, 961–970 (2022).
45. Patil, N. A. *et al.* Needleless electrospun phytochemicals encapsulated nanofibre based 3-ply biodegradable mask for combating COVID-19 pandemic. *Chemical Engineering Journal* **416**, 129152 (2021).
46. Liu, H., Zhang, S., Liu, L., Yu, J. & Ding, B. High-Performance PM0.3 Air Filters Using Self-Polarized Electret Nanofiber/Nets. *Advanced Functional Materials* **30**, 1909554 (2020).
47. Zhang, S. *et al.* A Controlled Design of Ripple-Like Polyamide-6 Nanofiber/Nets Membrane for High-Efficiency Air Filter. *Small* **13**, 1603151 (2017).
48. Kähler, C. J. & Hain, R. Fundamental protective mechanisms of face masks against droplet infections. *Journal of Aerosol Science* **148**, 105617 (2020).
49. Aydin, O. *et al.* Performance of fabrics for home-made masks against the spread of COVID-19 through droplets: A quantitative mechanistic study. *Extreme Mechanics Letters* **40**, 100924 (2020).
50. Löndahl, J. *et al.* Size-Resolved Respiratory-Tract Deposition of Fine and Ultrafine Hydrophobic and Hygroscopic Aerosol Particles During Rest and Exercise. *Inhalation Toxicology* **19**, 109–116 (2007).

51. Chen, R. *et al.* Beyond PM2.5: The role of ultrafine particles on adverse health effects of air pollution. *Biochimica et Biophysica Acta (BBA) - General Subjects* **1860**, 2844–2855 (2016).
52. Zhang, J. *et al.* Adverse effects of exposure to fine particles and ultrafine particles in the environment on different organs of organisms. *Journal of Environmental Sciences* **135**, 449–473 (2024).
53. Rajagopalan, S., Al-Kindi, S. G. & Brook, R. D. Air Pollution and Cardiovascular Disease: JACC State-of-the-Art Review. *Journal of the American College of Cardiology* **72**, 2054–2070 (2018).
54. Dastoorpoor, M. *et al.* Air pollution and hospital admissions for cardiovascular diseases in Ahvaz, Iran. *Science of The Total Environment* **652**, 1318–1330 (2019).
55. Pfeffer, P. E., Mudway, I. S. & Grigg, J. Air Pollution and Asthma: Mechanisms of Harm and Considerations for Clinical Interventions. *Chest* **159**, 1346–1355 (2021).
56. Koenig, J. Q. Air pollution and asthma. *Journal of Allergy and Clinical Immunology* **104**, 717–722 (1999).
57. Singh, D., Gupta, I. & Roy, A. The association of asthma and air pollution: Evidence from India. *Economics & Human Biology* **51**, 101278 (2023).
58. Duan, R.-R., Hao, K. & Yang, T. Air pollution and chronic obstructive pulmonary disease. *Chronic Diseases and Translational Medicine* **6**, 260–269 (2020).
59. Oliveira, A. E. de, Aguiar, M. & Guerra, V. Improved filter media with PVA/citric acid/Triton X-100 nanofibers for filtration of nanoparticles from air. *Polymer Bulletin* (2020) doi:10.1007/s00289-020-03431-w.
60. da Mata, G. C., Morais, M. S., de Oliveira, W. P. & Aguiar, M. L. Sustainable surgical masks: optimizing fine/ultrafine particle filtration using PVA/chitosan electrospun nanofibers. *Environ. Sci.: Nano* **10**, 2185–2200 (2023).
61. Almeida, D. S. *et al.* Biodegradable CA/CPB electrospun nanofibers for efficient retention of airborne nanoparticles. *Process Safety and Environmental Protection* **144**, 177–185 (2020).
62. Bonfim, D. P. F., Cruz, F. G. S., Guerra, V. G. & Aguiar, M. L. Development of Filter Media by Electrospinning for Air Filtration of Nanoparticles from PET Bottles. *Membranes* **11**, 293 (2021).
63. Bonfim, D. P. F., Cruz, F. G. S., Bretas, R. E. S., Guerra, V. G. & Aguiar, M. L. A Sustainable Recycling Alternative: Electrospun PET-Membranes for Air Nanofiltration. *Polymers* **13**, 1166 (2021).
64. Meli, L., Miao, J., Dordick, J. S. & Linhardt, R. J. Electrospinning from room temperature ionic liquids for biopolymer fiber formation. *Green Chem.* **12**, 1883–1892 (2010).
65. Zhang, B. *et al.* Chitosan nanostructures by in situ electrospinning for high-efficiency PM2.5 capture. *Nanoscale* **9**, 4154–4161 (2017).
66. Bonilla, J., Fortunati, E., Atarés, L., Chiralt, A. & Kenny, J. M. Physical, structural and antimicrobial properties of poly vinyl alcohol–chitosan biodegradable films. *Food Hydrocolloids* **35**, 463–470 (2014).
67. Mata, G. C. da, Morais, M. S., Oliveira, W. P. de & Aguiar, M. L. Composition Effects on the Morphology of PVA/Chitosan Electrospun Nanofibers. *Polymers* **14**, 4856 (2022).
68. Vu, T. H. N., Morozkina, S. N. & Uspenskaya, M. V. Study of the Nanofibers Fabrication Conditions from the Mixture of Poly(vinyl alcohol) and Chitosan by Electrospinning Method. *Polymers* **14**, 811 (2022).
69. Yan, J. *et al.* Preparation and property studies of chitosan-PVA biodegradable antibacterial multilayer films doped with Cu2O and nano-chitosan composites. *Food Control* **126**, 108049 (2021).
70. Panda, P. K., Sadeghi, K. & Seo, J. Recent advances in poly (vinyl alcohol)/natural polymer based films for food packaging applications: A review. *Food Packaging and Shelf Life* **33**, 100904 (2022).
71. Duru Kamaci, U. & Peksel, A. Fabrication of PVA-chitosan-based nanofibers for phytase immobilization to enhance enzymatic activity. *International Journal of Biological Macromolecules* **164**, 3315–3322 (2020).
72. Abbas, W. A., Sharafeldin, I. M., Omar, M. M. & Allam, N. K. Novel mineralized electrospun chitosan/PVA/TiO2 nanofibrous composites for potential biomedical applications: computational and experimental insights. *Nanoscale Advances* **2**, 1512–1522 (2020).
73. Morais, M. S., Bonfim, D. P. F., Aguiar, M. L. & Oliveira, W. P. Electrospun Poly (Vinyl Alcohol) Nanofibrous Mat Loaded with Green Propolis Extract, Chitosan and Nystatin as an Innovative Wound Dressing Material. *Journal of Pharmaceutical Innovation* 1–15 (2022) doi:10.1007/s12247-022-09681-7.
74. Rieger, K. A., Birch, N. P. & Schiffman, J. D. Designing electrospun nanofiber mats to promote wound healing – a review. *J. Mater. Chem. B* **1**, 4531–4541 (2013).
75. Konwarh, R., Karak, N. & Misra, M. Electrospun cellulose acetate nanofibers: The present status and gamut of biotechnological applications. *Biotechnology Advances* **31**, 421–437 (2013).
76. Rubenstein, D. A. *et al.* In Vitro Biocompatibility of Sheath–Core Cellulose-Acetate-Based Electrospun Scaffolds Towards Endothelial Cells and Platelets. *Journal of Biomaterials Science, Polymer Edition* **21**, 1713–1736 (2010).
77. Khatri, Z., Wei, K., Kim, B.-S. & Kim, I.-S. Effect of deacetylation on wicking behavior of co-electrospun cellulose acetate/polyvinyl alcohol nanofibers blend. *Carbohydrate Polymers* **87**, 2183–2188 (2012).
78. Liu, F. X., Liu, Y. J., Cai, H. L., Luan, J. S. & Zhang, M. Preparation and Mechanical Properties of Zein/PVA Nanofibrous Membranes. *Advanced Materials Research* **466–467**, 391–395 (2012).
79. Torres-Giner, S., Ocio, M. J. & Lagaron, J. M. Novel antimicrobial ultrathin structures of zein/chitosan blends obtained by electrospinning. *Carbohydrate Polymers* **77**, 261–266 (2009).
80. Torres-Giner, S., Pérez-Masiá, R. & Lagaron, J. M. A review on electrospun polymer nanostructures as advanced bioactive platforms. *Polymer Engineering & Science* **56**, 500–527 (2016).
81. Ali, S., Khatri, Z., Oh, K. W., Kim, I.-S. & Kim, S. H. Zein/cellulose acetate hybrid nanofibers: Electrospinning and characterization. *Macromol. Res.* **22**, 971–977 (2014).
82. Yao, C., Li, X., Song, T., Li, Y. & Pu, Y. Biodegradable nanofibrous membrane of zein/silk fibroin by electrospinning. *Polymer International* **58**, 396–402 (2009).
83. Lin, J., Li, C., Zhao, Y., Hu, J. & Zhang, L.-M. Co-electrospun Nanofibrous Membranes of Collagen and Zein for Wound Healing. *ACS Appl. Mater. Interfaces* **4**, 1050–1057 (2012).
84. Bhattacharya, S. Central Composite Design for Response Surface Methodology and Its Application in Pharmacy. in *Response Surface Methodology in Engineering Science* (IntechOpen, 2021). doi:10.5772/intechopen.95835.
85. He, H., Wang, Y., Farkas, B., Nagy, Z. K. & Molnar, K. Analysis and prediction of the diameter and orientation of AC electrospun nanofibers by response surface methodology. *Materials & Design* **194**, 108902 (2020).

86. Breig, S. J. M. & Luti, K. J. K. Response surface methodology: A review on its applications and challenges in microbial cultures. *Materials Today: Proceedings* **42**, 2277–2284 (2021).
87. Yördem, O. S., Papila, M. & Menceloğlu, Y. Z. Effects of electrospinning parameters on polyacrylonitrile nanofiber diameter: An investigation by response surface methodology. *Materials & Design* **29**, 34–44 (2008).
88. Souza, C., Bott, R. & Oliveira, W. Optimization of the extraction of flavonoids compounds from herbal material using experimental design and multi-response analysis. *LATIN AMERICAN JOURNAL OF PHARMACY* **26**, 682 (2007).
89. Das, D., Das, S. & Ishtiaque, S. M. Optimal design of nonwoven air filter media: Effect of fibre shape. *Fibers Polym* **15**, 1456–1461 (2014).
90. Costa, N. R., Lourenço, J. & Pereira, Z. L. Desirability function approach: A review and performance evaluation in adverse conditions. *Chemometrics and Intelligent Laboratory Systems* **107**, 234–244 (2011).
91. Jeong, I.-J. & Kim, K.-J. An interactive desirability function method to multiresponse optimization. *European Journal of Operational Research* **195**, 412–426 (2009).
92. Souza, A. M. de *et al.* Application of the desirability function for the development of new composite eco-efficiency indicators for concrete. *Journal of Building Engineering* **40**, 102374 (2021).
93. Varatharajulu, M. *et al.* Evaluation of Desirability Function Approach and Genetic Algorithm optimization of drilling characteristics on Duplex 2205. *Materials Today: Proceedings* **22**, 589–600 (2020).
94. Baldim, I., Paziani, M. H., Grizante Barião, P. H., Kress, M. R. von Z. & Oliveira, W. P. Nanostructured Lipid Carriers Loaded with Lippia sidoides Essential Oil as a Strategy to Combat the Multidrug-Resistant Candida auris. *Pharmaceutics* **14**, 180 (2022).
95. Baldim, I., Tonani, L., von Zeska Kress, M. R. & Pereira Oliveira, W. Lippia sidoides essential oil encapsulated in lipid nanosystem as an anti-Candida agent. *Industrial Crops and Products* **127**, 73–81 (2019).
96. Morgana, S., Casentini, B. & Amalfitano, S. Uncovering the release of micro/nanoplastics from disposable face masks at times of COVID-19. *Journal of Hazardous Materials* **419**, 126507 (2021).
97. Mello, L. R. P. F. & Mali, S. Use of malt bagasse to produce biodegradable baked foams made from cassava starch. *Industrial Crops and Products* **55**, 187–193 (2014).
98. Aguilar, G. J. & Tapia-Blácido, D. R. Evaluating how avocado residue addition affects the properties of cassava starch-based foam trays. *International Journal of Biological Macromolecules* **240**, 124348 (2023).
99. Leung, W. W. F. & Sun, Q. Charged PVDF multilayer nanofiber filter in filtering simulated airborne novel coronavirus (COVID-19) using ambient nano-aerosols. *Separation and Purification Technology* **245**, 116887 (2020).
100. Leung, W. W. F. & Sun, Q. Electrostatic charged nanofiber filter for filtering airborne novel coronavirus (COVID-19) and nano-aerosols. *Separation and Purification Technology* **250**, 116886 (2020).
101. Wang, Z. *et al.* Antibacterial and environmentally friendly chitosan/polyvinyl alcohol blend membranes for air filtration. *Carbohydrate Polymers* **198**, 241–248 (2018).
102. Bortolassi, A. C. C., Guerra, V. G. & Aguiar, M. L. Characterization and evaluate the efficiency of different filter media in removing nanoparticles. *Separation and Purification Technology* **175**, 79–86 (2017).
103. de Barros, P. M., Rodrigues Cirqueira, S. S. & Aguiar, M. L. Evaluation of the Deposition of Nanoparticles in Fibrous Filter. *Materials Science Forum* **802**, 174–179 (2014).
104. Granato, D. & Ares, G. *Mathematical and Statistical Methods in Food Science and Technology*. (John Wiley & Sons, 2014).
105. Wang, Y. & Chen, L. Fabrication and characterization of novel assembled prolamin protein nanofabrics with improved stability, mechanical property and release profiles. *J. Mater. Chem.* **22**, 21592–21601 (2012).
106. Matulevicius, J. *et al.* Design and Characterization of Electrospun Polyamide Nanofiber Media for Air Filtration Applications. *Journal of Nanomaterials* **2014**, e859656 (2014).
107. Yang, Y., Zhang, S., Zhao, X., Yu, J. & Ding, B. Sandwich structured polyamide-6/polyacrylonitrile nanonets/bead-on-string composite membrane for effective air filtration. *Separation and Purification Technology* **152**, 14–22 (2015).
108. Liu, F. *et al.* Sesamol incorporated cellulose acetate-zein composite nanofiber membrane: An efficient strategy to accelerate diabetic wound healing. *International Journal of Biological Macromolecules* **149**, 627–638 (2020).
109. Deng, L., Kang, X., Liu, Y., Feng, F. & Zhang, H. Characterization of gelatin/zein films fabricated by electrospinning vs solvent casting. *Food Hydrocolloids* **74**, 324–332 (2018).
110. Torres, S. J. V. *et al.* Mechanical and water absorption properties and morphology of melt processed Zein/PVAl blends. *Polímeros* **30**, (2021).
111. Soliman, S. *et al.* Controlling the porosity of fibrous scaffolds by modulating the fiber diameter and packing density. *Journal of Biomedical Materials Research Part A* **96A**, 566–574 (2011).
112. Geng, X., Kwon, O.-H. & Jang, J. Electrospinning of chitosan dissolved in concentrated acetic acid solution. *Biomaterials* **26**, 5427–5432 (2005).
113. Qasim, S. B. *et al.* Electrospinning of Chitosan-Based Solutions for Tissue Engineering and Regenerative Medicine. *Int J Mol Sci* **19**, 407 (2018).
114. Charernsriwilaiwat, N., Rojanarata, T., Ngawhirunpat, T. & Opanasopit, P. Electrospun chitosan/polyvinyl alcohol nanofibre mats for wound healing. *International Wound Journal* **11**, 215–222 (2014).
115. Chen, Z. *et al.* Mechanical properties of electrospun collagen–chitosan complex single fibers and membrane. *Materials Science and Engineering: C* **29**, 2428–2435 (2009).
116. Ojha, S. S. *et al.* Fabrication and Characterization of Electrospun Chitosan Nanofibers Formed via Templating with Polyethylene Oxide. *Biomacromolecules* **9**, 2523–2529 (2008).
117. Kohsari, I., Shariatinia, Z. & Pourmortazavi, S. M. Antibacterial electrospun chitosan–polyethylene oxide nanocomposite mats containing bioactive silver nanoparticles. *Carbohydrate Polymers* **140**, 287–298 (2016).
118. Li, H.-Z., Chen, S.-C. & Wang, Y.-Z. Preparation and characterization of nanocomposites of polyvinyl alcohol/cellulose nanowhiskers/chitosan. *Composites Science and Technology* **115**, 60–65 (2015).
119. Sun, C., Boluk, Y. & Ayranci, C. Investigation of nanofiber nonwoven meshes produced by electrospinning of cellulose nanocrystal suspensions in cellulose acetate solutions. *Cellulose* **22**, 2457–2470 (2015).
120. Jeong, J. S. *et al.* Mechanical properties of electrospun PVA/MWNTs composite nanofibers. *Thin Solid Films* **515**, 5136–5141 (2007).

121. Kamoun, E. A., Chen, X., Mohy Eldin, M. S. & Kenawy, E.-R. S. Crosslinked poly(vinyl alcohol) hydrogels for wound dressing applications: A review of remarkably blended polymers. *Arabian Journal of Chemistry* **8**, 1–14 (2015).
122. Kim, H. J., Pant, H. R., Choi, N. J. & Kim, C. S. Composite electrospun fly ash/polyurethane fibers for absorption of volatile organic compounds from air. *Chemical Engineering Journal* **230**, 244–250 (2013).
123. Silva, T. H., Oliveira, J. E. de & Medeiros, E. S. de. Obtenção de micro e nanofibras de PVC pela técnica de Fiação por Sopro em Solução. *Polímeros* **25**, 229–235 (2015).
124. Bazbouz, M. B. & Stylios, G. K. The tensile properties of electrospun nylon 6 single nanofibers. *Journal of Polymer Science Part B: Polymer Physics* **48**, 1719–1731 (2010).
125. Monjazeb Marvdashti, L., Koocheki, A. & Yavarmanesh, M. *Alyssum homolocarpum* seed gum-polyvinyl alcohol biodegradable composite film: Physicochemical, mechanical, thermal and barrier properties. *Carbohydrate Polymers* **155**, 280–293 (2017).
126. Lv, R. *et al.* Poly(vinylidene fluoride) fibrous membranes doped with polyamide 6 for highly efficient separation of a stable oil/water emulsion. *Journal of Applied Polymer Science* **134**, (2017).
127. Bianco, A. *et al.* Modification of surface properties of electrospun polyamide nanofibers by means of a perfluorinated acridine. *Applied Surface Science* **253**, 8360–8364 (2007).
128. Kurihara, K., Hokari, R. & Takada, N. Capillary Effect Enhancement in a Plastic Capillary Tube by Nanostructured Surface. *Polymers* **13**, 628 (2021).
129. Cao, Q., Zhang, Y., Chen, W., Meng, X. & Liu, B. Hydrophobicity and physicochemical properties of agarose film as affected by chitosan addition. *International Journal of Biological Macromolecules* **106**, 1307–1313 (2018).
130. Dang, K. M. & Yoksan, R. Morphological characteristics and barrier properties of thermoplastic starch/chitosan blown film. *Carbohydrate Polymers* **150**, 40–47 (2016).
131. Elsabee, M. Z. & Abdou, E. S. Chitosan based edible films and coatings: A review. *Materials Science and Engineering: C* **33**, 1819–1841 (2013).
132. Li, K., Zhu, J., Guan, G. & Wu, H. Preparation of chitosan-sodium alginate films through layer-by-layer assembly and ferulic acid crosslinking: Film properties, characterization, and formation mechanism. *International Journal of Biological Macromolecules* **122**, 485–492 (2019).
133. Jiang, Q., Reddy, N. & Yang, Y. Cytocompatible cross-linking of electrospun zein fibers for the development of water-stable tissue engineering scaffolds. *Acta Biomaterialia* **6**, 4042–4051 (2010).
134. Fairchild, C. I. & Stampfer, J. F. Particle concentration in exhaled breath. *Am Ind Hyg Assoc J* **48**, 948–949 (1987).
135. Edwards, D. A. *et al.* Inhaling to mitigate exhaled bioaerosols. *Proc Natl Acad Sci U S A* **101**, 17383–17388 (2004).
136. Chao, C. Y. H. *et al.* Characterization of expiration air jets and droplet size distributions immediately at the mouth opening. *Journal of Aerosol Science* **40**, 122–133 (2009).
137. Morawska, L. *et al.* Size distribution and sites of origin of droplets expelled from the human respiratory tract during expiratory activities. *Journal of Aerosol Science* **40**, 256–269 (2009).
138. Johnson, G. R. *et al.* Modality of human expired aerosol size distributions. *Journal of Aerosol Science* **42**, 839–851 (2011).
139. Alsved, M. *et al.* Exhaled respiratory particles during singing and talking. *Aerosol Science and Technology* **54**, 1245–1248 (2020).
140. Kravtsov, A., Brnig, H., Zhandarov, S. & Beyreuther, R. The electret effect in polypropylene fibers treated in a corona discharge. in (2000). doi:10.1002/1098-2329(200024)19:4<312::AID-ADV7>3.0.CO;2-X.
141. Konda, A. *et al.* Aerosol Filtration Efficiency of Common Fabrics Used in Respiratory Cloth Masks. *ACS Nano* **14**, 6339–6347 (2020).
142. Das, O. *et al.* The need for fully bio-based facemasks to counter coronavirus outbreaks: A perspective. *Science of The Total Environment* **736**, 139611 (2020).
143. Thakur, V. K. *Nanocellulose Polymer Nanocomposites: Fundamentals and Applications*. (John Wiley & Sons, 2014).
144. Xia, T., Bian, Y., Zhang, L. & Chen, C. Relationship between pressure drop and face velocity for electrospun nanofiber filters. *Energy and Buildings* **158**, 987–999 (2018).
145. Zhu, M. *et al.* A novel cellulose acetate/poly (ionic liquid) composite air filter. *Cellulose* **27**, 3889–3902 (2020).
146. Lee, D.-H., Jeong, I.-J. & Kim, K.-J. A desirability function method for optimizing mean and variability of multiple responses using a posterior preference articulation approach. *Quality and Reliability Engineering International* **34**, 360–376 (2018).
147. Wang, X., Ding, B., Sun, G., Wang, M. & Yu, J. Electro-spinning/netting: A strategy for the fabrication of three-dimensional polymer nano-fiber/nets. *Progress in Materials Science* **58**, 1173–1243 (2013).
148. Zhang, S., Chen, K., Yu, J. & Ding, B. Model derivation and validation for 2D polymeric nanonets: Origin, evolution, and regulation. *Polymer* **74**, 182–192 (2015).

7.6 Supplementary Materials

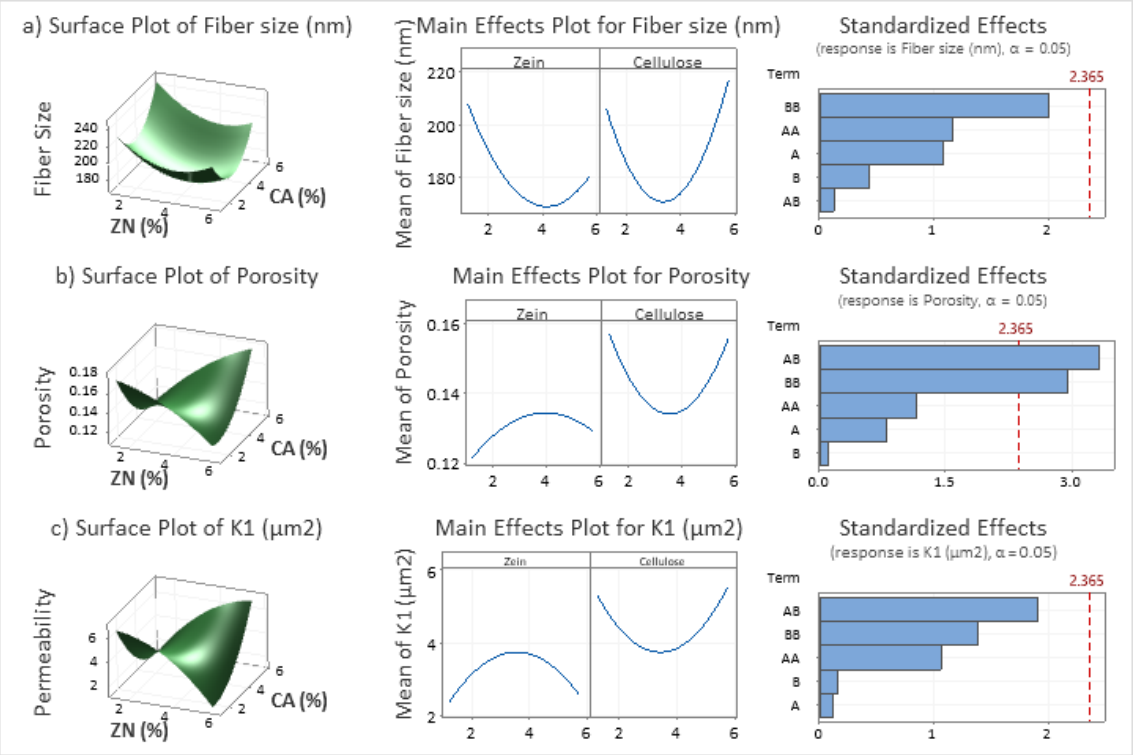

Figure S7.1: Surface plot, main effects plot and Pareto charts from the following fiber mat responses: **a)** fiber average diameter; **b)** mat's porosity; and **c)** mat's permeability. In the standardize effects "A" represents the zein content, and "B" represents the cellulose acetate content.

Table S7.1: Anova data for the model describing the Fiber Average Diameter response.

Analysis of Variance					
Source	DF	Adj SS	Adj MS	F-Value	P-Value
Model	5	3448.21	689.64	1.25	0.38
Linear	2	756.32	378.16	0.68	0.535
Zein	1	653.2	653.2	1.18	0.313
AcCell	1	103.12	103.12	0.19	0.679
Square	2	2683.12	1341.56	2.43	0.158
Zein*Zein	1	740.08	740.08	1.34	0.285
AcCell*AcCell	1	2232.73	2232.73	4.04	0.084
2-Way Interaction	1	8.77	8.77	0.02	0.903
Zein*AcCell	1	8.77	8.77	0.02	0.903
Error	7	3866.45	552.35		
Lack-of-Fit	3	2781.84	927.28	3.42	0.133
Pure Error	4	1084.61	271.15		
Total	12	7314.66			

Table S7.2: Anova data for the model describing the Porosity response.

Analysis of Variance					
Source	DF	Adj SS	Adj MS	F-Value	P-Value
Model	5	0.001801	0.00036	4.53	0.037
Linear	2	0.000051	0.000025	0.32	0.736
Zein	1	0.00005	0.00005	0.63	0.454
AcCell	1	0.000001	0.000001	0.01	0.914
Square	2	0.000878	0.000439	5.53	0.036
Zein*Zein	1	0.000105	0.000105	1.32	0.288
AcCell*AcCell	1	0.000688	0.000688	8.66	0.022
2-Way Interaction	1	0.000872	0.000872	10.98	0.013
Zein*AcCell	1	0.000872	0.000872	10.98	0.013
Error	7	0.000556	0.000079		
Lack-of-Fit	3	0.000249	0.000083	1.08	0.452
Pure Error	4	0.000307	0.000077		
Total	12	0.002358			

Table S7.3: Anova data for the model describing the Permeability response.

Analysis of Variance					
Source	DF	Adj SS	Adj MS	F-Value	P-Value
Model	5	14.2611	2.85222	1.43	0.32
Linear	2	0.0761	0.03807	0.02	0.981
Zein	1	0.027	0.02698	0.01	0.911
AcCell	1	0.0492	0.04916	0.02	0.879
Square	2	6.9534	3.4767	1.75	0.242
Zein*Zein	1	2.2458	2.24577	1.13	0.323
AcCell*AcCell	1	3.8248	3.82478	1.92	0.208
2-Way Interaction	1	7.2315	7.23155	3.64	0.098
Zein*AcCell	1	7.2315	7.23155	3.64	0.098
Error	7	13.9179	1.98828		
Lack-of-Fit	3	0.3131	0.10436	0.03	0.992
Pure Error	4	13.6049	3.40122		
Total	12	28.179			

Table 7.4: Models generated through the Central Composite Desing for the responses of Fiber Average Diameter, the Fiber Mat Porosity and Fiber Mat Permeability. “Cellulose” represents the cellulose acetate.

Response		Model	p-Value
Fiber Average Diameter (nm)	=	329.5 - 35.8 Zein - 51.0 Cellulose + 4.58 Zein*Zein	0.380
Porosity	=	0.2426 - 0.0092 Zein - 0.0542 Cellulose - 0.00173 Zein*Zein	0.037
Permeability (µm)	=	11.69 - 0.29 Zein - 4.35 Cellulose - 0.253 Zein*Zein + 0.330 Cellulose*Cellulose	0.320

Table S7.5: Data collected in the mechanical tests from the samples used to construct the Central Composite Design model, described in **Table 7.1**.

Sample	Thickness (mm)	Tension (MPa)	Elongation (%)	Young Modulus (MPa)
MR00	0.017 ± 0.001	10.170 ± 3.109	11.389 ± 4.385	280.100 ± 139.586
MR01	0.014 ± 0.002	7.458 ± 1.557	10.998 ± 3.209	143.817 ± 42.904
MR02	0.017 ± 0.001	4.858 ± 1.523	9.560 ± 1.523	156.000 ± 75.881
MR03	0.017 ± 0.001	7.022 ± 3.170	8.139 ± 3.321	178.167 ± 69.674
MR04	0.017 ± 0.002	10.114 ± 4.198	4.891 ± 2.073	330.250 ± 172.232
MR05	0.016 ± 0.001	4.280 ± 1.938	7.752 ± 6.148	128.886 ± 37.506
MR06	0.017 ± 0.001	6.896 ± 2.127	10.389 ± 8.830	174.850 ± 73.379
MR07	0.017 ± 0.002	11.110 ± 5.431	7.863 ± 3.351	317.417 ± 173.947
MR08	0.017 ± 0.001	12.366 ± 5.243	8.733 ± 1.959	322.267 ± 133.928
MR09	0.018 ± 0.001	8.642 ± 6.426	9.223 ± 6.157	152.728 ± 100.369
MR10	0.018 ± 0.001	10.784 ± 3.843	8.976 ± 2.759	335.000 ± 148.685
MR11	0.017 ± 0.001	8.418 ± 3.357	6.468 ± 3.542	286.100 ± 106.041
MR12	0.015 ± 0.001	3.690 ± 1.641	7.616 ± 2.937	142.550 ± 44.789
MR13	0.018 ± 0.001	9.780 ± 2.990	7.723 ± 3.854	260.583 ± 64.178

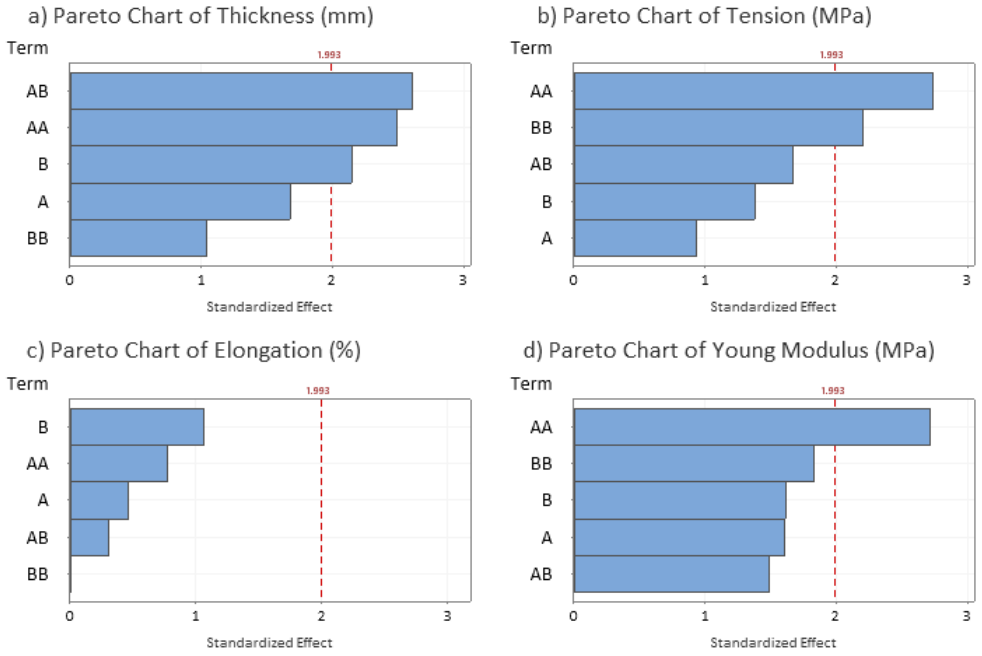

Figure S7.2: Pareto charts for each one of the mechanical resistance responses. In the standardize effects "A" represents the zein content, and "B" represents the cellulose acetate content.

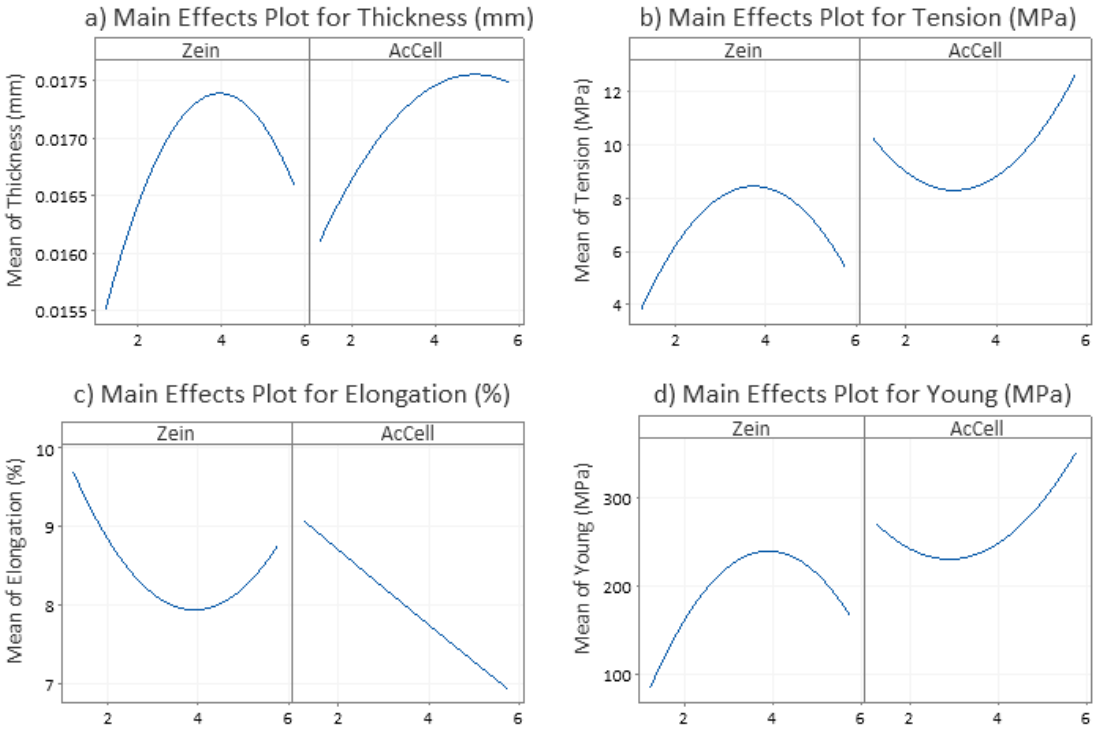

Figure S7.3: Main Effects Plot for each one of the mechanical resistance responses.

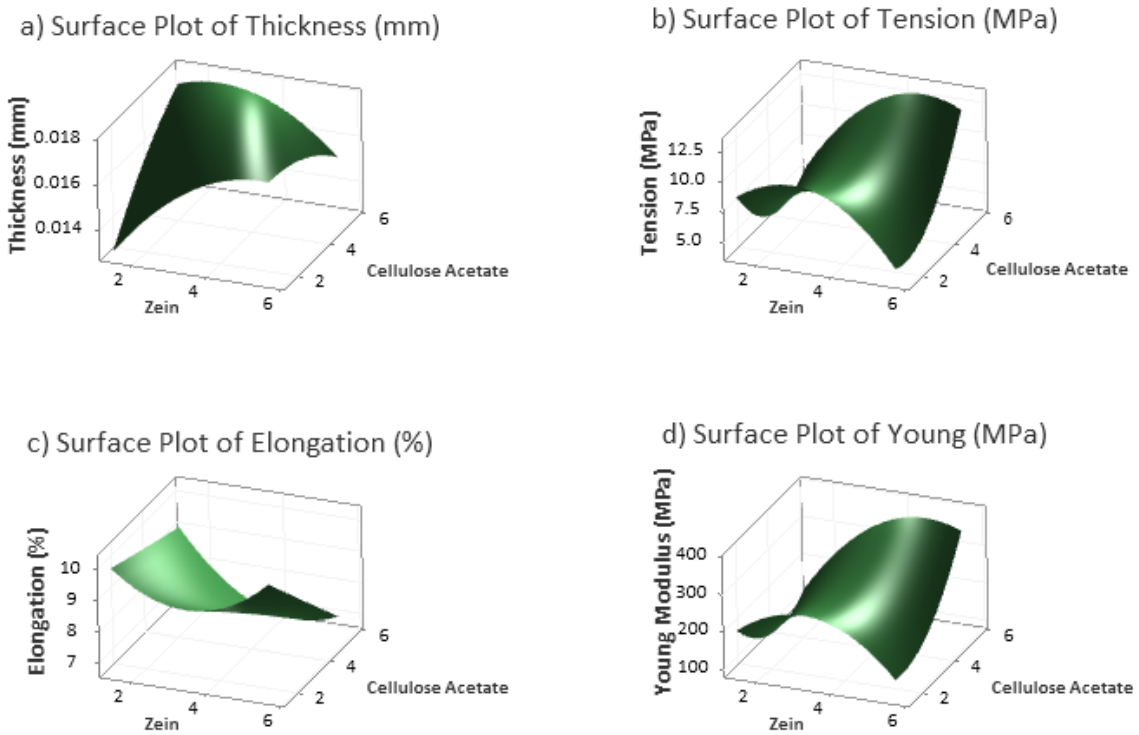

Figure S7.4: Surface Plot for each one of the mechanical resistance responses.

Table S7.6: Anova data for the model describing the Thickness response.

Analysis of Variance					
Source	DF	Adj SS	Adj MS	F-Value	P-Value
Model	5	0.000046	0.000009	4.2	0.002
Linear	2	0.000016	0.000008	3.71	0.029
Zein	1	0.000006	0.000006	2.81	0.098
AcCell	1	0.00001	0.00001	4.61	0.035
Square	2	0.000015	0.000007	3.37	0.04
Zein*Zein	1	0.000014	0.000014	6.22	0.015
AcCell*AcCell	1	0.000002	0.000002	1.09	0.3
2-Way Interaction	1	0.000015	0.000015	6.83	0.011
Zein*AcCell	1	0.000015	0.000015	6.83	0.011
Error	72	0.000159	0.000002		
Lack-of-Fit	3	0.000005	0.000002	0.82	0.49
Pure Error	69	0.000153	0.000002		
Total	77	0.000205			

Table S7.7: Anova data for the model describing the Tension response.

Analysis of Variance					
Source	DF	Adj SS	Adj MS	F-Value	P-Value
Model	5	312.57	62.51	3.95	0.003
Linear	2	43.85	21.93	1.39	0.257
Zein	1	13.73	13.73	0.87	0.355
AcCell	1	30.12	30.12	1.9	0.172
Square	2	224.43	112.22	7.09	0.002
Zein*Zein	1	118.91	118.91	7.52	0.008
AcCell*AcCell	1	76.78	76.78	4.85	0.031
2-Way Interaction	1	44.28	44.28	2.8	0.099
Zein*AcCell	1	44.28	44.28	2.8	0.099
Error	72	1139.04	15.82		
Lack-of-Fit	3	30.83	10.28	0.64	0.592
Pure Error	69	1108.22	16.06		
Total	77	1451.61			

Table S7.8: Anova data for the model describing the Elongation at break response.

Analysis of Variance					
Source	DF	Adj SS	Adj MS	F-Value	P-Value
Model	5	43.6	8.7193	0.41	0.841
Linear	2	28.67	14.3339	0.67	0.514
Zein	1	4.65	4.6503	0.22	0.642
AcCell	1	24.02	24.0174	1.13	0.292
Square	2	12.88	6.4378	0.3	0.74
Zein*Zein	1	12.7	12.6974	0.6	0.443
AcCell*AcCell	1	0	0.0022	0	0.992
2-Way Interaction	1	2.05	2.0533	0.1	0.757
Zein*AcCell	1	2.05	2.0533	0.1	0.757
Error	72	1535.47	21.326		
Lack-of-Fit	3	103.77	34.5904	1.67	0.182
Pure Error	69	1431.7	20.7493		
Total	77	1579.07			

Table S7.9: Anova data for the model describing the Young Modulus response.

Analysis of Variance					
Source	DF	Adj SS	Adj MS	F-Value	P-Value
Model	5	266621	53324	3.93	0.003
Linear	2	70460	35230	2.6	0.081
Zein	1	35124	35124	2.59	0.112
AcCell	1	35336	35336	2.61	0.111
Square	2	166128	83064	6.13	0.003
Zein*Zein	1	100353	100353	7.4	0.008
AcCell*AcCell	1	45350	45350	3.34	0.072
2-Way Interaction	1	30033	30033	2.21	0.141
Zein*AcCell	1	30033	30033	2.21	0.141
Error	72	976421	13561		
Lack-of-Fit	3	55624	18541	1.39	0.253
Pure Error	69	920797	13345		
Total	77	1243042			

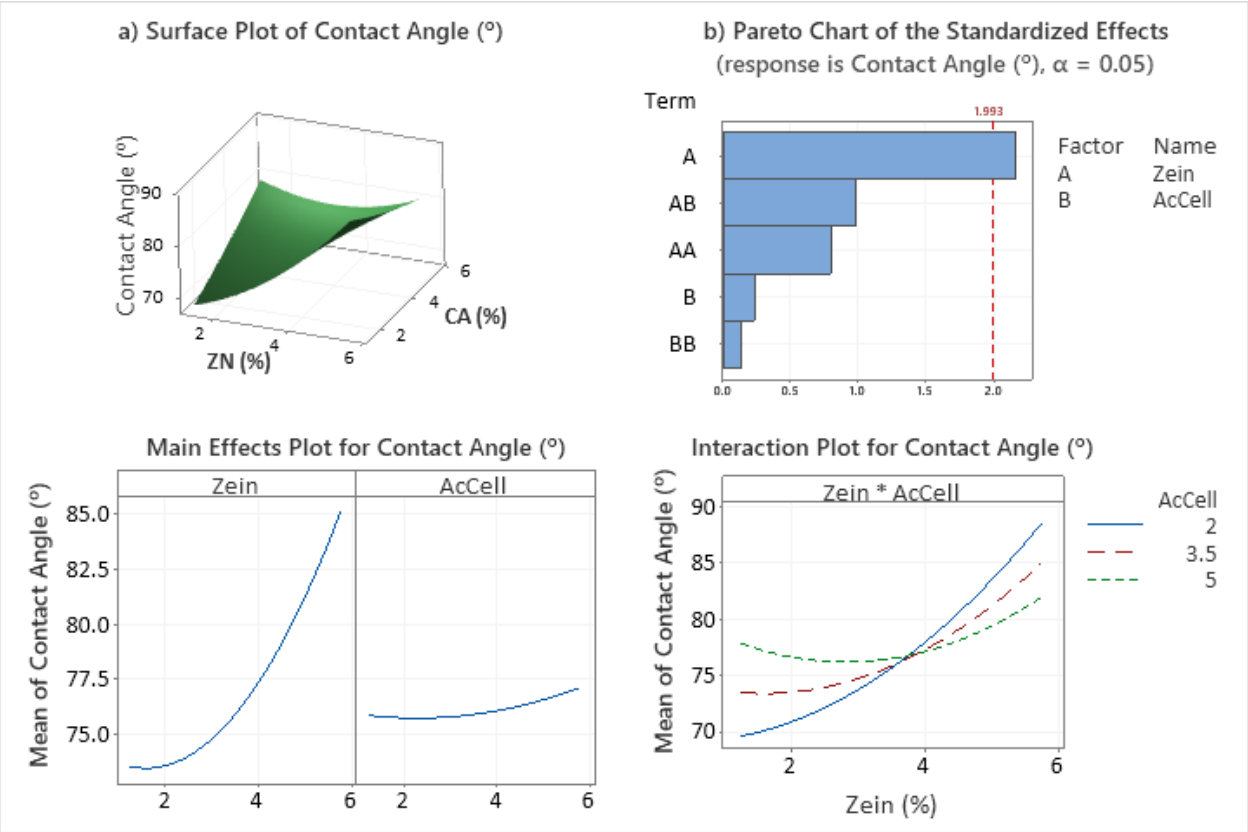

Figure S7.5: Graphs for the Contact angle response, being: **a)** the Surface Plot; **b)** the Pareto Chart; **c)** the Main Effects Plot; and **d)** the Interaction Plot.

Table S7.9: Anova data for the model describing the Young Modulus response.

Analysis of Variance					
Source	DF	Adj SS	Adj MS	F-Value	P-Value
Model	5	967.1	193.42	1.26	0.291
Linear	2	723.4	361.69	2.35	0.102
Zein	1	715.1	715.15	4.66	0.034
AcCell	1	8.2	8.24	0.05	0.817
Square	2	97	48.51	0.32	0.73
Zein*Zein	1	96.9	96.88	0.63	0.43
AcCell*AcCell	1	2.7	2.74	0.02	0.894
2-Way Interaction	1	146.7	146.72	0.96	0.332
Zein*AcCell	1	146.7	146.72	0.96	0.332
Error	72	11060.5	153.62		
Lack-of-Fit	3	8450.5	2816.83	74.47	0
Pure Error	69	2610	37.83		
Total	77	12027.6			

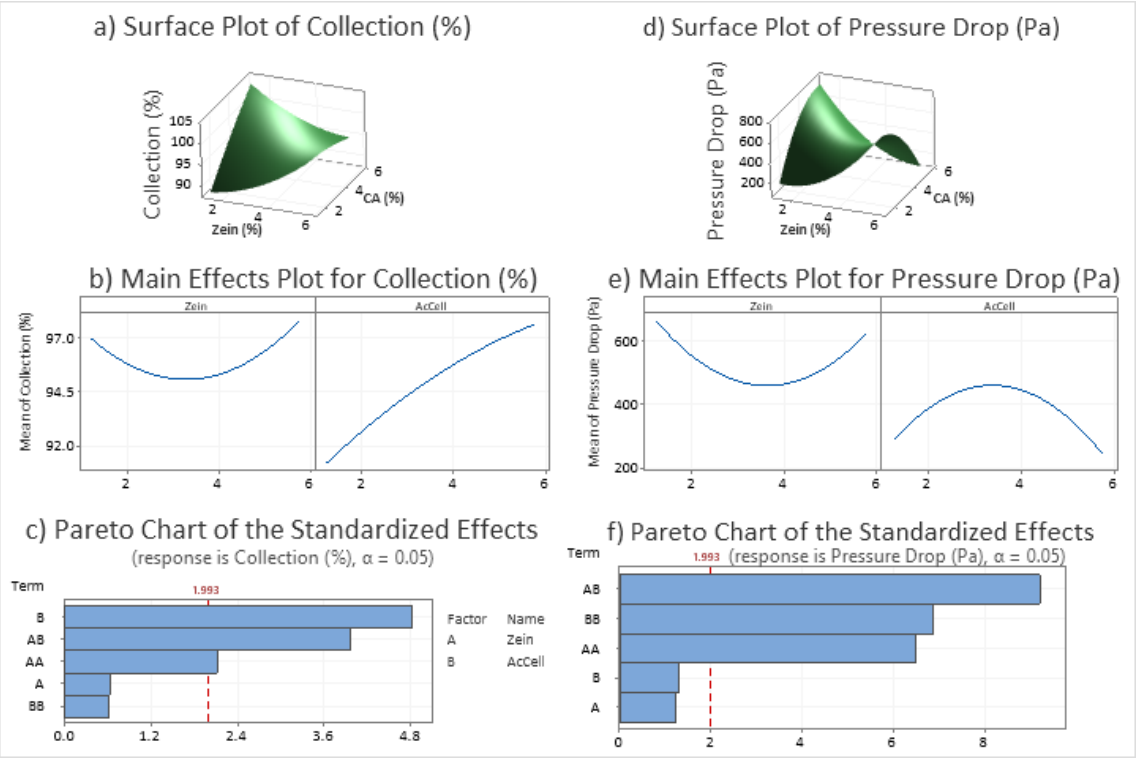

Figure S7.6: Graphs for the Collection response from the tests at 3.0 L.min^{-1}, being: **a)** the Surface Plot; **b)** the Main Effects Plot; **c)** the Pareto Chart; and graphs for the Pressure drop response, being: **d)** the Surface Plot; e**)** the Main Effects Plot; f**)** the Pareto Chart. Factor A represents the Zein and Factor B represents the cellulose acetate.

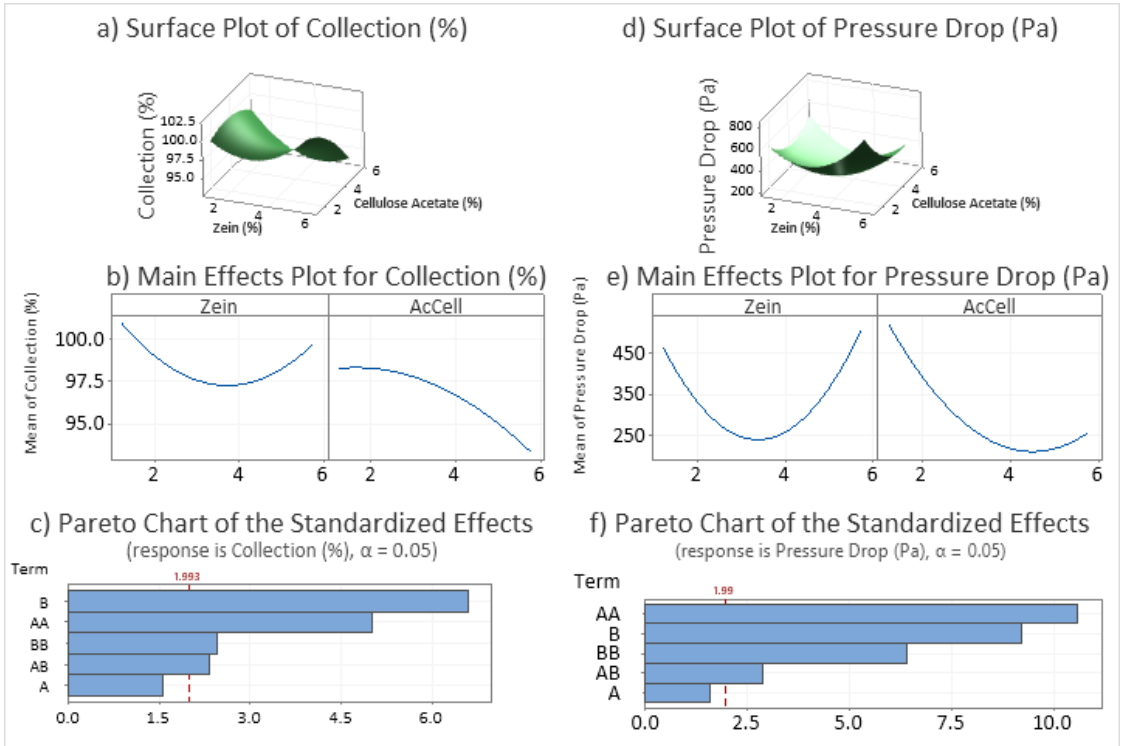

Figure S7.7: Graphs for the Collection response from the tests at 4.5 L.min^{-1}, being: **a)** the Surface Plot; **b)** the Main Effects Plot; **c)** the Pareto Chart; and graphs for the Pressure drop response, being: **d)** the Surface Plot; e**)** the Main Effects Plot; f**)** the Pareto Chart. Factor A represents the Zein and Factor B represents the cellulose acetate.

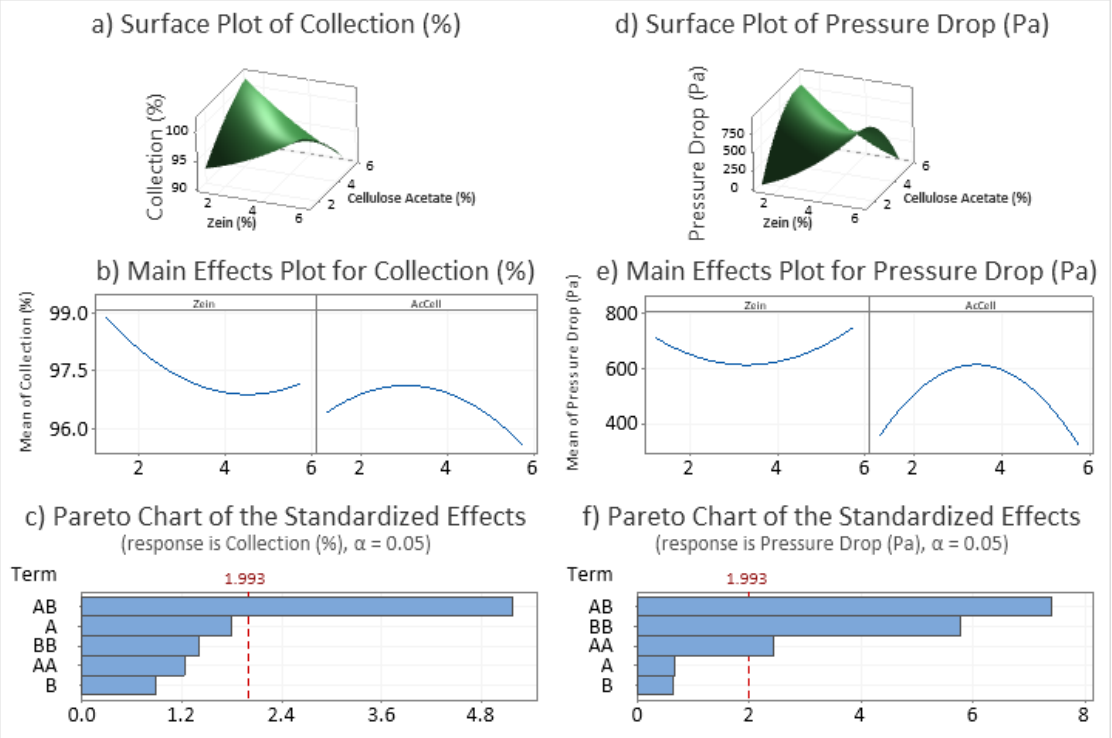

Figure S7.8: Graphs for the Collection response from the tests at 6.0 L.min^{-1}, being: **a)** the Surface Plot; **b)** the Main Effects Plot; **c)** the Pareto Chart; and graphs for the Pressure drop response, being: **d)** the Surface Plot; e**)** the Main Effects Plot; f**)** the Pareto Chart. Factor A represents the Zein and Factor B represents the cellulose acetate.

Table S7.10: Models generated by the Response Surface Methodology, for all the responses in this study.

Response		Model	p-Value
Thickness (mm)	=	0.00669 + 0.003253 ZN + 0.002286 CA – 0.000255 ZN×ZN – 0.000106 CA×CA – 0.000352 ZN×CA	0.002
Tension (MPa)	=	10.89 + 3.49 ZN – 5.80 CA – 0.750 ZN×ZN + 0.603 CA×CA + 0.604 ZN×CA	0.003
Elongation (%)	=	11.81 – 1.47 ZN – 0.04 CA + 0.245 ZN×ZN + 0.003 CA×CA – 0.130 ZN×CA	0.841
Young Modulus (MPa)	=	214 + 115.6 ZN – 139.5 CA – 21.79 ZN×ZN + 14.65 CA×CA + 15.7 ZN×CA	0.003
Contact Angle (°)	=	62.1 + 1.68 ZN + 3.33 CA + 0.677 ZN×ZN + 0.114 CA×CA - 1.10 ZN×CA	0.291
Collection (%) – 3.0 L.min^{-1}	=	79.93 + 0.90 ZN + 6.17 CA + 0.446 ZN*ZN - 0.131 CA*CA	0.000
Pressure Drop (Pa) – 3.0 L.min^{-1}	=	-325 - 26.0 ZN + 495.1 CA + 36.18 ZN*ZN - 38.35 CA*CA	0.000
Collection (%) – 4.5 L.min^{-1}	=	101.28 - 3.16 ZN + 2.24 CA + 0.597 ZN*ZN - 0.293 CA*CA	0.000
Pressure Drop (Pa) – 4.5 L.min^{-1}	=	1158 - 270.4 ZN - 206.0 CA + 48.95 ZN*ZN + 29.75 CA*CA	0.000
Collection (%) – 6.0 L.min^{-1}	=	86.16 + 1.90 ZN + 4.91 CA + 0.188 ZN*ZN - 0.214 CA*CA	0.000
Pressure Drop (Pa) – 6.0 L.min^{-1}	=	-905 + 171.0 ZN + 697.3 CA + 23.05 ZN*ZN - 54.65 CA*CA	0.000

Table S7.11: Anova data for the model describing the Collection efficiency response, for the filtration at 3.0 $L.min^{-1}$.

Analysis of Variance					
Source	DF	Adj SS	Adj MS	F-Value	P-Value
Model	5	415.38	83.076	8.92	0.000
Linear	2	219.95	109.974	11.81	0.000
Zein	1	3.76	3.760	0.40	0.527
AcCell	1	216.19	216.188	23.21	0.000
Square	2	49.68	24.838	2.67	0.076
Zein*Zein	1	41.98	41.975	4.51	0.037
AcCell*AcCell	1	3.63	3.633	0.39	0.534
2-Way Interaction	1	145.75	145.754	15.65	0.000
Zein*AcCell	1	145.75	145.754	15.65	0.000
Error	72	670.68	9.315		
Lack-of-Fit	3	287.89	95.965	17.30	0.000
Pure Error	69	382.79	5.548		
Total	77	1086.06			

Table S7.12: Anova data for the model describing the Pressure Drop response, for the filtration at 3.0 $L.min^{-1}$.

Analysis of Variance					
Source	DF	Adj SS	Adj MS	F-Value	P-Value
Model	5	1252607	250521.0	38.170	0.000
Linear	2	21088	10544.0	1.610	0.208
Zein	1	9948	9948.0	1.520	0.222
AcCell	1	11140	11140.0	1.700	0.197
Square	2	675197	337598.0	51.440	0.000
Zein*Zein	1	276553	276553.0	42.140	0.000
AcCell*AcCell	1	310689	310689.0	47.340	0.000
2-Way Interaction	1	556322	556322.0	84.760	0.000
Zein*AcCell	1	556322	556322.0	84.760	0.000
Error	72	472552	6563.0		
Lack-of-Fit	3	295344	98448.0	38.33	0.000
Pure Error	69	177208	2568.0		
Total	77	1725159			

Table S7.13: Anova data for the model describing the Collection response, for the filtration at 4.5 $L.min^{-1}$.

Analysis of Variance					
Source	DF	Adj SS	Adj MS	F-Value	P-Value
Model	5	259	51.9	17.260	0.000
Linear	2	138	69.0	22.960	0.000
Zein	1	7	7.5	2.490	0.119
AcCell	1	131	130.5	43.440	0.000
Square	2	105	52.5	17.460	0.000
Zein*Zein	1	75	75.3	25.060	0.000
AcCell*AcCell	1	18	18.2	6.06	0.016
2-Way Interaction	1	16	16.3	5.44	0.023
Zein*AcCell	1	16	16.3	5.44	0.023
Error	72	216	3.005		
Lack-of-Fit	3	145.602	48.534	47.31	0
Pure Error	69	70.779	1.026		
Total	77	475.698			

Table S7.14: Anova data for the model describing the Pressure Drop response, for the filtration at 4.5 $L.min^{-1}$.

Analysis of Variance					
Source	DF	Adj SS	Adj MS	F-Value	P-Value
Model	5	1057596	211519.0	46.500	0.000
Linear	2	395851	197926.0	43.510	0.000
Zein	1	11767	11767.0	2.590	0.112
AcCell	1	384085	384085.0	84.430	0.000
Square	2	623776	311888.0	68.560	0.000
Zein*Zein	1	506387	506387.0	111.320	0.000
AcCell*AcCell	1	187066	187066.0	41.12	0.000
2-Way Interaction	1	37969	37969.0	8.35	0.005
Zein*AcCell	1	37969	37969.0	8.35	0.005
Error	72	327521	4549		
Lack-of-Fit	3	314428	104809	552.34	0
Pure Error	69	13093	190		
Total	77	1385118			

Table S7.15: Anova data for the model describing the Collection response, for the filtration at 6.0 $L.min^{-1}$.

Analysis of Variance					
Source	DF	Adj SS	Adj MS	F-Value	P-Value
Model	5	168	33.5	6.940	0.000
Linear	2	20	9.8	2.020	0.140
Zein	1	16	15.6	3.220	0.077
AcCell	1	4	3.9	0.820	0.369
Square	2	20	9.8	2.040	0.138
Zein*Zein	1	7	7.5	1.540	0.218
AcCell*AcCell	1	10	9.7	2	0.161
2-Way Interaction	1	128	128.5	26.58	0.000
Zein*AcCell	1	128	128.5	26.58	0
Error	72	348	4.835		
Lack-of-Fit	3	225.494	75.165	42.31	0
Pure Error	69	122.594	1.777		
Total	77	515.766			

Table S7.16: Anova data for the model describing the Pressure Drop response, for the filtration at 6.0 $L.min^{-1}$.

Analysis of Variance					
Source	DF	Adj SS	Adj MS	F-Value	P-Value
Model	5	1881090	376218.0	19.870	0.000
Linear	2	16849	8424.0	0.450	0.643
Zein	1	8654	8654.0	0.460	0.501
AcCell	1	8195	8195.0	0.430	0.513
Square	2	826904	413452.0	21.840	0.000
Zein*Zein	1	112229	112229.0	5.930	0.017
AcCell*AcCell	1	631176	631176.0	33.34	0.000
2-Way Interaction	1	1037338	########	54.8	0.000
Zein*AcCell	1	1037338	########	54.8	0
Error	72	1363009	18931		
Lack-of-Fit	3	89044	29681	1.61	0.196
Pure Error	69	1273965	18463		
Total	77	3244099			

CONCLUSIONS

Through this study, we were able to understand the variables involved in the production process of nanofibers using the electrospinning technique. The variables could be manipulated to optimize the properties of natural polymers, equating them to the properties of synthetic materials. Polyvinyl alcohol (PVA) was used as the base polymer, with chitosan (CS) added to change the characteristics of the material, observing its rheological behavior and fiber morphology. The electrospun fibers were then tested for air filtration of fine and ultrafine particles, covering a range of pollutants and viruses in aerosols. The study also included the investigation of spider-nets, nanostructures formed between the main fibers of a fibrous medium. A mechanism for the formation of spider-nets was proposed, adapting and optimizing them to further improve nanoparticle collection efficiency. Finally, mechanical resistance studies were included, focused on air filtration, in order to maintain filtration efficiency at high speeds without compromising the material's effectiveness. Therefore, this study successfully achieved its objectives, contributing to science with new insights in the field of air pollution control.

PUBLISHED WORKS

Book Chapters

- Oliveira, A. E., Machry, K., Castro, B. J. C., **Mata, G. C.**, Bernardo, A., Guerra, V. G. & Aguiar, M. L. Physical Barrier Against COVID-19: Materials to Inhibit or Eliminate the Virus. in *Living with COVID-19* (Jenny Stanford Publishing, 2021). Chapter 14.
  DOI: https://doi.org/10.1201/9781003168287
  ISBN: 978-1-00-316828-7
- Paulo A. M. Chagas, Gabriela B. Medeiros, Edilton N. Silva, Maria Sirlene Morais, **Gustavo C. Mata**, Vádila G. Guerra, Mônica L. Aguiar, and Wanderley P. Oliveira. Desing and Characterization of the Electrospun Nanofibers Mats. In *Electrospun Nanofibers* (Taylor & Francis, 2023). Chapter 8.
  DOI: 10.12019781003333814
  ISBN: 978-1-003-33381-4
- **Gustavo C. Mata**, Paulo A. M. Chagas, Edilton N. Silva, Maria S. Morais, Gabriela B. Medeiros, Felipe A. Lima, Vádila G. G. Béttega, Wanderley P. Oliveira, Mônica L. Aguiar. Metal Oxide Nanofibers and Their Composites: Synthesis and Environmental Applications. In *Metal-oxide-based Nanomaterials and their Advanced Environmental Applications* (Elsevier, 2024). Chapter 21.
  DOI: -
  ISBN: 978-0-443-27308-7

Articles

- **Mata, G. C.**, Almeida, D. S. de, Oliveira, W. P. de & Aguiar, M. L. Nanofibers functionalized with surfactants to Eliminate SARS-CoV-2 and other airborne pathogens. *Conjecturas* **22**, 1929–1961 (2022). **(Review)**
  DOI: 10.53660/CONJ-708-A18

- **Mata, G. C. da**, Morais, M. S., Oliveira, W. P. de & Aguiar, M. L. Composition Effects on the Morphology of PVA/Chitosan Electrospun Nanofibers. *Polymers* **14**, 4856 (2022).
  DOI: https://doi.org/10.3390/polym14224856

- **da Mata**, G. C., Morais, M. S., de Oliveira, W. P. & Aguiar, M. L. Sustainable surgical masks: optimizing fine/ultrafine particle filtration using PVA/chitosan electrospun nanofibers. *Environ. Sci.: Nano* **10**, 2185–2200 (2023).
  DOI: http://dx.doi.org/10.1039/D3EN00182B

Congress Articles

- **Gustavo C. Mata**, Maria S. Morais, Wanderley P. Oliveira, Mônica L. Aguiar. Otimização da técnica de eletrofiação aplicada à filtração de sars-cov-2 simulado usando meios filtrantes biodegradáveis. Anais do XL Congresso Brasileiro de Sistemas Particulados (2022).
  DOI: http://dx.doi.org/10.17648/enemp-2022-159177

Submitted Articles

- **Gustavo C. Mata**, Maria S. Morais, Wanderley P. Oliveira, Mônica L. Aguiar. Spider-Nets in PVA/Chitosan Electrospun Nanofibers and their Influence on Nanoparticles Air Filtration. Environmental Science: Nano (2024).
- **Gustavo C. Mata**, Maria S. Morais, Guilherme J. Aguilar, Delia T. Tapia-Blácido, Wanderley P. Oliveira, Mônica L. Aguiar. Sustainable Surgical Masks II: Mechanical Properties Enhancement of Electrospun PVA/Chitosan Nanofibers. Journal of Cleaner Production (2024).

Appendix A

CONGRESS ARTICLE (PT-BR)

Otimização da Técnica de Eletrofiação Aplicada à Filtração de Sars-Cov-2 Simulado Usando Meios Filtrantes Biodegradáveis

GUSTAVO C. MATA[1*], MARIA S. MORAIS[2], WANDERLEY P. OLIVEIRA[2], MÔNICA L. AGUIAR[1]

[1]Universidade Federal de São Carlos, Programa de Pós-Graduação em Engenharia Química Laboratório de Controle Ambiental

[2]Universidade de São Paulo, Faculdade de Ciências Farmacêuticas de Ribeirão Preto

Laboratório de P&D em Processos Farmacêuticos

*gugs_cardoso@ufsj.edu.br

Resumo: A principal forma de contenção em surtos e pandemias é o uso de máscaras, como as cirúrgicas, mais acessíveis à população. Porém esses materiais são polímeros descartáveis, ajudando a poluir o meio ambiente. Este estudo usa polímeros como a quitosana (CS) e o álcool polivinílico (PVA) como uma alternativa biodegradável de meio filtrante. Foram testadas diferentes condições de produção de meios filtrantes pela técnica de eletrofiação usando soluções de PVA e CS e testando sua eficiência de filtração. Esses matérias foram avaliados sobre a metodologia de superfície de resposta, visando otimizar a eficiência de coleta e outros parâmetros de filtração. O material não só se mostrou promissor como foi capaz de ser mais eficiente que a máscara cirúrgica que serviu de base para este estudo.

A.1 Introdução

Entre os principais motivos para o espalhamento da pandemia de COVID-19 foi a alta transmissibilidade do SARS-CoV-2 (Morawska & Cao, 2020), gerando a expectativa de que pandemias surjam com maior frequência.

A primeira linha de defesa contra a disseminação de vírus de disseminação aérea é o uso de máscaras (Ippolito *et al.*, 2020). Entretanto, máscaras de tecido e máscaras cirúrgica têm suas limitações (Aydin *et al.*, 2020), sendo as N95 e FFP2 as mais eficientes contra o SARS-CoV-2 (Cheng *et al.*, 2021).

Máscaras cirúrgicas têm uma alta variedade de eficiência de filtração (Morais *et al.*, 2021), diminuindo sua confiabilidade. Sendo os vírus menores que $PM_{2.5}$ ou mesmo $PM_{0.1}$, a proteção de máscaras cirúrgicas precisa de ser efetiva contra bioaerossóis em escala nanométrica. Alguns vírus são capazes de se aderir a partículas pequenas ou às gotículas, e tendo estas suficiente momento, são capazes de ultrapassar os poros dos tecidos como projéteis carregados pelo fluxo de ar (Aydin *et al.*,2020).

Este estudo tem a inteção de avaliar a eficiência de filtração de nanopartículas de cloreto de sódio como simulação de vírus de SARS-CoV-2 e outros bioaerossóis em escala nanométrica. Como substitutos para os meios filtrantes convencionais usados em máscaras cirúrgicas, propõe-se o uso de matrizes poliméricas eletrofiadas de álcool polivinílico (PVA) e quitosana (CS). O meio filtrante foi funcionalizado com óleo essencial de *Lippia sidoides* para ação biocida e avaliadas as variações nos parâmetros de eletrofiação do material.

A.2 Metodologia

A.2.1 Solução precursora & Eletrospinning

PVA e CS foram dissolvidos em ácido acético 70%, sendo 6,0 e 1,0% em massa, respectivamente. O óleo de *Lippia sidoides* foi adicionado em 5% do teor de sólidos total. Baldim e colaboradores (2022) descrevem a obtenção e a caracterização do óleo utilizado. A eletrofiação da mesma solução variou os parâmetros de tensão do campo elétrico (20 a 25 kV), taxa de infusão (0,5 a 1,0 $mL.h^{-1}$) e o tempo de eletrofiação (30 a 60 min). As amostras resultantes estão descritas na **Tabela 1**.

Tabela 1: Parâmetros utilizados na construção do CCD rotacionável (variância constante no mesmo raio dentro do modelo) com $\alpha = 1,68$.

Amostra	Campo Elétrico (kV)	Taxa de Infusão (mL/h)	Tempo (min)
OE 1	20,00	0,50	30,00
OE 2	25,00	0,50	30,00
OE 3	20,00	1,00	30,00
OE 4	25,00	1,00	30,00
OE 5	20,00	0,50	60,00
OE 6	25,00	0,50	60,00
OE 7	20,00	1,00	60,00
OE 8	25,00	1,00	60,00
OE 9	18,29	0,75	45,00
OE 10	26,70	0,75	45,00
OE 11	22,50	0,33	45,00

OE 12	22,50	1,17	45,00
OE 13	22,50	0,75	19,77
OE 14	22,50	0,75	70,23
OE 15	22,50	0,75	45,00
OE 16	22,50	0,75	45,00
OE 17	22,50	0,75	45,00
OE 18	22,50	0,75	45,00
OE 19	22,50	0,75	45,00
OE 20	22,50	0,75	45,00

As fibras foram produzidas sobre a camada externa de máscaras cirúrgicas comerciais de três camadas. Depois de eletrofiadas, as fibras foram recobertas com outra camada externa, simulando uma máscara cirúrgica. A ideia central é construir um material similar às máscaras originais e compara a eficiência delas entre si.

A.2.2 Eficiência de Filtração

A eficiência de filtração, os fatores de qualidade e as permeabilidades do material foram testados no módulo disponível no Laboratório de Controle Ambiental do Departamento de Engenharia Química da Universidade Federal de São Carlos (DEQ/UFSCar). O módulo descrito na **Figura A.1** consiste em um compressor de ar, um filtro de ar para purificação, um gerador de nanopartículas, um secador por difusão, um neutralizador de criptônio e amerício um suporte para os filtros a serem testados. Acoplado ao aparato mencionado, tem-se um classificador eletrostático, um SMPS (*Scanning Mobility Particle Sizer spectometer*), e um contador de partículas (de Barros, 2014).

Os estudos de permeabilidade foram feitos com a passagem de ar limpo, com velocidade superficial (v_s) de 0,1 a 2,0 L.h^{-1} com vinte medições da queda de pressão. A partir da equação de Darcy (**Equação A.1**) é possível obter a constante de permeabilidade (k_1).

$$\frac{\Delta P}{L} = \frac{\mu}{k_1} v_s \qquad \textbf{(A.1)}$$

A técnica de mobilidade de partículas elétricas foi usada para obter a eficiência de filtração dos filtros (η). Este método calcula a diferença entre o número de partículas projetadas contra o filtro e aquelas que forem capazes de atravessá-lo (Bortolassi *et al*., 2017). Para a simulação do novo coronavírus (SARS-CoV-2), foi utilizado nanopartículas de cloreto de sódio (Leung & Sun, 2020) a uma velocidade superficial de 1,5 L.h^{-1}. A **Equação A.2** demonstra o cálculo.

$$\eta = \frac{C_0 - C_f}{C_0} . 100 \qquad \textbf{(A.2)}$$

onde C_0 e C_f são a concentração de nanopartículas antes e depois do meio filtrante, respectivamente.

O fator de de qualidade (Q_F), por sua vez, mede a performance geral do meio filtrante, e posse ser avaliada pela **Equação A.3**.

$$Q_f = \frac{-\ln(1-\eta)}{\Delta P} \qquad \textbf{(A.2)}$$

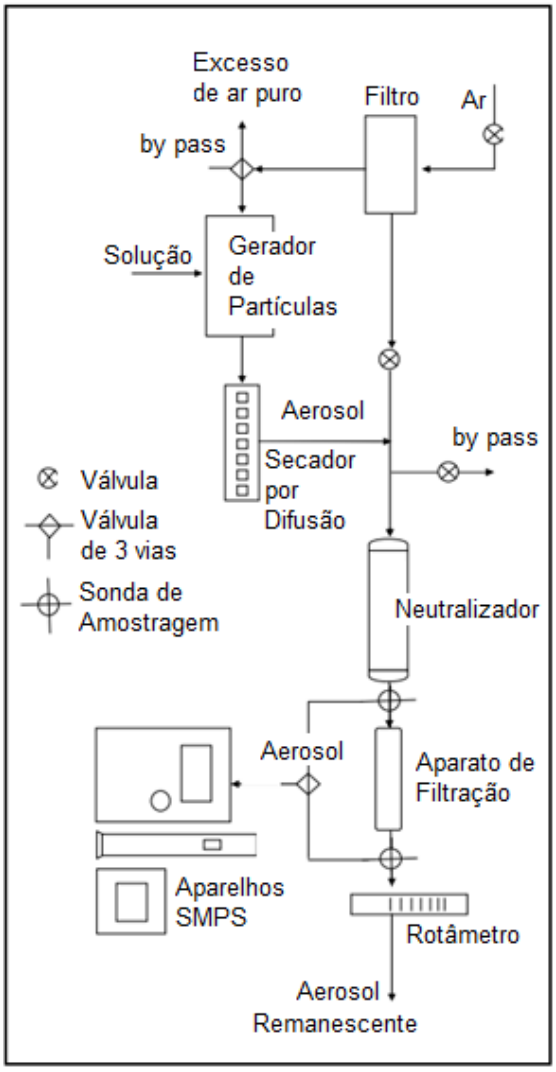

Figura A.1: Aparato experimental para avaliação de filtros do Laobratório de Controle Ambiental (DEQ/UFSCar).

A.2.3 Metodologia de Superfície de Resposta

Um Design de Compósito Central (CCD) é um típico planejamento fatorial fracionado usado na metodologia de superfície de resposta, como mostrado na **Figura A.2**. Este tipo de planejamento expande os pontos centrais para pontos externos ao modelo, chamados pontos axiais ou estrela (Bhattacharya, 2021). O CCD é mais preciso e nele não se faz necessária a construção de experimentos fatoriais de três níveis para gerar um modelo quadrático de segunda ordem (Granato & Alves, 2014).

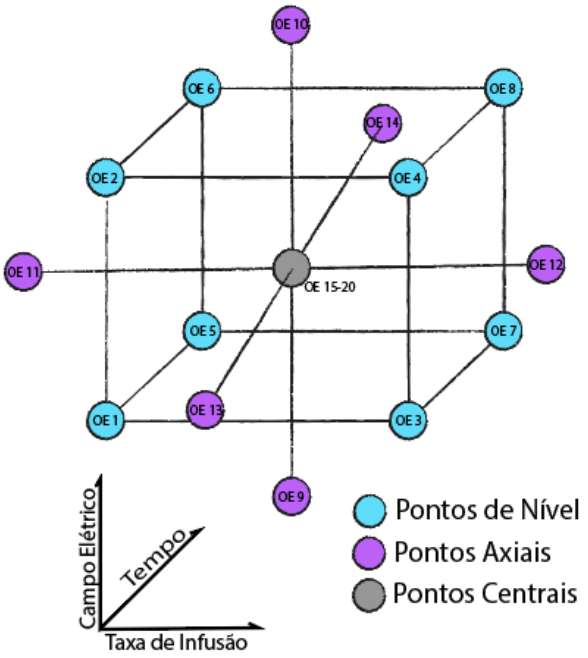

Figura A.2: Modelo de CCD 2^3 (três fatores com dois níveis cada) utilizado neste estudo de Superfície de Resposta.

Neste estudo foi utilizado três fatores (os eixos para cada dimensão do CCD cúbico), sendo o campo elétrico (kV), a taxa de infusão ($mL.h^{-1}$) e o tempo (min), com dois níveis para cada dimensão e seis repetições nos pontos centrais.

As respostas analizadas foram a eficiência global de filtração (η), a constante de permeabilidade dos gases (k_1) na lei de Darcy para a queda de pressão e o fator de qualidade final dos meios filtrantes (Q_F). Um modelo 2^3 em CCD (Modelo de compósito central) foi construído e analisado com Minitab® e o tratamento e regressão de dados foi feito utilizando-se o OriginPro® e Excel®.

A.3 Resultados & Discussão

A.3.1 Performance de Filtração

Os resultados obtidos neste estudo para a filtração estão dispostos na **Tabela A.2**.

Tabela A.2: Amostras produzidas por eletrofiação com os parâmetros utilizados no CCD. A queda de pressão ΔP foi avaliada a 4,8 $cm.s^{-1}$.

Sample	$K_1.10^{-12}$ (m^2)	η (%)	ΔP (Pa)	Q_F (Pa^{-1})
Mask	811	67,80	32,2	0,035
OE 1	17,8	94,10	122,9	0,023
OE 2	7,71	82,64	171,8	0,010
OE 3	68,8	70,93	33,1	0,046
OE 4	11,5	89,05	117,0	0,022
OE 5	26,4	88,80	107,5	0,020
OE 6	7,14	85,67	394,7	0,005
OE 7	14,3	98,40	253,0	0,016
OE 8	1,59	99,99	1793,3	0,006
OE 9	8,78	94,45	70,2	0,041
OE 10	3,96	99,65	559,3	0,010
OE 11	25,9	94,68	158,0	0,018
OE 12	3,76	99,90	398,4	0,017
OE 13	22,5	97,65	102,1	0,037
OE 14	5,18	99,51	419,2	0,013
OE 15	9,88	98,66	332,7	0,013
OE 16	6,71	99,60	333,0	0,017
OE 17	5,16	99,88	317,6	0,021
OE 18	4,02	99,90	312,5	0,022
OE 19	7,18	97,66	210,2	0,018
OE 20	7,52	99,62	267,1	0,021

Para velocidades próximas a deste estudo (5 $cm.s^{-1}$), um fator de qualidade próximo de 0,02 Pa^{-1} é considerado satisfatório (Leung *et al*., 2010), enquanto a análise teórica espera fatores de qualidade abaixo de 0,01 Pa^{-1} para fibras de 1 µm de tamanho médio (Bucher *et al*., 2013). Usando nanofibras de poliacrilonitrila (PAN), Bortolassi e colaboradores (2019) obtiveram fatores de qualidade entre 0,04 e 0,06, e Bonfim e colaboradores (2021) obtiveram uma faixa entre 0,02 e 3,5 usando amostra de diferentes concentrações de tereftalato de polietileno (PET) reciclado de garrafas plásticas. As **Figuras A.3** e **A.4** expõem os dados obtidos nos experimentos de filtração deste estudo.

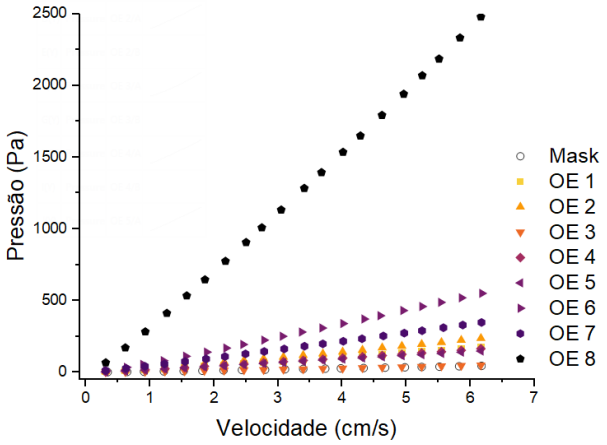

Figura A.3: Queda de pressão pela velocidade de filtração para os pontos de nível do CCD e para a máscara cirúrgica (mask).

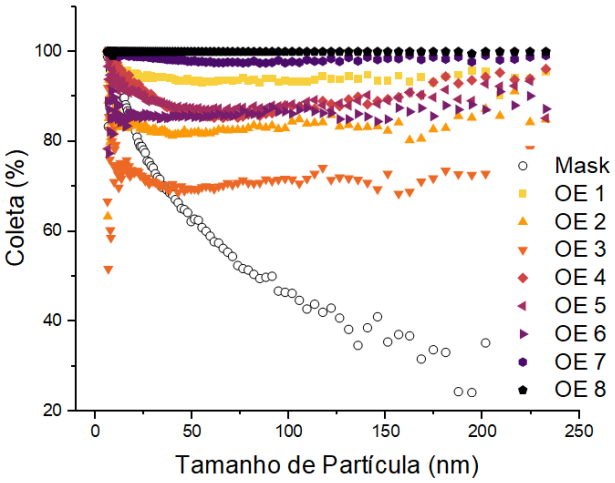

Figura A.4: Curvas de eficiência fracionada para os pontos de nível do CCD e para a máscara cirúrgica (mask). O diâmetro de distribuição de partícula variou de 7 a 250 nm, avaliado para velocidade de filtração de 4,8 $cm.s^{-1}$.

A queda nas curvas de eficiência de filtração (**Figura A.4**), especialmente na máscara cirúrgica, se deve pela MPPS (*most penetrating particle size*). Partículas menores que o diâmetro de MPPS são dominadas pelo mecanismo de difusão browniano, enquanto partículas maiores os mecanismos de interceptação têm mais influência *et al.*, 2015; Kravstov *et al.*, 2000; Lv *et al.*, 2018).

Partículas entre 100 e 250 nm são grandes o suficiente para sobrepor as forças difusivas, porém ainda muito pequenas para a coleta por impactação (Bortolassi *et al.*, 2019; Zhu *et al.*, 2017), portanto a eficiência de coleta tende a ser menos efetiva nesta faixa de tamanho de partículas. Partículas nanométricas (menores que 100 nm) podem facilmente atravessar os poros da matriz polimérica. Os efeitos de coleta predominantes são o de difusão Browniana e a atração eletrostática, quando partículas se aderem à superfície de fibras carregas, atraídas pelo seu campo elétrico (Konda *et al.*, 2020). As fibras com menor queda de pressão foram também as menos eficientes, enquanto as mais eficientes tiveram o custo de alta queda de pressão.

A.3.2 Metodologia de Superfície de Resposta

As curvas de nível obtidas pelo gráfico de superfície de resposta, estão expostas nas **Figuras A.5**, **A.6** e **A.7**.

Para as curvas de nível de k_1 é possível observar a influência de cada fator nas respostas. A interação binária entre a Taxa de Infusão, Campo Elétrico e Tempo mostra que o aumento desses fatores tende a diminuir a permeabilidade do material. Os dados são condizentes uma vez que uma alta Taxa de Infusão significa mais material sendo liberado pela agulha durante o processo de eletrofiação e, consequentemente, mais material está sendo dragado pelo campo elétrico em direção ao coletor. A fibra resultante será mais densa, menos porosa e como resultado terá sua permeabilidade reduzida.

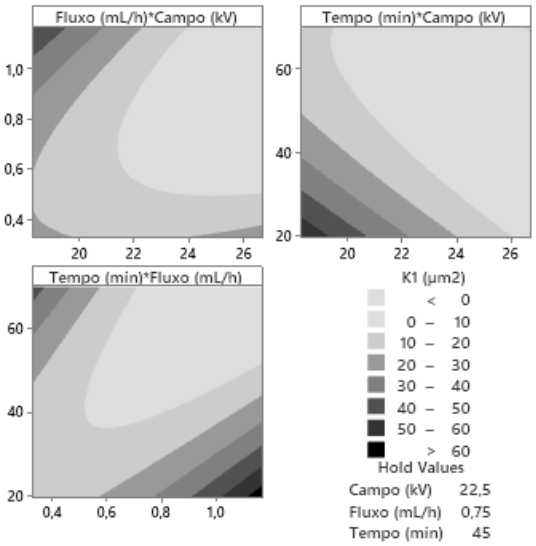

Figura A.5: Curvas de nível construída para a superfície de resposta, analisando a Constante de Permeabilidade (k_1) dos filtros estudados.

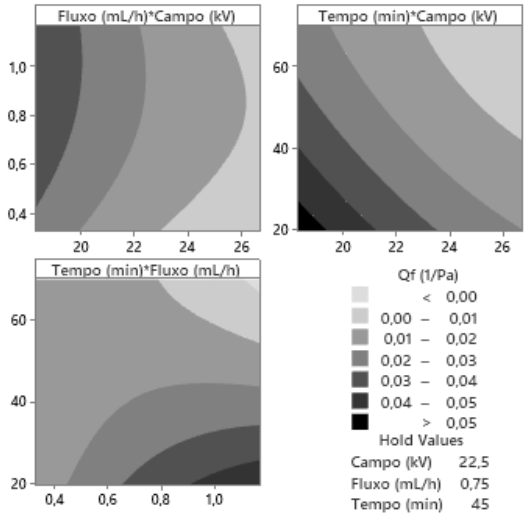

Figura A.6: Curvas de nível construída para a superfície de resposta, analisando o Fator de Qualidade (Q_F) dos filtros estudados.

Uma zona ótima foi encontrada para a eficiência de coleta para as curvas de Tempo e Campo Elétrico. Um tempo de eletrofiação entre 50 e 60 min e um campo elétrico próximo de 23 kV parece promover uma melhor filtração. Altas Taxas de Infusão seguem a mesma tendência, já que diminuem a permeabilidade. A sobreposição das diferentes curvas de nível é capaz de otimizar a filtração com adequada permeabilidade, afim de se melhor as propriedades do simulacro de máscara cirúrgica.

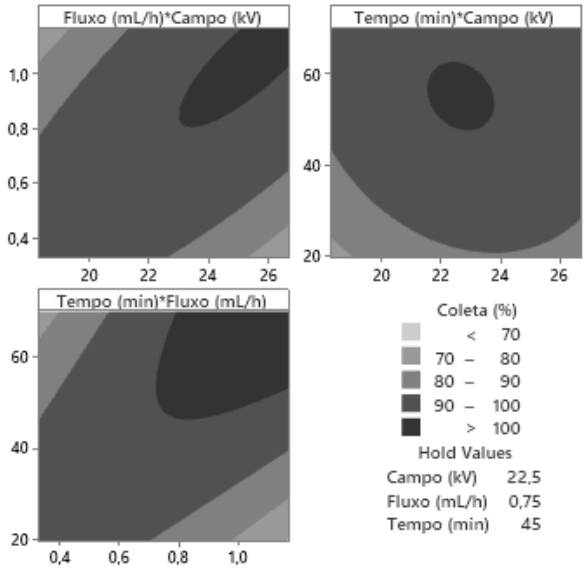

Figura A.7: Curvas de nível construída para a superfície de resposta, analisando a Eficiência de Coleta (η) dos filtros estudados.

A.4 Conclusão

O processo de produção de filtros de CS e PVA se mostrou eficiente durante a coleta e em alguns casos, apresentou fatores de qualidade superior ao da máscara cirúrgica comercial. As vantagens se apresentam principalmente pelo caráter natural e renovável, sendo tanto o PVA quanto a CS, materiais biodegradáveis. Ainda há uma série de estudo para tornar viável o uso das fibras eletrofiadas em máscaras, mas este estudo se mostrou promissor principalmente pela produção de meios filtrantes eficiente e de caráter ecológico, uma deficiência do mercado atual.

Agradecimentos

Os autores agradecem à Coordenação de Aperfeiçoamento de Pessoal de Nível Superior (CAPES Processo Nº 88887.505019/2020-00). Agradecemos também o apoio financeiro do Conselho Nacional de Desenvolvimento Científico e Tecnológico (CNPq – Processo Nº 424792/2018-4) e a Fundação de Amparo a Pesquisa de São Paulo (FAPESP – Processo Nº 2018/26069-0).

A.5 Referências

AYDIN, O., EMON, B., CHENG, S., HONG, L., CHAMORRO, L.P., SAIF, M.T.A., (2020), Performance of fabrics for home-made masks against the spread of COVID-19 through droplets: A quantitative mechanistic study. Extreme Mechanics Letters 40, 100924.

BALDIM, I., PAZIANI, M.H., GRIZANTE BARIÃO, P.H., KRESS, M.R. VON Z., OLIVEIRA, W.P., (2022), Nanostructured Lipid Carriers Loaded with Lippia sidoides Essential Oil as a Strategy to Combat the Multidrug-Resistant Candida auris. Pharmaceutics 14, 180.

BHATTACHARYA, S., (2021), Central Composite Design for Response Surface Methodology and Its Application in Pharmacy, Response Surface Methodology in Engineering Science. IntechOpen.

BONFIM, D.P.F., CRUZ, F.G.S., BRETAS, R.E.S., GUERRA, V.G., AGUIAR, M.L., (2021), A Sustainable Recycling Alternative: Electrospun PET-Membranes for Air Nanofiltration. Polymers 13, 1166.

BORTOLASSI, A.C.C., GUERRA, V.G., AGUIAR, M.L., (2017),

Characterization and evaluate the efficiency of different filter media in removing nanoparticles. Separation and Purification Technology 175, 79–86.

BORTOLASSI, A.C.C., NAGARAJAN, S., DE ARAÚJO LIMA, B., GUERRA, V.G., AGUIAR, M.L., HUON, V., SOUSSAN, L., CORNU, D., MIELE, P., BECHELANY, M., (2019), Efficient nanoparticles removal and bactericidal action of electrospun nanofibers membranes for air filtration. Mater Sci Eng C Mater Biol Appl 102, 718–729.

BUCHER, T.M., TAFRESHI, H.V., TEPPER, G.C., (2013), Modeling performance of thin fibrous coatings with orthogonally layered nanofibers for improved aerosol filtration. Powder Technology 249, 43–53.

CHENG, Y., MA, N., WITT, C., RAPP, S., WILD, P.S., ANDREAE, M.O., PÖSCHL, U., SU, H., (2021), Face masks effectively limit the probability of SARS-CoV-2 transmission. Science 372, 1439–1443.

DE BARROS, P.M., RODRIGUES CIRQUEIRA, S.S., AGUIAR, M.L., (2014), Evaluation of the Deposition of Nanoparticles in Fibrous Filter. Materials Science Forum 802, 174–179.

GRANATO, D., ARES, G., (2014), Mathematical and Statistical Methods in Food Science and Technology. John Wiley & Sons.

IPPOLITO, M., VITALE, F., ACCURSO, G., IOZZO, P., GREGORETTI, C., GIARRATANO, A., CORTEGIANI, A., (2020), Medical masks and Respirators for the Protection of Healthcare Workers from SARS-CoV-2 and other viruses. Pulmonology 26, 204–212.

KONDA, A., PRAKASH, A., MOSS, G.A., SCHMOLDT, M., GRANT, G.D., GUHA, S., (2020), Aerosol Filtration Efficiency of Common Fabrics Used in Respiratory Cloth Masks. ACS Nano 14, 6339–6347.

KRAVTSOV, A., BRNIG, H., ZHANDAROV, S., BEYREUTHER, R., (2000), The electret effect in polypropylene fibers treated in a corona discharge.

LEUNG, W.W.-F., HUNG, C.-H., YUEN, P.-T., (20100, Effect of face velocity, nanofiber packing density and thickness on filtration performance of filters with nanofibers coated on a substrate. Separation and Purification Technology 71, 30–37.

LEUNG, W.W.F., SUN, Q., (2020), Electrostatic charged nanofiber filter for filtering airborne novel coronavirus (COVID-19) and nano-aerosols. Separation and Purification Technology 250, 116886.

LV, D., ZHU, M., JIANG, Z., JIANG, S., ZHANG, Q., XIONG, R., HUANG, C., (2018), Green Electrospun Nanofibers and Their Application in Air Filtration. Macromolecular Materials and Engineering 303, 1800336.

MORAIS, F.G., SAKANO, V.K., LIMA, L.N. DE, FRANCO, M.A., REIS, D.C., ZANCHETTA, L.M., JORGE, F., LANDULFO, E., CATALANI, L.H., BARBOSA, H.M.J., JOHN, V.M., ARTAXO, P., (2021), Filtration efficiency of a large set of COVID-19 face masks commonly used in Brazil. Aerosol Science and Technology 0, 1–21.

MORAWSKA, L., CAO, J., (2020),. Airborne transmission of SARS-CoV-2: The world should face the reality. Environment International 139, 105730.

ZHU, M., HAN, J., WANG, F., SHAO, W., XIONG, R., ZHANG, Q., PAN, H., YANG, Y., SAMAL, S.K., ZHANG, F., HUANG, C., (2017), Electrospun Nanofibers Membranes for Effective Air Filtration. Macromolecular Materials and Engineering 302, 1600353.

Appendix B

CELLULOSE & IONIC LIQUIDS

Electrospinning of Cellulose using Ionic Liquids

B.1 Introduction

Cellulose is a biocompatible, biodegradable, and abundant environmentally friendly material. Cellulose fibers have great applications potential for membranes, biosensors, electronics, and catalytic supports [1]. However, cellulose is insoluble in water and common organic solvents due to the extensive intra and intermolecular hydrogen bonds[1,2]. For air filtration purposes, cellulose nanofibers have a low removal efficiency for PM 2.5 due to the lack of active chemical groups on the surface of cellulose nanofibers[3].

Only in 2002 the dissolution of cellulose in an ionic liquid (IL) was reported[4], opening the synthesis of a new class of strongly hydrogen-bonded organic compounds and the dissolution of energetic materials[5]. The high solvating power of ILs[6] makes them recognized as "green solvents"[1] due to properties such as low melting points, negligible vapor pressure, general non-flammability, thermal stability, and recycling simplicity[7,8]. They also possess a bactericide effect[9], however, their virucidal action is still inconclusive[10].

Since electrospinning has been routinely based on aggressive organic solvents, biopolymers' dissolution in ILs has gained attention[11]. Electrospinning of cellulose solubilized in ILs[12] is already possible, even for lignocellulose[13], and when tested for air filtration, increased the PM 2.5 removal when compared with traditional cellulose filters[9]. This study intents to produce cellulose filters using ILs as the solvent and test the resulting fibers for air filtration. 1-ethyl-3-methylimidazolium acetate ([Emim][Ac]) was reported as the most effective ionic liquid for cellulose dissolution[14,15], and was already tested for electrospinning of cellulose solutions[1,12,16]. **Figure B.1** describes an ionic liquid's general structure compared with an ionic solid.

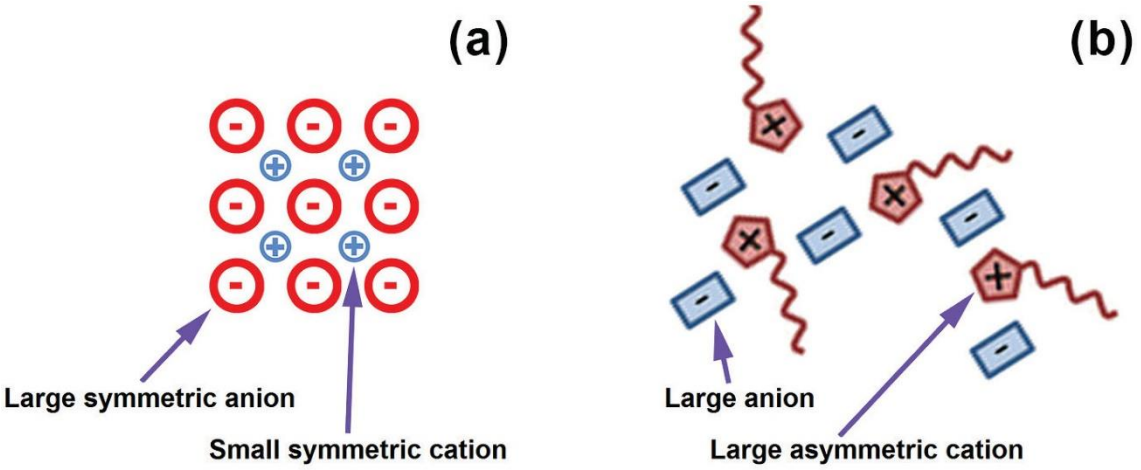

Figure B.1: Structures in room temperature of **a)** an ionic solid and **b)** an ionic liquid. Adapted from[17].

B.2 Materials & Methods

B.2.1 Cellulose Solubilization

The cellulose sample was dried at 70 and 100 °C for 5h to reduce the water content. Cellulose was solubilized in ionic liquid 1-ethyl-3-methylimidazolium acetate ([EMIM][Ac], Sigma Aldrich) as the main solvent, using N,N-dimethylformamide (DMF) as cosolvent. The proportion varies from [EMIM][Ac]/DMF, using from 1:0 (pure IL), 9:1, 1:1 and 2:3 (v/v), to teste the different conditions that are able to dissolve cellulose. The tests were all conducted in three different sets of temperature: room temperature, 50 and 90 °C. Cellulose concentration was also tested, ranging from 2.5 to 15%. The experiments were conducted by 2 hours of dissolution time with a magnetic stirrer at 100 rpm.

B.2.2 Electrospinning

The electrospinning process was conducted differently than usual. Once ionic liquids are not volatile (low vapor pressure), so the ILs remain inside the fibers during the elongation and deposition process. The technique applied was the Dry-jet Wet Electrospinning due to the necessity of an ethanol coagulation bath. The procedure scheme is outlined in **Figure B.2**. This adjustment is necessary for the ILs removal from the fiber after the deposition onto the collector. This modification introduces a coagulation bath between the needle and the charged metal plate to serve as a collector[12].

In this system, a PTFE tube changes the polymer flow's direction to a vertical position, directing the polymer solution to a coagulation bath, for the complete removal of the solvent from de fiber, *in situ*[16].

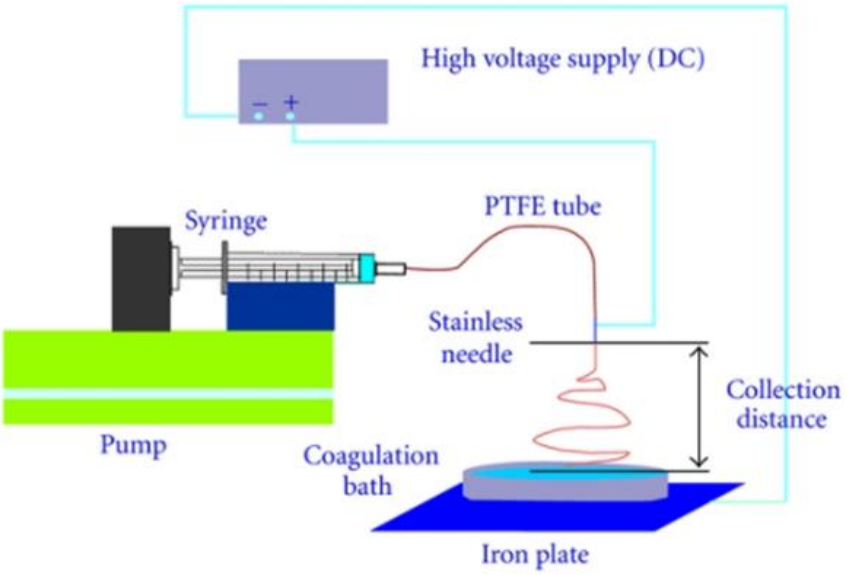

Figure B.2: Schematic design of dry-jet wet electrospinning [12].

Microcrystalline cellulose (MCC) was chosen to serve as a cellulose basis. The MCC will be dissolved in the ionic liquid 1-ethyl-3-methylimidazolium acetate ([EMIM][Ac]) under magnetic stirring for 2 hours. To improve the viscosity and the spinnability of the polymer solution, we added a cosolvent to the primary solvent (*i.e.*, [EMIM][Ac]). The cosolvent that is used is dimethylformamide (DMF) because of its good interaction with [EMIM][Ac][18]. The tests conducted varying the proportion of solvent and cosolvent as the following proportions of [EMIM][Ac]:DMF, temperature, and MCC content.

- Proportions: 1:0; 9:1; 7:1; 5:1; 3:2; 1:1 and 2:3;
- Cellulose content: 2.5, 5.0, 7.5, 10.0, 12.5, and 15.0.

All the experiments will be conducted at the Laboratory of Environmental Control I at the Department of Chemical Engineering of the Federal University of São Carlos (DEQ/UFSCar).

B.2.3 Fiber Functionalization

It is known that Ionic liquids kill bacteria, but their action against viruses is still in discussion[10]. So, it is necessary to functionalize the fibers properly for application as a biocidal membrane. Cellulose fibers were impregnated with a quaternary ammonium salt (QAS), a cationic surfactant, to modify the produced filters granting a biocidal activity.

Cellulose and QAS have good molecule interactions[19]. So it was chosen the cetyltrimethylammonium bromide (CTAB) was used as QAS to functionalize the cellulose fibers. The produced filter media was washed with an aqueous solution with 1% of CTAB content.

B.3 Results

B.3.1 Cellulose Dissolution

Figure B.3 show the difference in drying the cellulose at 70 and 100 °C. The cellulose dissolution process was conducted in a different set of parameters to avail the best conditions to dissolve the cellulose.

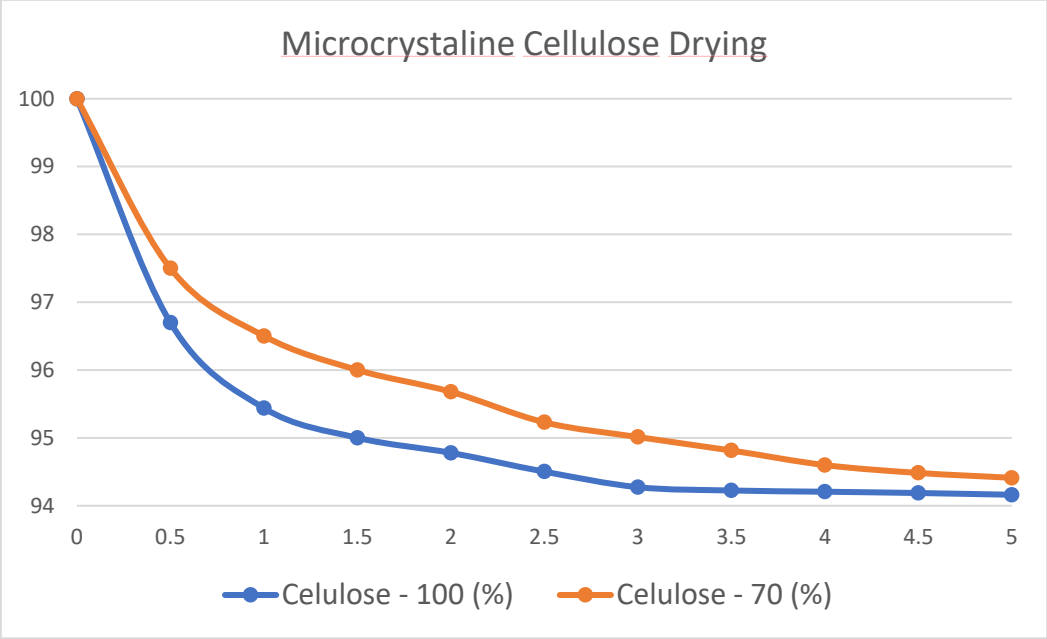

Figure B.3: water loss during the time for cellulose at 70 °C (orange) and 100 °C (blue) during 5h period.

It was observed that the dissolution process is difficult in cellulose contents above 7.5 % (w/v) at room temperatures. It is known that the [EMIM][Ac] is a powerful solvent for cellulose, but the process of dissolution of higher contents needs too much time under agitation or heating to occur[1,11,14,15,20]. The cellulose crystal type significantly impacts its dissolution, and the solubility decreases with increases in cellulose molecular weight and crystallinity[2]. Nonetheless, a higher degree of crystallinity usually indicates enhanced thermal properties [1].

Both IL anions and cations were involved in the dissolution of cellulose[21]. Still, it occurs when the IL anions form hydrogen bonds with the cellulose[22]. The disruption of the cellulose intramolecular bonds is the new bonds (*i.e.*, IL-cellulose) more robust than the previous intramolecular bond[1,2]. The presence of water can also decrease the solubility of cellulose due to competitive hydrogen bonding.

It was also observed that adding DMF helped dissolve cellulose in all samples at room temperature to different degrees. Cosolvents can diminish the interactions of the cations and anions inside the ionic liquid molecule, separating the $[EMIM]^+$ from $[Ac]^-$ ions[18], with significant effects on the viscosity of the IL[15]. This phenomenon increases the availability of the ionic liquid ions to interact with the cellulose chains and disrupts their strong intermolecular hydrogen bond.

It is worth mentioning that all the solutions could solubilize the cellulose content after heating. At 50 °C, all the solutions dissolved the complete content of cellulose with approximately 1 hour of heating. All the collected data were summarized in **Table B.1**.

Table B.1: Dissolution of cellulose on different compositions of [EMIM][Ac]:DMF, by temperature.

[EMIM][Ac]:DMF	Temperature (°C)	Cellulose Concentration					
		2.5	5	7.5	10	12.5	15
P-IL*	RT**	+++	+++	++	++	+	+
9:1	RT**	+++	+++	+++	+++	+++	++
1:1	RT**	+++	+++	+++	+++	+++	++
2:3	RT**	+++	+++	+++	+++	+++	+
P-IL*	50	+++	+++	+++	+++	+++	+++
9:1	50	+++	+++	+++	+++	+++	+++
1:1	50	+++	+++	+++	+++	+++	+++
2:3	50	+++	+++	+++	+++	+++	+++

Legend: (+) poor dissolution; (++) partial dissolution; (+++) complete dissolution. * P-IL: Pure ionic liquid. ** RT: Room temperature.

The sample with 15 % of cellulose was the only one that did not completely dissolve the cellulose at room temperature after adding DMF. Notably, the proportion of 2:3 ([EMIM][Ac]:DMF) had the poorest dissolution. It can be explained by the low content of [EMIM][Ac], which was incapable of properly interacting with the cellulose chains due to the excess DMF in the solution.

B.3.2 Cellulose electrospinning

The following set, exposed in **Figure B.4,** was constructed. Unfortunately, after several adaptations, the electrospinning process was not concluded due to coagulation on the needle tip. We expected that the ethanol vapor was responsible for the early coagulation of the fibers.

The traditional electrospinning set was tested with small progresses, but other hindrances appeared. Electrospinning using ILs needs higher electrical fields (above 20 kV), but due to the high conductivity of the ILs, the electrical charges in the needle pole passed through the fibers towards the collector. These discharges generated current on the equipment, oscillating the electrical field potential. The highest electrical field possible for our apparatus without discharge was 12 kV, below the required for IL electrospinning. The first fibers were only obtained by reducing the distance between the needle tip and the collector to 8 cm, but did not result in a fiber mat.

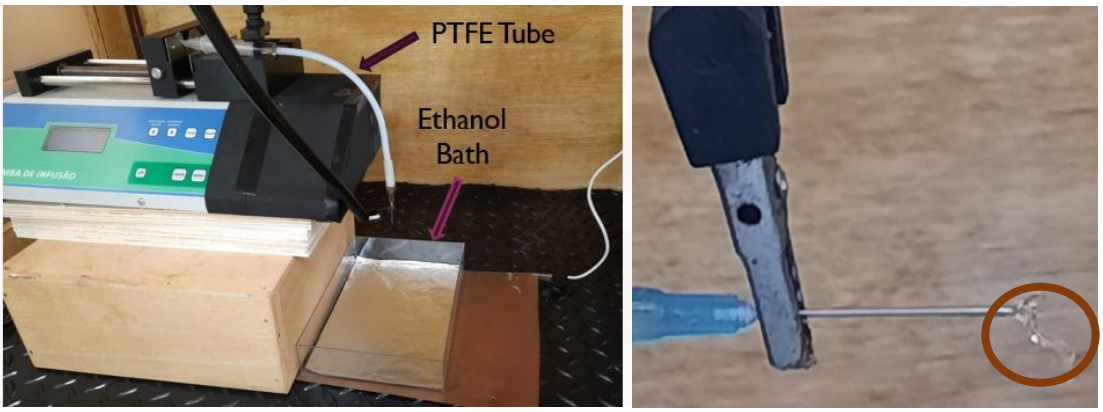

Figure B.4: On the left, dry-jet wet apparatus at the LCA/UFSCar. On the right, the coagulated solution is at the needle tip.

B.4 Conclusions

Cellulose was properly solubilized in ionic liquids with and without the cosolvent DMF. The temperature rise was necessary, especially for the high contents of cellulose. Unfortunately, the electrospinning of cellulose in fiber mats was impossible due to technical issues. Not only the ILs are highly conductive, causing descharges between the needle and the collector, as the humidity and the ethanol vapor of the bath seems to interfere in the coagulation process, solidifying the fibers precociously.

Acknowledgments

The authors would like to acknowledge the Coordination for the Improvement of Higher Education Personnel (Coordenação de Aperfeiçoamento de Pessoal de Nível Superior – CAPES), process No. 88887.505019/2020-00; we also would like to thanks the National Council for Scientific and Technological Development (Conselho Nacional de Desenvolvimento Científico e Tecnológico - CNPq), process No. 424792/2018-4, for all the support.

B.5 References

1. Freire, M. G. *et al.* Electrospun nanosized cellulose fibers using ionic liquids at room temperature. *Green Chem.* **13**, 3173–3180 (2011).
2. Mohd, N., Draman, S. F. S., Salleh, M. S. N. & Yusof, N. B. Dissolution of cellulose in ionic liquid: A review. *AIP Conference Proceedings* **1809**, 020035 (2017).
3. Jiang, F., Kittle, J. D., Tan, X., Esker, A. R. & Roman, M. Effects of Sulfate Groups on the Adsorption and Activity of Cellulases on Cellulose Substrates. *Langmuir* **29**, 3280–3291 (2013).
4. Swatloski, R. P., Spear, S. K., Holbrey, J. D. & Rogers, R. D. Dissolution of Cellose with Ionic Liquids. *J. Am. Chem. Soc.* **124**, 4974–4975 (2002).
5. Zhu, H. X., Li, J. S., Xu, R. & Yang, S. Y. An environmental friendly approach for the synthesis of the ionic liquid 1-ethyl-3-methylimidazolium acetate and its dissolubility to 1, 3, 5-triamino-2, 4, 6-trinitrobenzene. *Journal of Molecular Liquids* **165**, 173–176 (2012).
6. Rodríguez, H., Gurau, G., Holbrey, J. D. & Rogers, R. D. Reaction of elemental chalcogens with imidazolium acetates to yield imidazole-2-chalcogenones: direct evidence for ionic liquids as proto-carbenes. *Chem. Commun.* **47**, 3222–3224 (2011).

7. MacFarlene, D. R., Kar, M. & Pringle, J. M. Synthesis of Ionic Liquids. in *Fundamentals of Ionic Liquids* 81–102 (John Wiley & Sons, Ltd, 2017). doi:10.1002/9783527340033.ch4.
8. Nicosia, A. *et al.* Air filtration and antimicrobial capabilities of electrospun PLA/PHB containing ionic liquid. *Separation and Purification Technology* **154**, 154–160 (2015).
9. Zhu, M. *et al.* A novel cellulose acetate/poly (ionic liquid) composite air filter. *Cellulose* **27**, 3889–3902 (2020).
10. Fister, S. *et al.* Virucidal Influence of Ionic Liquids on Phages P100 and MS2. *Front. Microbiol.* **0**, (2017).
11. Silva, B. A. *et al.* Electrospinning of cellulose using ionic liquids: An overview on processing and applications. *European Polymer Journal* **147**, 110283 (2021).
12. Bazbouz, M. B., Taylor, M., Baker, D., Ries, M. E. & Goswami, P. Dry-jet wet electrospinning of native cellulose microfibers with macroporous structures from ionic liquids. *Journal of Applied Polymer Science* **136**, 47153 (2018).
13. Ahn, Y. *et al.* Electrospinning of lignocellulosic biomass using ionic liquid. *Carbohydrate Polymers* **88**, 395–398 (2012).
14. Mikkola, J.-P. *et al.* Ultrasound enhancement of cellulose processing in ionic liquids: from dissolution towards functionalization. *Green Chem.* **9**, 1229–1237 (2007).
15. Verma, C. *et al.* Dissolution of cellulose in ionic liquids and their mixed cosolvents: A review. *Sustainable Chemistry and Pharmacy* **13**, 100162 (2019).
16. Meli, L., Miao, J., Dordick, J. S. & Linhardt, R. J. Electrospinning from room temperature ionic liquids for biopolymer fiber formation. *Green Chem.* **12**, 1883–1892 (2010).
17. Harada, L. K. *et al.* Insights into Protein-Ionic Liquid Interactions Aiming at Macromolecule Delivery Systems. *Journal of the Brazilian Chemical Society* **29**, 1983–1998 (2018).
18. Phadagi, R. *et al.* Understanding the role of Dimethylformamide as co-solvents in the dissolution of cellulose in ionic liquids: Experimental and theoretical approach. *Journal of Molecular Liquids* **328**, 115392 (2021).
19. Tavakolian, M., Jafari, S. M. & van de Ven, T. G. M. A Review on Surface-Functionalized Cellulosic Nanostructures as Biocompatible Antibacterial Materials. *Nano-Micro Lett.* **12**, 73 (2020).
20. Sirviö, J. A. & Heiskanen, J. P. Room-temperature dissolution and chemical modification of cellulose in aqueous tetraethylammonium hydroxide–carbamide solutions. *Cellulose* **27**, 1933–1950 (2020).
21. Bentivoglio, G. *et al.* Cellulose processing with chloride-based ionic liquids. *Lenzinger Berichte* **86**, (2006).
22. Novoselov, N. P., Sashina, E. S., Petrenko, V. E. & Zaborsky, M. Study of dissolution of cellulose in ionic liquids by computer modeling. *Fibre Chem* **39**, 153–158 (2007).

Appendix C

DATA AUTOMATIZATION

Treatment & Automatization of Air Filtration Data using Algorithms in Python Language

C.1 Introduction

During the development of a research project, the process of data treatment can be a dispendious and tiring process. As the science evolves, the usage of tools like computer science became essential to help researchers during the day-by-day tasks, especially the repetitive work. Following this trend, some parts of this study was automatized using a versatile language for coding the solutions: Python. To show the power of the nowadays algorithms, a description of the Python language was created using an artificial intelligence, called ChatGPT-3 (Generative Pretrained Transformer 3), from OpenIA®.

> "*Python is a high-level, interpreted and general-purpose programming language that was created by Guido van Rossum in the late 1980s. It has a design philosophy that prioritizes readability and simplicity, making it an ideal language for beginners to learn.*
>
> *One of the most notable features of Python is its dynamically-typed variables, which allows for great flexibility in terms of data types. It supports multiple programming paradigms, including procedural, object-oriented, and functional programming. This makes it a versatile language that can be used for a variety of tasks, from web development to scientific computing.*
>
> *Python also has a vast library of pre-written code, known as the Python Standard Library, which provides developers with tools for various tasks such as connecting to the web, reading and writing files, and working with data. Additionally, Python has an active community of users and developers who have created thousands of third-party packages, making it easy to add functionality to a project.*
>
> *Another advantage of Python is its ease of use, making it a popular language for prototyping and testing ideas. Its simple syntax and*

readability allow developers to focus on problem-solving and getting things done, rather than struggling with complex syntax.

In conclusion, Python is a powerful, versatile and easy-to-learn programming language that has become one of the most widely-used programming languages in the world. Its popularity is due to its simplicity, versatility, and the vast array of libraries and packages available. Whether you're a beginner or an experienced developer, Python is a language worth considering for your next project."

This section will merely describe the considerations and the algorithm used to treat the data obtained for the air filtration process, from the study exposed in **Chapter 4**.

C.2 Definitions

Before proceed with the development of the algorithm, some patters need to be stablished during the process of retrieving the air filtration data. The standardization is necessary, since the result of the data treatment can be influenced by minor issues, details and minutiae that varies from one operator to another when using the laboratory equipment (described in **Figure 4.2** and repeated below as **Figure C.1**). So, it was stablished some parameters:

- The Particle Generator (MARCA E MODELO) has a rotameter in its backside to control the number of nanoparticles generates, being the value set as 100 (UNIDADE);
- The NaCl solution concentration was defined in 0.1 g/L;
- The air flow rate used in the experiment was 1.5 $L.min^{-1}$;

The collection of particles was performed before (B) and after (A) the filtration device, in triplicate. However, the *modus operandi* during the collection can be performed in different ways. Some researchers collect the data in two batches, being:

- Two batches: a first batch of three collections before the filtration device, and then a new batch with three collections after the filtration device. (B-B-B, then A-A-A).

Other researchers in the lab have the preference of collect the data in a single batch, collecting all the data at once. They can perform their experiments in two ways:

- Multiple alternation batch: One collector before the filtration device, then a collection after, alternating the collections (B-A-B-A-B-A).
- Single alternation batch: Three collections before the filtration device, then three collections after the filtration device (B-B-B-A-A-A).

This is a simple question, related to the preference of each researcher that does not interfere in the final results. It appears to be a simple question, however during the data treatment, those minor issues change the disposition of the data in the files generated by the computer, and consequently, changes the data treatment. The final program can also be adapted to recognize the different batches, but this is a functionality that will be further implemented in the program. To perform this study, we choose the "single alternation batch" (B-B-B-A-A-A).

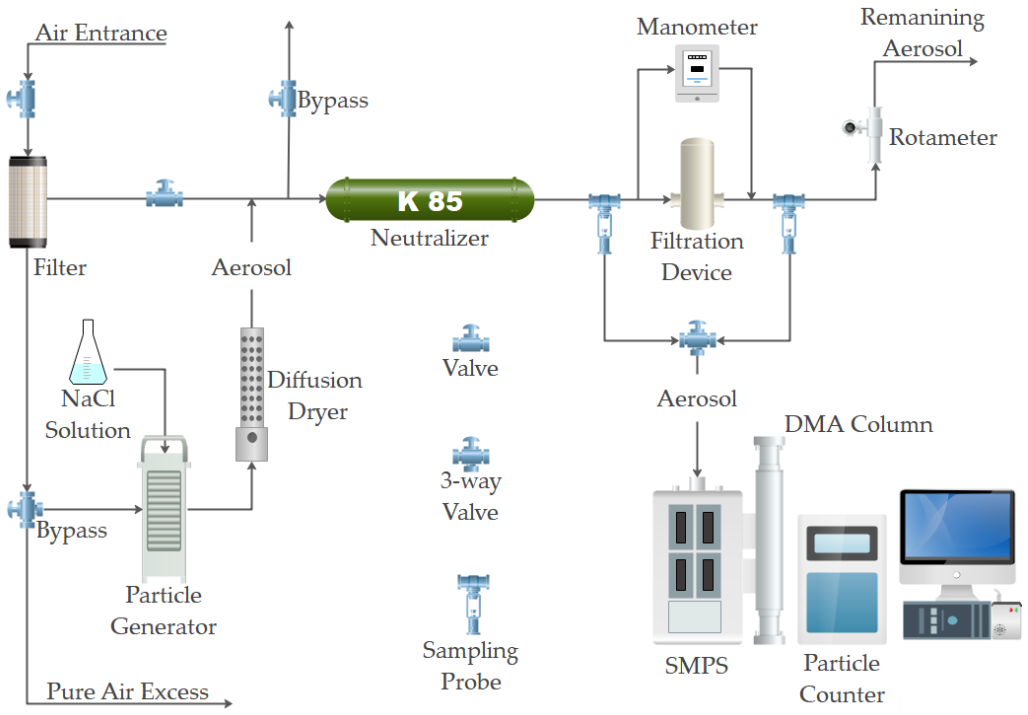

Figure C.1: Experimental apparatus to evaluate filter media efficiency (Repeated from **Chapter 4**, **Figure 4.2**).

C.3 The Python Algorithm

The following algorithm was constructed in Python language, version 3.10.1, using PyCharm 2021.3.1 (Community Edition) as compilator. The equations used to perform the calculus of efficiency was the described in **Equation 4.2**, or here, as **Equation C.1:**

$$\eta = \frac{C_0 - C_f}{C_0} . 100$$

where C_0 and C_f are the concentration of nanoparticles before and after the filter, respectively.

```
#PYTHON PROGRAM FOR AIR FILTRATION DATA TREATMENT

import os           #library responsible to operate system files
import csv          #library responsible to read CSV and TXT files
import openpyxl     #library responsible to manipulate excel files
(.xlsx)

def get_names(): #Function to retrieve the names of the files to be
treated
    # Set the directory to the folder containing the text files
    directory =
r"C:\Users\gugs_\Dropbox\UFSCar\Doutorado\Python\Input"

    # Get a list of all the files in the directory
    files: list[str] = os.listdir(directory)

    # Filter the list to include only text files
    text_files = [f for f in files if f.endswith(".txt")]
    return text_files

def TXTconverter():
    # Specify the directory where the ".txt" files are located
    input_directory =
r"C:\Users\gugs_\Dropbox\UFSCar\Doutorado\Python\Input"

    # Get a list of ".txt" files in the input directory
    txt_files = [f for f in os.listdir(input_directory) if
f.endswith('.txt')]

    # Create a new workbook
    workbook = openpyxl.Workbook()

    for i, txt_file_name in enumerate(txt_files):
        txt_file_path = os.path.join(input_directory, txt_file_name)

        # Extract the base name of the file (without extension) for
the sheet title
        sheet_name = os.path.splitext(txt_file_name)[0]

        # Create a new sheet in the workbook
        sheet = workbook.create_sheet(index=i, title=sheet_name)

        # Open the text file
        with open(txt_file_path, "r") as txt_file:
            # Create a CSV reader
            reader = csv.reader(txt_file, delimiter="\t")

            # Write the data from the text file to the Excel sheet
            for row in reader:
                sheet.append(row)

    # Specify the directory where you want to save the Excel file
    output_directory =
r"C:\Users\gugs_\Dropbox\UFSCar\Doutorado\Python\Manipulation"

    # Create the full path to save the Excel file
    excel_file_path = os.path.join(output_directory, "test.xlsx")

    # Save the workbook
    workbook.save(excel_file_path)
```

```
    # Load the saved workbook
    workbook = openpyxl.load_workbook(excel_file_path)

    for sheet_name in workbook.sheetnames:
        sheet = workbook[sheet_name]

        for row in sheet.iter_rows():
            for cell in row:
                if cell.data_type == "s":
                    try:
                        value = float(cell.value)
                        cell.value = value
                    except ValueError:
                        pass

    # Save the modified workbook
    modified_excel_file_path = os.path.join(output_directory,
"data.xlsx")
    workbook.save(modified_excel_file_path)

def Efficiency(username):
    from openpyxl import workbook, load_workbook
    wb =
load_workbook(r"C:\Users\gugs_\Dropbox\UFSCar\Doutorado\Python\Manipul
ation\data.xlsx")
    wb.sheetnames
    std = wb['Sheet']
    wb.remove(std)

wb.save(r"C:\Users\gugs_\Dropbox\UFSCar\Doutorado\Python\Manipulation\
data_exploring.xlsx")

    wb2 =
load_workbook(r"C:\Users\gugs_\Dropbox\UFSCar\Doutorado\Python\Manipul
ation\data_exploring.xlsx")
    for sheets in wb2:
        ws = sheets
        print(ws)

        ws['H21'] = 'Ef. Part.'
        ws['I21'] = 'Mean In.'
        ws['J21'] = 'Mean Out.'

        kst = 22
        while kst < 124:

            if ws[f'B{kst}'].value == 0 and ws[f'E{kst}'].value == 0:
                ws[f'B{kst}'] = 1
                ws[f'E{kst}'] = 1

            if ws[f'C{kst}'].value == 0 and ws[f'F{kst}'].value == 0:
                ws[f'C{kst}'] = 1
                ws[f'F{kst}'] = 1

            if ws[f'D{kst}'].value == 0 and ws[f'G{kst}'].value == 0:
                ws[f'D{kst}'] = 1
                ws[f'G{kst}'] = 1

            kst+=1

    for sheets in wb2:
```

```
        ws = sheets

        i = 22
        while i < 124:


            ws[f'H{i}'] = ((((ws[f'B{i}'].value + ws[f'D{i}'].value +
ws[f'C{i}'].value)/3)
                           - ((ws[f'F{i}'].value + ws[f'E{i}'].value
+ ws[f'G{i}'].value)/3))
                          /((ws[f'B{i}'].value + ws[f'D{i}'].value +
ws[f'C{i}'].value)/3))*100

            ws[f'I{i}'] = (ws[f'B{i}'].value + ws[f'D{i}'].value +
ws[f'C{i}'].value)/3

            ws[f'J{i}'] = (ws[f'F{i}'].value + ws[f'E{i}'].value +
ws[f'G{i}'].value) / 3

            i += 1

        ws['H10'] = 'Col. Ef.'
        ws['I10'] = 'Total In'
        ws['J10'] = 'Total Out'

        k = 22
        Tot_in = 0
        Tot_out = 0
        while k < 124:

            Tot_in = Tot_in + ws[f'I{k}'].value
            Tot_out = Tot_out + ws[f'J{k}'].value
            k += 1

        ws['I11'] = Tot_in
        ws['J11'] = Tot_out
        ws['H11'] = ((ws['I11'].value - ws['J11'].value) /
ws['I11'].value) * 100


wb2.save(rf"C:\Users\gugs_\Dropbox\UFSCar\Doutorado\Python\Manipulatio
n\data_resuming.xlsx")

def PressureDrop():
    pass

def Resume(username):
    from openpyxl import Workbook, load_workbook
    from openpyxl.utils import get_column_letter

    Resume = openpyxl.Workbook()

    wb =
load_workbook(rf"C:\Users\gugs_\Dropbox\UFSCar\Doutorado\Python\Manipu
lation\data_resuming.xlsx")
    wb.sheetnames
    new_sheet_name = "Resume"
    new_sheet = wb.create_sheet(title=new_sheet_name)

    Resumebook = wb['Resume']
```

```
    # Inicializing a list to keep the data from another tabs
    total_data = []

    # Iteration through the tabs
    for sheet in wb.sheetnames[:-1]:  # Excluding the last one
        table = wb[sheet]

        # Copying data
        sheet_data = []
        for line in range(21, 124):
            column_value_A = table[f'A{line}'].value
            column_value_H = table[f'H{line}'].value
            sheet_data.append((column_value_A, column_value_H))

        # Addind data to the list
        total_data.extend(sheet_data)

    # Pasting the data in the Resume sheet
    destiny_line = 2  # starting line
    for data in total_data:
          # First Column
        destiny_column = 1
        for value in data:
            Resumebook.cell(row=destiny_line, column=destiny_column,
value=value)
            destiny_column += 1  # Next column
        destiny_line += 1  # Next line

    sheet_list = wb.sheetnames
    # Counting the sheets number
    sheet_number = len(sheet_list)

    line_collect = 105
    column_destiny2 = 3
    line_destiny2 = 2

    while line_collect < (sheet_number-1)*105:

        # Defining the cell coordination
        origin_cell_A = f'A{line_collect}'
        origin_cell_B = f'B{line_collect}'

        # Obtaining the cell value
        origin_cell_value_A = Resumebook[origin_cell_A].value
        origin_cell_value_B = Resumebook[origin_cell_B].value

        destiny_cell_A =
f'{get_column_letter(column_destiny2)}{line_destiny2}'
        destiny_cell_B = f'{get_column_letter(column_destiny2 +
1)}{line_destiny2}'

        # Pasting the cell value on the destiny
        Resumebook[destiny_cell_A] = origin_cell_value_A
        Resumebook[destiny_cell_B] = origin_cell_value_B

        line_destiny2 += 1
        line_collect += 1

        if line_destiny2 >= 105:
            line_destiny2 = 2
            column_destiny2 += 2
```

```
        # Stop criteria
        if column_destiny2 > (sheet_number-1)*105:
            break

    cell_line = 1
    cell_column = 1

    sheet_list2 = get_names()

    # Iserting elements
    line2 = 1
    column2 = 1
    Resume_sheet = "Resume"
    sheet = wb[Resume_sheet]

    for data in sheet_list2:
        sheet.cell(row=line2, column=column2, value=data)
        column2 += 2  # Advancing to the next column

    # Selecting the data to erase
    sheet_cleaner = wb["Resume"]

    # Defining the interval to erase
    initial_line = 105
    final_line = 105*(sheet_number-2)
    columnA = "A"
    columnB = "B"

    # Removing the cell value
    for line in range(initial_line, final_line + 1):
        sheet_cleaner[f"{columnA}{line}"] = None
        sheet_cleaner[f"{columnB}{line}"] = None

    insertion_position = 2
    sheet.insert_rows(insertion_position, amount=1)

    #Saving the final excel file

wb.save(rf"C:\Users\gugs_\Dropbox\UFSCar\Doutorado\Python\Output\treat
ed_data {username}.xlsx")

def main():
    print("Filtration Data Treatment")
    username = input("What is the name you want in the end of your
file? ")

    TXTconverter()

    Efficiency(username)

    Resume(username)

    print(f"Hi! The file ending with {username} in folder 'Output'
contains your data.")
    print(f"The last sheet will present a resume of the data.")

main()
```

C.4 How to Use It

The algorithm and some examples to be tested will be available in the Git-Hub repository of the author. It can be found in the link below:

https://github.com/ti-guh/Air-Filtration

Worth to mention that the computed used to perform the data treatment was set the official language to English. Some nuances between languages, as the punctuation used to separate decimal numbers (“,” or “.”), can also interfere during the program process.

The program is very simple. Just put the files to be treated in the same folder of the program. Execute the program, and it will generate a file called “treated_data.xlsx”. The excel file will contain all the results.